
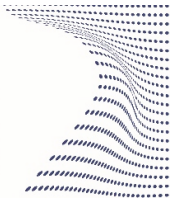

Doctoral Dissertation
Doctoral Program in Electrical, Electronics and Communication Engineering
(30th Cycle)

Analysis, Modeling and Excitation Control of Three-Stage Brushless Starter-Generators for Aircraft Applications

Adel Deriszadeh

Supervisors
Prof. Radu Bojoi, Supervisor
Prof. Alberto Tenconi, Co-Supervisor

Doctoral Examination Committee:
Prof. Angelo Tani, Referee, Università di Bologna
Prof. Davide Barater, Referee, Università di Modena e Reggio Emilia

Politecnico di Torino
April 30, 2018

I hereby declare that, the contents and organisation of this dissertation constitute my own original work and does not compromise in any way the rights of third parties, including those relating to the security of personal data.

…….....

Adel Deriszadeh

Turin, April 30, 2018

Summary

In aircraft application, due to space constraints, employing integrated starter-generator is an efficacious solution. Among various electric machines, wound rotor synchronous machine (WRSM) offers advantages of high reliability, sufficient controllability, high power factor in a wide range of torque-speed plan, etc. Requirement of supplying rotor of WRSM is its main drawback. Since in aircraft application, safety is a critical demand, brushless type of WRSM is a practical solution. A conventional structure of brushless WRSM consists three electrical machines which are mounted on a same shaft. Therefore, this kind of WRSM is called three-stage brushless synchronous machine. First stage of the machine is Pre-exciter which is usually a small PMG. Second stage in an inverse synchronous machine with stationary single-phase field and rotating armature which is called Main Exciter (ME). Third stage is the Main Generator (MG). Electrically, ME is connected to the MG by means of a rotating rectifier. Existence of the rotating rectifier connected between armature windings of ME and field winding of MG significantly increases nonlinearity of the system. In consequence, investigating nonlinear behavior of the rotating rectifier plays a key role in studying of the brushless synchronous starter-generator.

In this thesis, using analytical, numerical and experimental analysis, different operation modes of three-stage brushless synchronous machine are investigated. Using revolving field theory, analytical description of relationship between the stationary pulsating field flux of ME and its armature voltages is presented. Because of single-phase field winding of ME, at standstill and low speed operations, for exciting field winding of ME, AC excitation is required. Then, by speed increasing, AC excitation must be switched to DC. Since field excitation of ME is variable, induced armature voltages of ME are different in various operating points.

In this thesis, it is explained that during starting process of the starter-generator, armature voltages of ME are severely unbalanced. Therefore, for the sake of modelling and studying, a model of rotating rectifier with ability to deal with wide range of unbalanced conditions is required. As the first step, in this thesis a novel model of uncontrolled rectifier with capability of considering unbalanced input voltages and harmonics in AC-side is proposed.

Acknowledgment

First and foremost, I would like to express my deepest gratitude to my supervisors, professor. Radu Bojoi and Professor Alberto Tenconi, for their constant help with patience throughout my PhD research.

Special thanks are also owed to professor Andrea Cavagnino for his kind and valuable helps and advices.

Also, I am thankful to professors Eric Armando and Silvio Vaschetto whose supports are greatly appreciated.

This thesis is sincerely dedicated to my parents, Hasneh Solhamal and Vahab Deriszadeh, who showed me the true love in life and to my loving brothers, Abbas Deriszadeh and Ali Deriszadeh.

Contents

List of Tables

List of Figures

Chapter 1

Introduction

1.1 Motivation and Background

The main on-board source of power in a conventional aircraft is the engine that is used to create thrust and feed the other systems (bleed air for hydraulics and pneumatics, auxiliary gearbox to drive electrical generators and pumps). For a typical aircraft with 150-200 passenger capacity like Airbus A320 and Boeing 737, the thrust power is about 40 MW and non-thrust power is about 1.5 MW. Electrical power is the secondary power in an aircraft. In above-mentioned aircrafts, only 200 KW of the non-thrust power is used to convert into the electric power. By increasing attractiveness of more electric aircrafts (MEA), due to their significant benefits in terms of weight, volume, and reliability, trend of the industry is to increase the electrical power level of aircraft. For example, in Boeing 787, by eliminating the pneumatic bleed systems, about 1.5 MW of non-thrust power is converted to the electric power. The transition from bleed-air power to electric powered systems in Boeing 787 has been performed for the following systems:

- Engine start
- Auxiliary power unit (APU) start
- Wing ice protection
- Cabin pressurization
- Hydraulic pumps

Although the MEA concept is not a new concept, its feasibility significantly depends on the improvement of reliability and capability of power electronics and electrical machine design technologies.

Power electronics devices are used to convert the generated electric power to the demanded power level in terms of frequency and voltage. For example, the Boeing 787 has four different kinds of electric power buses which are:

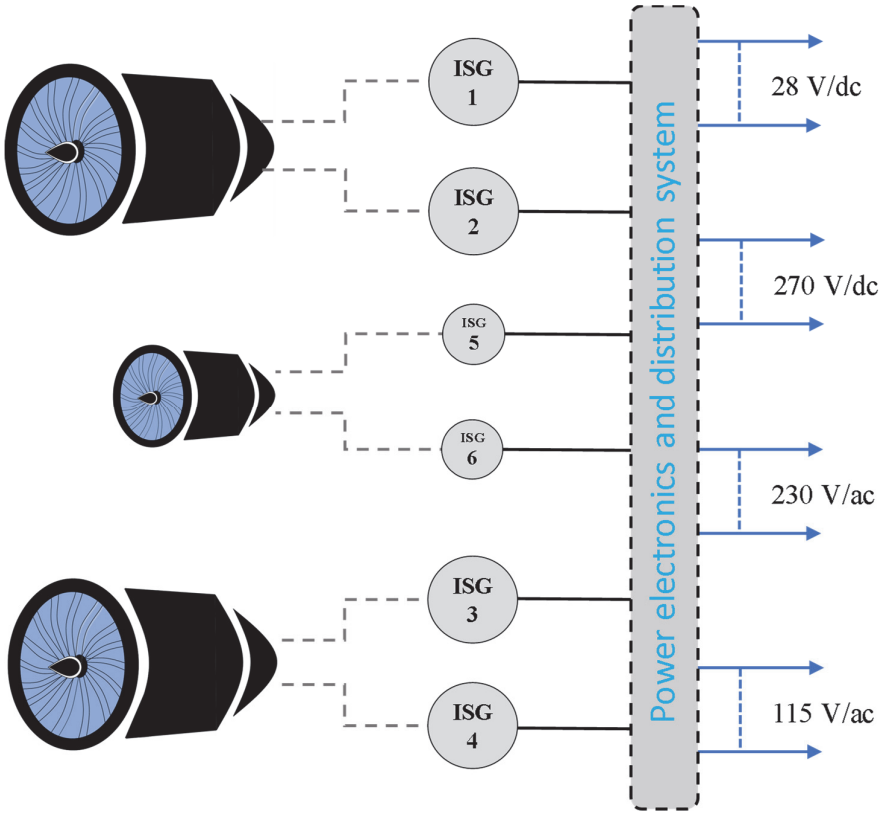

Figure. 1. 1. The electric power system of the Boeing 787

- 230 V, three-phase AC electric power bus with variable frequency (360-800Hz) to feed large loads.
- 115 V, three-phase AC electric power bus with constant frequency (400 Hz) to feed existing legacy loads such as the galley, windows heat systems and cooling fans of equipment.
- 28 V DC for avionic and small loads.
- 270 V DC for the environmental control system (ECS) which provides air supply, thermal control and cabin pressurization

In addition, the power electronics devices are used to control and drive the generators and actuators.

Electric machines play an important role in the MEA in order to replace hydraulic, pneumatic and gearbox driven subsystems with electrical driven subsystems. Implementing this replacement needs high-performance Integrated Starter/generator (ISG) electric machines and compact lightweight motor drives. The size of the electrical starter/generator system is determined by requirements of starting and power generation stages. The ISG must be able to start turbine engine in the prescribed amount of time under worst case condition. The ISG and Generator Control Unit (GCU) must be designed appropriately in order to perform the required start attempt sequences (starting duty cycles). The required sequence may be as follows:

1. First attempt: 30 seconds ON - 60 seconds OFF
2. Second attempt: 30 seconds ON – 5 minutes OFF
3. Third attempt: 30 seconds ON – 60 minutes OFF

The power generation requirement for an ISG is the amount of needed power for supplying the electric loads with sufficient redundancy regarding fault-tolerant requirements. Fig.1.1 shows the power system of the Boeing 787. As can be seen, it contains four 250 KVA main ISGs and two smaller ISGs as Auxiliary power units (APU).

1.2 Aims and Objectives

In start operation, the ISG must meet the load torque requirements with available power source limitations. In this thesis, a three-stage brushless synchronous machine is investigated as the ISG. Since during the starting mode, the ISG is fed by the APU or battery pack (small aircrafts), finding an efficient approach to excite the field winding of the machine for guarantee maximum exploiting of available power is necessary. In this regard, this thesis deals with describing nonlinear dynamics of the machine when is excited by variant excitation methods, in order to find the most efficient excitation method.

In the light of reliability and safety concerns for the aircraft power system, instead of machines with commutator and collector rings, brushless electrical machines are used as an ISG. The conventional brushless exciter synchronous starter/generator is a three-stage machine which comprises of a permanent magnet generator (PMG) which is called pre-exciter (PE), an AC exciter which is called Main Exciter (ME), an uncontrolled diode bridge rotating rectifier and a Main synchronous Generator (MG) which are mounted on a same shaft. Fig.1.2 shows the schematic of this kind of machine.

The PE has a rotating PM field and a stationary three-phase armature. The output of PE supplies the GCU. GCU contains a controlled DC/DC regulator and will be described in more details in this thesis. GCU provides a regulated DC power for the stationary single-phase field of ME. ME has a rotating armature which generates three-phase outputs and feeds a rotating rectifier through its armature windings. The rectified voltage of the rotating rectifier provides the rotating field of the MG. Through the magnetic coupling between the field and armature, the rotating field of the MG induces three-phase voltages (or multiphase voltages, as the case may be) in the stationary armature windings of the MG.

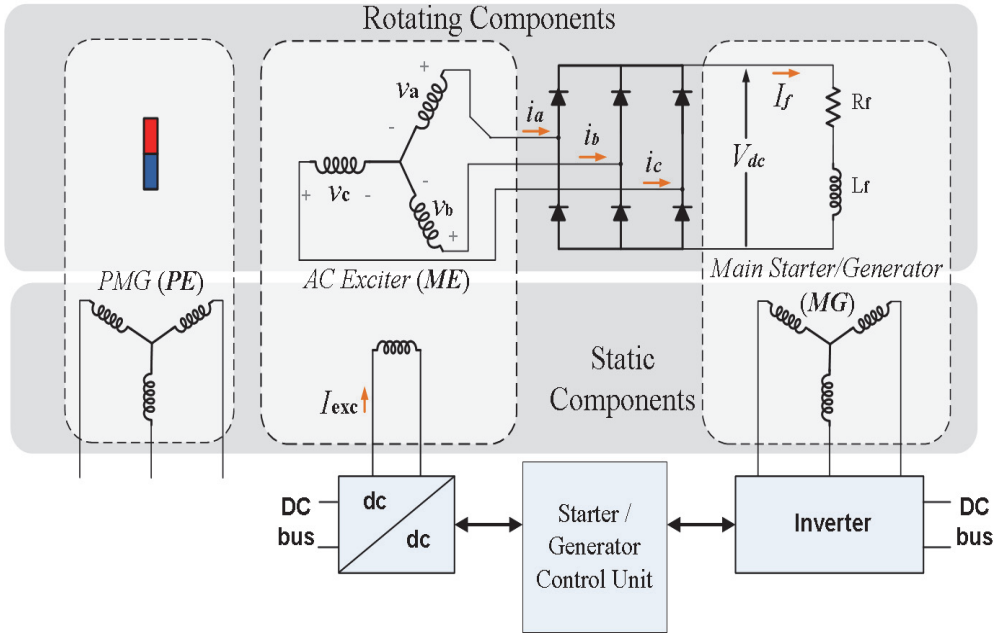

Figure. 1. 2. Three-stage brushless synchronous starter/generator

During operating of the under study ISG, injected power to the single-phase field (stator) winding of the ME transfers to the three-phase rotor windings by transformer effect between field and armature windings. Then, the transferred AC voltages are converted to DC via the rotating rectifier. The output of the rotating rectifier supplies excitation power to the field winding of MG. The existence of the rotating rectifier connected between the armature windings of ME and field winding of MG significantly increases the nonlinearity of the system. In consequence, investigating the nonlinear behavior of the rotating rectifier plays a key role in studying of the brushless synchronous starter-generator.

The special and variable form of ME's armature voltages, which are input voltages of the rotating rectifier, adds to the nonlinearity of behavior of the rectifier. At standstill, since there is no relative speed between single-phase field of ME and armature windings of ME, DC excitation fails to induce voltages in armature windings. Therefore, AC excitation is needed for field excitation of ME. AC excitation of the single-phase field winding leads generating a pulsating field flux. Increasing rotation speed, the excitation must be changed from AC to DC.

In this thesis, it will be described that during operating of the brushless synchronous generator, induced voltages in armature windings of ME are of different forms. At standstill where AC field excitation is applied, always two phases of armature voltages are in-phase with each other while they are 180̊ out of phase with another armature phase voltage. In addition, amplitudes of armature voltages are different. Therefore, in this case, input voltages of the rotating rectifier are severely unbalanced. Consequently, the capability of dealing with unbalanced input voltages is a prerequisite of the required model of rotating rectifier.

Once the ISG starts rotating, AC excitation of field winding induces modulated voltages in armature windings of ME. In this case, each input voltage of rectifier (armature voltages of ME) consists of two voltage components with different phases, amplitudes, and frequency. Accordingly, besides the ability to manage unbalanced conditions, the required model of the rotating rectifier must be able to handle coupling between all AC side harmonics and DC side quantities.

Although modeling of uncontrolled diode bridge rectifier is a mature research topic, to the best knowledge of the author, considering all operating modes of ME, none of the existing analytical modeling approaches for uncontrolled diode bridge rectifier are capable of describing the nonlinear coupling between AC and DC sides of the rotating rectifier. Therefore, in this thesis, as the first step, a model of uncontrolled diode bridge rectifier which meets all above-mentioned requirements is proposed. The proposed model is capable of describing nonlinear relationships between armature windings of ME and field winding of MG in all operating modes of ME.

The final goal of this study is to investigate relationships between the field of ME and field of MG. To provide required tools for the study, a given brushless starter-generator which is potentially able to meet starting torque requirement has been simulated by a finite element software. Then, Matlab/Simulink model of the machine has been extracted from finite element analysis data. This provides the possibility of fast simulating.

Using provided models of entire machine, different operating modes of the ISG are studied. From analytical investigations, two methods for excitation control of ME are proposed.

1.3 Thesis Organization

This thesis is organized into eight chapters. The structure of the thesis and briefly outlines of each chapter are as follows:

Chapter 1 describes background, motivations, and objectives of the thesis. In this chapter, the necessity of efficient excitation of ISG is described. Different parts of the three-stage brushless synchronous starter-generator are introduced. Challenges and requirements of studying and modeling of the under study ISG are explained. Regarding the requirements, contributions of the thesis are outlined. At the end, the structure of the thesis is presented.

In **Chapter 2** background of the industry trend to move from conventional aircraft to MEA is described. Different state of art architectures of aircraft electric power system are explained. It is indicated that application of power electronics in aircraft power system is becoming increasingly significant.

Chapter 3 deals with modeling of uncontrolled diode bridge rectifier. This modeling is performed taking into account the requirements corresponding to special forms of ME's armature voltages. All the proposed models are presented in time-domain and Dynamic Phasor (DP) domain. Both time-domain and DP-domain models are able to describe interactions between harmonics.

In **Chapter 4** Finite element model of a given ISG is presented. After identifying magnetic characteristics of the machine, two Matlab/Simulink models of the machine are built. First Simulink model employs Look-up table in order to simulate nonlinear flux-current relationships. Second Simulink model uses Fourier series method to approximate nonlinear functions which are describing nonlinear flux-current relationships. The presented models provide the possibility of fast simulation while they have enough accuracy. In the presented models, Geometry dependencies of inductances and saturation effects are taken into account.

In **Chapter 5** magnetics maps of a given ISG are experimentally extracted. These magnetic maps are used in control systems to improve the performance of the drive control systems. Since ISG driving in starting process must be performed by a high-performance drive system, magnetic maps which are able to estimate optimum current combination are of importance for control purpose. These magnetics maps are determined for a constant field of MG. At the end, the effectiveness of Maximum Torque Per Ampere (MTPA) obtained from magnetics maps is validated by the experimental test.

In **Chapter 6** a new excitation procedure is proposed. As indicated in Chapter. 5, for implementing a high-performance control, magnetic mapping of the ISG is needed. Since MG is a wound rotor machine, magnetic characteristics of MG vary corresponding to combinations of its stator and field currents. The magnetic mapping is performed by an extensive experimental procedure. Therefore, it is more convenient and feasible to obtain magnetic maps for a constant MG field current.

On the other hand, since MG field winding is mounted on the rotor, there is no possibility to measure and control it. In Chapter. 5 with the purpose of high-performance torque control, an excitation procedure to keep MG field current constant is proposed. In addition, transient operation modes of MG field current are studied and taken into account. Experimental validation of the proposed method is performed.

In **Chapter 7**, a new method to estimate MG field current is proposed. Based on the proposed method, MG field current in all operating modes of the starter-generator can be estimated with excellent accuracy. Estimating the MG field current, one more degree of freedom is added for control purpose.

Chapter 8 presents summary and contributions of the thesis.

Chapter 2

Power Electronics for Aircraft Power System

2.1 Industry Trends of More Electric Aircraft

The main on-board source of power in a conventional aircraft is the engine that is used to create thrust and feed the other systems (bleed air for hydraulics and pneumatics, auxiliary gearbox to drive electrical generators and pumps) [1]. For a typical aircraft with 150-200 passenger capacity like Airbus A320 [2] and Boeing 737 [3], the thrust power is about 40 MW and non-thrust power is about 1.5 MW. Electrical power is the secondary power in an aircraft. In above-mentioned aircrafts, only 200 KW of the non-thrust power is used to convert into the electric power. By increasing attractiveness of more electric aircrafts (MEA), due to their significant benefits in terms of weight, volume and reliability, the trend of the industry is to increase the electrical power level of aircrafts. For example, in Boeing 787, by eliminating the pneumatic bleed systems, about 1.5 MW of non-thrust power is converted to the electric power [4]. The transition from bleed-air power to electric powered systems in Boeing 787 has been performed for the following systems [5]:

- Engine start
- Auxiliary power unit (APU) start
- Wing ice protection
- Cabin pressurization
- Hydraulic pumps

Aircraft power system is going toward major changes. These changes are in respect of size and architecture.

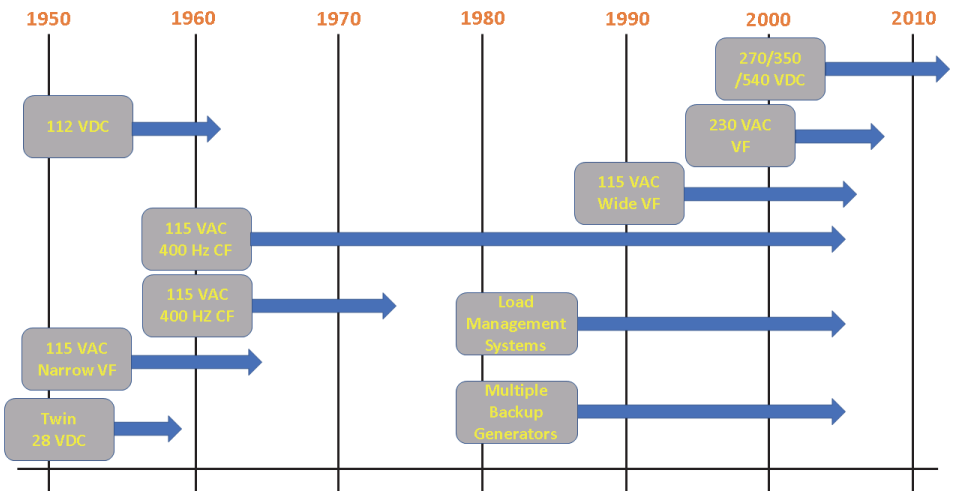

Figure. 2. 1. Evolution of aircraft electric power system technologies based on frequency and voltage level

Regarding the size of components, there is a dominant and increasing trend to use electric power for driving aircraft subsystems [6]. Toward this change, driving power of many subsystems driven by mechanical, hydraulic, and pneumatic are fully or partially replaced by electric power. As an example, new aircrafts such as Boeing 787, use set of compressors close to the cabin of the aircraft to provide bleed air for the environmental control system.

In conventional aircrafts, the bleed air for cabin environment control system was provided by mechanical driven compressors connected to the main aircraft engine [7]. The conventional bleed air system needed a set of pneumatic system and air ducts from the main engine to the cabin of the aircraft. Replacing the conventional bleed air system with the electrically driven system leads to significantly decreasing the size of the replaced subsystem and a significant weight saving [8]. On the other hand, these substitutions result in significant increase of the required onboard power generation and the increase of the size of the aircraft power system.

2.2 Architecture of MEA Power Distribution System

In effect of increasing number of electric driven subsystems, the architecture of the aircraft power system has been changed [9]. One reason for this change is that now loads are a mixture of AC and DC loads. Moreover, some big loads are not sensitive to frequency. So, there is no need to have an AC bus for all AC loads with the constant frequency. This leads to increase the number of required local power electronics converters [10]- [11]. Generally speaking, evolution of nature of loads leads to a requirement for new power system structures which is more adapted with the newly introduced loads. Fig. 2.1 shows the evolution of aircraft electric power system strategies based on frequency and power level [12]. As can be seen from the Fig. 2.1, aircraft power system evolution is from low-level voltages with constant frequency toward higher voltage levels and variable frequencies.

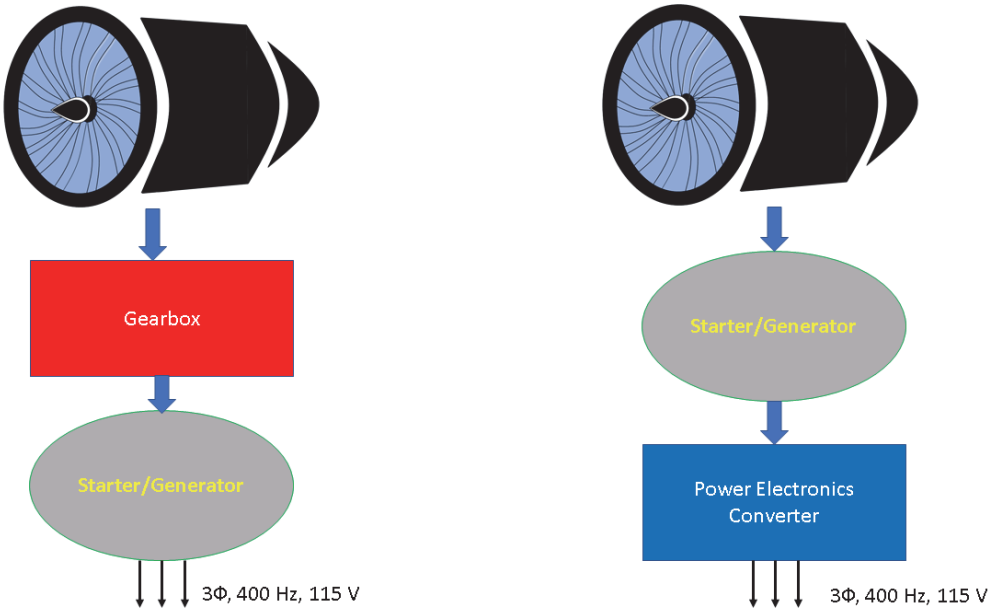

(a) (b)

Figure. 2. 2. Aircraft constant frequency power generation systems. (a) Mechanical constant frequency power generation. (b) VSCF power generation system

The constant frequency power systems are categorized into mechanical constant frequency and power electronics constant frequency power generation systems. Fig. 2.2.a shows schematics of the mechanical constant frequency power generation system and Fig. 2.2.b shows schematic of Variable Speed-Constant Frequency (VSCF) power generation system [13]- [14]. The mechanical constant frequency power generation system uses a mechanical gearbox to create a constant speed shaft for the electric generator. So, the frequency of the generated electric power is constant. The VSCF exploits power electronics converters to convert the generated electric power with variable frequency to a constant frequency electric power.

By increasing diversity of the aircraft power system loads, more-electric aircrafts exploit a variable frequency power generation [15]-[17]. In this architecture, voltage level control is performed by the generator, but frequency adoption and further voltage level control are performed by local power electronics converters. Respect to the constant frequency power generation architecture, the new aircraft power system architecture (VF) contains a large number of power electronics converters. Fig. 2.3 shows schematic of the variable frequency power generation concept. Block diagram of aircraft VSCF and VF power distribution systems are shown in Fig 2.4 and Fig 2.5, respectively [18]. As can be seen, in VSCF power distribution system, the frequency adaption is performed for entire AC loads at the AC bus. While in the VF architecture, the frequency adaption is performed by local power electronics converters.

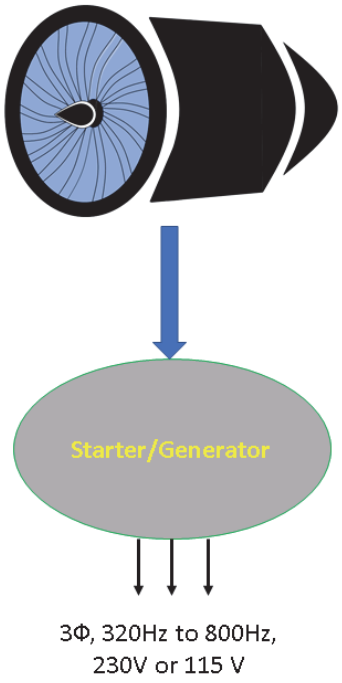

Figure. 2. 3. The aircraft variable-frequency power-generation system

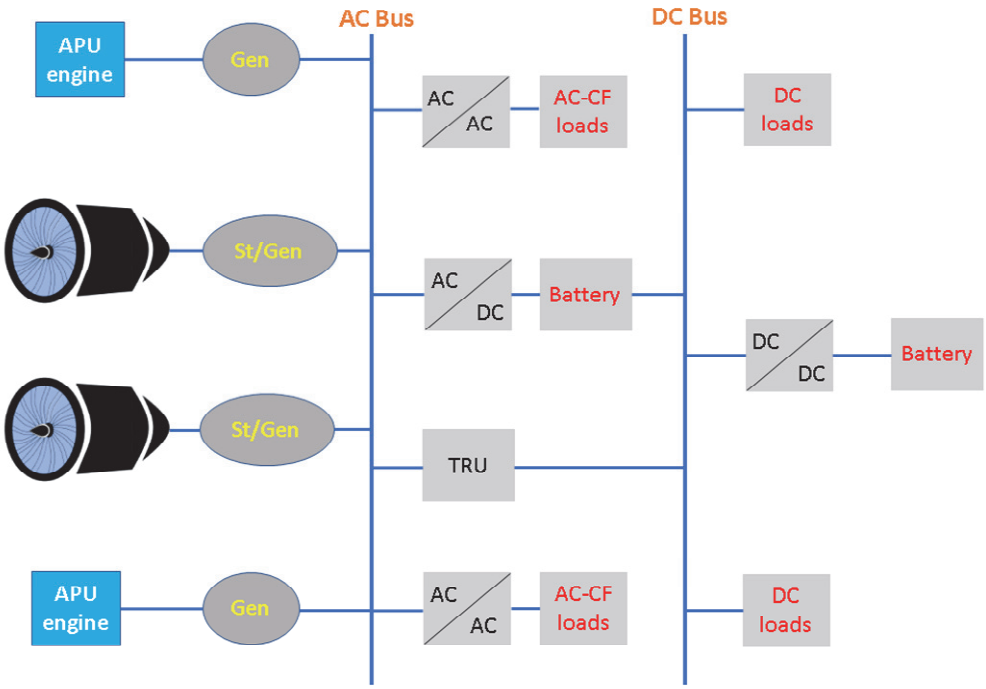

Figure. 2. 4. Block diagram of the VSCF power distribution system

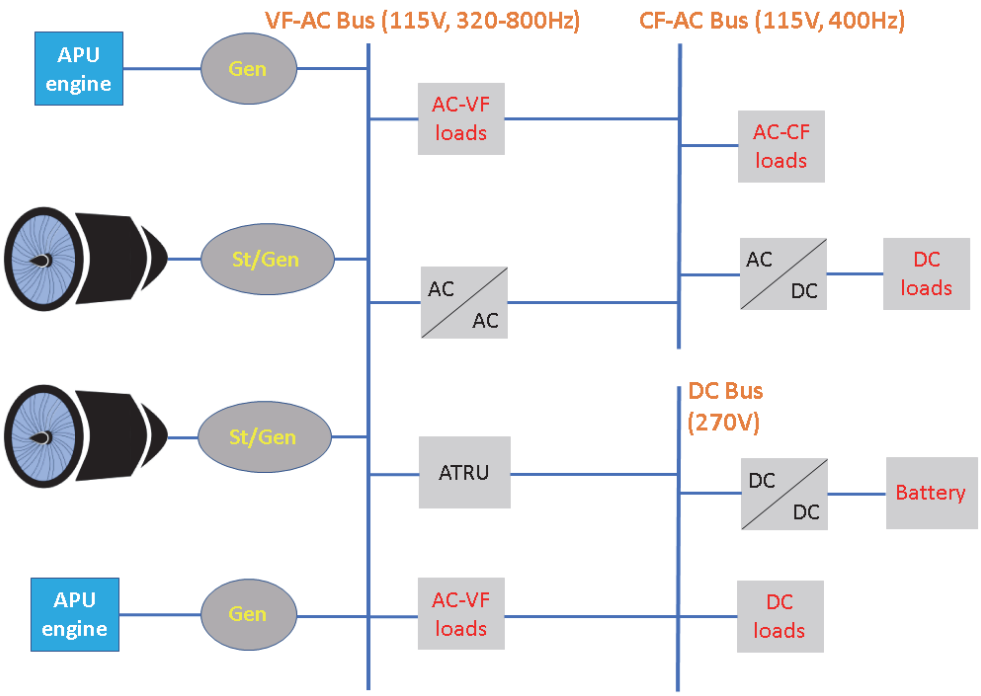

Figure. 2. 5. Block diagram of the VF power distribution system

Chapter 3

Modeling of Uncontrolled Rectifier

3.1 Introduction

As mentioned in the Chapter.2, modern aircraft power systems contain a large number of power electronics converters. This promotes the necessity of accurate modeling of the power electronics converters, and electric machine with power electronics loads.

The focus of this thesis is investigation and modeling of the three-stage brushless synchronous starter-generator. Since the starter-generator contains two synchronous machine-rectifier systems (exciter-rotating rectifier, and MG-rectifier), this chapter leads with modeling of diode bridge rectifier used in aircraft power system.

In addition, in the aircraft power system, most of the on-board power electronics systems such as switching power supplies, electric motor drives, etc., contain uncontrolled rectifier [19]. Therefore, an accurate average, dynamic model of the uncontrolled rectifier is needed in order to assess the stability and dynamic behaviour of the power electronics systems containing uncontrolled rectifier [20]-[23].

In part of the starting process of the brushless starter-generator, field excitation of main exciter machine is AC. Since field winding of the exciter machine is single-phase, induced voltages in armature windings of the main exciter have special non-ideal form. In the future chapters, this phenomenon will be described in detail. At standstill with AC excitation, only two voltages contribute in rectification, so the model of rectifier must be able to take unbalanced input voltages into account. Also, applying AC excitation when the rotor is rotating, armature voltages are composed of two harmonics components which have varying amplitude and phase. Therefore, for modeling the brushless starter-generator, a rectifier model is needed with ability to consider the effect of harmonics in AC side on DC outputs.

In this chapter, first, a detailed and an average value models for uncontrolled rectifier are presented, then a selective harmonic model based on Dynamic Phasor (DP) method is presented. Due to the complexity of the aircraft power system with a large number of power electronics converters, the model of the converters must be able to take in account desired harmonics while is efficient in respect of computation time. Another desired feature of the model is its performance under unbalanced and transient condition. Contributions presented in this chapter are as following:

- ✓ **Correct voltage and current switching functions in DP-domain are presented in Section 3.10.**
- ✓ **Proposed models in this chapter are presented in both time- and DP-domains. While the time-domain model has a fast dynamic, the DP-domain model offers flexible accuracy and efficient performance in respect of required computation time.**
- ✓ **A new model of uncontrolled diode bridge rectifier in unbalanced condition based on switching function method in time-domain and DP-domain is presented in Section 3.7.**
- ✓ **In addition, unbalance factor (amount of unbalance) does not affect the performance of the proposed model. Therefore, the proposed model can deal with wide range of unbalance and fault conditions.**
- ✓ **Considering all harmonics in AC-side, two new methods for modeling of uncontrolled diode bridge rectifier are proposed in Section 3.15 and .17.**
- ✓ **Unlike other methods in time-domain and DP-domain presented in the literature, performance of the proposed model is not limited by the amplitude of harmonics even when due to harmonics presence, phase sequence of AC-side voltages changes. Therefore, for the case of modeling and investigation of the three-stage brushless synchronous machine, the proposed models are able to fully and accurately describe the relationships between AC-side (armature windings of ME) and DC-side (field winding of MG).**

3.2 Benchmark Model of Uncontrolled Rectifier (Detailed Model)

Fig. 3.1 shows a three-phase uncontrolled rectifier. The three-phase uncontrolled rectifier converts input alternating current/voltage into DC current/voltage. A three-phase uncontrolled rectifier consists of three diode legs which form a three-phase bridge using diodes D_1 to D_6. According to the diode switching logic, the input AC current is switched between legs and their corresponding diodes. In Fig. 3.1, L_c indicates the commutation inductance. At the presence of L_c, the output current of the rectifier (i_f) cannot be switched between diode instantaneously. This leads to a finite commutation process which will be discussed in detail in this chapter. First, the performance of the rectifier without the presence of L_c is considered.

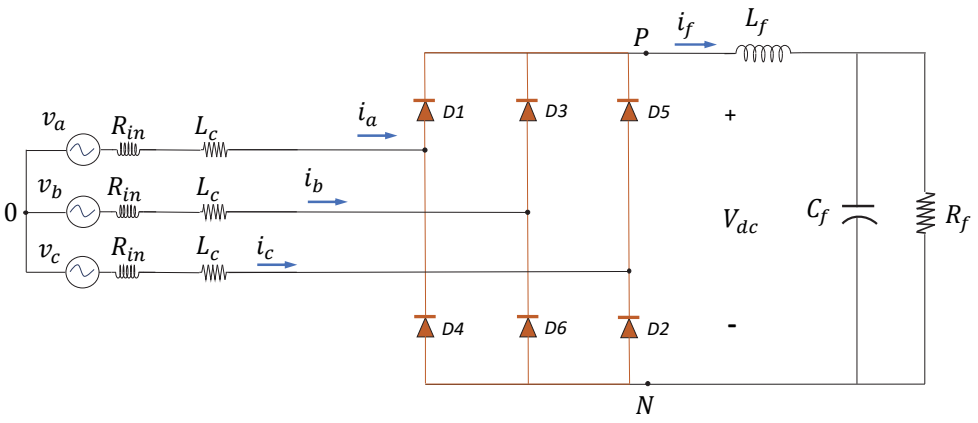

Figure. 3. 1. Benchmark model of uncontrolled rectifier

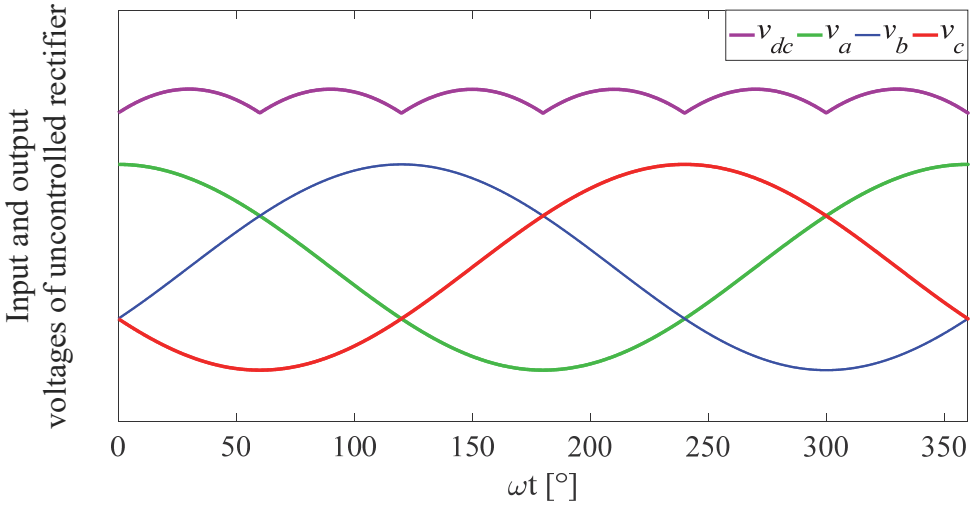

Figure. 3. 2. Input and output voltages of the uncontrolled diode bridge rectifier

Fig. 3.2, shows the input and output voltages of the uncontrolled rectifier without considering the commutation effect. In this chapter, detailed model of the uncontrolled rectifier is simulated using Matlab/Simpowersystem model of the uncontrolled diode bridge rectifier.

3.3 Transfer Function Method

In the transfer function method, the uncontrolled rectifier is considered as a black box and its transfer function determines its functionality based on input variables. To implement the transfer function method, relationships between input and output voltages and currents of the rectifier are obtained either from detailed simulation or experimental tests and are stored in look-up tables. To find these relationships, comprehensive simulation or experimental tests must be performed for various operating points [24]. Fig. 3.3 shows a schematic of the transfer function modeling.

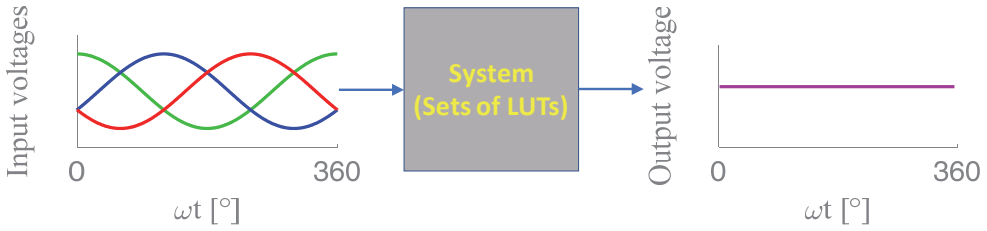

Figure. 3. 3. Transfer function modelling

In [25],[26], the nonlinear behaviour of the uncontrolled rectifier fed by a synchronous generator was modeled. The presented models are based upon sets of data obtained from comprehensive simulation or experimental tests. These data are saved into lookup tables and used to estimate output voltage and current of the rectifier. The estimation is based on nonlinear relationships between the magnitude of input and output voltages of the rectifier. These relationships are interpreted from data saved in lookup tables. In [27]-[31], the same method was implemented and called parametric model. Since the only magnitude of voltages and currents are considered and the frequency of input voltages was not taken into account, these models are not able to describe the behaviour of the uncontrolled rectifier completely. In [32], in addition to the magnitude of input/output voltages and currents, the frequency of AC-side was considered in parameters obtaining process. This one variable increasing led to needing for 3D look-up tables instead of 2D look-up tables to create the dataset for the parametric model of uncontrolled diode bridge rectifier.

Although the transfer function method is simple and does not require to calculate complex mathematical equations, it is not generic to be used for various operating points, unbalanced or fault conditions.

3.4 Switching Function Method

Switching functions represent a bidirectional relationship between input and output variables of power electronics converters by means of emulating switching action of active/passive switches of the converter [33]. Neglecting the effect of commutation phenomena, Fig. 3.4 shows switching functions of uncontrolled diode bridge rectifier respecting its three-phase input. These phase switching functions are obtained from state functions of corresponding diodes of each phase (Table .3.1) as follows:

$$S_a = S_{d1} - S_{d4}$$

$$S_b = S_{d3} - S_{d6}$$

$$S_c = S_{d5} - S_{d2}$$

$$\mathbf{S}_{abc} = \begin{bmatrix} S_a \\ S_b \\ S_c \end{bmatrix} = \begin{bmatrix} S_{d1} - S_{d4} \\ S_{d3} - S_{d6} \\ S_{d5} - S_{d2} \end{bmatrix} \quad (3.1)$$

where S_a, S_b, and S_c are switching functions of phase a, b, and c, respectively. S_{d1} to S_{d6} are switching functions of diodes D_1 to D_6, respectively (Fig. 3.1).

Table. 3. 1. Switching states of diodes in the uncontrolled rectifier

ωt	S_{d1}	S_{d2}	S_{d3}	S_{d4}	S_{d5}	S_{d6}
$0^\circ<\omega t<60^\circ$	1	0	0	0	0	1
$60^\circ<\omega t<120^\circ$	0	0	1	0	0	1
$120^\circ<\omega t<180^\circ$	0	1	1	0	0	0
$180^\circ<\omega t<240^\circ$	0	1	0	0	1	0
$240^\circ<\omega t<300^\circ$	0	0	0	1	1	0
$300^\circ<\omega t<360^\circ$	1	0	0	1	0	0

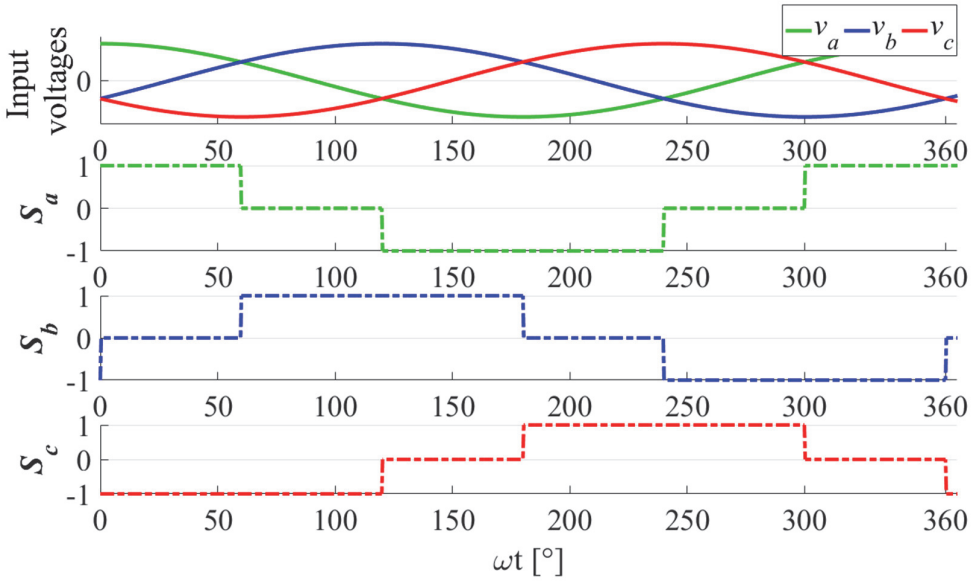

Figure. 3. 4. Piecewise switching functions of the uncontrolled rectifier under balance condition

These switching functions are called Piecewise switching functions. Since they represent a complete association between input voltages/currents with output voltage/current of the rectifier considering all harmonics, in time-domain, they cannot be used for selective harmonics average value modeling.

Using switching function method, the relation between input and output voltages/currents are as follows:

$$\boldsymbol{V}_{abc,in} = \begin{bmatrix} v_a \\ v_b \\ v_c \end{bmatrix} = \begin{bmatrix} V_m \cdot cos(\omega t) \\ V_m \cdot cos\left(\omega t - \frac{2 \cdot \pi}{3}\right) \\ V_m \cdot cos\left(\omega t + \frac{2 \cdot \pi}{3}\right) \end{bmatrix}$$

$$v_{dc} = \boldsymbol{S}_{abc}^T \cdot \boldsymbol{V}_{abc,in} \tag{3.2}$$

$$\boldsymbol{I}_{abc,in} = \boldsymbol{S}_{abc} \cdot \boldsymbol{i}_{dc} \tag{3.3}$$

Where $\mathbf{I}_{abc,\ in}$ is:

$$\mathbf{I}_{abc,in} = \begin{bmatrix} i_a \\ i_b \\ i_c \end{bmatrix}$$

The piecewise switching function can be represented by approximation using series Fourier of quasi-square wave functions. Using series Fourier makes it possible to select harmonics of interest in the averaging process of modeling. Fourier series of piecewise switching functions are as follows:

$$S_i = \sum_{n=1}^{\infty} A_n \cdot \cos(n\omega t + \varphi_i),\ i = a, b, c \tag{3.4}$$

$$A_n = \left(\frac{4}{n\pi}\right) \cdot \sin\left(\frac{n\pi}{2}\right) \cdot \cos\left(\frac{n\pi}{6}\right) \tag{3.5}$$

The fundamental components of the diode switching functions are as follows (n=1).

$$\mathbf{S}_{abc}|_{n=1} = \frac{2\sqrt{3}}{\pi} \cdot \begin{bmatrix} \cos(\omega t) \\ \cos\left(\omega t - \frac{2\cdot\pi}{3}\right) \\ \cos\left(\omega t + \frac{2\cdot\pi}{3}\right) \end{bmatrix} \tag{3.6}$$

Fig. 3.5 shows switching functions of three-phase input voltages using Fourier series approximation by considering first ten components of switching functions (1st, 5th, 7th, 9th, 13th, 15th, 19th, 21st, 25th, and 27th components).

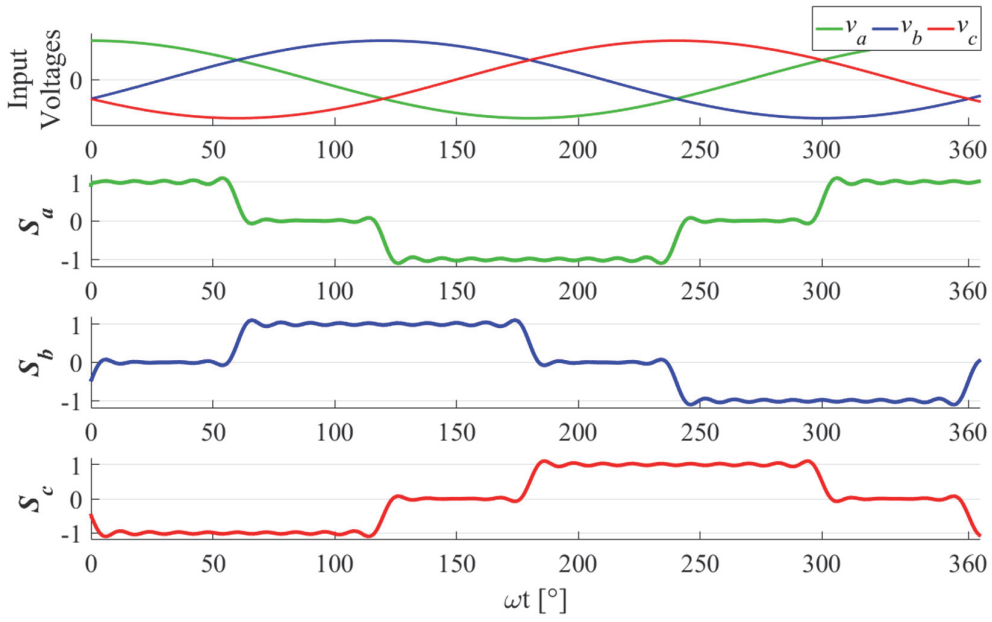

Figure. 3. 5. Fourier series approximation of the switching functions

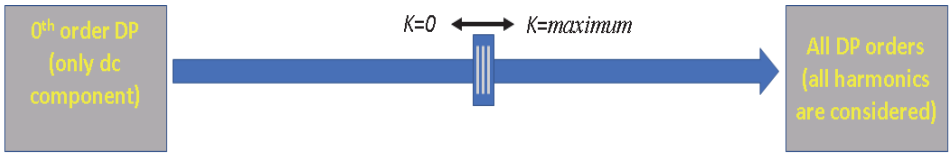

Figure. 3. 6. DP method for selective harmonic modelling

3.5 Dynamic Phasor (DP) method

Dynamic Phasors (DP) are used to simulate power system by representing instantaneously high-frequency time-domain signals as low-variant signals [34]-[37]. Based on the Nyquist sampling theory, low-pass signals needs fewer samplings than the original high-frequency signals. Therefore, using DPs, it is possible to reduce the unnecessary time steps in the simulation. In [38], functional model of diode bridge rectifier in DP-domain is presented. DP modeling method for autotransformer rectifier unit (ATRU) has been addressed in [39].

In fact, DPs are time-varying Fourier series coefficient of a quasi-periodic signal. DPs are calculated for a sliding window over time. Usually, the fundamental period of the signal is chosen as the time window. As a result, each DP is the K^{th} Fourier series coefficient of the original signal. For signal x(τ) in complex Fourier series form, DPs are defined as:

$$\langle X\rangle_k = X_k(t) = \frac{1}{T}\int_{t-T}^{t} x(\tau)\cdot e^{-jk\omega t}\cdot d\tau \tag{3.7}$$

where k is order of DP. T, and ω are fundamental period and frequency of the signal, respectively. Transformation from DP-domain to time-domain is as

$$x(t) = \sum_{k=-\infty}^{\infty}\langle X\rangle_k \cdot e^{jk\omega t} \tag{3.8}$$

Some useful feature of DPs are as follows:

$$\langle X\rangle_{-k} = \langle X\rangle_k^* \tag{3.9}$$

where the superscript '*' refers to conjugate operation.

$$\langle X \cdot Y \rangle_k = \sum_n \langle X \rangle_{k-n} \cdot \langle Y \rangle_n \tag{3.10}$$

$$\langle \frac{dX}{dt} \rangle_k = \frac{d}{dt} \langle X \rangle_k + jkw \cdot \langle X \rangle_k \tag{3.11}$$

Despite that DP method offers an efficient simulation time, the main advantage of the DP method is that it is flexible in considering the number of harmonics of interest (Fig. 3.6). Therefore, using DP method, it is possible to select desired harmonics and include them in the model.

3.5.1 DP Model of Uncontrolled Rectifier

The Fourier series switching function method provides a straightforward and explicit presentation of the detailed piecewise switching function. DP calculation can be easily implemented on the Fourier series switching functions of the uncontrolled rectifier. Representation of uncontrolled rectifier switching function (equation 3.4) in DP-domain is as follows:

$$\langle S_i \rangle_k = \frac{A_k}{2} \cdot e^{j\varphi_i}, \qquad i = a, b, and\ c \tag{3.12}$$

where *k* indicates DP's indexes.

Based on (3.2), output voltage of the uncontrolled rectifier in DP-domain can be calculated as:

$$\langle v_{dc} \rangle_k = \langle v_a \cdot s_a \rangle_k + \langle v_b \cdot s_b \rangle_k + \langle v_c \cdot s_c \rangle_k \tag{3.13}$$

According to (3.10), in DP-domain, product of voltages and switching functions can be expanded. Zero order DP of output voltage is:

$$\langle v_{dc} \rangle_0 = [\dots + \langle v_a \rangle_1 \cdot \langle S_a \rangle_{-1} + \langle v_a \rangle_{-1} \cdot \langle S_a \rangle_1 + \cdots] + [\dots + \langle v_b \rangle_1 \cdot \langle S_b \rangle_{-1} + \langle v_b \rangle_{-1} \cdot \langle S_b \rangle_1 + \cdots] + [\dots + \langle v_c \rangle_1 \cdot \langle S_c \rangle_{-1} + \langle v_c \rangle_{-1} \cdot \langle S_c \rangle_1 + \cdots] \tag{3.14}$$

As can be derived from (3.14), DC component of the uncontrolled rectifier output voltage is calculated by first harmonic (fundamental component) of switching functions of input voltages. For other orders of DP representation of output voltage, there is the same procedure. For example, under balanced condition, output voltage of the uncontrolled rectifier contains 6^{th} harmonic component. 6^{th} harmonic component of the output voltage of the uncontrolled rectifier in DP-domain under balance condition can be expressed as:

$$\langle v_{dc}\rangle_6 = [\dots + \langle v_a\rangle_1 \cdot \langle S_a\rangle_5 + \langle v_a\rangle_{-1} \cdot \langle S_a\rangle_7 + \cdots] + [\dots + \langle v_b\rangle_1 \cdot \langle S_b\rangle_5 + \langle v_b\rangle_{-1} \cdot \langle S_b\rangle_7 + \cdots] + [\dots + \langle v_c\rangle_1 \cdot \langle S_c\rangle_5 + \langle v_c\rangle_{-1} \cdot \langle S_c\rangle_7 + \cdots] \quad (3.15)$$

From (3.15), it can be concluded that 6^{th} harmonics of uncontrolled rectifier output voltage is obtained from 5^{th} and 7^{th} harmonics components of input voltages switching functions.

3.6 Unbalanced condition modelling

As mentioned in the previous chapter, by increasing power electronics loads, a new architecture and optimization are required for the aircraft power system. Adequate comprehending of the dynamic behaviour of the aircraft power system in relation to design parameters is an important prerequisite for studying and improving the stability of the aircraft power system. Such a model should be adequately precise and be able to indicate the dynamic behaviour of the system in various operating points.

The trend toward employing variable frequency power generation systems for aircrafts leads to increasing use of the uncontrolled rectifiers. The advantages of uncontrolled rectifier are high reliability, simple structure, and low cost. However, it is well known that the uncontrolled rectifier injects a considerable number of harmonics into the power system. These harmonics caused by power electronics loads and other unexpectable faults or dynamic conditions make aircraft power system variables (voltage, current, and frequency) distorted. These result in unbalanced condition and degraded power quality. A small amount of voltage unbalance in AC-side can lead to a large number of current harmonics which affect AC-side currents and DC-side voltage and current of rectifier [40]-[42]. Hence, a proper model for studying of the aircraft power system must be able to deal with unbalanced conditions.

Regarding the above-mentioned requirements for an adequate modeling method for aircraft power system, in this chapter, modeling method for uncontrolled rectifier is proposed. The proposed model can be able to keep its accuracy in various operating points containing unbalanced conditions.

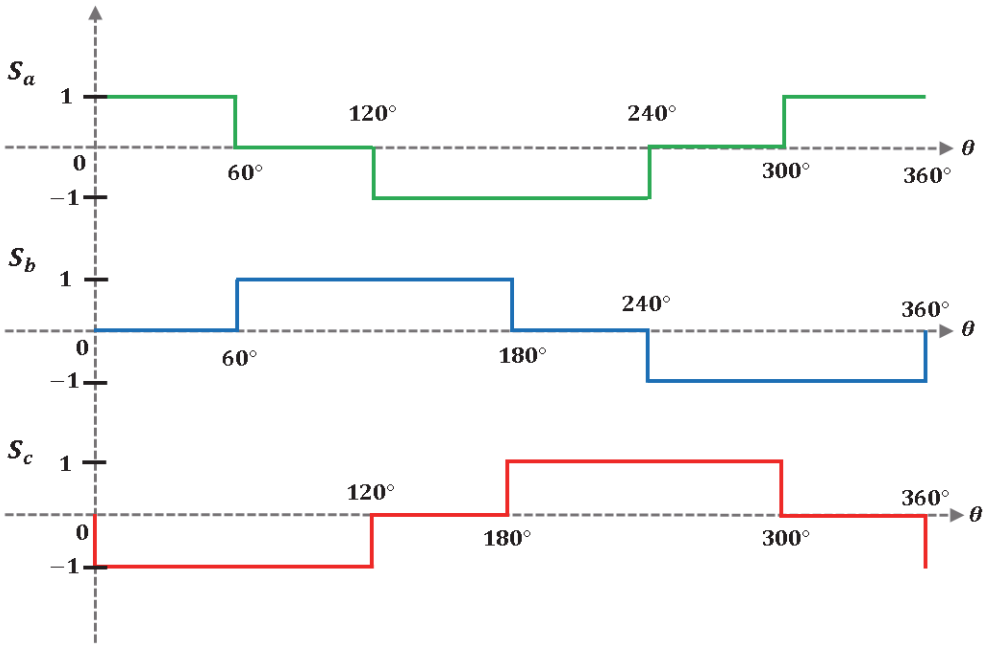

Figure. 3. 7. switching functions of the uncontrolled rectifier under balanced condition

3.7 Proposed Improved DP Model of Uncontrolled Rectifier for Unbalanced conditions

Fig .3.7 shows piecewise switching function of three-phase input voltages of uncontrolled rectifier under balanced condition. Previously presented Fourier series of switching functions in the literature are calculated for this balanced condition.

Equation (3.5) which indicates the coefficient of the Fourier series of switching function has been calculated based on intersection points between phase voltages, therefore this equation only is valid for the balanced condition. This has not been considered in presented DP-domain models in the literature. For example, in [43]-[45]. The general expression of Fourier series for a periodic signal ($x(t)$) with the period equal to T is:

$$x(t) = a_0 + \sum_{n=1}^{\infty}[a_n \cdot \cos(n\omega t) + b_n \cdot \sin(n\omega t)] \tag{3.16}$$

where

$$a_n = \frac{2}{T}\int_T x(t) \cdot \cos(n\omega t) \cdot dt, \quad n \neq 0 \tag{3.17}$$

$$b_n = \frac{2}{T}\int_T x(t) \cdot \sin(n\omega t) \cdot dt, \quad n \neq 0 \tag{3.18}$$

As can be seen in Fig .3.7, under the balance condition, the switching functions are even functions. So, Fourier series representation of switching functions has the following features.

$$\begin{cases} s_i(t) is\ an\ even\ function\ with\ half-wave\ symmetry & i = a, b, and\ c \\ b_n = 0 \\ a_n = 0 \quad n\ \ is\ \ even \end{cases}$$

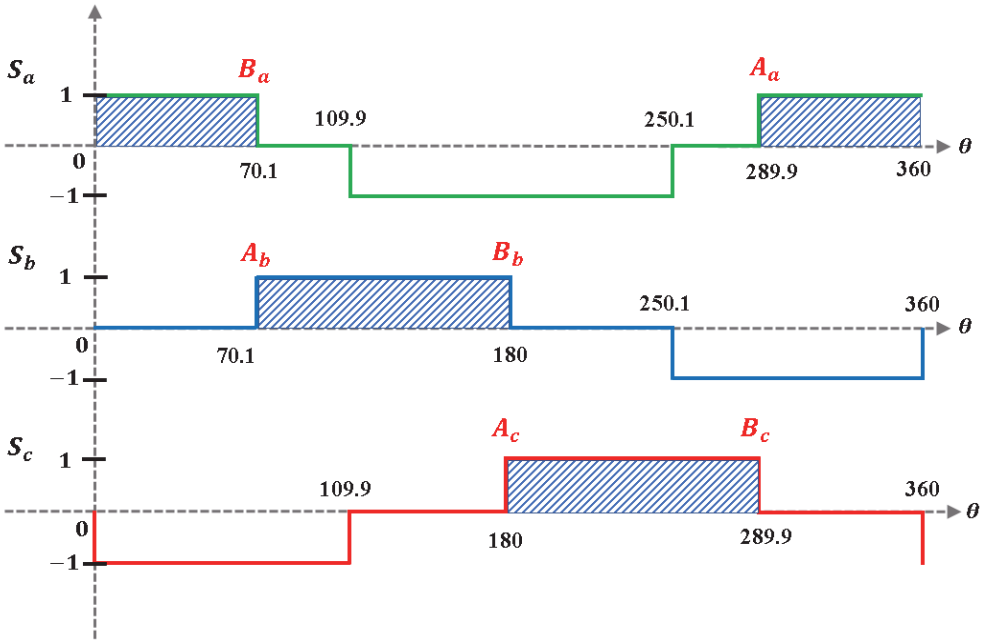

Figure. 3. 8. Switching functions of the uncontrolled rectifier under an unbalanced condition.

Fig .3.8 shows piecewise switching functions of the uncontrolled rectifier under an unbalanced condition, where input voltages are:

$$v_a = 2 \cdot V_m \cdot \cos(\omega t)$$

$$v_b = V_m \cdot \cos\left(\omega t - \frac{2 \cdot \pi}{3}\right)$$

$$v_c = V_m \cdot \cos\left(\omega t + \frac{2 \cdot \pi}{3}\right)$$

As can be seen in Fig 3.8, the switching functions are neither even or odd functions. But, always they have half-wave symmetry. So, the equations (3.4) and (3.5) which represent the uncontrolled rectifier output voltage are not valid for unbalanced conditions. Fourier series expression of switching functions of the uncontrolled rectifier under unbalanced condition has the following features:

$$\begin{cases} s_i(t)\ \ may\ be\ neither\ even\ nor\ odd, & i = a, b, and\ c \\ S_i\ \ always\ has\ half-wave\ symmetry \\ a_n = \ b_n = 0, \quad n\ \ is\ even \end{cases}$$

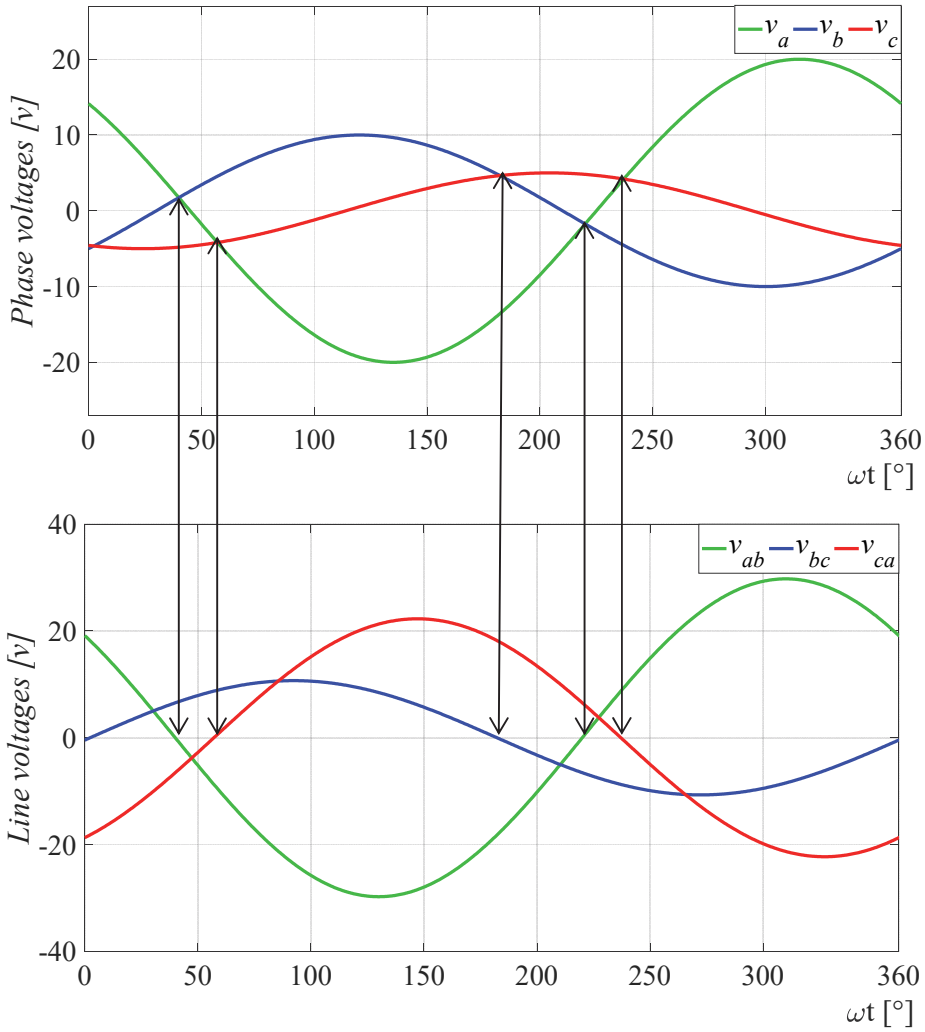

Figure. 3. 9. Relationship between zero-crossing points of line-to-line voltages and intersection points of phase voltages

Therefore, under unbalanced conditions, the coefficients of the Fourier series must be recalculated. This can be done easily using DP representation of the variables. Recalculating the Fourier series coefficients requires knowledge of intersection points between phase voltages. These intersection points can be easily found from DP expressions of line voltage. Zero-crossing points of line voltages are intersection points of phase voltages. This is shown in Fig .3.9. Applying (3.7) on line voltages, DP representation of line voltages are obtained. The angle of line voltages DPs are zero-crossing points of line voltages (intersection points of phase voltages). Therefore, first, line voltages should be converted into DP-domain as time-varying phasors:

$$\langle v_{ab} \rangle_1 = \frac{\boldsymbol{V}_{ab}}{2} \cdot e^{j\vartheta_{ab}} \tag{3.19}$$

$$\langle v_{bc} \rangle_1 = \frac{\boldsymbol{V}_{bc}}{2} \cdot e^{j\vartheta_{bc}} \tag{3.20}$$

$$\langle v_{ca} \rangle_1 = \frac{\boldsymbol{V}_{ca}}{2} \cdot e^{j\vartheta_{ca}} \tag{3.21}$$

where $\boldsymbol{V}_{ab}$, $\boldsymbol{V}_{bc}$, and $\boldsymbol{V}_{ca}$ are the magnitude of three-phase line voltages. ϑ_{ab}, ϑ_{bc}, and ϑ_{ca} are the phase of line voltages.

In Fig .3.8, A_i and B_i ($i = a, b$, and c) indicate the beginning and end points of each switching function pulse. Using the value of this points, it is possible to calculate the switching function Fourier series. Exploiting symmetry of the switching functions, intersection points of three-phase input voltages of the uncontrolled rectifier can be expressed as:

$$A_a = \frac{\pi}{2} - \vartheta_{ca} \tag{3.22}$$

$$B_a = \frac{\pi}{2} - \vartheta_{ab} \tag{3.23}$$

$$A_b = B_a \tag{3.24}$$

$$B_b = \frac{\pi}{2} - \vartheta_{bc} \tag{3.25}$$

$$A_c = B_b \tag{3.26}$$

$$B_c = A_a \tag{3.27}$$

Since Line voltages in DP-domain have 90̊ phase shift with respect to their actual waveform, the term $\frac{\pi}{2}$ is included in above relations. For example, when phase voltages are cosine functions, line voltages are sine functions, but in DP-domain line voltages are expressed as cosine. Fourier series of switching functions for three-phase input voltages of the uncontrolled rectifier under unbalanced condition can be expressed as:

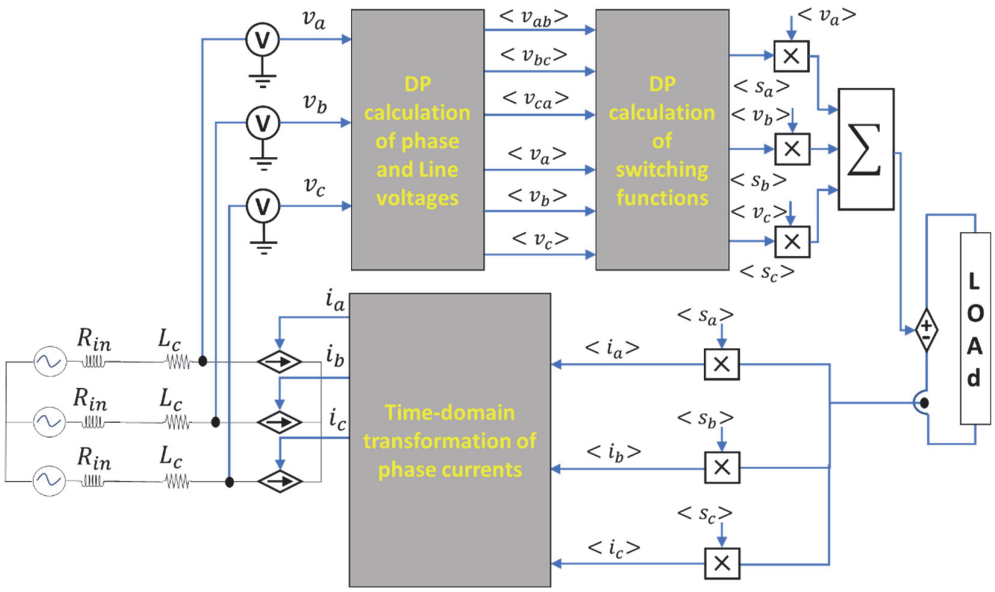

Figure. 3. 10. The proposed DP model of the uncontrolled rectifier

$$A_n = \frac{2}{n\cdot\pi}\cdot[\sin(n\cdot B_i) - \sin(n\cdot A_i)] \tag{3.28}$$

$$B_n = \frac{2}{n\cdot\pi}\cdot[\cos(n\cdot A_i) - \cos(n\cdot B_i)] \tag{3.29}$$

$$S_i(t) = \sum_{n=1}^{\infty}[A_n\cdot\cos(n\omega t) + B_n\cdot\sin(n\omega t)] \qquad i = a, b, and\ c \tag{3.30}$$

Equation (3.30) is a general expression for Fourier series of uncontrolled rectifier under unbalance conditions where three-phase input voltages have not 120° phase differences and/or not have equal amplitude. DP expression of (3.30) is as:

$$\langle S_a\rangle_k = \frac{A_k}{2}\cdot e^{j0} - j\frac{B_k}{2}\cdot e^{j0} \tag{3.31}$$

After some manipulation, (3.31) can be rewritten as:

$$\langle S_i\rangle_k = \frac{2}{k\cdot\pi}\cdot\sin\left(\frac{k\cdot(B_i - A_i)}{2}\right)\cdot e^{-j\left(\frac{k\cdot(A_i+B_i)}{2}\right)}, \quad i = a, b, and\ c \tag{3.32}$$

A DP model can be interfaced to the time-domain models. After estimation desired DP orders for each variable, according to (3.8), each variable can be transformed from DP-domain into the time-domain. This transformation is essential for interfacing a converter model in DP-domain to other parts of the overall time-domain model. For rectifier output voltage, the transformation from DP-domain into time-domain is as follows:

$$v_{dc}(t) = \langle v_{dc}\rangle_0 + \sum_{k=1}^{max}\langle v_{dc}\rangle_k(t)\cdot e^{jk\omega t} = \langle v_{dc}\rangle_0 + 2\cdot\sum_{k=1}^{max}(\Re e[\langle v_{dc}\rangle_k]\cdot \cos(k\omega t) - \Im m[\langle v_{dc}\rangle_k]\cdot\sin(k\omega t)) \quad (3.33)$$

Fig .3.10 shows overall schematic of uncontrolled rectifier model in DP-domain and its interfacing with time-domain model.

3.8 Case Study and Validation of the Proposed Model of Uncontrolled Rectifier

To examine the performance and accuracy of the proposed model, the model is comprised with detailed benchmark model simulated is Simpowersystem Matlab/Simulink environment. Four different conditions are considered for examination of the model as follows:

- ***Case.1*** : Balanced three-phase inputs with Continuous Current Mode (CCM) of output current.
- ***Case. 2*** : One phase open circuit fault.
- ***Case. 3***: Three-phase Unbalanced input voltages
- ***Case. 4***: CCM to DCM transient

3.8.1 Case. 1: Balanced three-phase inputs with Continuous Current Mode (CCM) of output current.

In this case of study, input voltages of the rectifier are considered as:

$$v_a = 10\cdot\cos(\omega t)$$

$$v_b = 10\cdot\cos\left(\omega t - \frac{2\cdot\pi}{3}\right)$$

$$v_c = 10\cdot\cos\left(\omega t + \frac{2\cdot\pi}{3}\right)$$

where

$$\omega = 400\cdot 2\cdot\pi$$

Fig .3.11 and Fig .3.12 show the rectifier output voltage and current respectively. The switching function contains odd harmonics from 0^{th} to 29^{th}. Figs .3.13a to 3.13c show input phase currents. Frequency spectrum of the rectifier output voltage (v_{dc}) and switching function of phase a (S_a) are shown in Fig .3.14. As can be seen in Fig .3.14, the rectifier output voltage contains characteristics harmonic orders of 0^{th}, 6^{th}, 12^{th}, 18^{th}, etc. Also, the switching function (S_a) contains odd harmonics.

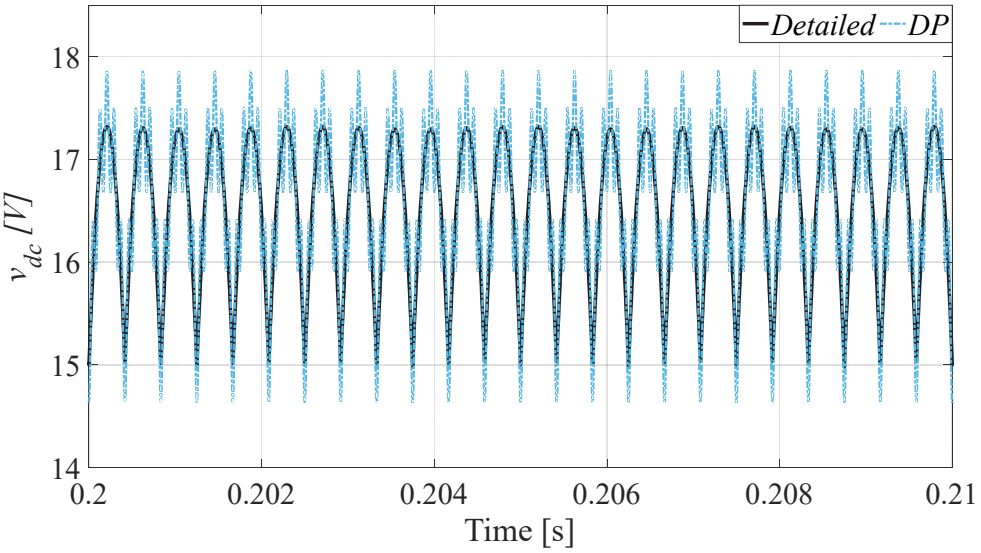

Figure. 3. 11. Uncontrolled rectifier output voltage obtained from detailed and DP models under balance input voltages condition

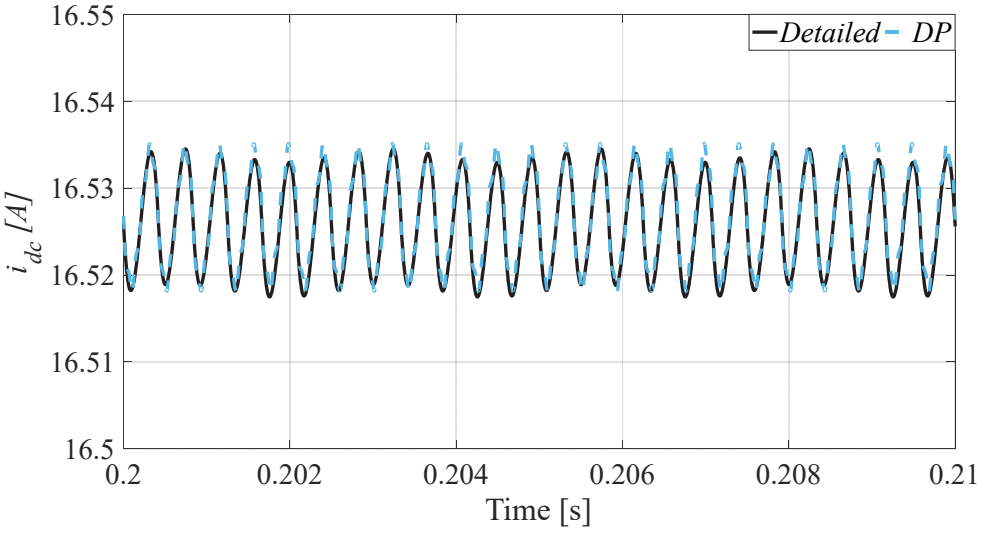

Figure. 3. 12. Uncontrolled rectifier output current obtained from detailed and DP models under balance input voltages condition

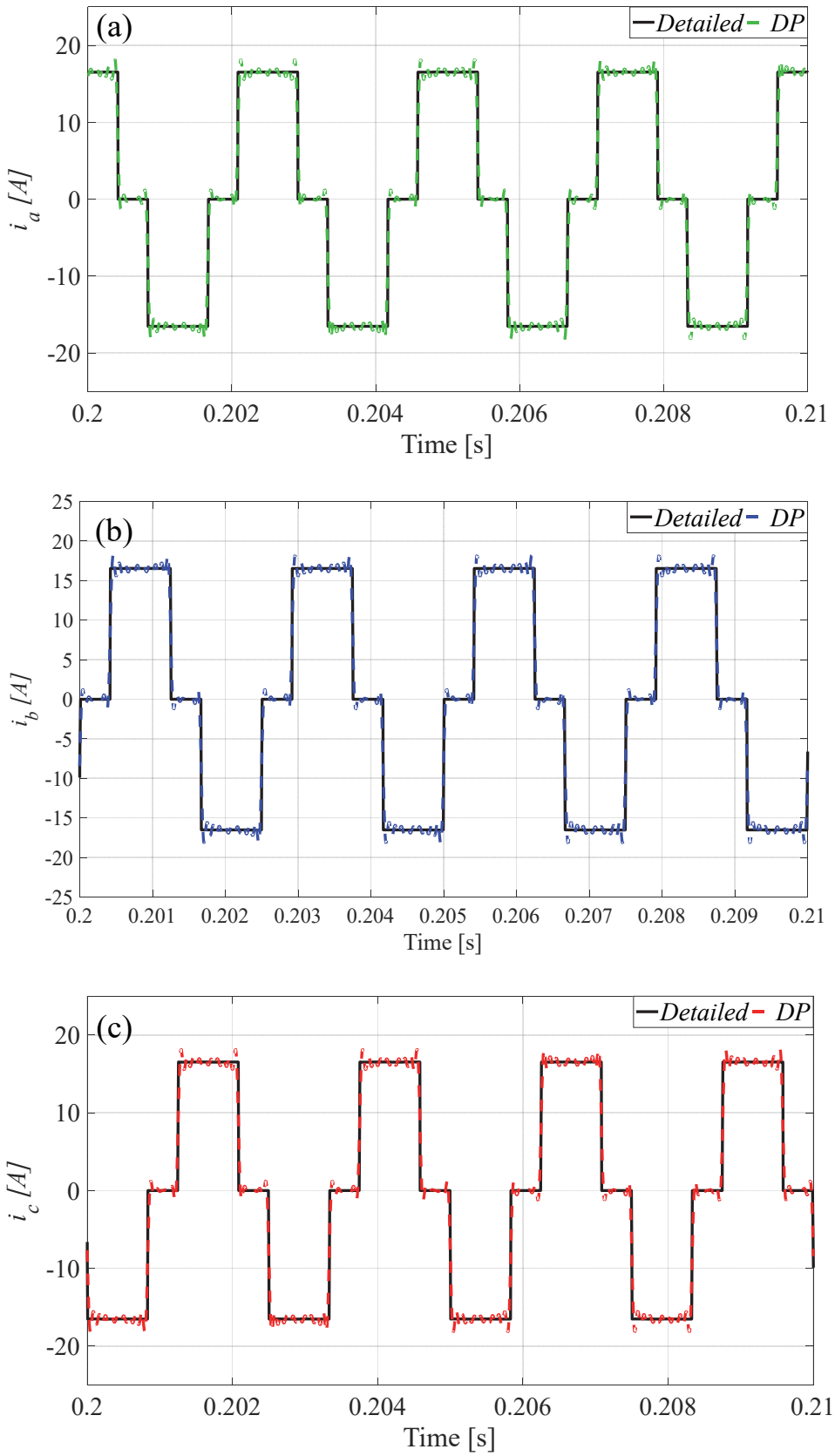

Figure. 3. 13. Three-phase input currents of uncontrolled rectifier obtained by the detailed and DP models. (a) i_a, (b) i_b, (c) i_c

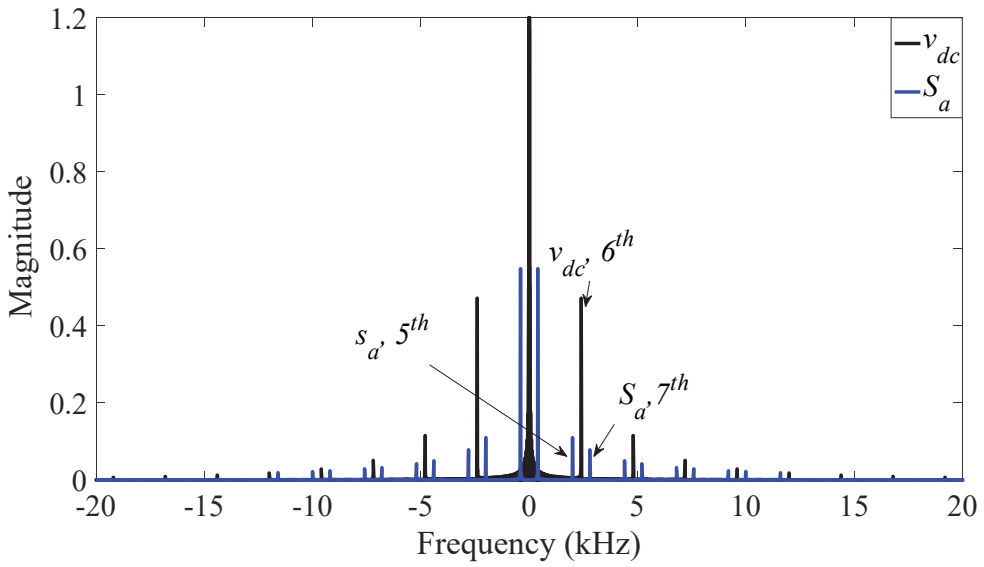

Figure. 3. 14. Frequency spectrum of the rectifier output voltage (v_{dc}) and switching function of phase *a*

As can be derived from (3.14) and can be seen in Fig .3.14, first harmonic of S_a multiplied by the phase voltage represents the zero-order component of v_{dc}. Also, fifth and seventh harmonics of S_a are representative of 6^{th} harmonic of v_{dc}.

0^{th} order component of the rectifier output current and voltage are shown in Fig .3.15 and Fig .3.16, respectively. Fig .3.17 .a to .d show the effect of adding 6^{th}, 12^{th}, 18^{th}, and 24^{th} harmonics of v_{dc}. As can be seen, by increasing the order of harmonics, their influence decreases (As can be derived from Fig .3.14.).

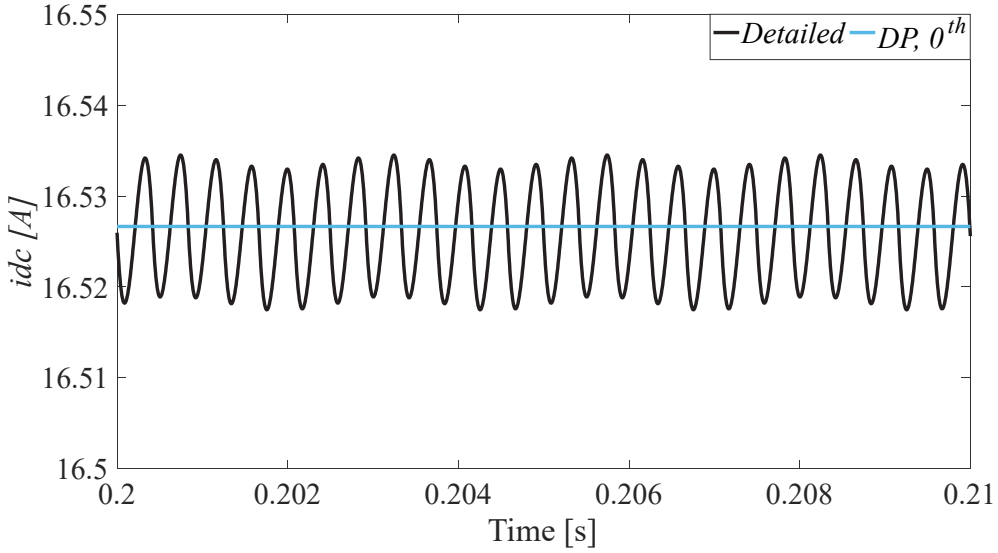

Figure. 3. 15. Uncontrolled rectifier output current obtained from the detailed model versus its 0^{th} component obtained from the DP model

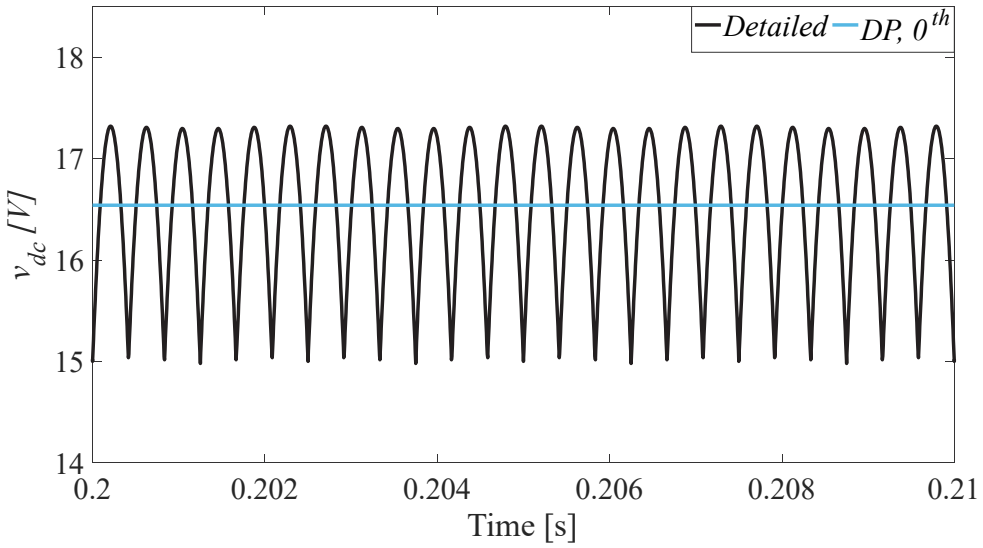

Figure. 3. 16. Uncontrolled rectifier output voltage obtained from the detailed model versus its 0th component obtained from the DP model

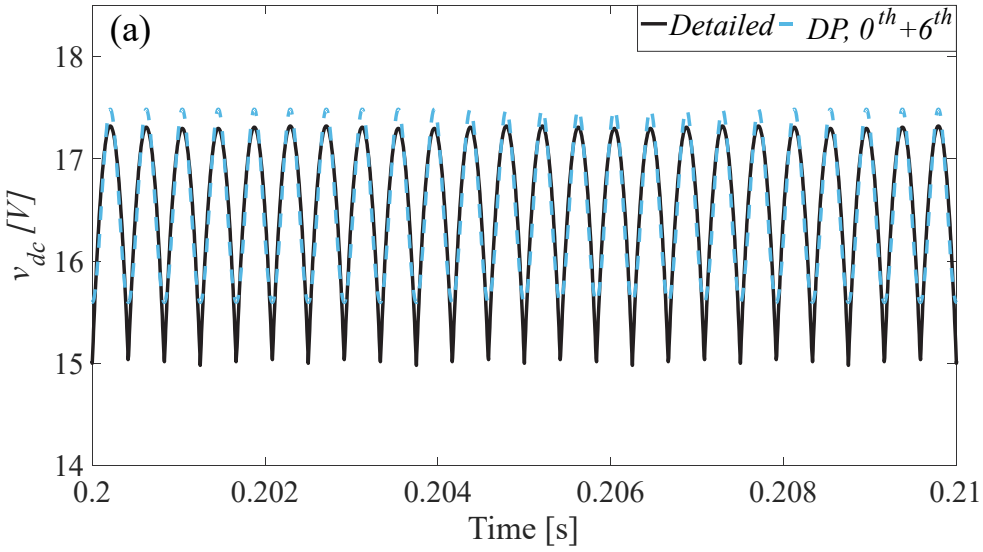

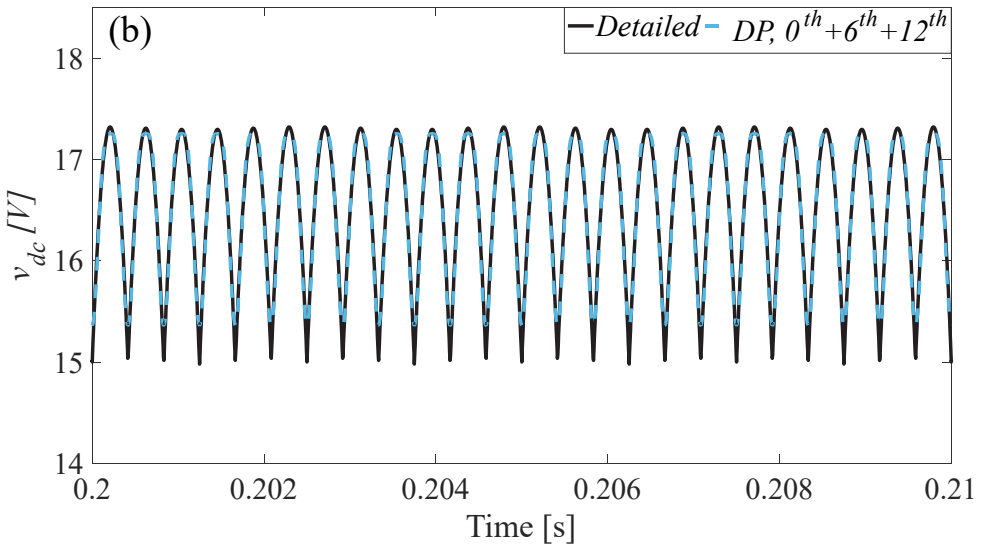

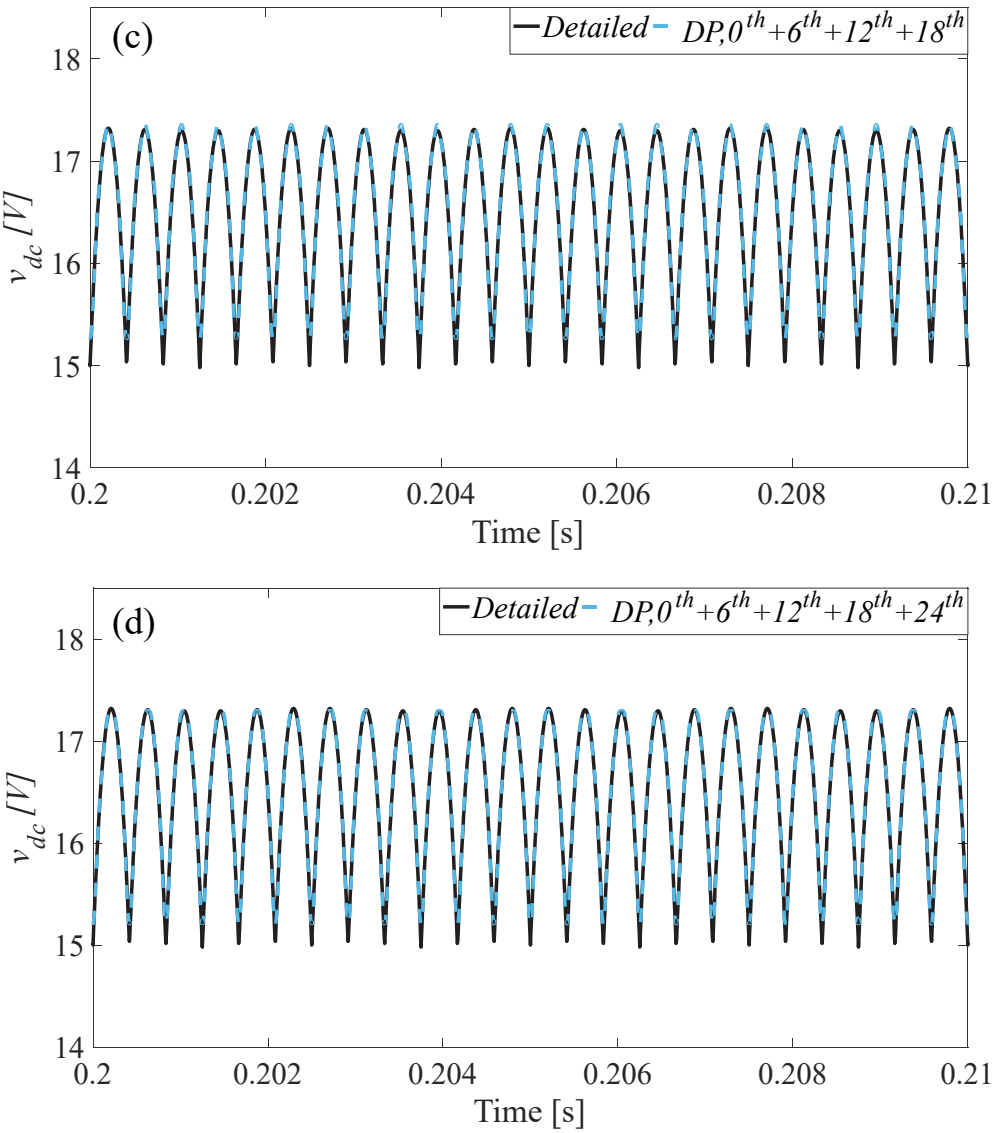

Figure. 3. 17. Uncontrolled rectifier output voltage. (a) detailed model versus $0^{th}+6^{th}$ component of the DP model, (b) detailed model versus $0^{th}+6^{th}+12^{th}$ components of the DP model, (c) detailed model versus $0^{th}+6^{th}+12^{th}+18^{th}$ components of the DP model, (d) detailed model versus $0^{th}+6^{th}+12^{th}+18^{th}+24^{th}$ components of the DP model

3.8.2 Case. 2: One phase open circuit fault.

In this case of study, at $t = 0.2\ s$, phase *b* of input voltages is disconnected from the rectifier input. Input voltages are same as in Case. 1. Fig .3.18 shows the three-phase input voltages. Fig .3.19 and Fig .3.20 show the rectifier output voltage and current, respectively. As can be seen in Fig .3.19 and Fig .3.20, at the beginning of the transient condition (at $t = 0.2s$) v_{dc} and i_{dc} obtained from the DP model are not perfectly matched with the waveforms obtained from the detailed model. The reason is that after the fault occurred, the intersection between phases and consequently the switching functions must be updated.

Since in the DP method, the intersection angles are calculated from line voltages in DP-domain, and in fact, DP is one period average of a signal, one period delay is imposed. This is shown in Fig .3.21. Fig .3.22 shows three-phase input currents of the rectifier estimated by the detailed model and the DP model. Frequency spectrum of the v_{dc} and S_a after occurring the fault are shown in Fig. 3.23. As can be seen, in addition to characteristic harmonics (0^{th}, 6^{th}, 12^{th}, etc.) the rectifier output voltage contains non-characteristic harmonic orders such as 2^{th}, 4^{th}, 8^{th} etc. [46].

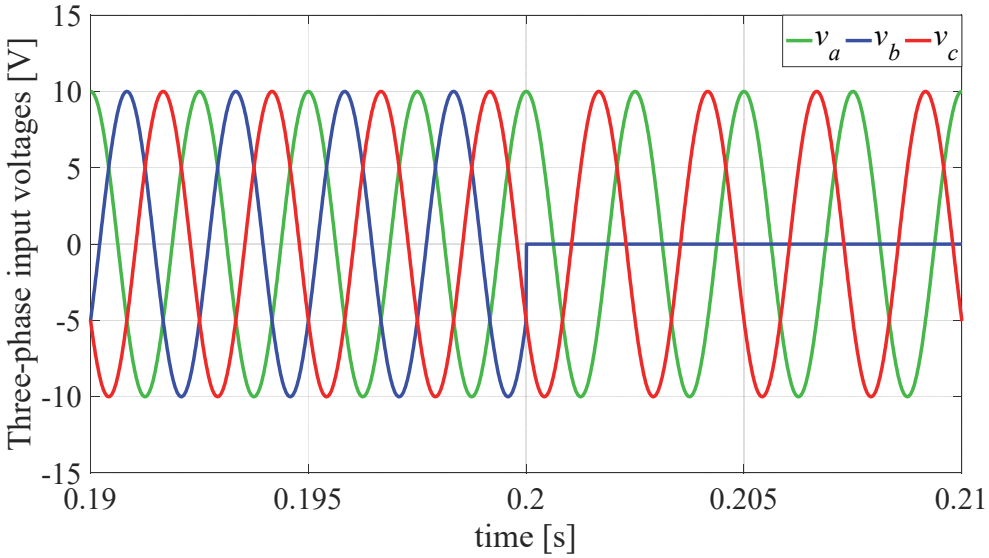

Figure. 3. 18. Three phase input voltages of the rectifier

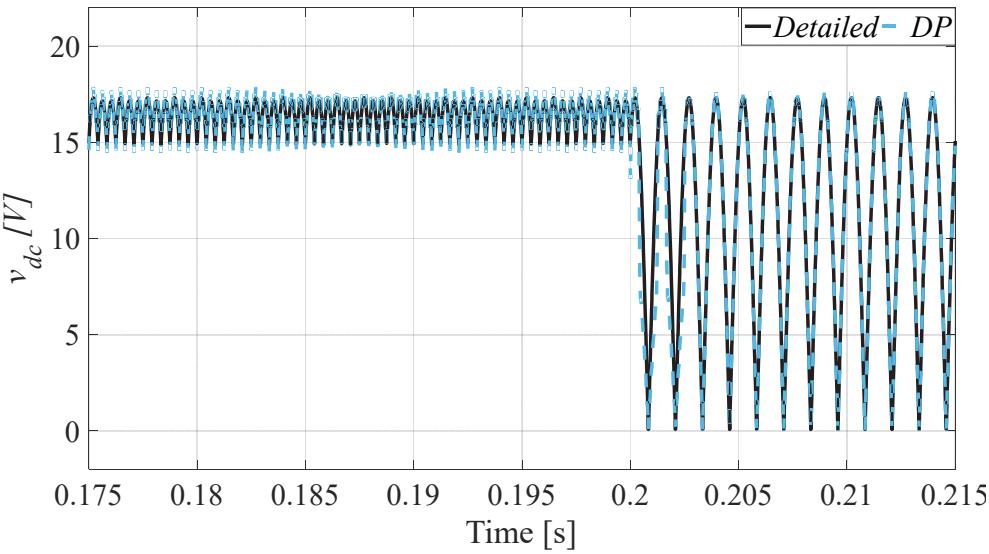

Figure. 3. 19. Rectifier output voltage under one phase open-circuit fault

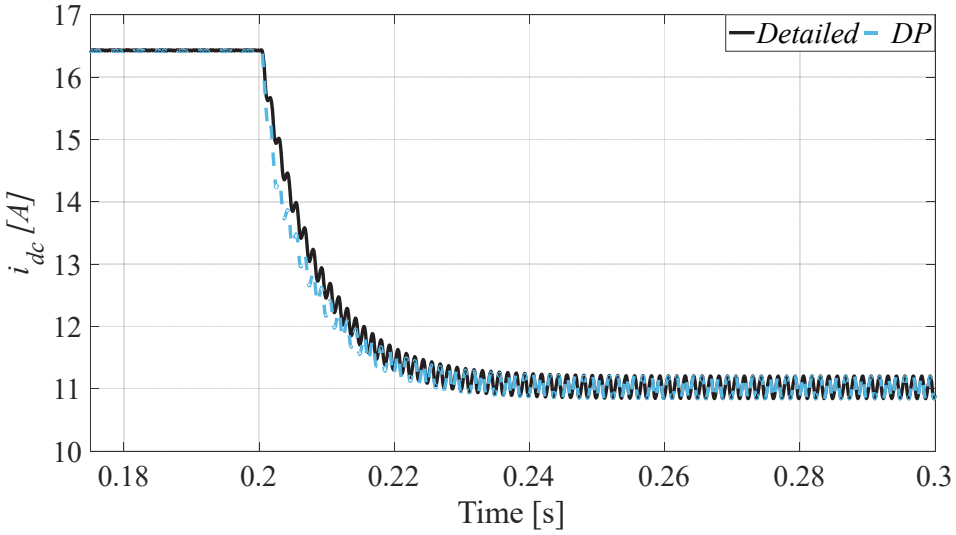

Figure. 3. 20. Rectifier output current under one phase open-circuit fault

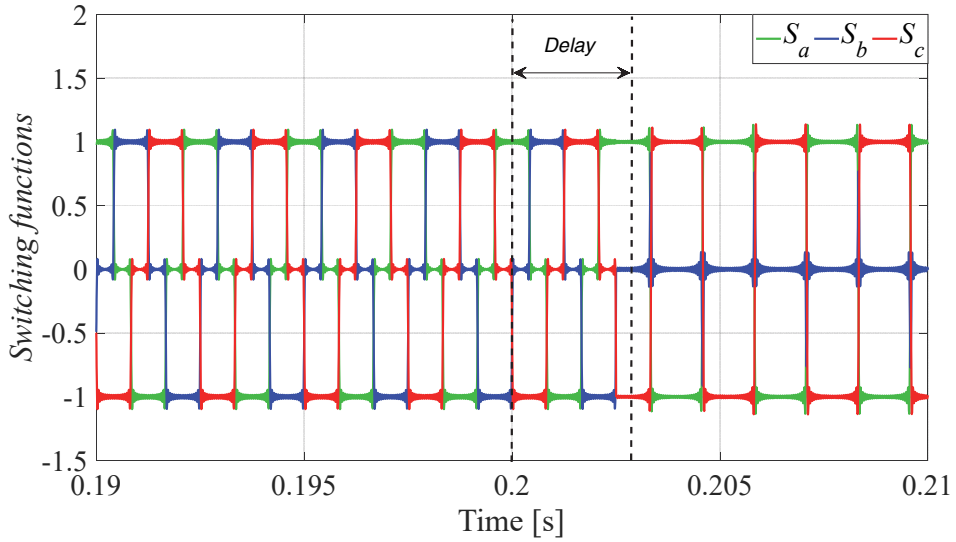

Figure. 3. 21. Switching functions of the rectifier before and after of the fault occurrence

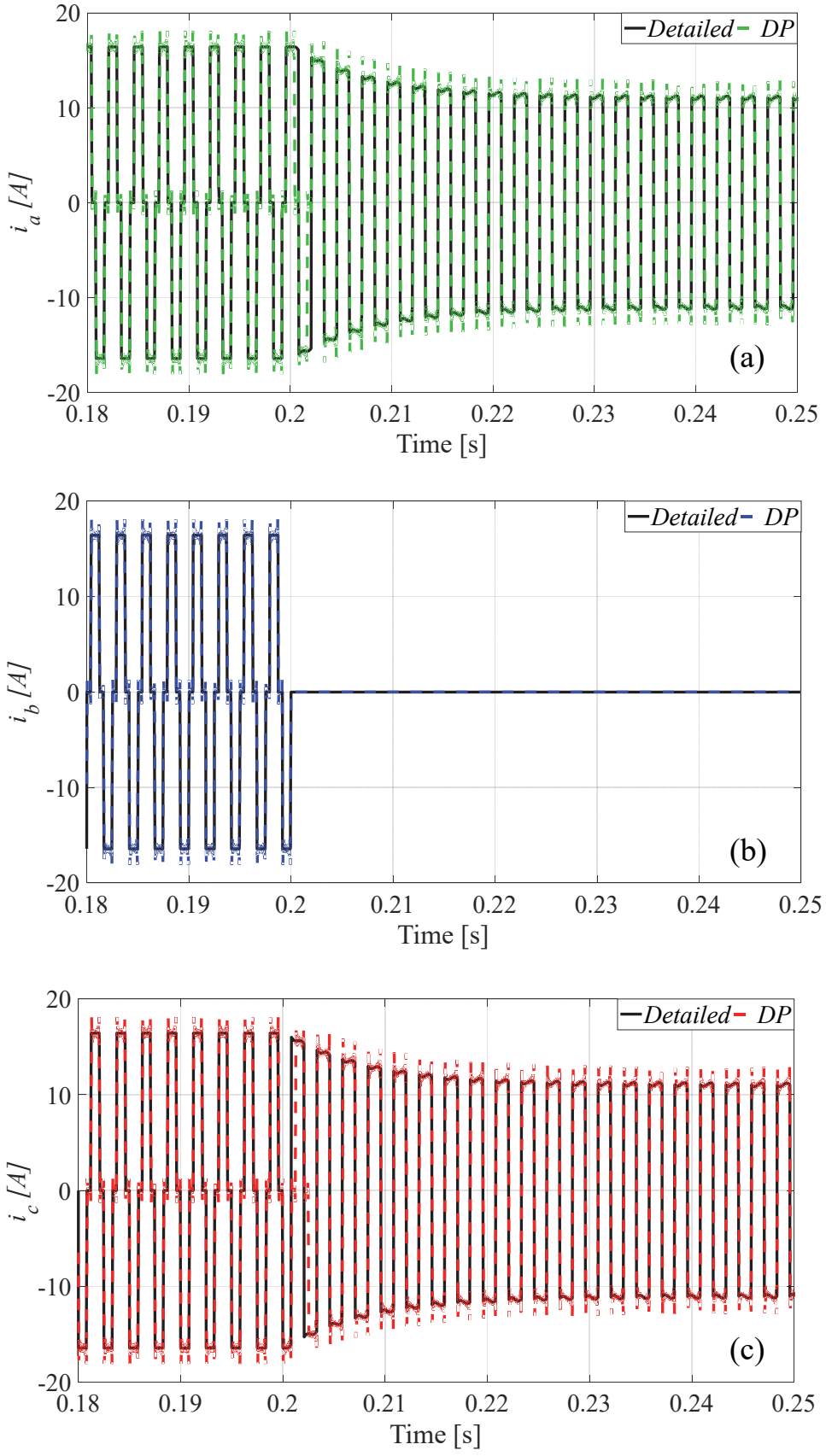

Figure. 3. 22. Rectifier input currents before and after of the fault occurrence obtained from the detailed model and the DP model. (a) i_a, (b) i_b, (c) i_c

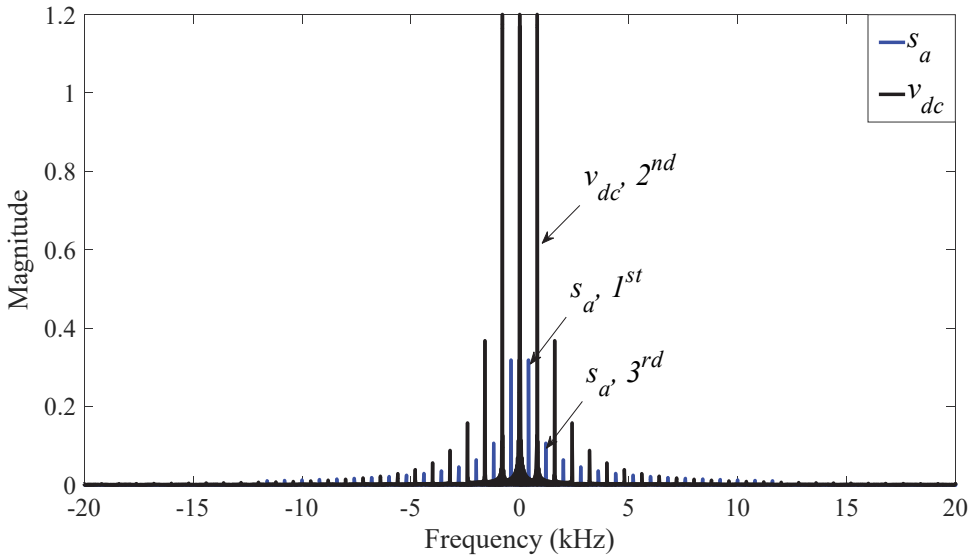

Figure. 3. 23. Frequency spectrum of the rectifier output voltage (v_{dc}) and switching function of phase *a*

3.8.3 Case. 3: Three-phase unbalance input voltages

In this case of study, the input voltages are set as:

$$v_a = 20 \cdot \cos\left(\omega t + \frac{\pi}{4}\right)$$

$$v_b = 10 \cdot \cos\left(\omega t - \frac{2 \cdot \pi}{3}\right)$$

$$v_c = 14 \cdot \cos\left(\omega t + \frac{3 \cdot \pi}{2}\right)$$

where

$$\omega = 400 \cdot 2 \cdot \pi$$

Fig .3.24 shows three-phase input voltages. Fig .3.25 and Fig .3.26 show the rectifier output voltage and current, respectively. Comparing the results obtained from the detailed model with the results obtained from the DP model, the proposed DP model that is able to update Fourier series coefficients shows a successful performance even in the unbalanced condition. Three-phase input currents of the rectifier are shown in Fig .3.27a to .3.27c. The frequency spectrum of the rectifier output voltage and switching function of phase *a* are shown in Fig .3.28. As can be seen in Fig .3.28, under the unbalanced condition, v_{dc} contains non-characteristic harmonics (2^{th}, 4^{th}, 8^{th}, etc.).

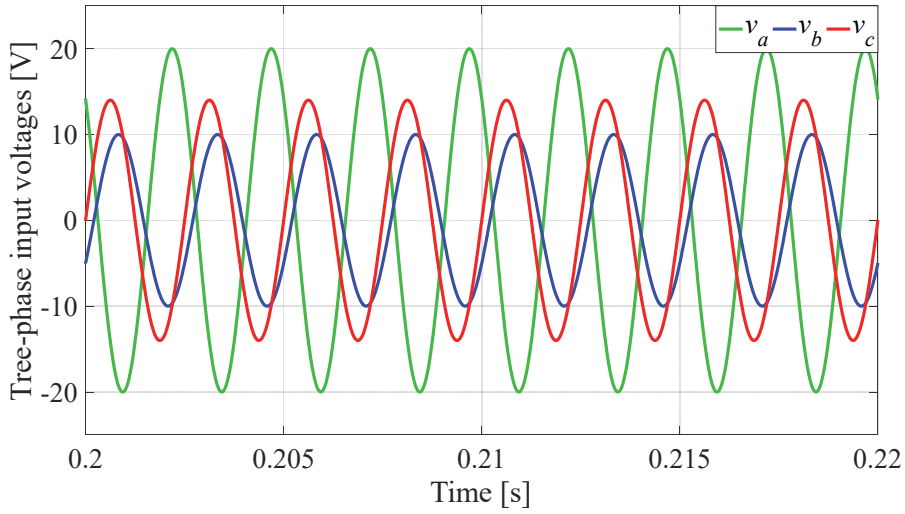

Figure. 3. 24. Three phase input voltages of the rectifier

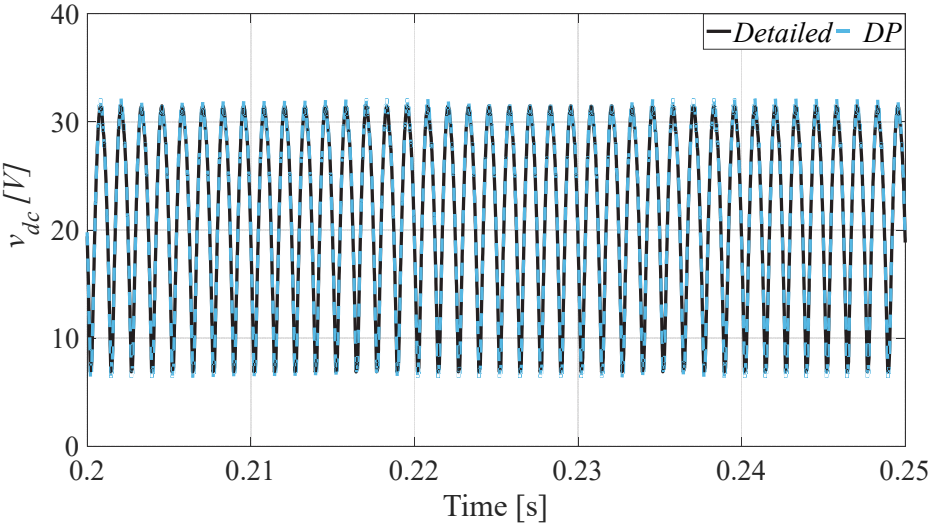

Figure. 3. 25. Rectifier output voltage under unbalanced input voltages condition

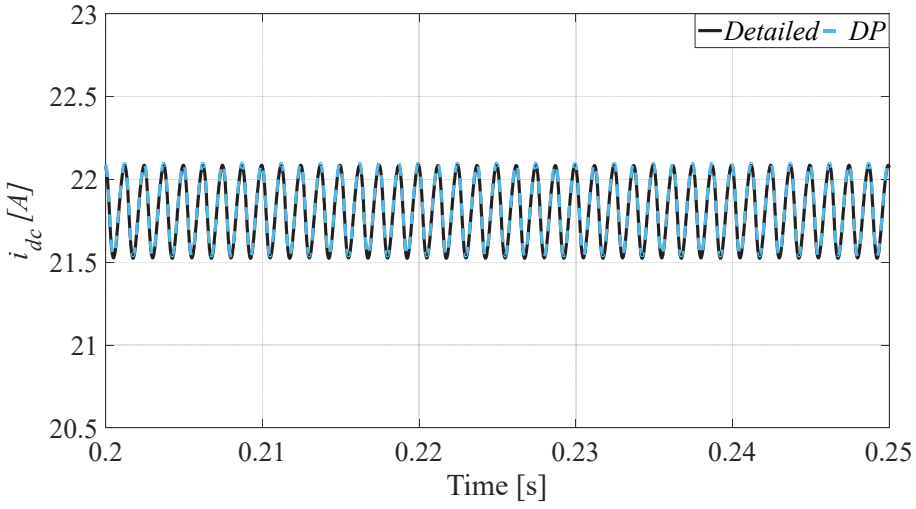

Figure. 3. 26. Rectifier output current under unbalanced input voltages condition

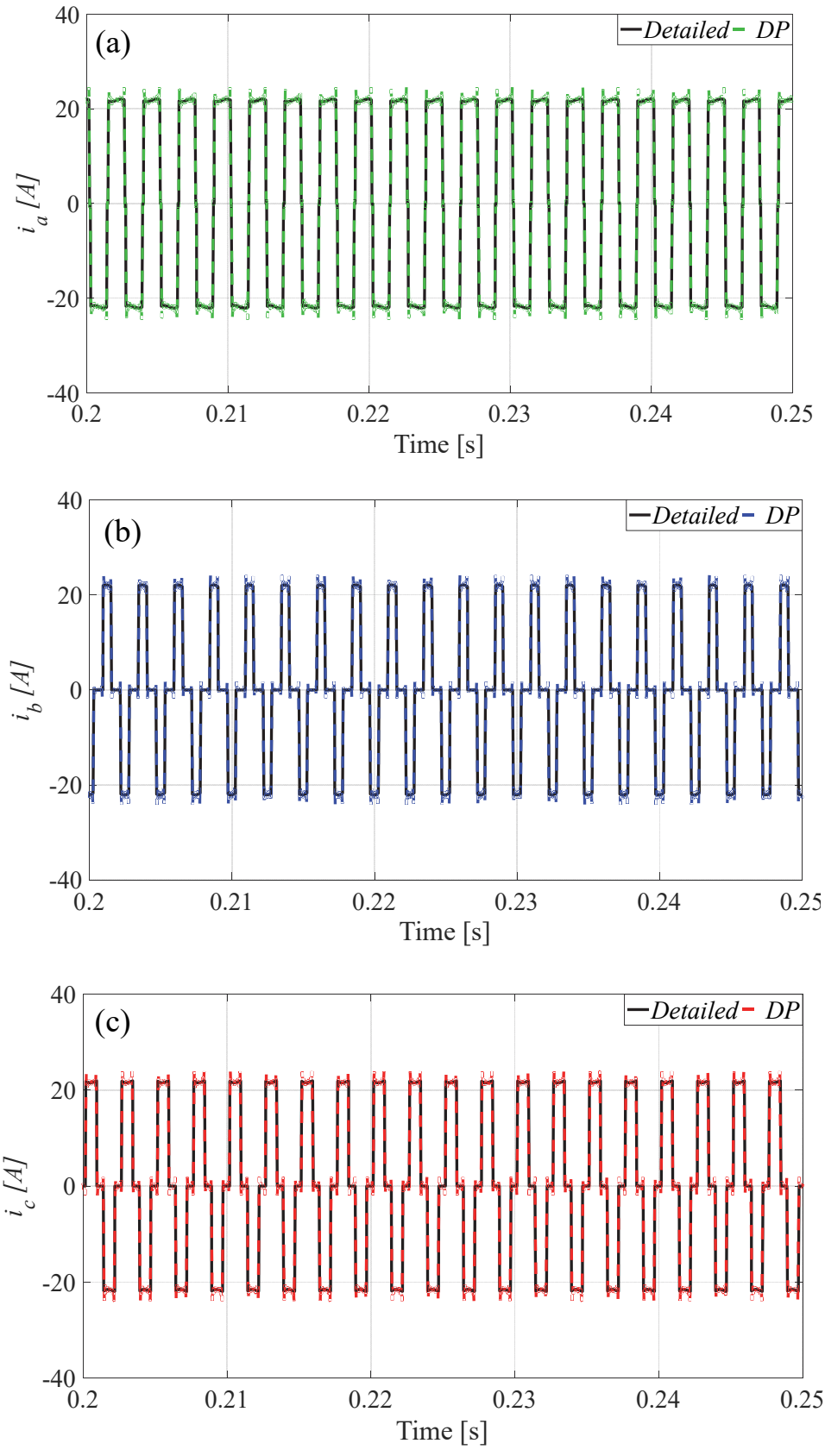

Figure. 3. 27. Unbalanced rectifier input currents obtained from the detailed model versus the DP model. (a) i_a, (b) i_b, (c) i_c

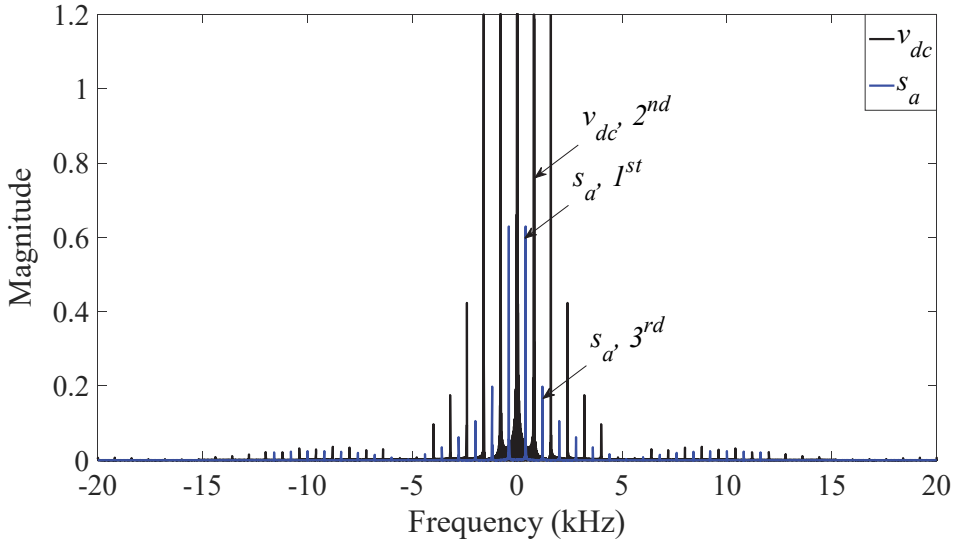

Figure. 3. 28. Frequency spectrum of the rectifier output voltage (v_{dc}) and switching function of phase *a*.

3.8.4 Case. 5: Transient from CCM to DCM

In this case of study, the uncontrolled diode bridge rectifier is fed by unbalanced voltages as same as in case 4, but at $t = 0.1\ s$, the rectifier load is switched to a lighter load that makes the rectifier to operate in DCM condition. Fig .3.29 shows the frequency spectrum of the rectifier output voltage in the tested CCM operation. As can be seen, rectifier output voltage contains more harmonics than other previous cases (odd and even orders). Therefore, the switching function must contain more harmonics to be able to represent the actual output voltage of the rectifier. Fig .3.30 and Fig .3.31 show the rectifier output voltage (v_{dc}) and output current (i_{dc}), respectively. As can be seen, DP model has a good performance at the transient interval. Fig .3.32a to 3.32.c show three-phase input currents of the rectifier.

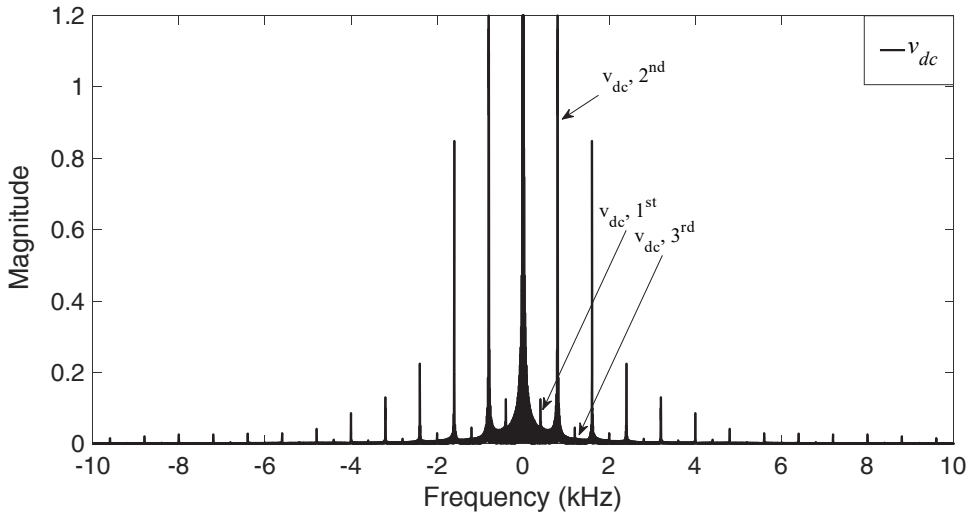

Figure. 3. 29. Frequency spectrum of the rectifier output voltage (v_{dc}) in DCM.

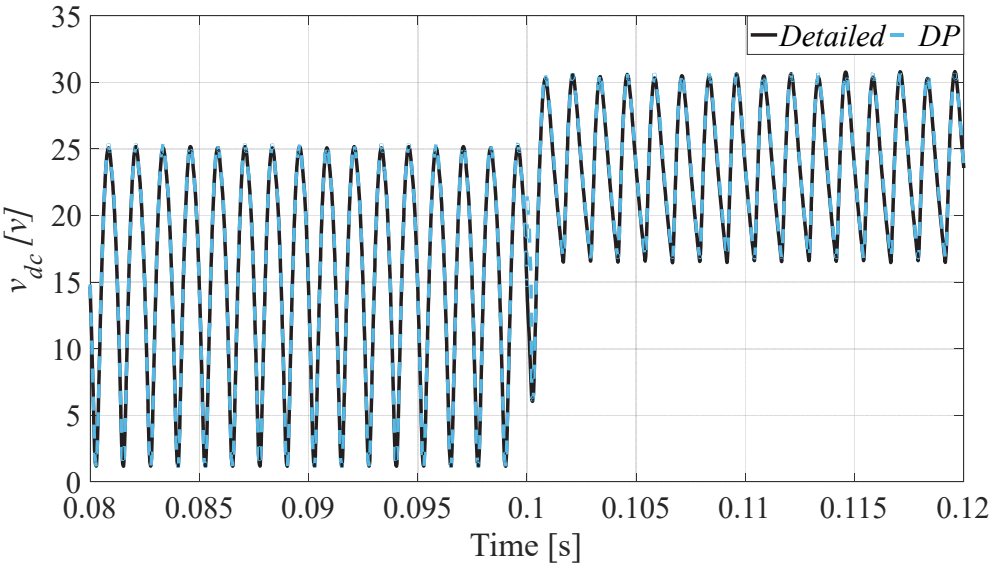

Figure. 3. 30. Rectifier output voltage under transition from CCM to DCM

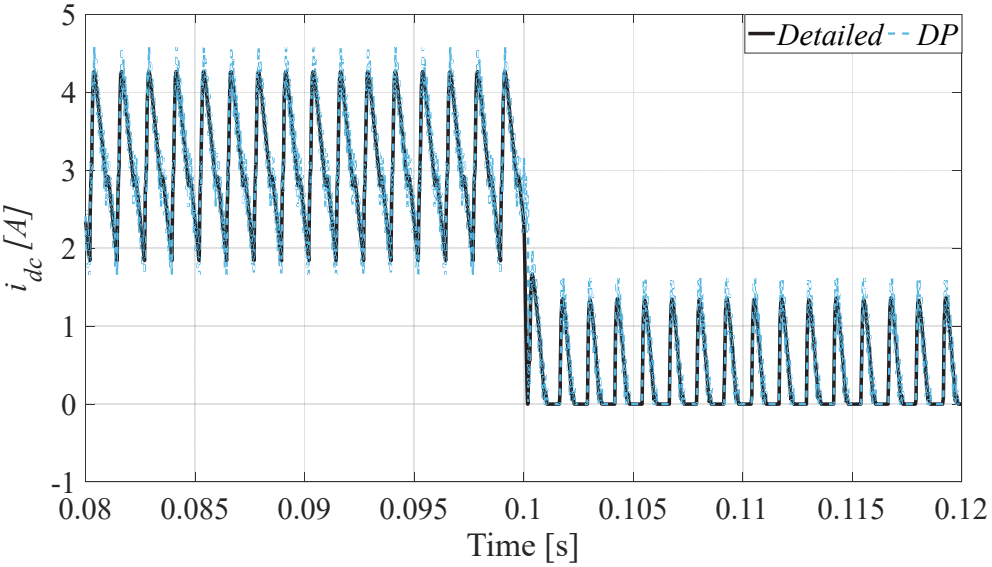

Figure. 3. 31. Rectifier output current under transition from CCM to DCM

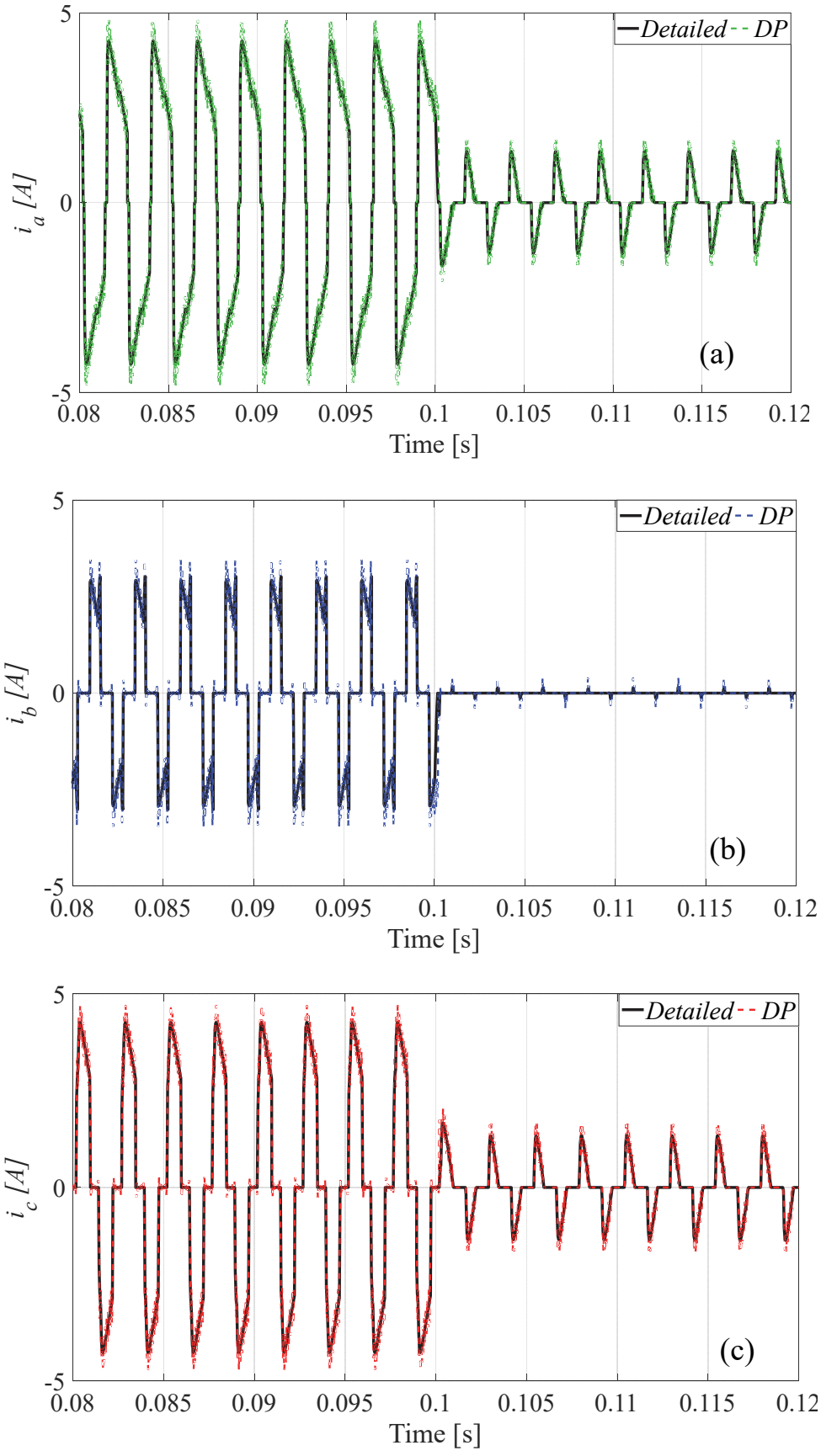

Figure. 3. 32. Rectifier input currents under transition from CCM to DCM. (a) i_a, (b) i_b, (c) i_c

3.9 Effect of front-end inductance on rectifier output voltage

In the previous section, the idealized circuit for the rectifier was considered. The main assumption considered for the idealized circuit was that the AC power source has zero reactance. So, DC output current of the rectifier switches instantaneously between rectifier diodes. In real condition, this assumption is far from true. In this section, the effect of the AC-side reactance is included in the rectifier model.

AC-side front-end inductances (hereafter is called commutation inductance) lead to a finite commutation interval when the output current of rectifier switches between rectifier legs. Presence of the commutation inductance prevents the instantaneous current transfer between diodes. Thus, during the commutation interval, two or more diodes are carrying current which makes line-to-line short-circuit between armature phases. Based on commutation duration, there are three operation modes for a rectifier which are described in detail in [47]. The first mode in which two-phase short circuit occurs is the most likely (commutation interval is less than $\frac{\pi}{6}$ degrees).

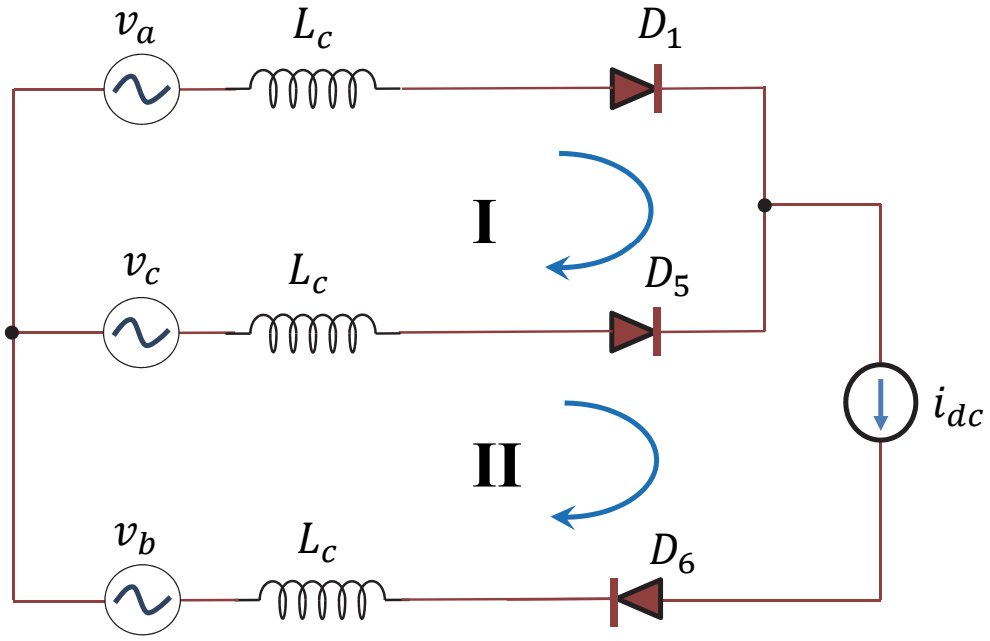

Figure. 3. 33. Equivalent circuit of the rectifier during current commutation between phase *a* and *c*

Fig 3.33 shows the equivalent circuit of the rectifier during current commutation between phase *a* and *c*. In this case, commutation current flows between phase *a* and *c*. Fig 3.34 shows the current of phase *a* and *c* during the commutation. The beginning of the commutation process is considered as time origin and end of the commutation process is shown by μ. Voltages of phase *a* and *c* during the commutation are shown in Fig 3.35. The dashed area indicates the voltage drop of the commutation process.

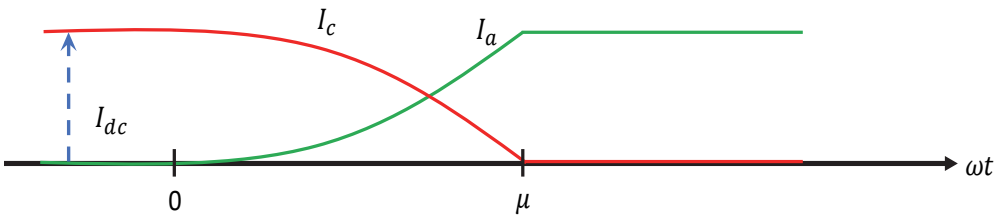

Figure. 3. 34. Current of phase *a* and *c* during the commutation process between phase *a* and *c*

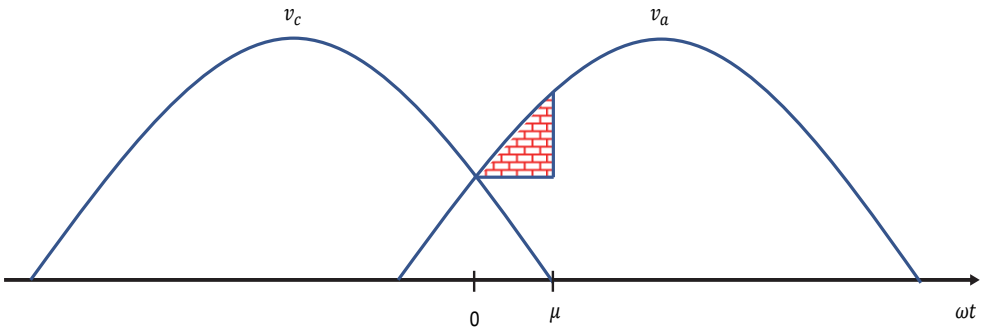

Figure. 3. 35. Voltage of phase *a* and *c* during commutation process between phase *a* and *c*.

Current constraints for the commutation process between phase *a* and *c* are as follows:

$$i_b = I_{dc}$$

$$i_a = i_\mu$$

$$i_c = I_{dc} - i_\mu$$

where, i_μ is circulating current between phase *a* and *c* during the commutation.

Applying KVL in the loop I (Fig 3.33), relationship between phase voltages and circulating commutation current can be derived as:

$$v_a - v_c = 2 \cdot L_c \cdot \frac{di_\mu}{dt} \tag{3.34}$$

Multiplying both sides of (3.34) by ω and integrating for the commutation interval:

$$\omega \cdot L_c \int_0^{I_{dc}} di_\mu = \int_0^{\mu} \frac{v_a - v_c}{2} d(\omega t) \tag{3.35}$$

where

$$v_a - v_c = V_{LL} \sin(\omega t) \tag{3.36}$$

Substituting (3.36) in (3.35)

$$\omega \cdot L_c \cdot I_{dc} = \frac{V_{LL} \cdot (1 - \cos(\mu))}{2} \tag{3.37}$$

Simplifying (3.37) for μ

$$\mu = \cos^{-1}\left(1 - \frac{2 \cdot \omega \cdot L_c \cdot i_{dc}}{V_{LL}}\right) \tag{3.38}$$

3.10 Including commutation effect in switching functions

Fig 3.36.a shows input and output voltages of the rectifier under the existence of commutation inductance. Fig 3.36b and Fig 3.36.c show currents of upper and bottom diodes. The effect of commutation process on voltages and currents can be seen in Fig 3.36a, Fig 3.36b, and Fig 3.36c. Fig 3.37 shows voltage switching function waveform for phase *a*, with considering the commutation effect. As can be seen in Fig 3.36, taking the commutation effect in the account, during the commutation interval, the value of the switching function is 0.5 instead of 1 in the ideal case (without considering the commutation effect).

As mentioned before, due to the presence of the commutation inductance, current changes in the circuit have a finite slope. Thus, during the commutation interval, the switching function of the currents should be different from voltages. Fig 3.38 shows current switching function of phase *a*.

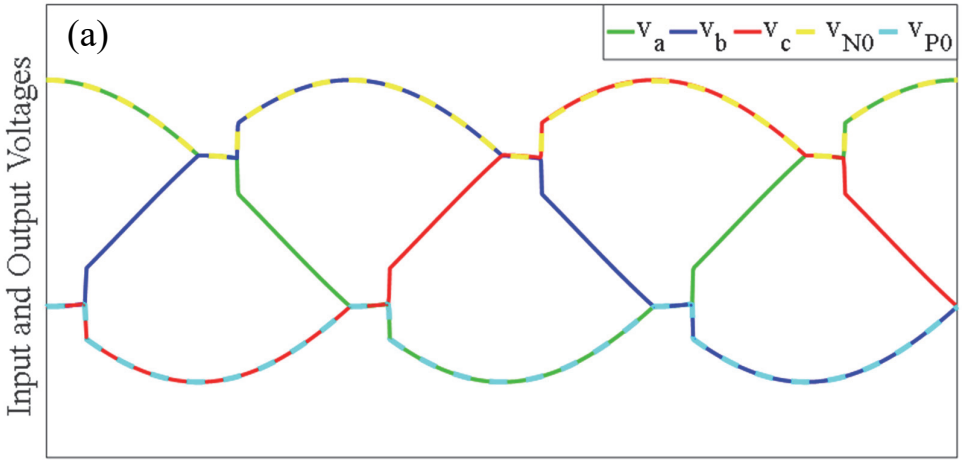

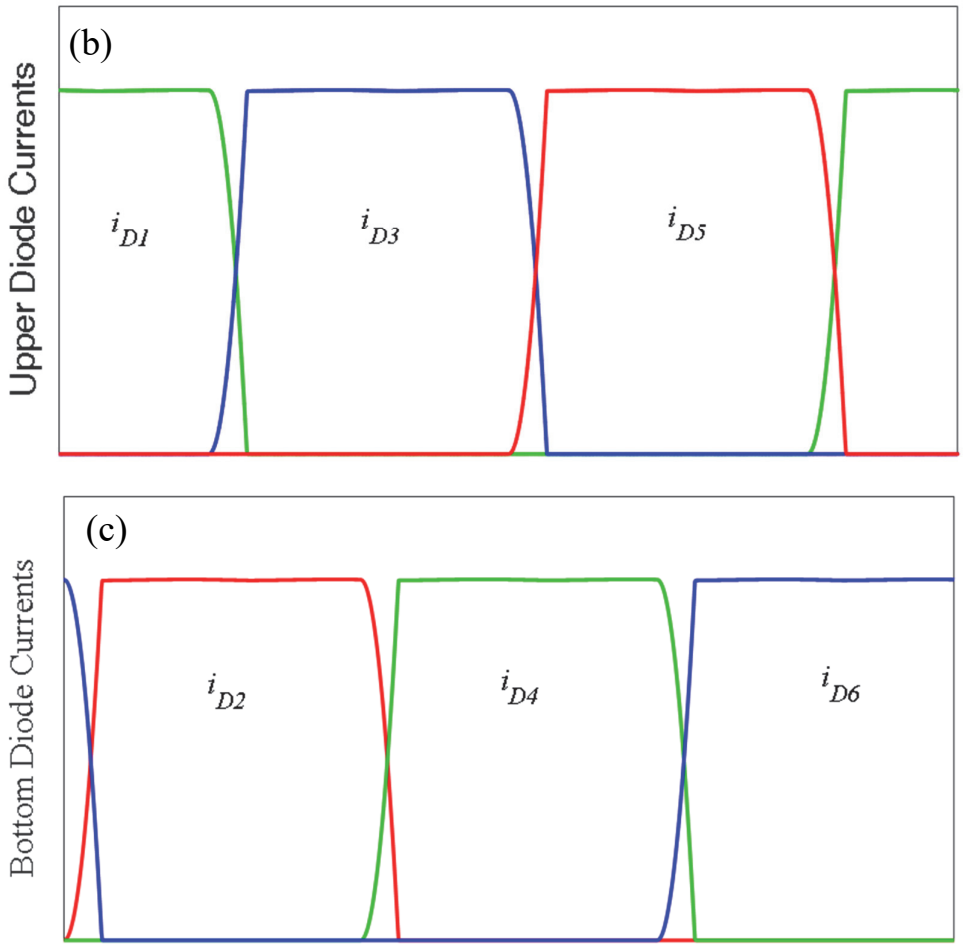

Figure. 3. 36. Diode bridge rectifier performance under existence of commutation inductance. (a) input and output voltages of the rectifier, (b) currents of upper and bottom diodes

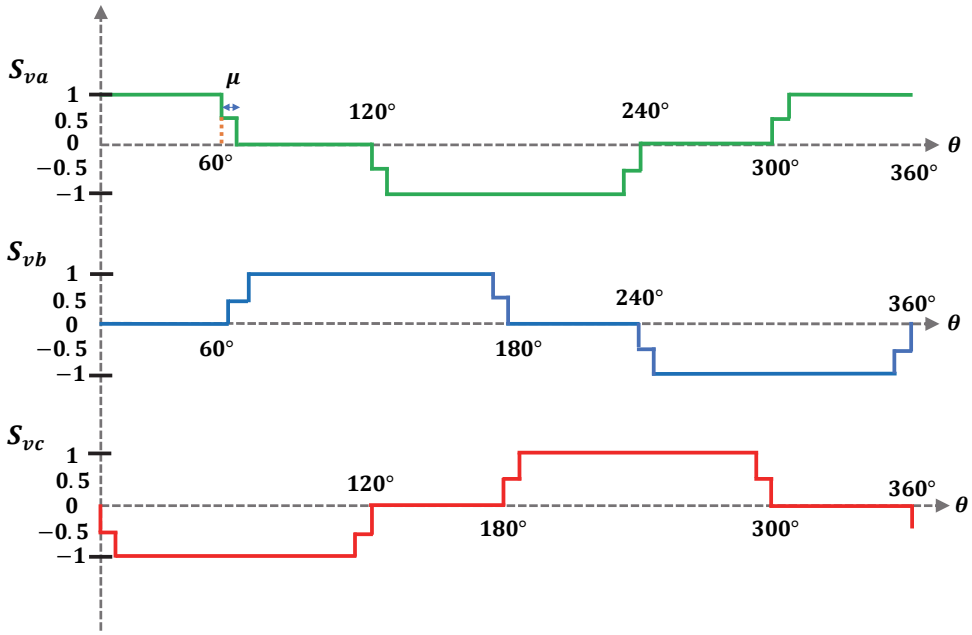

Figure. 3. 37. Voltage switching function waveforms, with considering the commutation effect

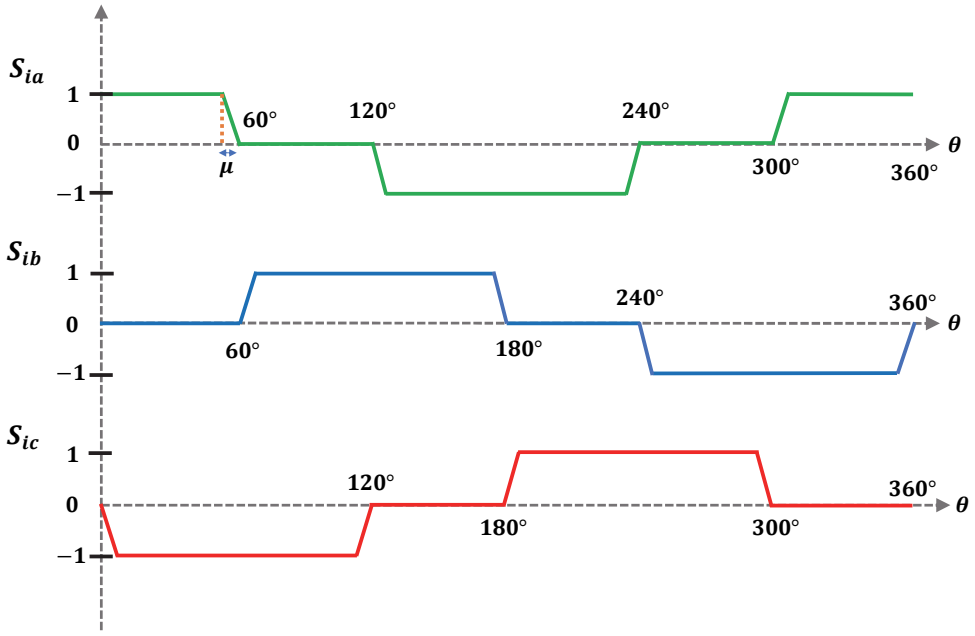

Figure. 3. 38. Current switching function waveforms, with considering the commutation effect

3.10.1 Switching functions with considering the commutation effect in time-domain

Commutation angle is calculated from (3.38). Phase shifting the switching functions by $\frac{\mu}{2}$ to the left, even waveforms can be achieved. This makes the calculation of Fourier series easier. Then, after calculation of Fourier series coefficients, a phase shift of $\frac{\mu}{2}$ to the right must be applied. To the best knowledge of the author, in the literature, reported Fourier series formula of switching functions under the existence of commutation inductance is incorrect [44] and [48]. In the papers, the second phase shift in the calculation process of Fourier series was not applied. For voltage switching functions, correct Fourier series approximation of Switching functions (equations (3.28) to (3.30)) is:

$$A_n = \frac{2}{n\cdot\pi}\cdot[\sin(n\cdot B_i) - \sin(n\cdot A_i)]\cdot\cos\left(\frac{n\cdot\mu}{2}\right) \tag{3.39}$$

$$B_n = \frac{2}{n\cdot\pi}\cdot[\cos(n\cdot A_i) - \cos(n\cdot B_i)]\cdot\cos\left(\frac{n\cdot\mu}{2}\right) \tag{3.40}$$

$$S_{V,i}(t) = \sum_{n=1}^{\infty}\left[A_n\cdot\cos\left(n\omega t - \frac{n\cdot\mu}{2}\right) + B_n\cdot\sin\left(n\omega t - \frac{n\cdot\mu}{2}\right)\right], \quad i = a, b, and\ c \tag{3.41}$$

As mentioned before, under existence of commutation inductance, switching functions of currents are different from voltages. In time-domain, switching functions of rectifier input currents are:

$$S_{I,i}(t) = \sum_{n=1}^{\infty}\left[A_n \cdot \cos\left(n\omega t - \frac{n\cdot\mu}{2}\right) + B_n \cdot \sin\left(n\omega t - \frac{n\cdot\mu}{2}\right)\right] \cdot \frac{\sin\left(\frac{n\cdot\mu}{2}\right)}{\frac{n\cdot\mu}{2}} , \quad i = a, b, and\ c \tag{3.42}$$

3.10.2 Switching functions with considering the commutation effect in DP-domain

Representation of voltage switching functions (equation (3.41)) in DP-domain is:

$$\langle S_{v,i}\rangle_k = \frac{2}{k\cdot\pi} \cdot \sin\left(\frac{k\cdot(B_i - A_i)}{2}\right) \cdot e^{-j\left(\frac{k\cdot(A_i+B_i)}{2}\right)} \cdot \cos\left(\frac{k\cdot\mu}{2}\right) \cdot e^{-j\left(\frac{k\cdot\mu}{2}\right)} , \quad i = a, b, and\ c \tag{3.43}$$

And, for current switching functions (equation (3.42)), DP expression is:

$$\langle S_{I,i}\rangle_k = \frac{2}{k\cdot\pi} \cdot \sin\left(\frac{k\cdot(B_i - A_i)}{2}\right) \cdot e^{-j\left(\frac{k\cdot(A_i+B_i)}{2}\right)} \cdot \frac{\sin\left(\frac{k\cdot\mu}{2}\right)}{\frac{k\cdot\mu}{2}} \cdot e^{-j\left(\frac{k\cdot\mu}{2}\right)} , \quad i = a, b, and\ c \tag{3.44}$$

3.11 Validation of switching function model considering the commutation effect in balanced condition

Using formulas of switching functions, uncontrolled diode bridge rectifier is modeled. To validate the presented model of rectifier in DP-domain, comparison between detailed model and switching function model in DP-domain is performed. Fig 3.39 shows input voltages of the rectifier. Voltage switching function of input phases and current switching function of phase *a* are shown in Fig 3.40.

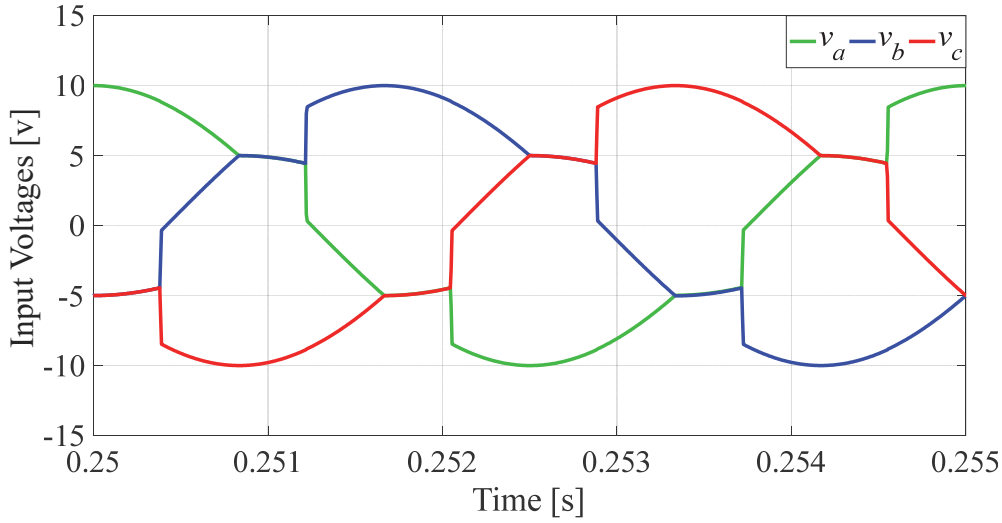

Figure. 3. 39. Input voltages of the rectifier

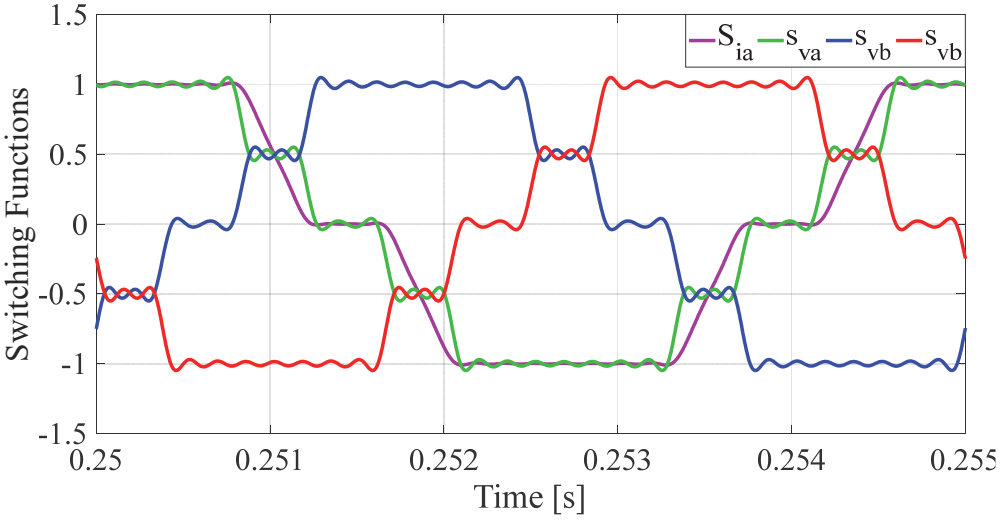

Figure. 3. 40. Switching functions of the diode bridge rectifier

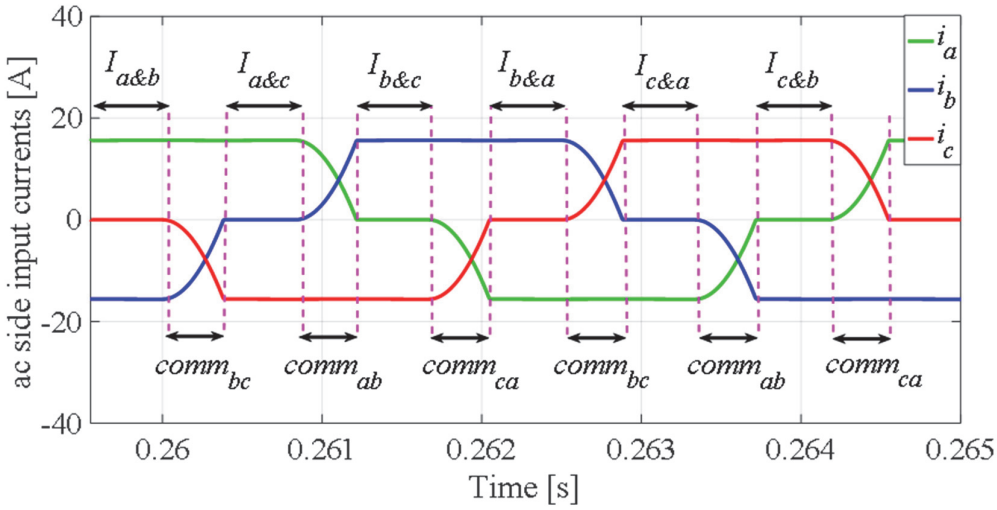

Figure. 3. 41. Waveforms of AC-side currents

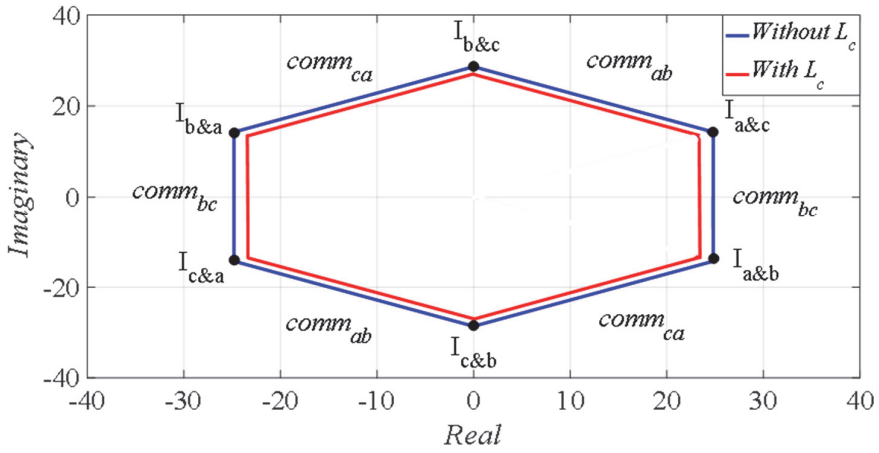

Figure. 3. 42. Trajectory of AC-side currents

Considering commutation inductance and based on number of simultaneous conducting diodes, there are two operation modes for uncontrolled diode bridge rectifier. These modes are called interlude and commutation modes. During interlude mode, only two diodes (one upper diode and one bottom diode) are conducting. While, during commutation mode, more than two diodes are carrying current. These modes are shown in Fig 3.41, where interlude intervals are indicated by '*I*'. For example, I_{ab} represents interlude interval where phase *a* carries positive current and phase *b* carries negative current. Also, commutation intervals are indicated by "*Comm*". For instance, $Comm_{bc}$ indicates commutation interval where current transfers from phase *b* to phase *c*.

To show the influence of commutation inductance on the output voltage and current of the rectifier, this test is repeated without the existence of commutation inductance. Then, space phasor of input currents is calculated and plotted in Fig. 3.42.

As can be seen in Fig 3.42, trajectory of input currents of the rectifier is a hexagon. Corners of the hexagon represent interlude states and its sides represent commutation intervals. As can be seen in Fig 3.42, amplitudes of input currents of the rectifier are reduced. This is consequence of commutation voltage drop.

Output voltage and current of the rectifier are shown in Fig 3.43 and 3.44. The current of phase a is shown in Fig 3.45. As can be seen, in switching function method, the exponential increment of current during commutation interval is approximated by linear increment. Fig 3.46 shows the frequency spectrum of the rectifier output voltage and voltage switching function of phase *a*.

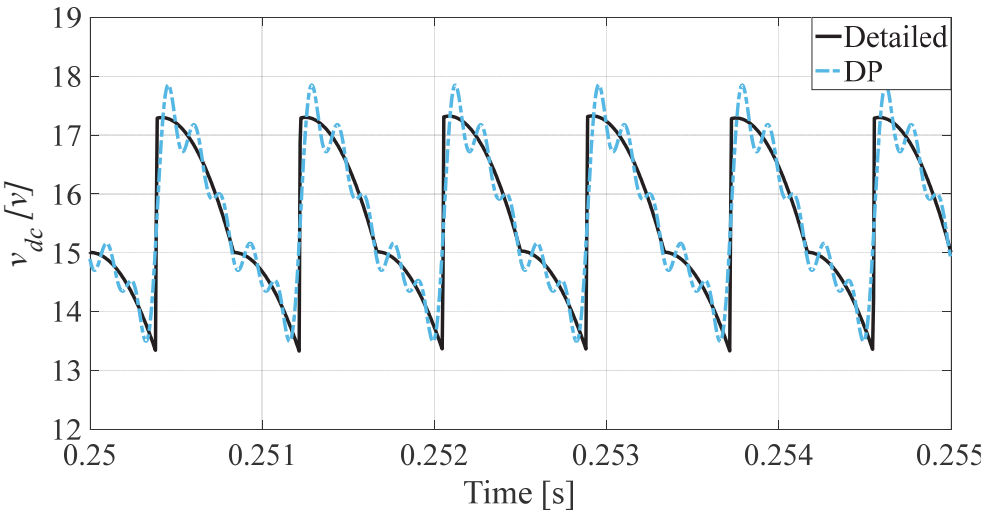

Figure. 3. 43. Rectifier output voltage

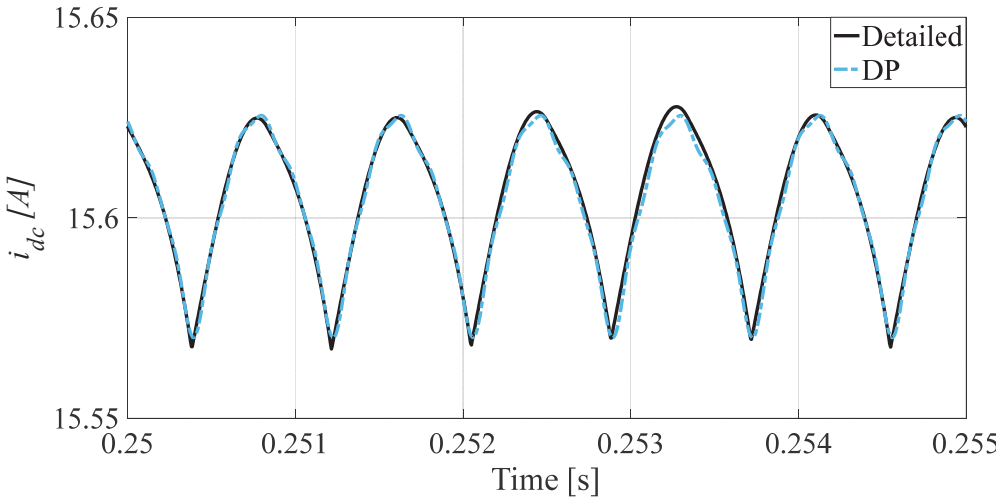

Figure. 3. 44. Rectifier output current

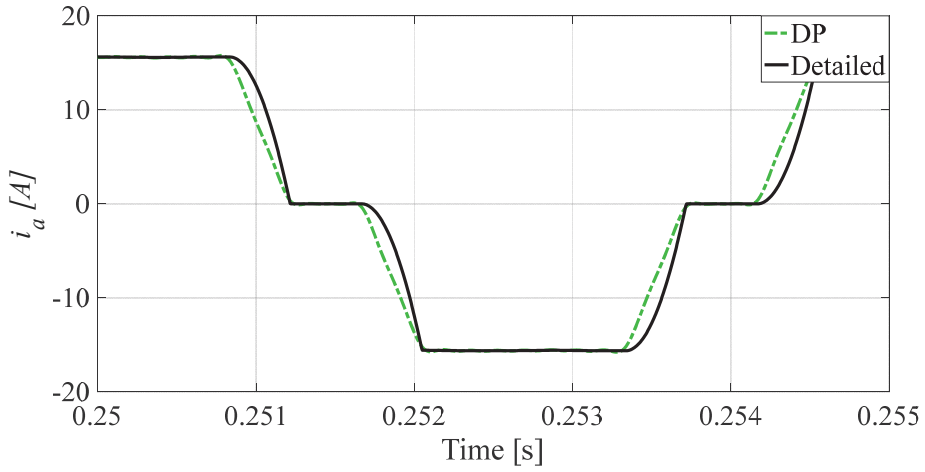

Figure. 3. 45. An input current of the rectifier, phase *a*

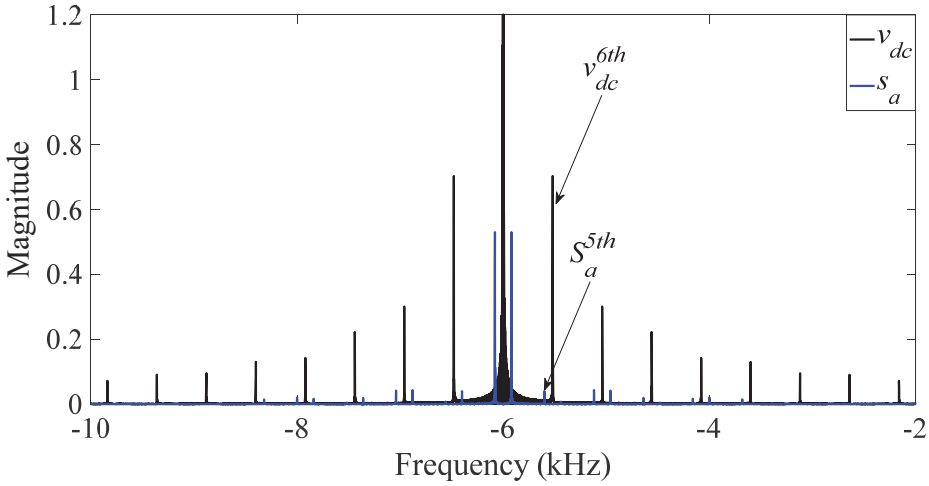

Figure. 3. 46. Frequency spectrum of the rectifier output voltage (v_{dc}) and switching function of phase *a*

3.12 Switching functions with considering the commutation effect in Unbalance conditions

Since commutation duration is related to amplitude of phase voltages that are commutating, in unbalanced condition, commutation interval between each two phases is different from other two phases. Therefore, commutation angle must be calculated for each combinations of commutating phases.

$$\mu_{ab} = \cos^{-1}\left(1 - \frac{2\cdot\omega\cdot L_c\cdot i_{dc}}{V_{ab}}\right) \tag{3.45}$$

$$\mu_{bc} = \cos^{-1}\left(1 - \frac{2\cdot\omega\cdot L_c\cdot i_{dc}}{V_{bc}}\right) \tag{3.46}$$

$$\mu_{ca} = \cos^{-1}\left(1 - \frac{2\cdot\omega\cdot L_c\cdot i_{dc}}{V_{ca}}\right) \tag{3.47}$$

3.12.1 Time-domain Representation of Switching Functions with considering the commutation effect in Unbalance conditions

Since commutation angles for different combination of commutating phases is not equal, switching functions have uneven commutation interval at each of their sides. Coefficients of voltage switching functions in time-domain are calculated as:

For phase *a*:

$$A_n = \frac{1}{n\cdot\pi}\cdot\left[\sin(n\cdot B_i) - \sin(n\cdot A_i) + \sin\left(n\cdot(B_i+\mu_{ab})\right) - \sin\left(n\cdot(A_i+\mu_{ca})\right)\right] \quad (3.48)$$

$$B_n = \frac{1}{n\cdot\pi}\cdot\left[\cos(n\cdot A_i) - \cos(n\cdot B_i) + \cos\left(n\cdot(A_i+\mu_{ca})\right) - \cos\left(n\cdot(B_i+\mu_{ab})\right)\right] \quad (3.49)$$

For phase *b*:

$$A_n = \frac{1}{n\cdot\pi}\cdot\left[\sin(n\cdot B_i) - \sin(n\cdot A_i) + \sin\left(n\cdot(B_i+\mu_{bc})\right) - \sin\left(n\cdot(A_i+\mu_{ab})\right)\right] \quad (3.50)$$

$$B_n = \frac{1}{n\cdot\pi}\cdot\left[\cos(n\cdot A_i) - \cos(n\cdot B_i) + \cos\left(n\cdot(A_i+\mu_{ab})\right) - \cos\left(n\cdot(B_i+\mu_{bc})\right)\right] \quad (3.51)$$

For phase *c*:

$$A_n = \frac{1}{n\cdot\pi}\cdot\left[\sin(n\cdot B_i) - \sin(n\cdot A_i) + \sin\left(n\cdot(B_i+\mu_{ca})\right) - \sin\left(n\cdot(A_i+\mu_{bc})\right)\right] \quad (3.52)$$

$$B_n = \frac{1}{n\cdot\pi}\cdot\left[\cos(n\cdot A_i) - \cos(n\cdot B_i) + \cos\left(n\cdot(A_i+\mu_{bc})\right) - \cos\left(n\cdot(B_i+\mu_{ca})\right)\right] \quad (3.53)$$

Formula of Fourier series of voltage switching functions is:

$$S_{V,i}(t) = \sum_{n=1}^{\infty}[A_n\cdot\cos(n\omega t) + B_n\cdot\sin(n\omega t)], \quad i = a, b, and\ c \quad (3.54)$$

Coefficients of current switching functions in time-domain are calculated as:

For phase *a*:

$$A_n = \frac{2}{n\cdot\pi}\cdot\left[\sin\left(n\cdot\left(B_i+\frac{\mu_{ab}}{2}\right)\right)\cdot\frac{\sin\left(\frac{n\cdot\mu_{ab}}{2}\right)}{\frac{n\cdot\mu_{ab}}{2}}-\sin\left(n\cdot\left(A_i+\frac{\mu_{ca}}{2}\right)\right)\cdot\frac{\sin\left(\frac{n\cdot\mu_{ca}}{2}\right)}{\frac{n\cdot\mu_{ca}}{2}}\right] \quad (3.55)$$

$$B_n = \frac{2}{n\cdot\pi}\cdot\left[\cos\left(n\cdot\left(A_i+\frac{\mu_{ca}}{2}\right)\right)\cdot\frac{\sin\left(\frac{n\cdot\mu_{ca}}{2}\right)}{\frac{n\cdot\mu_{ca}}{2}}-\cos\left(n\cdot\left(B_i+\frac{\mu_{ab}}{2}\right)\right)\cdot\frac{\sin\left(\frac{n\cdot\mu_{ab}}{2}\right)}{\frac{n\cdot\mu_{ab}}{2}}\right] \quad (3.56)$$

For phase *b*:

$$A_n = \frac{2}{n\cdot\pi}\cdot\left[\sin\left(n\cdot\left(B_i+\frac{\mu_{bc}}{2}\right)\right)\cdot\frac{\sin\left(\frac{n\cdot\mu_{bc}}{2}\right)}{\frac{n\cdot\mu_{bc}}{2}}-\sin\left(n\cdot\left(A_i+\frac{\mu_{ab}}{2}\right)\right)\cdot\frac{\sin\left(\frac{n\cdot\mu_{ab}}{2}\right)}{\frac{n\cdot\mu_{ab}}{2}}\right] \quad (3.57)$$

$$B_n = \frac{2}{n\cdot\pi}\cdot\left[\cos\left(n\cdot\left(A_i+\frac{\mu_{ab}}{2}\right)\right)\cdot\frac{\sin\left(\frac{n\cdot\mu_{ab}}{2}\right)}{\frac{n\cdot\mu_{ab}}{2}}-\cos\left(n\cdot\left(B_i+\frac{\mu_{bc}}{2}\right)\right)\cdot\frac{\sin\left(\frac{n\cdot\mu_{bc}}{2}\right)}{\frac{n\cdot\mu_{bc}}{2}}\right] \quad (3.58)$$

For phase *c*:

$$A_n = \frac{2}{n\cdot\pi}\cdot\left[\sin\left(n\cdot\left(B_i+\frac{\mu_{ca}}{2}\right)\right)\cdot\frac{\sin\left(\frac{n\cdot\mu_{ca}}{2}\right)}{\frac{n\cdot\mu_{ca}}{2}}-\sin\left(n\cdot\left(A_i+\frac{\mu_{bc}}{2}\right)\right)\cdot\frac{\sin\left(\frac{n\cdot\mu_{bc}}{2}\right)}{\frac{n\cdot\mu_{bc}}{2}}\right] \quad (3.59)$$

$$B_n = \frac{2}{n\cdot\pi}\cdot\left[\cos\left(n\cdot\left(A_i+\frac{\mu_{bc}}{2}\right)\right)\cdot\frac{\sin\left(\frac{n\cdot\mu_{bc}}{2}\right)}{\frac{n\cdot\mu_{bc}}{2}}-\cos\left(n\cdot\left(B_i+\frac{\mu_{ca}}{2}\right)\right)\cdot\frac{\sin\left(\frac{n\cdot\mu_{ca}}{2}\right)}{\frac{n\cdot\mu_{ca}}{2}}\right] \quad (3.60)$$

Formula of Fourier series of current switching functions is:

$$S_{I,i}(t) = \sum_{n=1}^{\infty}[A_n\cdot\cos(n\omega t)+B_n\cdot\sin(n\omega t)],\ \ i=a,b,and\ c \quad (3.61)$$

3.12.2 DP-domain Representation of Switching Functions with considering the commutation effect in Unbalance conditions

In this section, time-domain voltage and current switching functions are transformed into DP-domain.

Voltage switching functions in DP-domain:

For phase *a*:

$$\langle S_{V,a}\rangle_k = \frac{1}{k\cdot\pi}\cdot\left[\sin\left(\frac{k\cdot(B_i-A_i)}{2}\right)\cdot e^{-j\left(\frac{k\cdot(A_i+B_i)}{2}\right)} + \sin\left(\frac{k\cdot(B_i-A_i+\mu_{ab}-\mu_{ca})}{2}\right)\cdot e^{-j\left(\frac{k\cdot(A_i+B_i+\mu_{ab}+\mu_{ca})}{2}\right)}\right] \quad (3.62)$$

For phase *b*:

$$\langle S_{V,b}\rangle_k = \frac{1}{k\cdot\pi}\cdot\left[\sin\left(\frac{k\cdot(B_i-A_i)}{2}\right)\cdot e^{-j\left(\frac{k\cdot(A_i+B_i)}{2}\right)} + \sin\left(\frac{k\cdot(B_i-A_i+\mu_{bc}-\mu_{ab})}{2}\right)\cdot e^{-j\left(\frac{k\cdot(A_i+B_i+\mu_{bc}+\mu_{ab})}{2}\right)}\right] \quad (3.63)$$

For phase *c*:

$$\langle S_{V,c}\rangle_k = \frac{1}{k\cdot\pi}\cdot\left[\sin\left(\frac{k\cdot(B_i-A_i)}{2}\right)\cdot e^{-j\left(\frac{k\cdot(A_i+B_i)}{2}\right)} + \sin\left(\frac{k\cdot(B_i-A_i+\mu_{ca}-\mu_{bc})}{2}\right)\cdot e^{-j\left(\frac{k\cdot(A_i+B_i+\mu_{ca}+\mu_{bc})}{2}\right)}\right] \quad (3.64)$$

Current switching functions in DP-domain:

For phase *a*:

$$\langle S_{I,a}\rangle_k = \frac{-j}{k\cdot\pi}\left[\frac{\sin\left(\frac{k\cdot(\mu_{ca})}{2}\right)}{\frac{k\cdot(\mu_{ca})}{2}}\cdot e^{-j\left(\frac{k\cdot\left(A_i+\frac{\mu_{ca}}{2}\right)}{2}\right)} - \frac{\sin\left(\frac{k\cdot(\mu_{ab})}{2}\right)}{\frac{k\cdot(\mu_{ab})}{2}}\cdot e^{-j\left(\frac{k\cdot\left(B_i+\frac{\mu_{ab}}{2}\right)}{2}\right)}\right] \quad (3.65)$$

For phase *b*:

$$\langle S_{I,b}\rangle_k = \frac{-j}{k\cdot\pi}\left[\frac{\sin\left(\frac{k\cdot(\mu_{ab})}{2}\right)}{\frac{k\cdot(\mu_{ab})}{2}}\cdot e^{-j\left(\frac{k\cdot\left(A_i+\frac{\mu_{ab}}{2}\right)}{2}\right)} - \frac{\sin\left(\frac{k\cdot(\mu_{bc})}{2}\right)}{\frac{k\cdot(\mu_{bc})}{2}}\cdot e^{-j\left(\frac{k\cdot\left(B_i+\frac{\mu_{bc}}{2}\right)}{2}\right)}\right] \tag{3.66}$$

For phase *c*:

$$\langle S_{I,c}\rangle_k = \frac{-j}{k\cdot\pi}\left[\frac{\sin\left(\frac{k\cdot(\mu_{bc})}{2}\right)}{\frac{k\cdot(\mu_{bc})}{2}}\cdot e^{-j\left(\frac{k\cdot\left(A_i+\frac{\mu_{bc}}{2}\right)}{2}\right)} - \frac{\sin\left(\frac{k\cdot(\mu_{ca})}{2}\right)}{\frac{k\cdot(\mu_{ca})}{2}}\cdot e^{-j\left(\frac{k\cdot\left(B_i+\frac{\mu_{ca}}{2}\right)}{2}\right)}\right] \tag{3.67}$$

3.13 Case study and validation of proposed models of uncontrolled rectifier under unbalanced condition.

In order to validate effectiveness of the proposed model of uncontrolled diode rectifier for unbalanced conditions, the performance of the proposed model is investigated by two cases of study. First, the performance of the proposed model is comprised with the detailed model. In this case, input voltages are highly unbalanced, and one phase open-circuit fault happens in input voltages. The second case examines the performance of the proposed model in transient from CCM to DCM operations.

3.13.1 Case. 1: Arbitrary three-phase unbalanced input voltages, and one phase open-circuit Fault

In this case of study, input voltages of the rectifier are assumed as:

$$v_a = 10\cdot\cos\left(\omega t+\frac{\pi}{6}\right)$$

$$v_b = 18\cdot\cos\left(\omega t-\frac{2\cdot\pi}{3}\right)$$

$$v_c = 15\cdot\cos\left(\omega t+\frac{\pi}{2}\right)$$

where

$$\omega = 400\cdot 2\cdot\pi$$

At *t=0.2 s* open-circuit fault occurs in phase *b*. Fig 3.47 shows input voltages of the rectifier. Voltage switching functions and current switching function of phase a are shown in Fig 3.48. As can be seen, commutation intervals are not equal. For example, commutation interval between phase *b* and phase *c* is shorter than phase *a* and phase *c*.

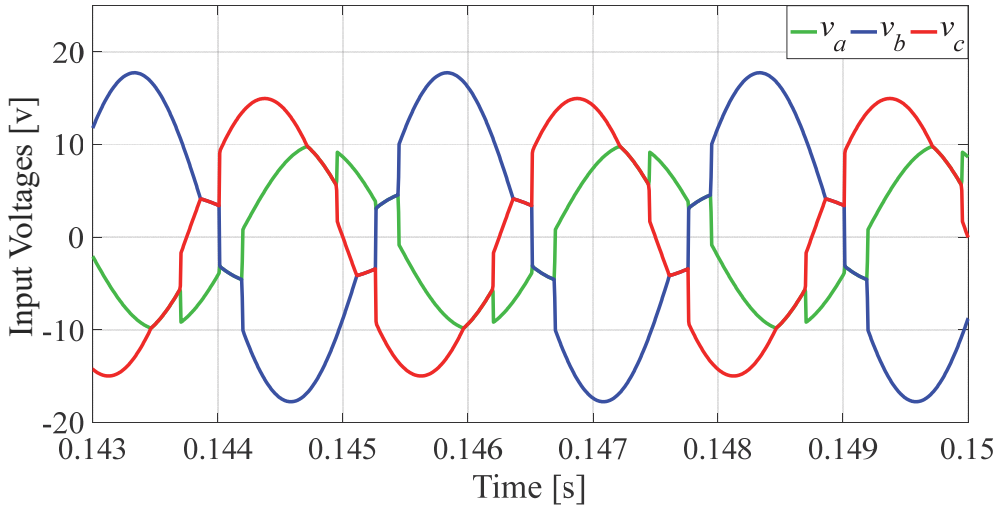

Figure. 3. 47. Input voltages of the rectifier

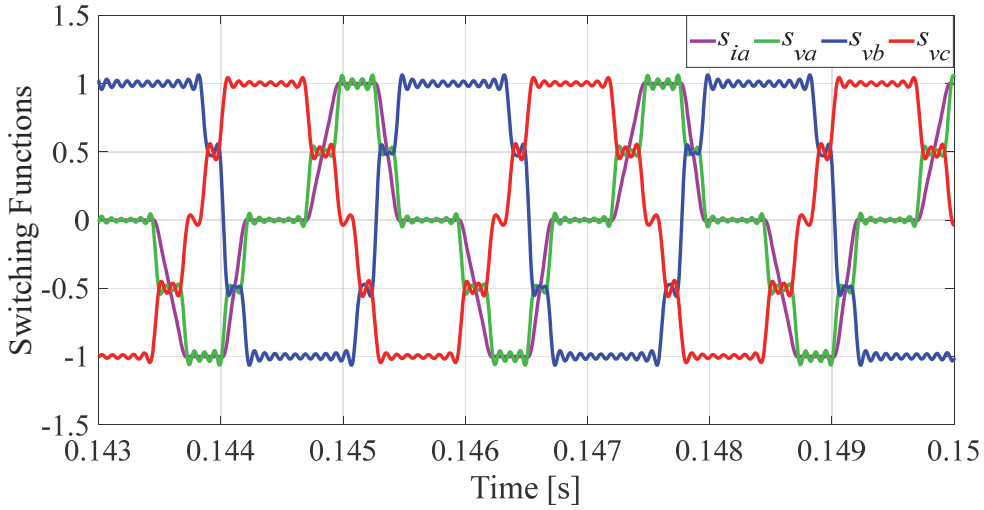

Figure. 3. 48. Voltage switching functions and current switching function of phase *a*

Fig 3.49 and Fig 3.50 show rectifier output voltage and current, respectively. Current of phase *a* is shown in Fig 3.51. Frequency spectrum of the rectifier output voltage (v_{dc}) and voltage switching function of phase *a* before and after occurrence of fault are shown in Fig 3.52 and 3.53, respectively. As can be derived from Fig 3.52, and Fig 3.53, before occurrence of fault because of unbalanced input voltages, output voltage of rectifier and switching functions contain non-characteristic harmonics. Amplitude of non-characteristic harmonics increases after occurrence of the fault.

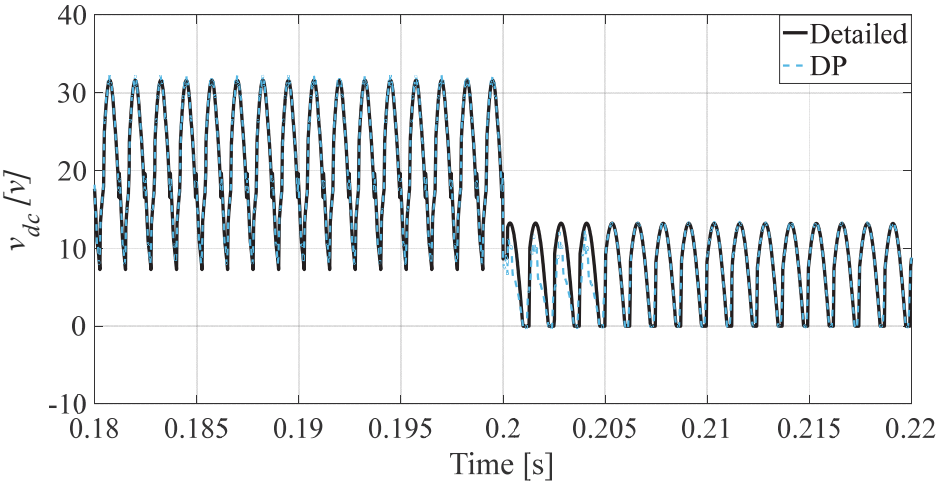

Figure. 3. 49. Output voltage of the rectifier under unbalanced input voltages and one phase open-circuit fault

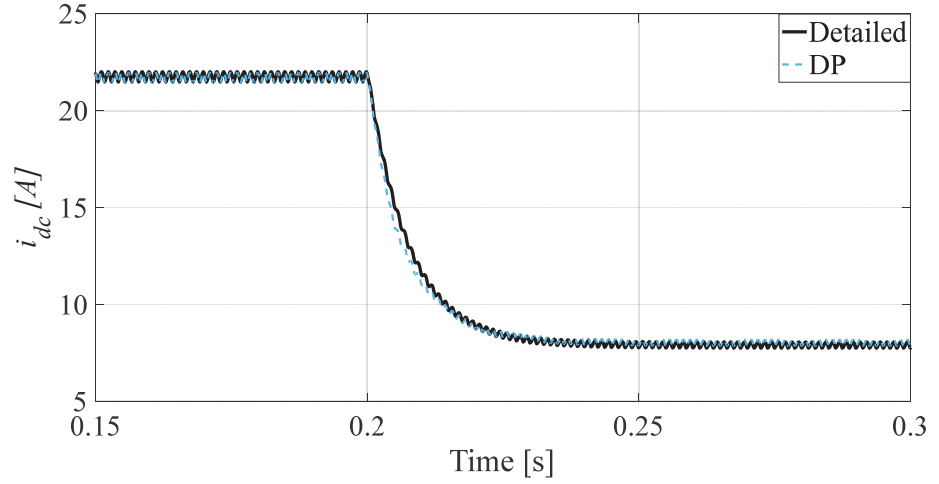

Figure. 3. 50. Output current of the rectifier under unbalanced input voltages and one phase open-circuit fault

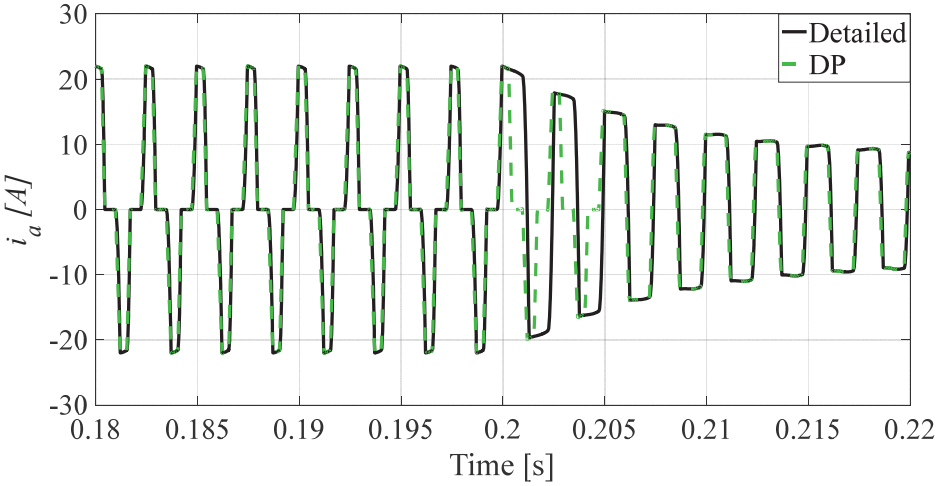

Figure. 3. 51. Current of phase *a* under unbalanced input voltages and one phase open-circuit fault

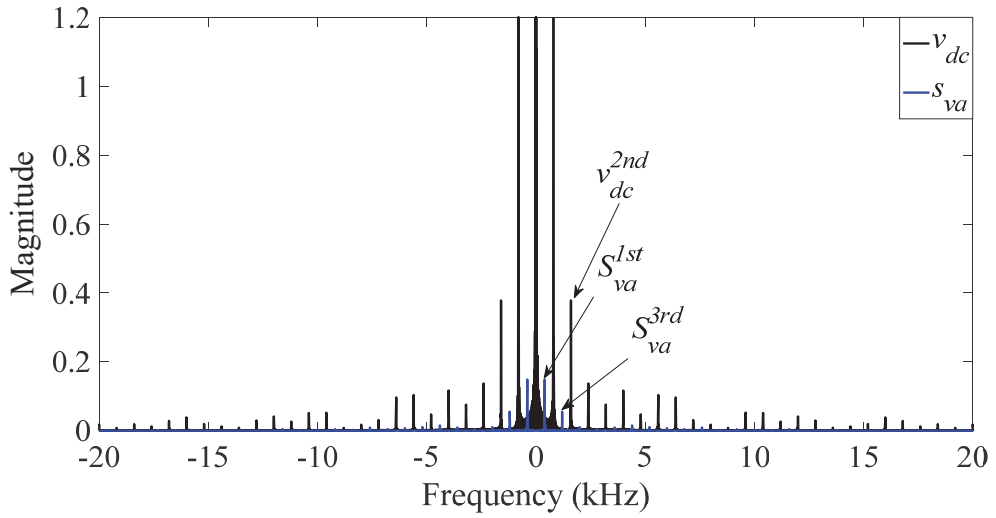

Figure. 3. 52. Frequency spectrum of the rectifier output voltage (v_{dc}) and voltage switching function of phase *a* before occurrence of fault

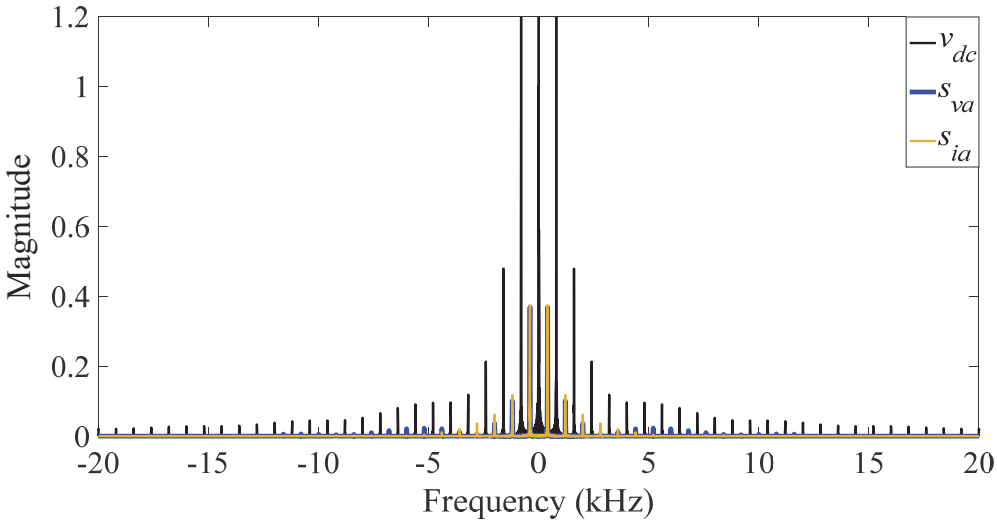

Figure. 3. 53. Frequency spectrum of the rectifier output voltage (v_{dc}), voltage, and current switching function of phase *a* after occurrence of fault

3.13.2 Case. 2: Transient from CCM to DCM

In this case of study, performance of the proposed uncontrolled rectifier model is examined in transient from CCM to DCM operation modes. At *t=0.1 s*, load of the rectifier is reduced. The lighter load makes the rectifier to operate in DCM. Input voltages are shown in Fig 3.54. Fig 3.55 shows voltage switching functions and current switching function of phase *b.* Fig 3.56 and Fig 3.57 show rectifier output voltage and current, respectively. The current of phase *b* under unbalanced input voltages and transient from CCM to DCM is shown in Fig 3.58.

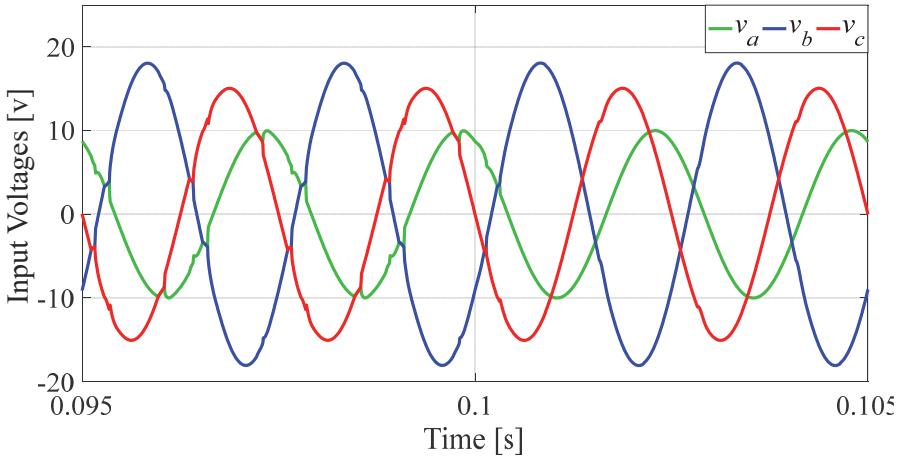

Figure. 3. 54. Input voltages of the rectifier

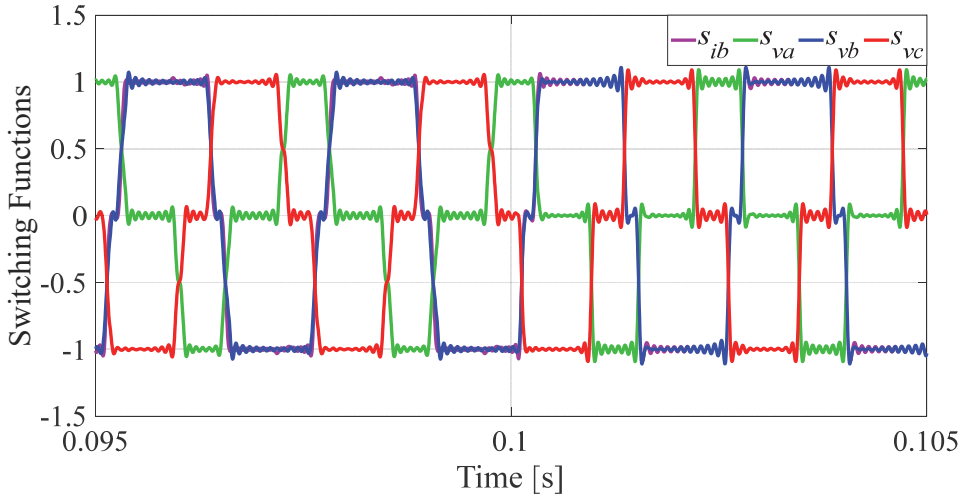

Figure. 3. 55. Voltage switching functions and current switching function of phase *b*

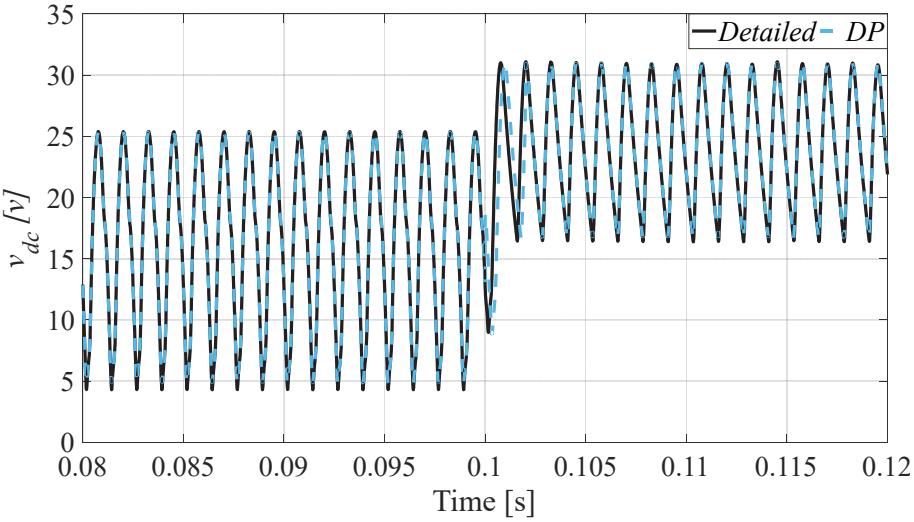

Figure. 3. 56. Output voltage of the rectifier under unbalanced input voltages and in transient from CCM to DCM.

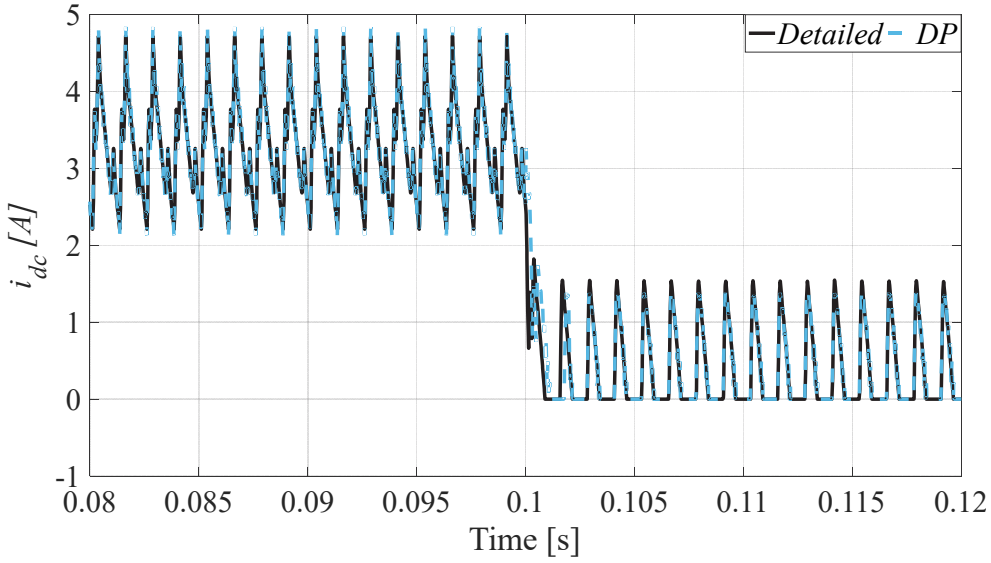

Figure. 3. 57. Output current of the rectifier under unbalanced input voltages and in transient from CCM to DCM.

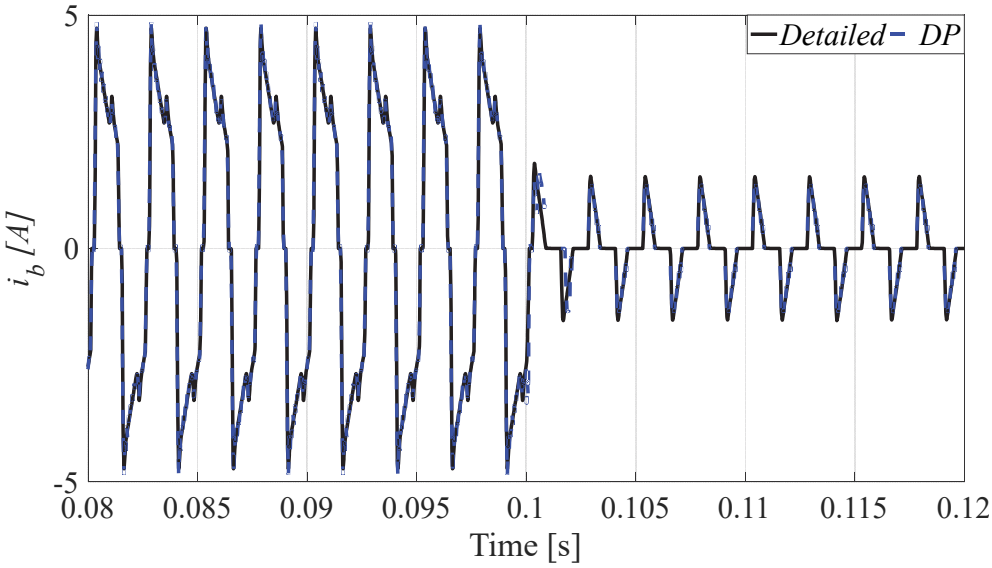

Figure. 3. 58. Current of phase *b* under unbalanced input voltages and transient from CCM to DCM.

Fig 3.59 and Fig 3.60 show Frequency spectrum of the rectifier output voltage (v_{dc}) and voltage switching function of phase *a* in CCM and DCM, respectively. Comparing with Fig 3.49 and Fig 3.50, it can be derived that DCM operation results in lower non-characteristic harmonics than one phase open-circuit fault.

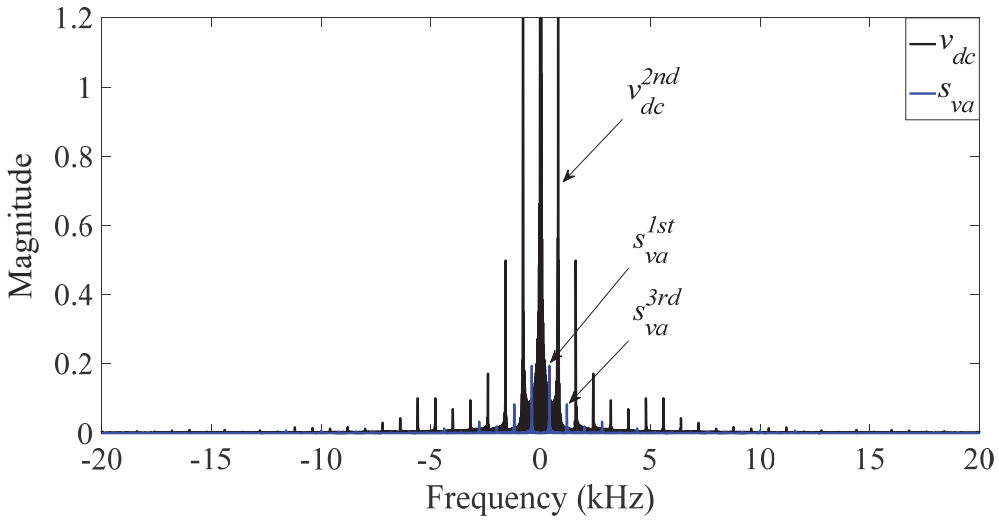

Figure. 3. 59. Frequency spectrum of the rectifier output voltage (v_{dc}) and voltage switching function of phase *a* in CCM

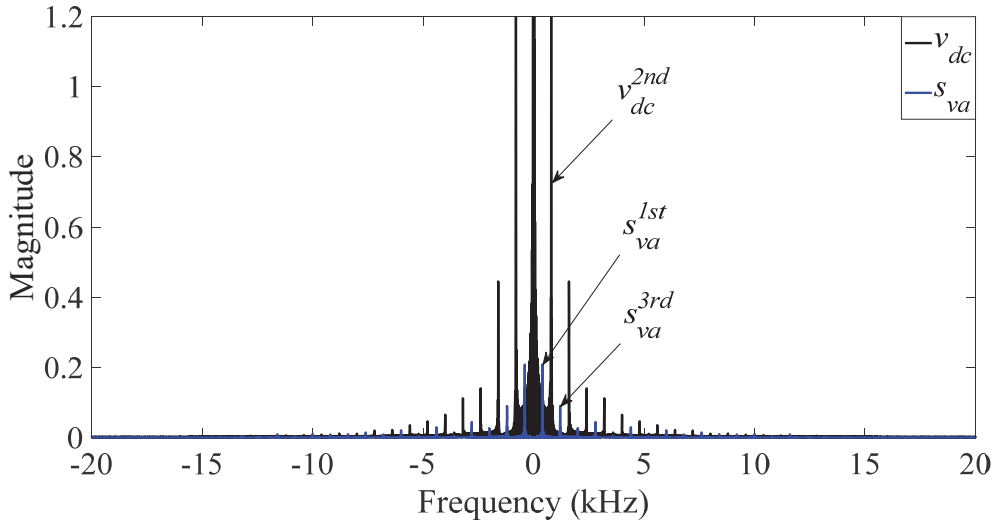

Figure. 3. 60. Frequency spectrum of the rectifier output voltage (v_{dc}) and voltage switching function of phase *a* in DCM

3.14 Model of the Uncontrolled Rectifier with harmonic consideration

In the previous sections, it was considered that input voltages of uncontrolled rectifier only contain fundamental component and harmonic components are negligible. However, in some conditions such as fault condition input voltages of the rectifier may contain significant harmonic contents [49]-[51].

For the three-stage brushless synchronous machine, during starting process where field excitation of the main exciter is AC, induced voltages in armature winding of the exciter are comprised of two components with different amplitude and frequency. Amplitude and frequency of the armature voltages are related to excitation frequency and rotation speed of the machine. Therefore, the model of uncontrolled rotating rectifier connected to armature winding must be able to consider different harmonics of input voltages.

In [52], transferred harmonics from AC-side to DC-side of rectifier were studied analytically. The presented method in [52] uses approximated Fourier series representation of switching functions in balance condition. Therefore, the presented method only is applicable to low amplitude harmonics. In [53], frequency-domain harmonic matrix model of uncontrolled diode bridge rectifier has been proposed. The proposed harmonic matrix can describe relationships between harmonics of input voltages and generated input currents in balance condition. However, the unbalanced condition was not considered. Therefore, application of the proposed harmonic matrix is limited to slightly unbalanced condition and low amplitude harmonics. Using double Fourier series method, approximated transfer function of uncontrolled rectifier has been proposed in [54]. In this work, the procedure of transfer function calculation only was reported for considering one harmonic. In addition, it was assumed that amplitude of the harmonic component is less than the fundamental component and does not change phase sequence of input voltages. From the presented methods in the literature, it can be concluded that for starting process of the starter-generator, neither of addressed methods are able to model relationships between AC- and DC-sides of the rotating rectifier.

3.15 Time-domain and DP-domain Representation of Switching Functions by considering AC-side harmonics (Method 1)

As mentioned in the former section, under unbalanced input voltages, commutation intervals are not even. In the case that input voltages contain a significant amount of harmonics, commutation intervals not only are unequal but also are variable. In this section, considering harmonics of input voltages, the switching function of uncontrolled diode bridge rectifier are derived. The proposed switching-function model is fully capable to deal with input harmonics even when amplitudes of harmonics are more than the fundamental component.

First, input voltages with two components are considered. In this case, input voltages are comprised of the fundamental component with the frequency of ω_f and a harmonic component.

$$v_a = a_1 \cos\left(\omega_f t + \vartheta_{a_1}\right) + a_2 \cos\left(\omega_{a_2} t + \vartheta_{a_2}\right) \tag{3.68}$$

$$v_b = b_1 \cos\left(\omega_f t + \vartheta_{b_1}\right) + b_2 \cos\left(\omega_{b_2} t + \vartheta_{b_2}\right) \tag{3.69}$$

$$v_c = c_1 \cos\left(\omega_f t + \vartheta_{c_1}\right) + c_2 \cos\left(\omega_{c_2} t + \vartheta_{c_2}\right) \tag{3.70}$$

For phase *a*, complex form of the two cosine terms is:

$$v_a = Re\left\{a_1 \cdot e^{j(\omega_f t + \vartheta_{a_1})} + b \cdot e^{j(\omega_{a_2} t + \vartheta_{a_2})}\right\} \tag{3.71}$$

where *Re* indicates real part of a complex term.

Factoring of fundamental frequency and phase, (3.71) can be rewritten as:

$$v_a = R_e\left\{ e^{j(\omega_f t + \vartheta_{a_1})} \cdot \left[a_1 + a_2 \cdot e^{j\left((\omega_{a_2} - \omega_f)t + \vartheta_{a_2} - \vartheta_{a_1}\right)}\right]\right\} \tag{3.72}$$

Magnitude and angle of (3.72) are:

$$|v_a| = \sqrt{a_1^2 + a_2^2 + 2 \cdot a_1 \cdot a_2 \cdot \cos\left(\left(\omega_{a_2} - \omega_f\right)t + \vartheta_{a_2} - \vartheta_{a_1}\right)} \tag{3.73}$$

$$\angle v_a = \tan^{-1}\left[\frac{a_2 \sin\left((\omega_{a_2} - \omega_f)t + \vartheta_{a_2} - \vartheta_{a_1}\right)}{a_1 + a_2 \cos\left((\omega_{a_2} - \omega_f)t + \vartheta_{a_2} - \vartheta_{a_1}\right)}\right] + \vartheta_{a_1} \tag{3.74}$$

Now, sum of the two cosines with different amplitude, frequency, and phase can be expressed as one cosine:

$$v_a = |v_a| \cos\left(\omega_f t + \angle v_a\right) \tag{3.75}$$

For phase *b*, magnitude and phase are calculated as:

$$|v_b| = \sqrt{b_1^2 + b_2^2 + 2 \cdot b_1 \cdot b_2 \cdot \cos\left(\left(\omega_{b_2} - \omega_f\right)t + \vartheta_{b_2} - \vartheta_{b_1}\right)} \quad (3.76)$$

$$\angle v_b = \tan^{-1}\left[\frac{b_2 \sin\left(\left(\omega_{b_2}-\omega_f\right)t+\vartheta_{b_2}-\vartheta_{b_1}\right)}{b_1+b_2 \cos\left(\left(\omega_{b_2}-\omega_f\right)t+\vartheta_{b_2}-\vartheta_{b_1}\right)}\right] + \vartheta_{b_1} \quad (3.77)$$

So, v_b in (3.69) can be rewritten as:

$$v_b = |v_b| \cos\left(\omega_f t + \angle v_b\right) \quad (3.78)$$

And for phase *c*:

$$|v_c| = \sqrt{c_1^2 + c_2^2 + 2 \cdot c_1 \cdot c_2 \cdot \cos\left(\left(\omega_{c_2} - \omega_f\right)t + \vartheta_{c_2} - \vartheta_{c_1}\right)} \quad (3.79)$$

$$\angle v_c = \tan^{-1}\left[\frac{c_2 \sin\left(\left(\omega_{c_2}-\omega_f\right)t+\vartheta_{c_2}-\vartheta_{c_1}\right)}{c_1+c_2 \cos\left(\left(\omega_{c_2}-\omega_f\right)t+\vartheta_{c_2}-\vartheta_{c_1}\right)}\right] + \vartheta_{c_1} \quad (3.80)$$

So, v_c in (3.70) can be rewritten as:

$$v_c = |v_c| \cos\left(\omega_f t + \angle v_c\right) \quad (3.81)$$

Then, phase of line voltages should be calculated. These phases are used in Fourier series expressions of switching functions (intersection points of phase voltages). Line voltages are:

$$v_{ab} = |v_a| \cos(\omega_f t + \angle v_a) - |v_b| \cos(\omega_f t + \angle v_b) \tag{3.82}$$

$$v_{bc} = |v_b| \cos(\omega_f t + \angle v_b) - |v_c| \cos(\omega_f t + \angle v_c) \tag{3.83}$$

$$v_{ca} = |v_c| \cos(\omega_f t + \angle v_c) - |v_a| \cos(\omega_f t + \angle v_a) \tag{3.84}$$

The line voltages are sum of two cosines with different amplitude. First, they should be expressed as a single cosine functions. Using the same approach as was employed to phase voltages, amplitudes and phases of line voltage are calculated as:

$$|v_{ab}| = \sqrt{|v_a|^2 + |v_b|^2 - 2 \cdot |v_a| \cdot |v_b| \cdot \cos(\angle v_b - \angle v_a)} \tag{3.85}$$

$$|v_{bc}| = \sqrt{|v_b|^2 + |v_c|^2 - 2 \cdot |v_b| \cdot |v_c| \cdot \cos(\angle v_c - \angle v_b)} \tag{3.86}$$

$$|v_{ca}| = \sqrt{|v_c|^2 + |v_a|^2 - 2 \cdot |v_c| \cdot |v_a| \cdot \cos(\angle v_a - \angle v_c)} \tag{3.87}$$

$$\angle v_{ab} = \tan^{-1}\left[\frac{-|v_b| \sin(\angle v_b - \angle v_a)}{|v_a| - |v_b| \cos(\angle v_b - \angle v_a)}\right] + \angle v_a \tag{3.88}$$

$$\angle v_{bc} = \tan^{-1}\left[\frac{-|v_c| \sin(\angle v_c - \angle v_b)}{|v_b| - |v_c| \cos(\angle v_c - \angle v_b)}\right] + \angle v_b \tag{3.89}$$

$$\angle v_{ca} = \tan^{-1}\left[\frac{-|v_a| \sin(\angle v_a - \angle v_c)}{|v_c| - |v_a| \cos(\angle v_a - \angle v_c)}\right] + \angle v_c \tag{3.90}$$

After expressing line voltages as one cosine functions, starting and ending points of switching functions can be calculated as:

$$A_a = \frac{\pi}{2} - \angle v_{ca} \tag{3.91}$$

$$B_a = \frac{\pi}{2} - \angle v_{ab} \tag{3.92}$$

$$A_b = B_a \tag{3.93}$$

$$B_b = \frac{\pi}{2} - \angle v_{bc} \tag{3.94}$$

$$A_c = B_b \tag{3.95}$$

$$B_c = A_a \tag{3.96}$$

Now, commutation angles must be calculated. Commutation angles are:

$$\mu_{ab} = \cos^{-1}\left(1 - \frac{2 \cdot \omega_{ab} \cdot L_c \cdot i_{dc}}{|V_{ab}|}\right) \tag{3.97}$$

$$\mu_{bc} = \cos^{-1}\left(1 - \frac{2 \cdot \omega_{bc} \cdot L_c \cdot i_{dc}}{|V_{bc}|}\right) \tag{3.98}$$

$$\mu_{ca} = \cos^{-1}\left(1 - \frac{2 \cdot \omega_{ca} \cdot L_c \cdot i_{dc}}{|V_{ca}|}\right) \tag{3.99}$$

where ω_{ab}, ω_{bc}, and ω_{ca} are:

$$\omega_{ab} = \frac{\angle v_{ab} - \vartheta_{a_1}}{t} \tag{3.100}$$

$$\omega_{bc} = \frac{\angle v_{bc} - \vartheta_{b_1}}{t} \tag{3.101}$$

$$\omega_{ca} = \frac{\angle v_{ca} - \vartheta_{c_1}}{t} \tag{3.102}$$

Now, Fourier series coefficients for voltage switching functions can be calculated using (3.48) to (3.53). Then, Fourier series expression of voltage switching functions in time-domain is:

$$S_{V,i}(t) = \sum_{n=1}^{\infty}\left[A_n \cdot \cos\left(n\omega_f t\right) + B_n \cdot \sin\left(n\omega_f t\right)\right], \quad i = a, b, and\ c \tag{3.103}$$

Fourier series coefficients for current switching functions are calculated using (3.55) to (3.60). Fourier series expression of current switching functions is:

$$S_{I,i}(t) = \sum_{n=1}^{\infty}[A_n \cdot \cos(n\omega t) + B_n \cdot \sin(n\omega t)], \ \ i = a, b, and\ c \tag{3.104}$$

Voltage switching function in DP-domain are calculated by (3.62) to (3.64). Current switching function in DP-domain are calculated using (3.65) to (3.67).

If more than two harmonics are desired to be considered, the mentioned method can be applied to every two harmonics and at the end, single cosine expression of voltages can be obtained. As an example, if three harmonics of phase *a* voltage are desired to be considered, single cosine expression of v_a can be calculated as:

$$v_a = a_1 \cos\left(\omega_f t + \vartheta_{a_1}\right) + a_2 \cos\left(\omega_{a_2} t + \vartheta_{a_2}\right) + a_3 \cos\left(\omega_{a_3} t + \vartheta_{a_3}\right) \tag{3.105}$$

Sum of the first two terms in (3.105) can be replaced by their single-term expression as:

$$a_1 \cos\left(\omega_f t + \vartheta_{a_1}\right) + a_2 \cos\left(\omega_{a_2} t + \vartheta_{a_2}\right) = |v_a|_1 \cos\left(\omega_f t + (\angle v_a)_1\right) \tag{3.106}$$

where $|v_a|_1$ and $(\angle v_a)_1$ are calculated by (3.73) and (3.74), respectively.

Now v_a contains two terms.

$$v_a = |v_a|_1 \cos\left(\omega_f t + (\angle v_a)_1\right) + a_3 \cos\left(\omega_{a_3} t + \vartheta_{a_3}\right) \tag{3.107}$$

Its amplitude, phase and final single-term expression are:

$$|v_a| = \sqrt{|v_a|^2 + a_3^2 + 2 \cdot |v_a| \cdot a_3 \cdot \cos\left(\left(\omega_{a_3} - \omega_f\right)t + \vartheta_{a_3} - (\angle v_a)_1\right)} \tag{3.108}$$

$$\angle v_a = \tan^{-1}\left[\frac{a_3 \sin\left(\left(\omega_{a_3} - \omega_f\right)t + \vartheta_{a_3} - (\angle v_a)_1\right)}{|v_a| + a_3 \cos\left(\left(\omega_{a_3} - \omega_f\right)t + \vartheta_{a_3} - (\angle v_a)_1\right)}\right] + (\angle v_a)_1 \tag{3.109}$$

Final single-term expression of v_a can be written as (3.75). After re-expressing the phase voltages, line voltages contain two terms and their phase angle can be calculated by (3.88) to (3.90). As before, from the phase angle of line voltages, switching functions can be calculated.

3.16 Case Study and Validation of the Method. 1:

In this section, performance and accuracy of the proposed model are examined by simulation. Simulation results of the proposed model are compared with results obtained from a detailed benchmark model simulated in SimPowerSystem Matlab/Simulink environment.

3.16.1. Case 1: Three-phase unbalanced arbitrary input voltages

In this case of study, input voltages of the rectifier are assumed as:

$$v_a = 5 + 10 \cdot \cos(\omega \cdot t) + 7 \cdot \cos(5 \cdot \omega \cdot t)$$

$$v_b = 10 \cdot \cos\left(\omega \cdot t - \frac{2 \cdot \pi}{3}\right) + 15 \cdot \cos\left(2 \cdot \omega \cdot t - \frac{2 \cdot \pi}{3}\right)$$

$$v_c = 5 \cdot \cos\left(\omega \cdot t + \frac{2 \cdot \pi}{3}\right) + 15 \cdot \cos\left(3 \cdot \omega \cdot t + \frac{2 \cdot \pi}{3}\right)$$

where

$$\omega = 400 * 2 * \pi$$

First, simulation is performed without the existence of commutation inductance. Fig 3.61 shows input voltages. Switching functions are shown in Fig 3.62. Output voltage and current of the rectifier are shown in Fig 3.63 and 3.64, respectively. Fig 3.65 shows the current of phase *a*.

The frequency spectrum of the rectifier output voltage (v_{dc}) and switching function of phase *a* are shown in Fig 3.66. From the results, excellent performance of the proposed model can be proved.

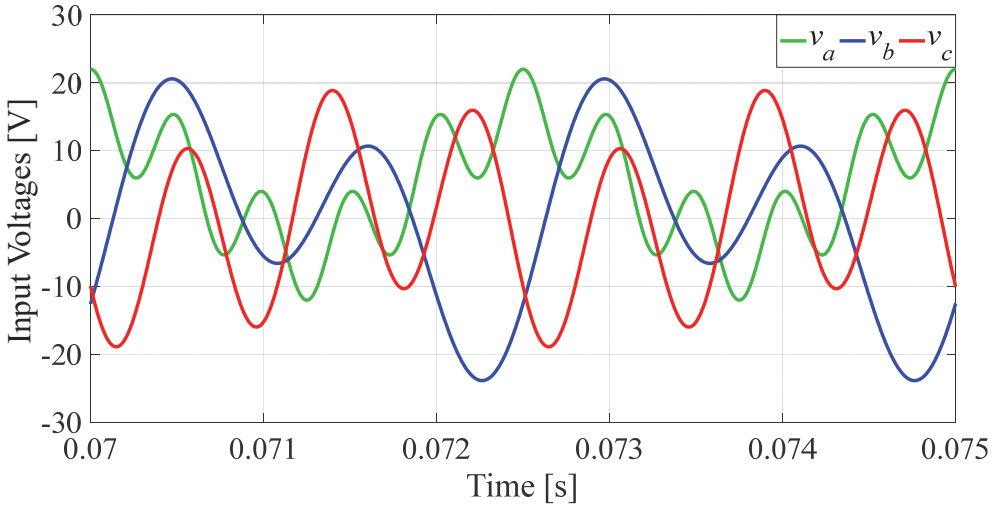

Figure. 3. 61. Input voltages of the rectifier

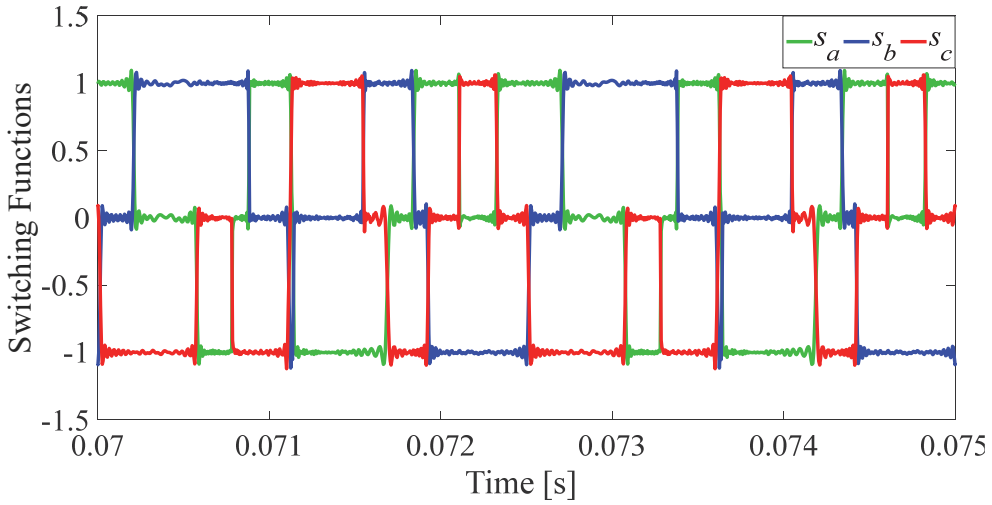

Figure. 3. 62. Switching functions

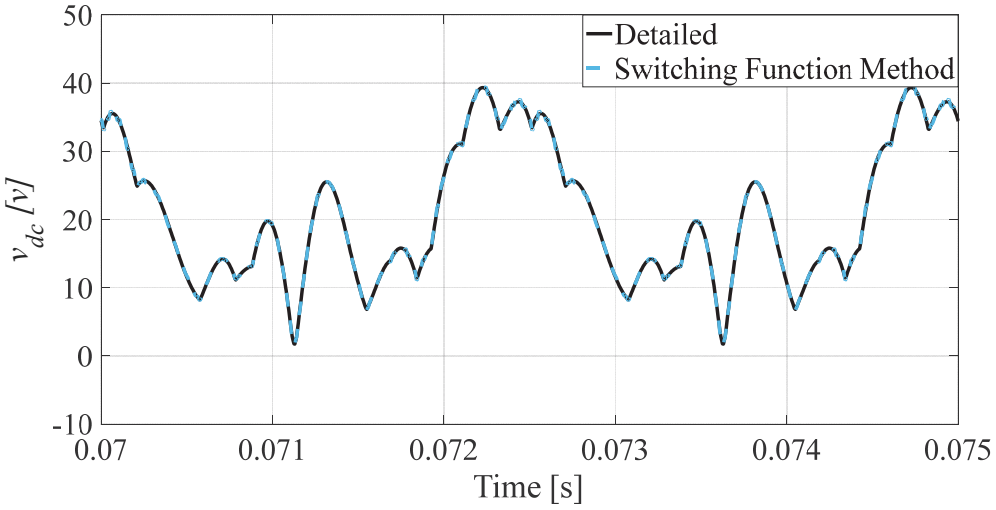

Figure. 3. 63. Output voltage of the rectifier

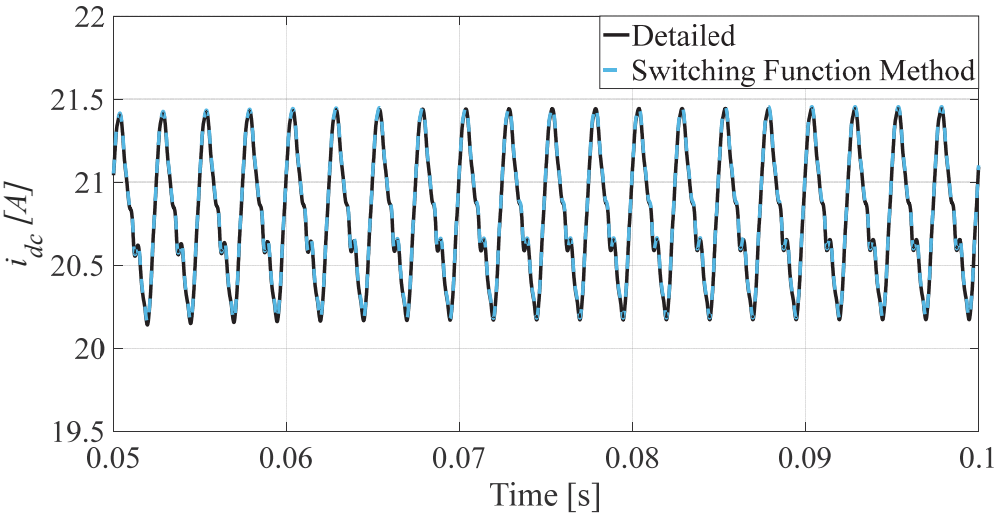

Figure. 3. 64. Output current of the rectifier

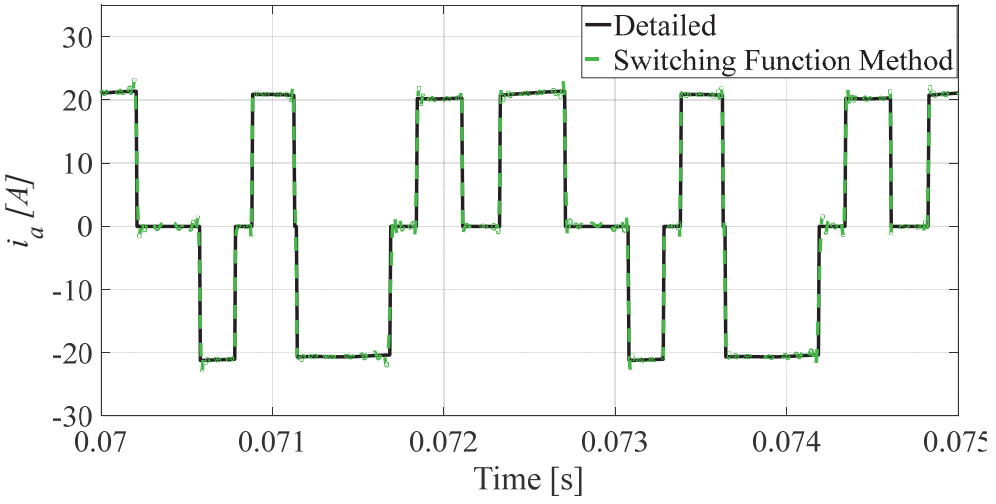

Figure. 3. 65. Current of phase *a*

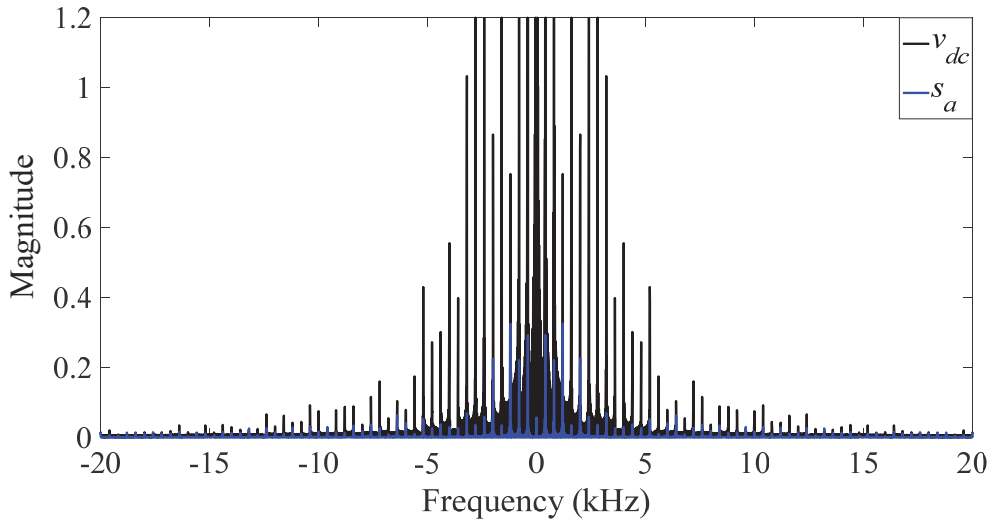

Figure. 3. 66. Frequency spectrum of the rectifier output voltage (v_{dc}) and switching function of phase *a*

3.16.2. Case 2: Three-phase unbalanced arbitrary input voltages with existence of commutation inductance.

In this case, input voltages are same as in the previous test, but commutation inductances exist in AC-side. Fig 6.67 shows input voltages of the rectifier. Voltage switching functions and current switching function of phase *a* are shown in Fig 3.68. Output voltage and current of the rectifier are shown in Fig 3.69 and 3.70, respectively. The frequency spectrum of the rectifier output voltage (v_{dc}) and voltage switching function of phase *a* are shown in Fig 3.71. Effect of commutation inductance in increasing harmonics of v_{dc} can be seen in Fig 3.71.

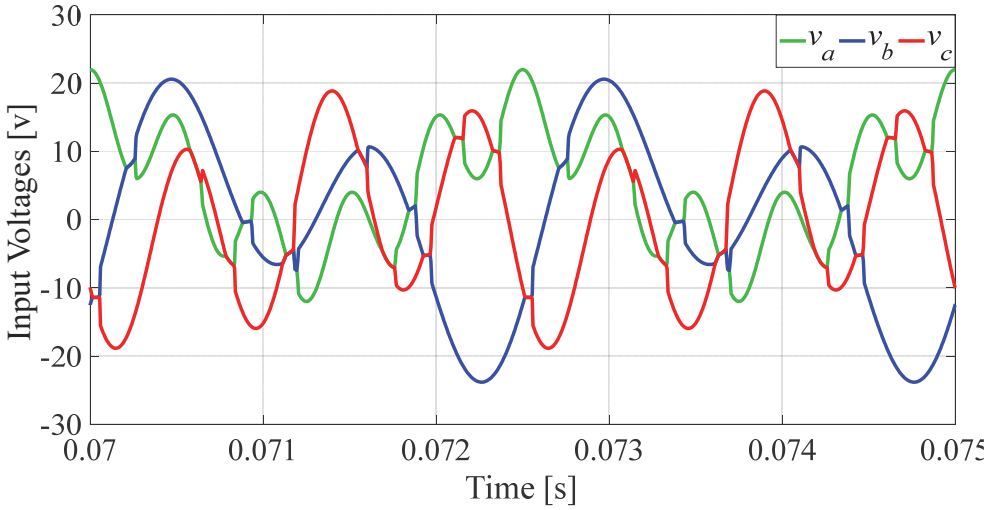

Figure. 3. 67. Input voltages of the rectifier

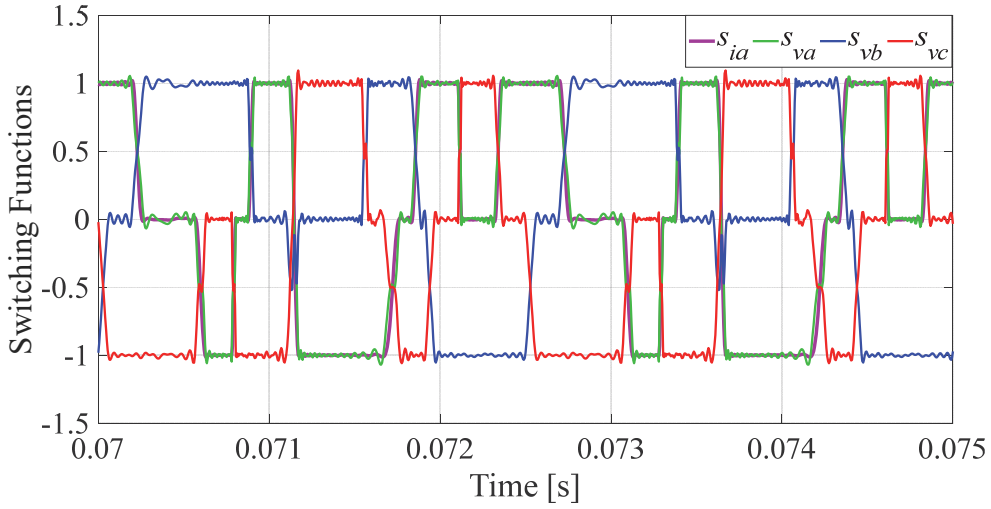

Figure. 3. 68. Voltage switching functions and current switching function of phase *a*

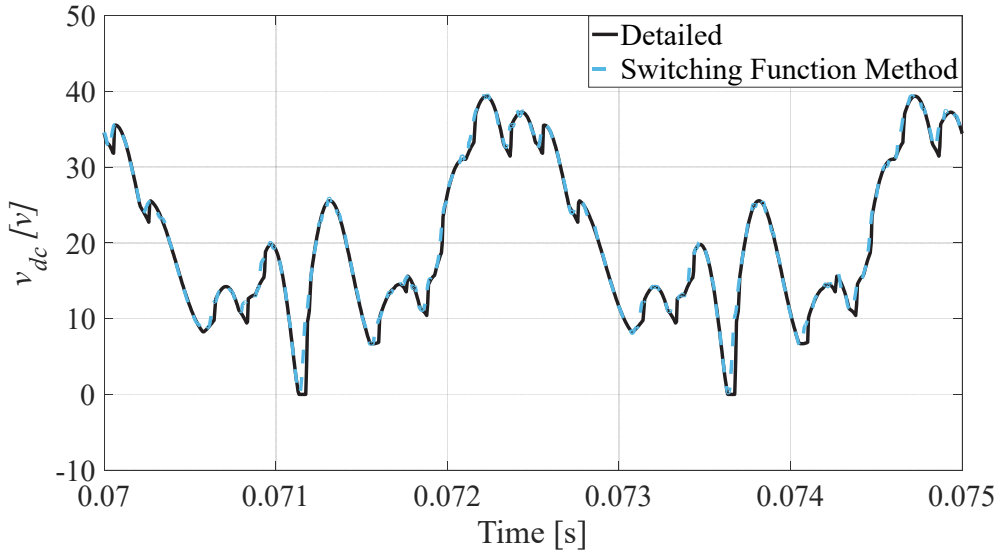

Figure. 3. 69. Output voltage of the rectifier

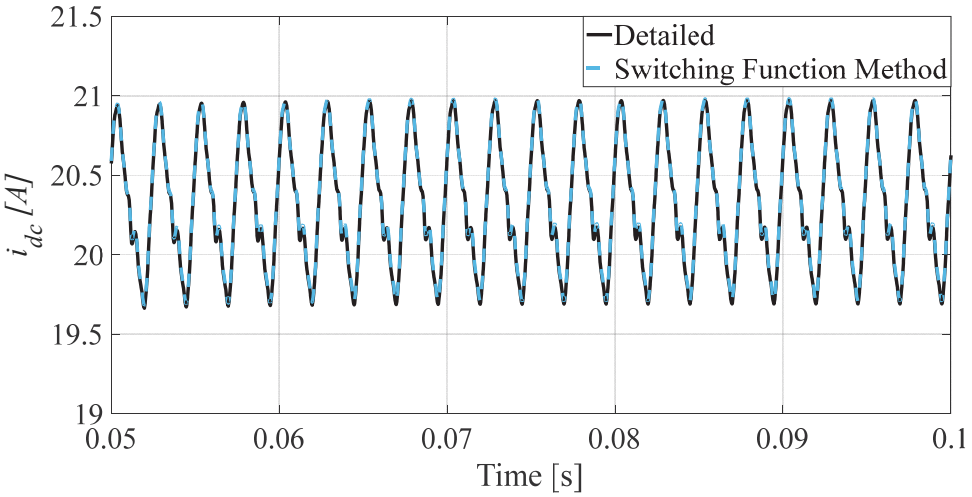

Figure. 3. 70. Output current of the rectifier

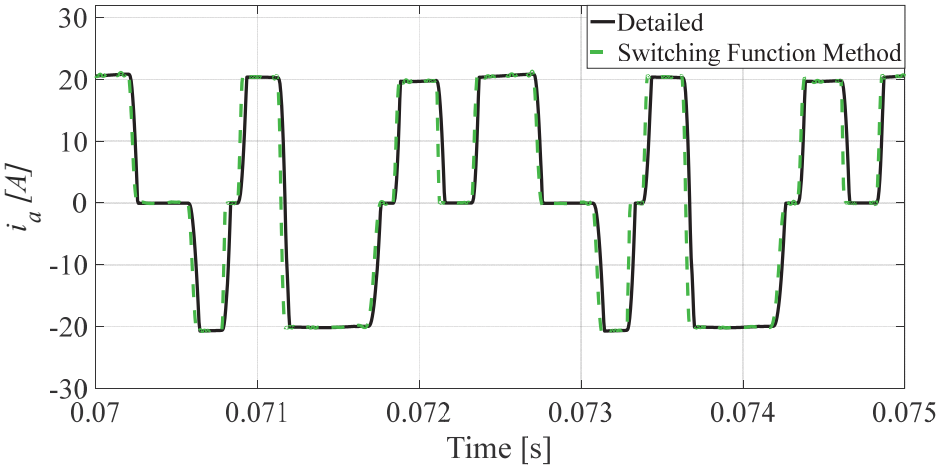

Figure. 3. 71. Current of phase *a*

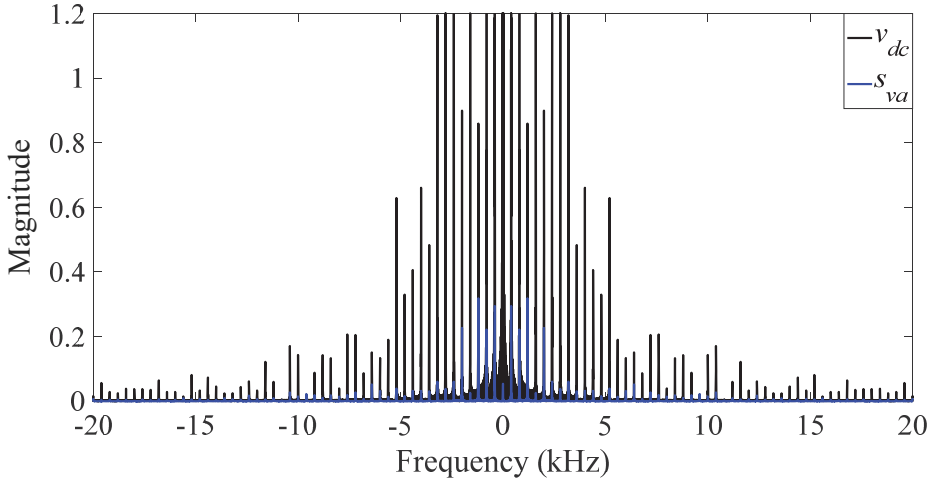

Figure. 3. 72. Frequency spectrum of the rectifier output voltage (v_{dc}) and voltage switching function of phase *a*

3.17 Time-domain and DP-domain Representation of Switching Functions by considering AC-side harmonics (Method 2)

In addition to the previous method (*Method 1*), in this section, another method to consider input harmonics in modeling of the uncontrolled rectifier is proposed. Step by step modeling approach is as follows:

First, Signum function is applied on line voltages. Sign of line voltages can be obtained by (3.110) to (3.115). In this thesis, (3.113) to (3.115) are used.

$$S_{v_{ab}}^{\prime} = \frac{v_{ab}}{|v_{ab}|} = \frac{v_{ab}}{\sqrt{(v_{ab})^2}} \tag{3.110}$$

$$|v_{ab}| = Magnitude[v_{ab} + j0] \tag{3.111}$$

Or

$$S_{v_{ab}}^{\prime} = \cos(\tan^{-1}(v_{ab} + j0)) \tag{3.112}$$

Another representation of above formula in DP-domain is:

$$S_{v_{ab}}^{\prime} = \cos\left[\angle\left(\sum_{i=0}^{k}\left((\langle v_a\rangle_i - \langle v_b\rangle_i)\cdot e^{j\cdot i\cdot\omega\cdot t}\right)\right)\right] \tag{3.113}$$

For phase *b* and *c*

$$S_{v_{bc}}^{\prime} = \cos\left[\angle\left(\sum_{i=0}^{k}\left((\langle v_b\rangle_i - \langle v_c\rangle_i)\cdot e^{j\cdot i\cdot\omega\cdot t}\right)\right)\right] \tag{3.114}$$

$$S_{v_{ca}}^{\prime} = \cos\left[\angle\left(\sum_{i=0}^{k}\left((\langle v_c\rangle_i - \langle v_a\rangle_i)\cdot e^{j\cdot i\cdot\omega\cdot t}\right)\right)\right] \tag{3.115}$$

Equation (3.113) to (3.115) can be used in the case where input voltages come from DP-domain. Using (3.113) to (3.115), implicit zero-crossing points of line voltages can be obtained. This is shown in Fig 3.73.

Now, switching functions can be obtained by finding pulses which their zero-crossing points are intersection points of phase voltages.

$$S_a = \frac{1}{2} \cdot \left(S_{v_{ab}}^{'} - S_{v_{ca}}^{'}\right) \tag{3.116}$$

$$S_b = \frac{1}{2} \cdot \left(S_{v_{bc}}^{'} - S_{v_{ab}}^{'}\right) \tag{3.117}$$

$$S_c = \frac{1}{2} \cdot \left(S_{v_{ca}}^{'} - S_{v_{bc}}^{'}\right) \tag{3.118}$$

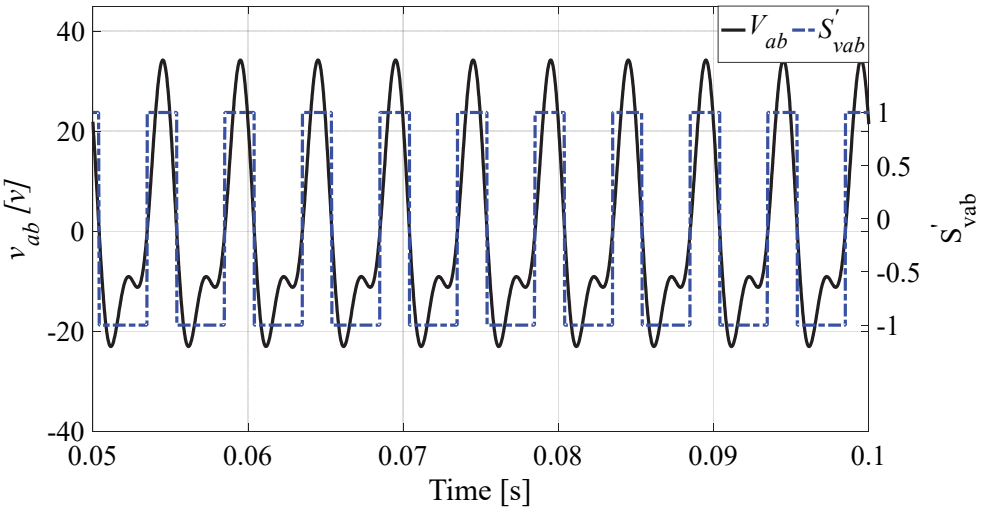

Figure. 3. 73. V_{ab} and $S'_{v_{ab}}$

Commutation process effect has been not considered in switching functions obtained from (3.116) to (3.117). To consider commutation inductance effect, in this thesis, two approaches are proposed. The first approach to calculate voltage switching functions is as follows.

First, line voltages are shifted to the right by their corresponding commutation angle. These shifted line voltages are indicated by $S_{v_{ab\_\mu_{ab}}}^{'}$, $S_{v_{bc\_\mu_{bc}}}^{'}$, and $S_{v_{ca\_\mu_{ca}}}^{'}$.

$$S_{v_{ab\_\mu_{ab}}^{'}} = \cos\left[\measuredangle\left(\sum_{i=0}^{k}\left((\langle v_a\rangle_i - \langle v_b\rangle_i)\cdot e^{j\cdot(i\cdot\omega\cdot t - i\cdot\mu_{ab})}\right)\right)\right] \quad (3.119)$$

$$S_{v_{bc\_\mu_{bc}}^{'}} = \cos\left[\measuredangle\left(\sum_{i=0}^{k}\left((\langle v_b\rangle_i - \langle v_c\rangle_i)\cdot e^{j\cdot(i\cdot\omega\cdot t - i\cdot\mu_{bc})}\right)\right)\right] \quad (3.120)$$

$$S_{v_{ca\_\mu_{ca}}^{'}} = \cos\left[\measuredangle\left(\sum_{i=0}^{k}\left((\langle v_c\rangle_i - \langle v_a\rangle_i)\cdot e^{j\cdot(i\cdot\omega\cdot t - i\cdot\mu_{ca})}\right)\right)\right] \quad (3.121)$$

Then, from (3.113) to (3.115) and (3.119) to (3.121), voltage switching functions are calculated as:

$$S_{V,a} = \frac{1}{2}\cdot\left\{\left(S_{v_{ab}}^{'} - S_{v_{ca}}^{'}\right) - \left[\frac{1}{2}\cdot\left(S_{v_{ab}}^{'} - S_{v_{ab_{\mu_{ab}}}}^{'}\right) - \frac{1}{2}\cdot\left(S_{v_{ca}}^{'} - S_{v_{ca\_\mu_{ca}}}^{'}\right)\right]\right\} \quad (3.122)$$

$$S_{V,b} = \frac{1}{2}\cdot\left\{\left(S_{v_{bc}}^{'} - S_{v_{ab}}^{'}\right) - \left[\frac{1}{2}\cdot\left(S_{v_{bc}}^{'} - S_{v_{bc\_\mu_{bc}}}^{'}\right) - \frac{1}{2}\cdot\left(S_{v_{ab}}^{'} - S_{v_{ab\_\mu_{ab}}}^{'}\right)\right]\right\} \quad (3.123)$$

$$S_{V,c} = \frac{1}{2}\cdot\left\{\left(S_{v_{ca}}^{'} - S_{v_{bc}}^{'}\right) - \left[\frac{1}{2}\cdot\left(S_{v_{ca}}^{'} - S_{v_{ca\_\mu_{ca}}}^{'}\right) - \frac{1}{2}\cdot\left(S_{v_{bc}}^{'} - S_{v_{bc\_\mu_{bc}}}^{'}\right)\right]\right\} \quad (3.124)$$

Equations (3.122) to (3.124) present absolute voltage switching functions. If harmonics interactions are desired, and also in order to calculate current switching functions, second approach is presented.

Applying (3.7) on (3.113) to (3.115), DPs of line voltages are calculated. Voltage switching functions in DP domain are:

$$\langle S_{V,a}\rangle_k = \langle S_{v_{ab}}^{'}\rangle_k \cdot \cos\left(k\cdot\frac{\mu_{ab}}{2}\right)\cdot e^{-\frac{j\cdot k\cdot\mu_{ab}}{2}} - \langle S_{v_{ca}}^{'}\rangle_k \cdot \cos\left(k\cdot\frac{\mu_{ca}}{2}\right)\cdot e^{-\frac{j\cdot k\cdot\mu_{ca}}{2}} \quad (3.125)$$

$$\langle S_{V,b}\rangle_k = \langle S_{v_{bc}}^{'}\rangle_k \cdot \cos\left(k\cdot\frac{\mu_{bc}}{2}\right)\cdot e^{-\frac{j\cdot k\cdot\mu_{bc}}{2}} - \langle S_{v_{ab}}^{'}\rangle_k \cdot \cos\left(k\cdot\frac{\mu_{ab}}{2}\right)\cdot e^{-\frac{j\cdot k\cdot\mu_{ab}}{2}} \quad (3.126)$$

$$\langle S_{V,c}\rangle_k = \langle S'_{v_{ca}}\rangle_k \cdot \cos\left(k \cdot \frac{\mu_{ca}}{2}\right) \cdot e^{-\frac{j \cdot k \cdot \mu_{ca}}{2}} - \langle S'_{v_{bc}}\rangle_k \cdot \cos\left(k \cdot \frac{\mu_{bc}}{2}\right) \cdot e^{-\frac{j \cdot k \cdot \mu_{bc}}{2}} \tag{3.127}$$

Current switching functions are:

$$\langle S_{I,a}\rangle_k = \langle S'_{v_{ab}}\rangle_k \cdot \frac{\sin\left(k \cdot \frac{\mu_{ab}}{2}\right)}{k \cdot \frac{\mu_{ab}}{2}} \cdot e^{-\frac{j \cdot k \cdot \mu_{ab}}{2}} - \langle S'_{v_{ca}}\rangle_k \cdot \frac{\sin\left(k \cdot \frac{\mu_{ca}}{2}\right)}{k \cdot \frac{\mu_{ca}}{2}} \cdot e^{-\frac{j \cdot k \cdot \mu_{ca}}{2}} \tag{3.128}$$

$$\langle S_{I,b}\rangle_k = \langle S'_{v_{bc}}\rangle_k \cdot \frac{\sin\left(k \cdot \frac{\mu_{bc}}{2}\right)}{k \cdot \frac{\mu_{bc}}{2}} \cdot e^{-\frac{j \cdot k \cdot \mu_{bc}}{2}} - \langle S'_{v_{ab}}\rangle_k \cdot \frac{\sin\left(k \cdot \frac{\mu_{ab}}{2}\right)}{k \cdot \frac{\mu_{ab}}{2}} \cdot e^{-\frac{j \cdot k \cdot \mu_{ab}}{2}} \tag{3.129}$$

$$\langle S_{I,c}\rangle_k = \langle S'_{v_{ca}}\rangle_k \cdot \frac{\sin\left(k \cdot \frac{\mu_{ca}}{2}\right)}{k \cdot \frac{\mu_{ca}}{2}} \cdot e^{-\frac{j \cdot k \cdot \mu_{ca}}{2}} - \langle S'_{v_{bc}}\rangle_k \cdot \frac{\sin\left(k \cdot \frac{\mu_{bc}}{2}\right)}{k \cdot \frac{\mu_{bc}}{2}} \cdot e^{-\frac{j \cdot k \cdot \mu_{bc}}{2}} \tag{3.130}$$

3.18 Validation of the Method. 2

Method .2 of modeling the uncontrolled diode bridge rectifier with considering input harmonics is examined by performing a simulation. Results obtained from the proposed model is compared to results obtained from the detailed model.

3.18.1 Case 1: Without existence of commutation inductance

Input voltages of rectifier are as follows:

$$v_a = 20 \cdot \cos\left(\omega \cdot t + \frac{\pi}{4}\right)$$

$$v_b = 3 \cdot \cos\left(\omega \cdot t - \frac{2 \cdot \pi}{3}\right) + 12 \cdot \cos\left(2 \cdot \omega \cdot t - \frac{2 \cdot \pi}{3}\right)$$

$$v_c = 7 \cdot \cos\left(\omega \cdot t + \frac{2 \cdot \pi}{3}\right)$$

where

$$\omega = 200 * 2 * \pi$$

The first test is performed without the existence of commutation inductance. At $t= 0.2\ s$ one phase open-circuit happens in phase a. Fig 3.74 shows waveforms of input voltages. Absolute switching function calculated by (3.116) to (3.118) are shown in Fig 3.75. Output voltage and current of the rectifier are shown in Fig 3.76 and Fig 3.77, respectively. Fig 3.78 shows the current of phase b. The frequency spectrum of the rectifier output voltage (v_{dc}) and voltage switching function of phase a before fault occurrence are shown in Fig 3.79.

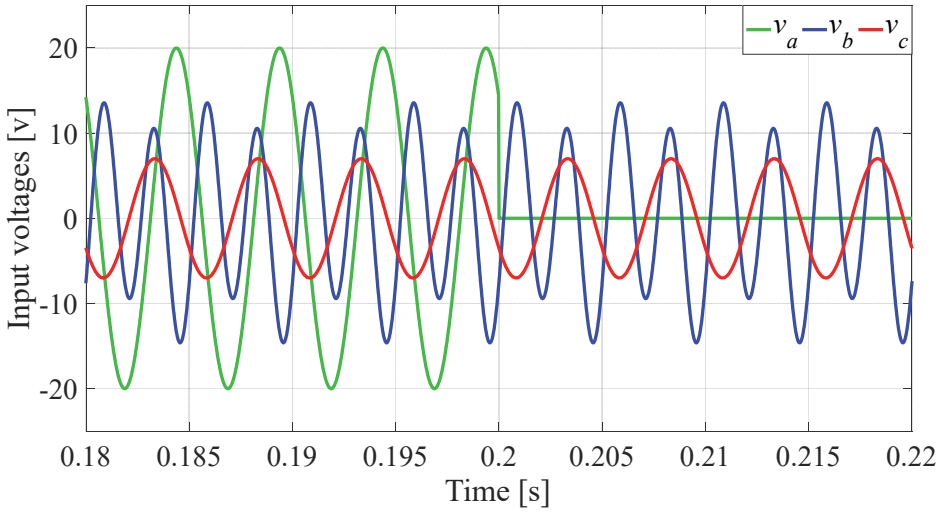

Figure. 3. 74. Input voltages of the rectifier

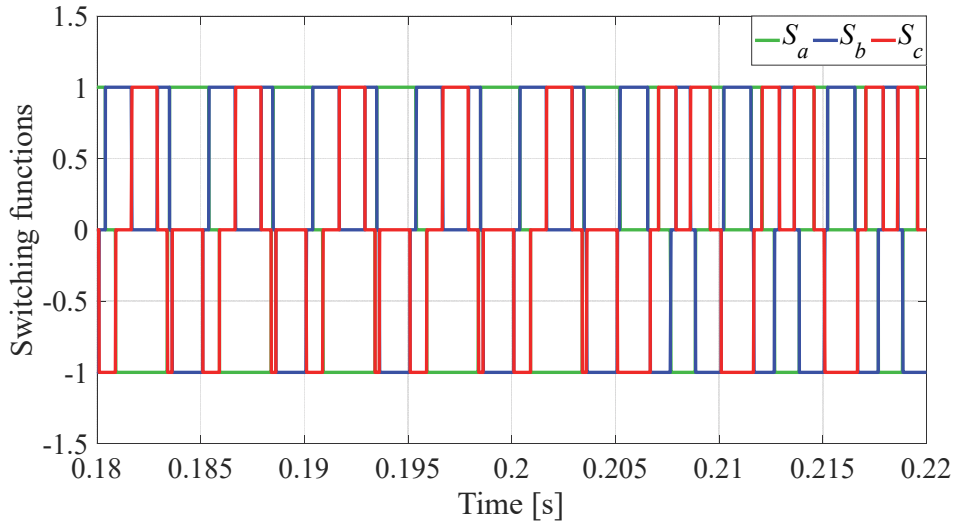

Figure. 3. 75. Switching Functions

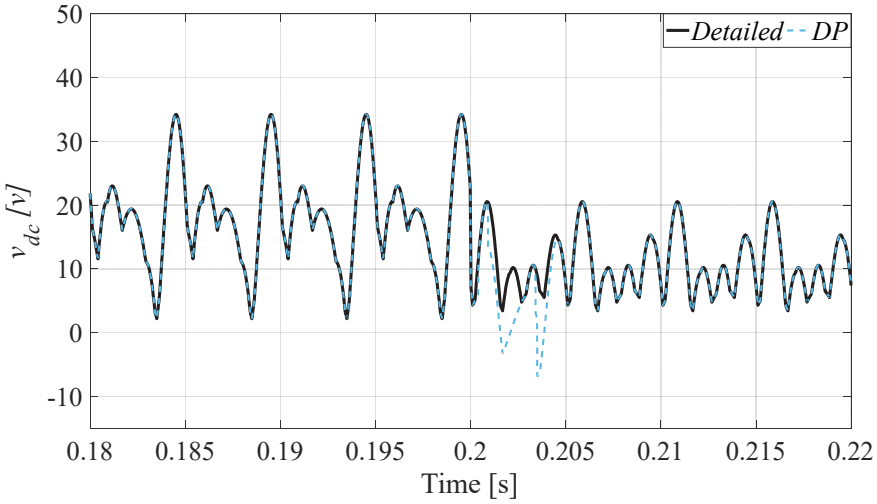

Figure. 3. 76. Output voltage of the rectifier

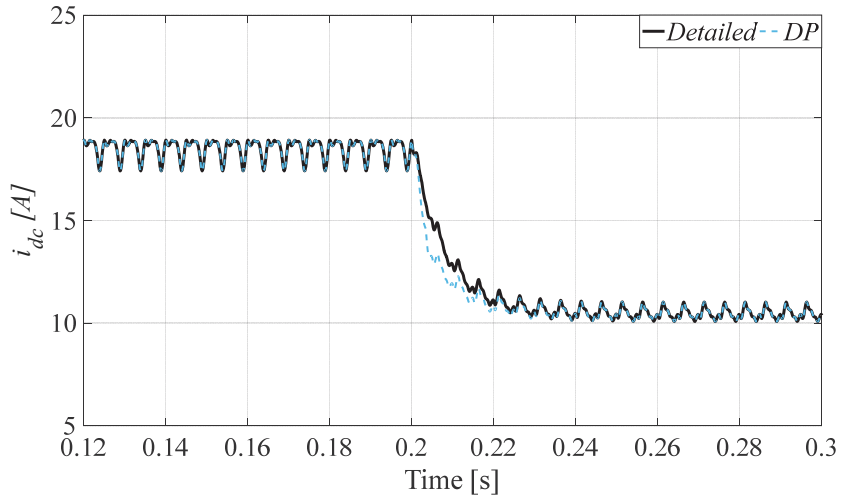

Figure. 3. 77. Output current of the rectifier

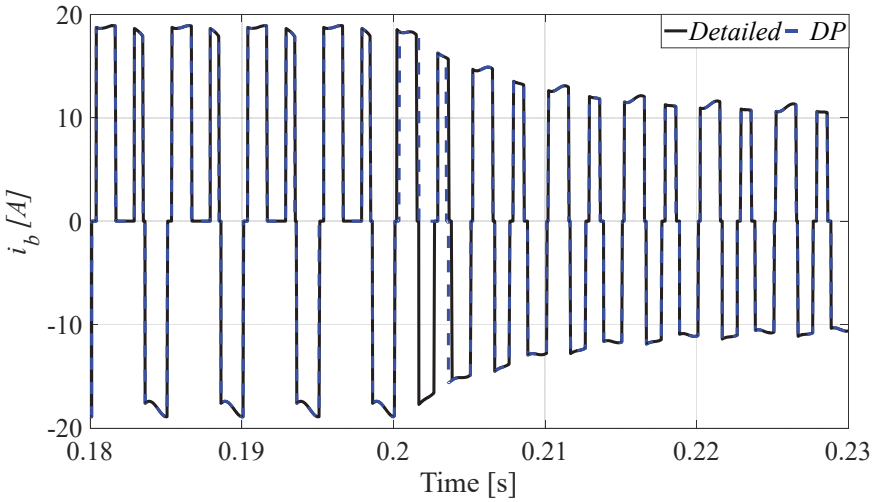

Figure. 3. 78. Current of phase *a*

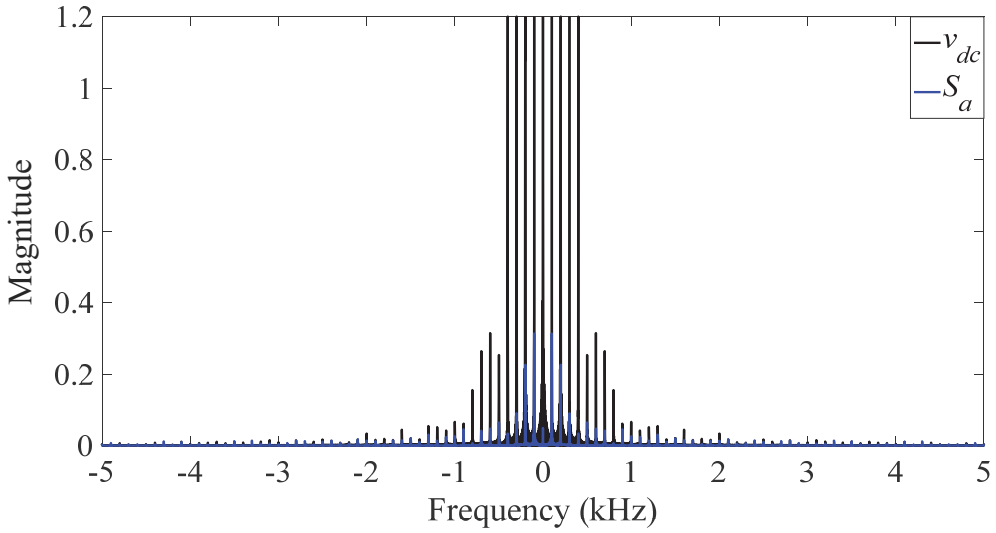

Figure. 3. 79. Frequency spectrum of the rectifier output voltage (v_{dc}) and voltage switching function of phase *a*.

3.18.2 Case 2: With existence of commutation inductance

Another test is performed with commutation inductances in AC-side of the rectifier. Fig 3.80 shows waveforms of input voltages. Absolute and DP-domain voltage switching functions of phase *a* are shown in Fig 3.81. The current switching function of phase *a* and its absolute voltage switching function are shown in Fig 3.82. Uneven commutation intervals can be seen in Fig 3.81 and 3.82. Fig 3.83 and 3.84 show absolute voltage switching function of phase *b* and its DP-domain voltage and current switching functions. The same for phase *c* are shown in Fig 3.85 and 3.86. Fig 3.87 and Fig 3.88 show output voltage of the rectifier using absolute and DP-domain switching functions, respectively. Fig 3.89 and Fig 3.90 show output current of the rectifier using absolute and DP-domain switching functions, respectively. Input phase currents using DP-domain method are shown in Fig 3.91, Fig 3.92, and Fig 3.93. The frequency spectrum of the rectifier output voltage (v_{dc}) and voltage switching function of phase *a* are shown in Fig 3.94. Comparing Fig 3.94 with Fig 3.79, it can be derived that commutation inductance in AC-side of the rectifier increases harmonics of the output voltage of rectifier. Therefore, to achieve a precise modeling, order of considered switching functions' DPs must be increased.

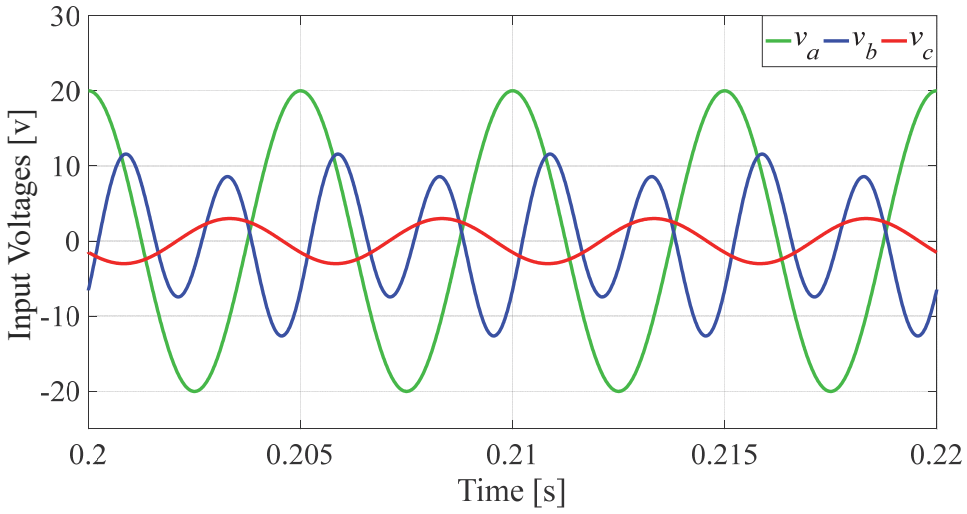

Figure. 3. 80. Input voltages of the rectifier

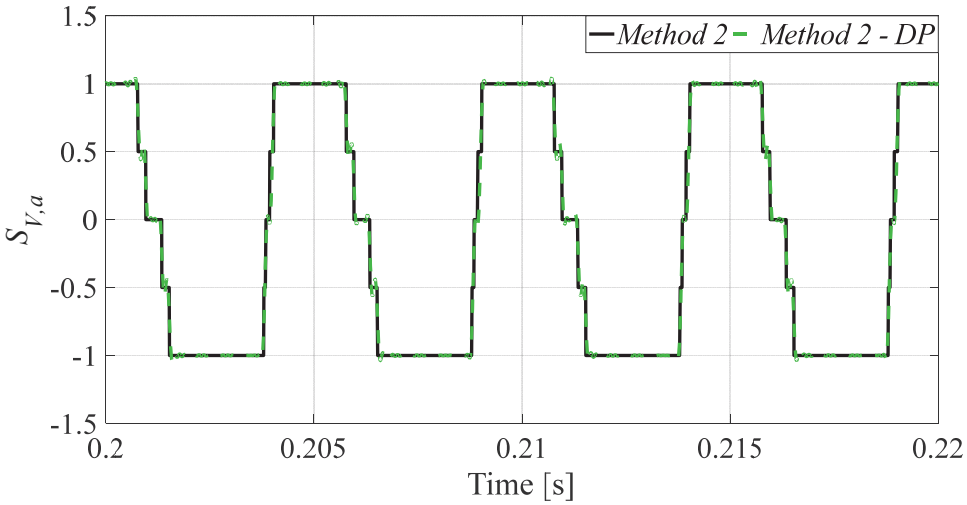

Figure. 3. 81. Absolute and DP-domain voltage switching functions of phase *a*

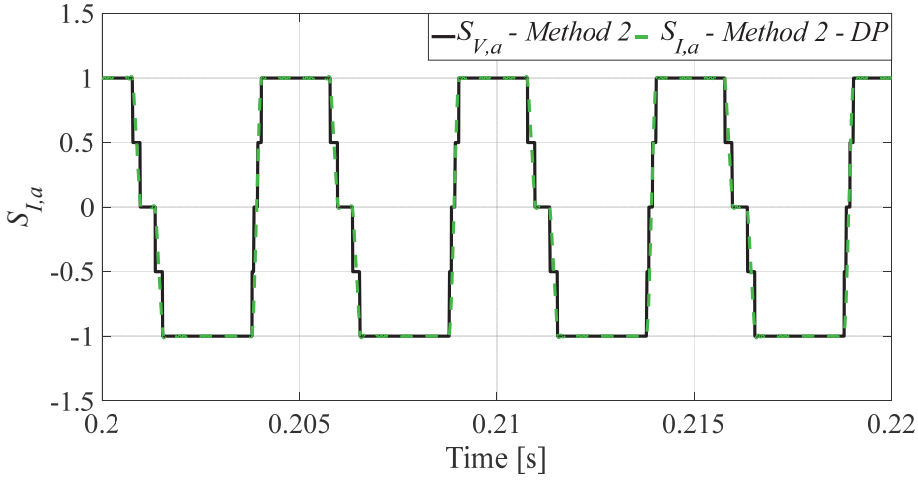

Figure. 3. 82. Absolute voltage switching function of phase *a* and its current switching function in DP-domain

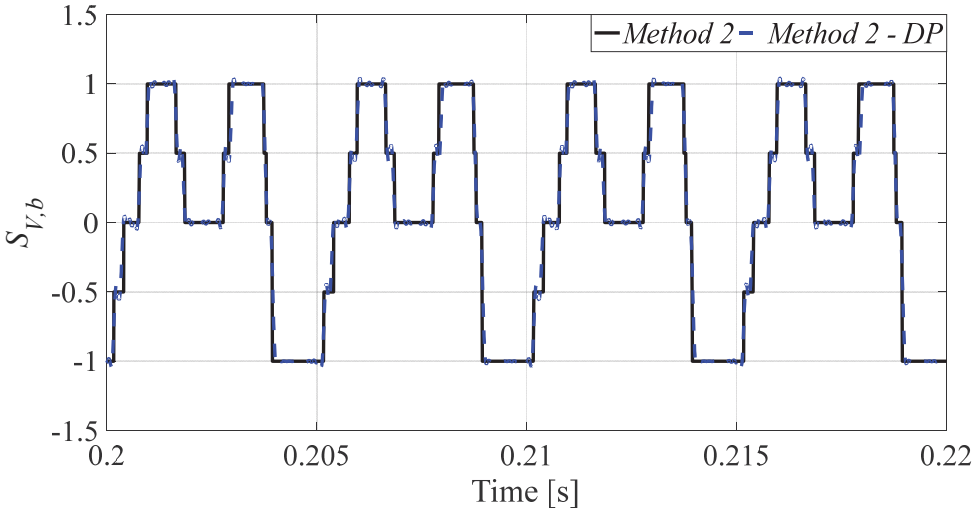

Figure. 3. 83. Absolute and DP-domain voltage switching functions of phase *b*

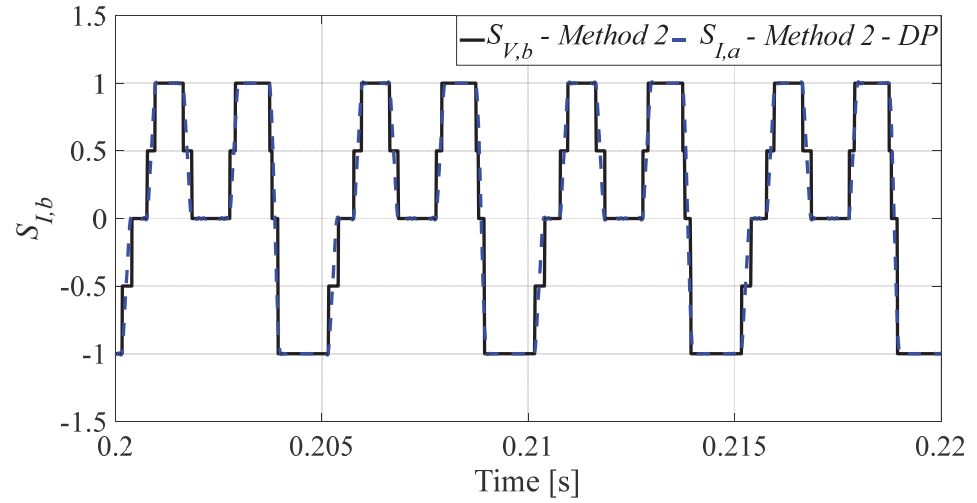

Figure. 3. 84. Absolute voltage switching function of phase *b* and its current switching function in DP-domain

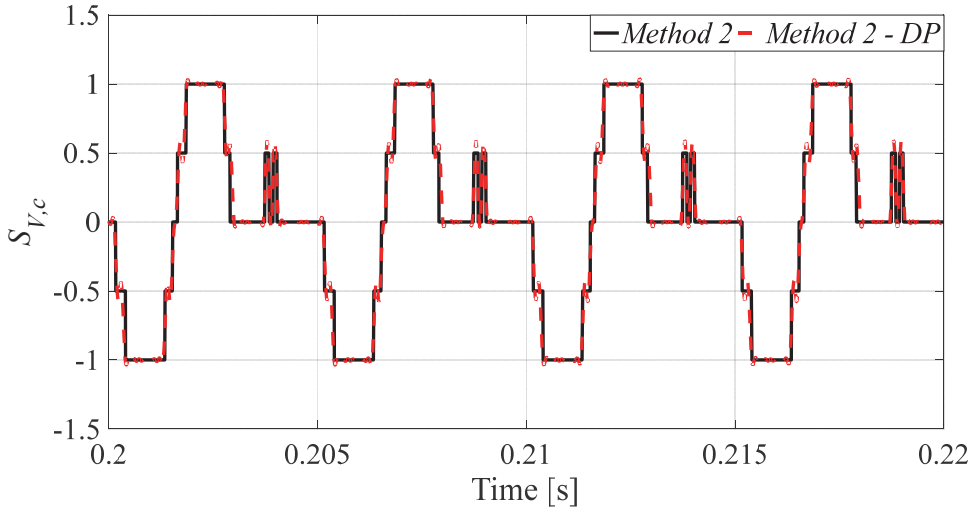

Figure. 3. 85. Absolute and DP-domain voltage switching function of phase *c*

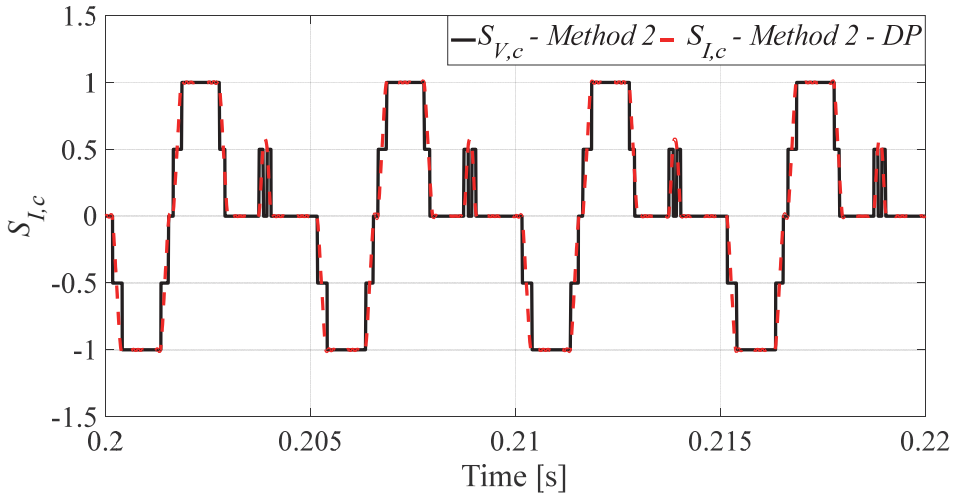

Figure. 3. 86. Absolute voltage switching function of phase *c* and its current switching function in DP-domain.

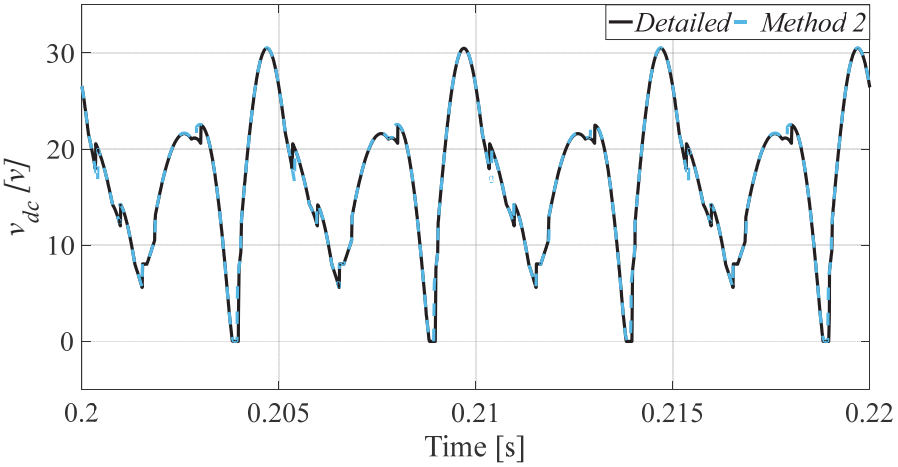

Figure. 3. 87. Output voltage of the rectifier obtained from the detailed model and method 2 using absolute switching functions

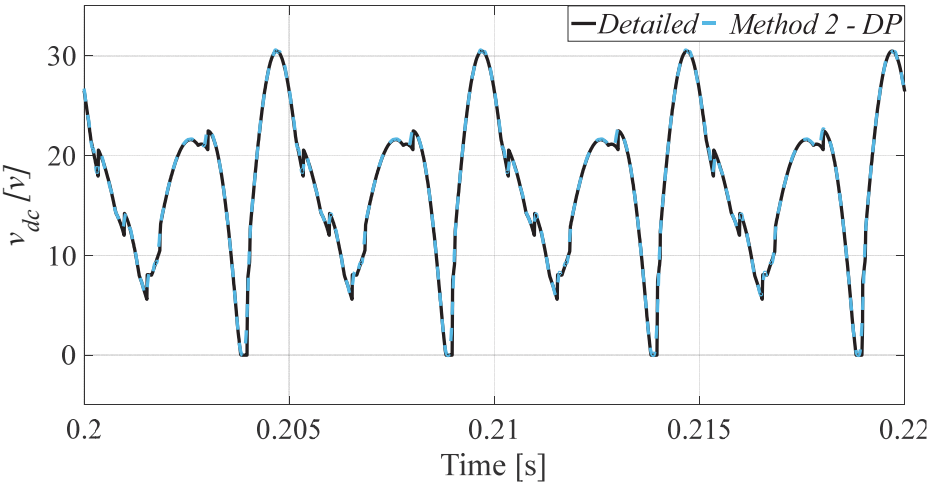

Figure. 3. 88. Output voltage of the rectifier obtained from the detailed model and method 2 using switching functions in DP-domain

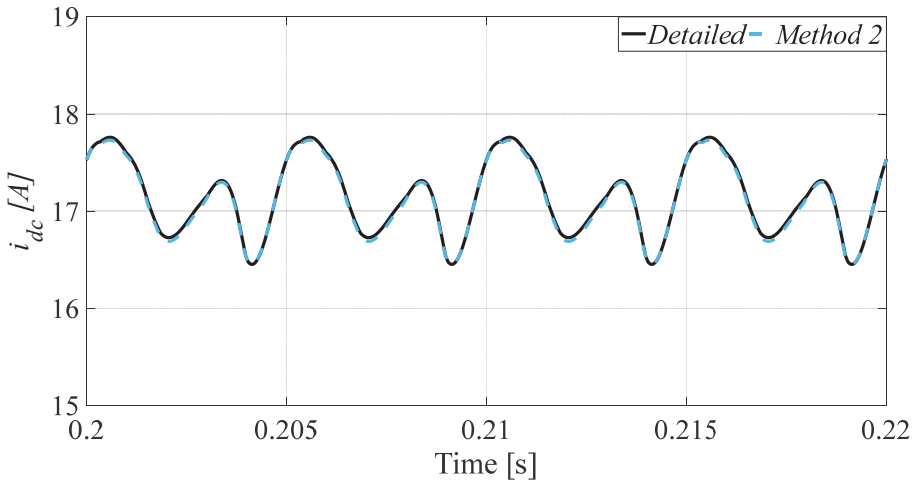

Figure. 3. 89. Output current of the rectifier obtained from the detailed model and method 2 using absolute switching functions

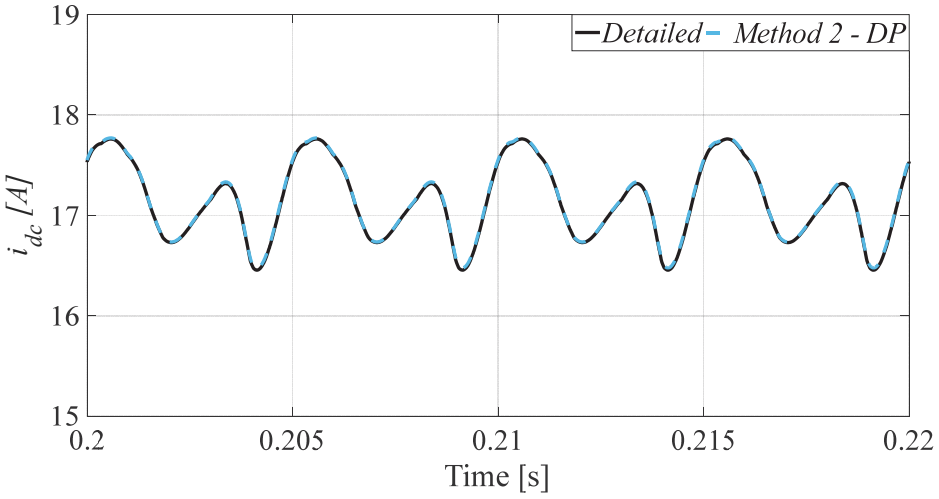

Figure. 3. 90. Output current of the rectifier obtained from the detailed model and method 2 using switching functions in DP-domain

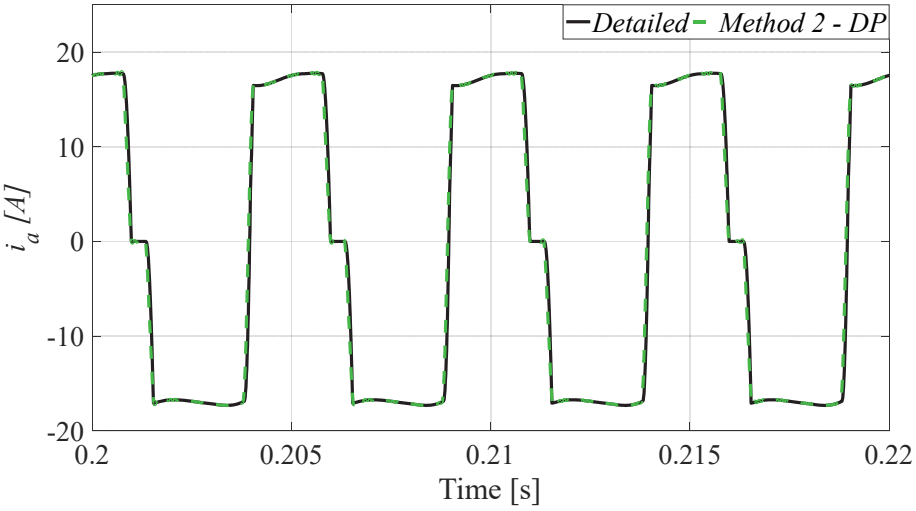

Figure. 3. 91. Current of phase *a*

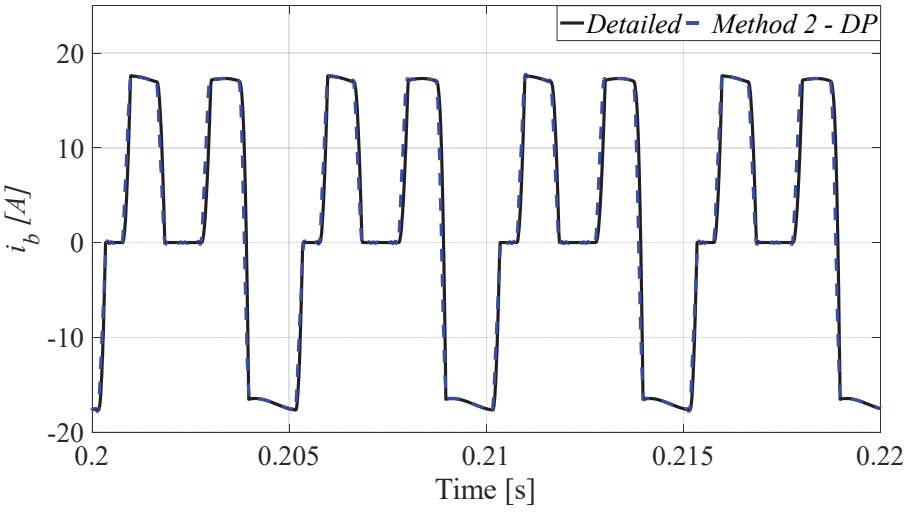

Figure. 3. 92. Current of phase *b*

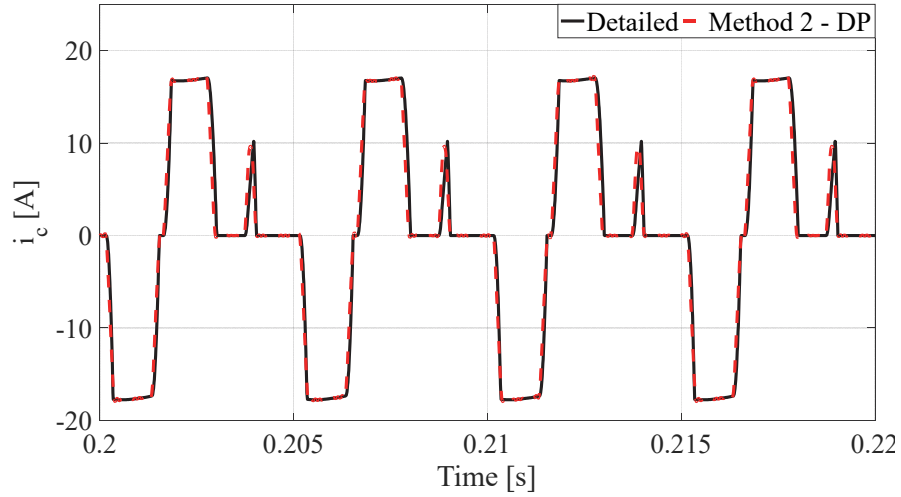

Figure. 3. 93. Current of phase *c*

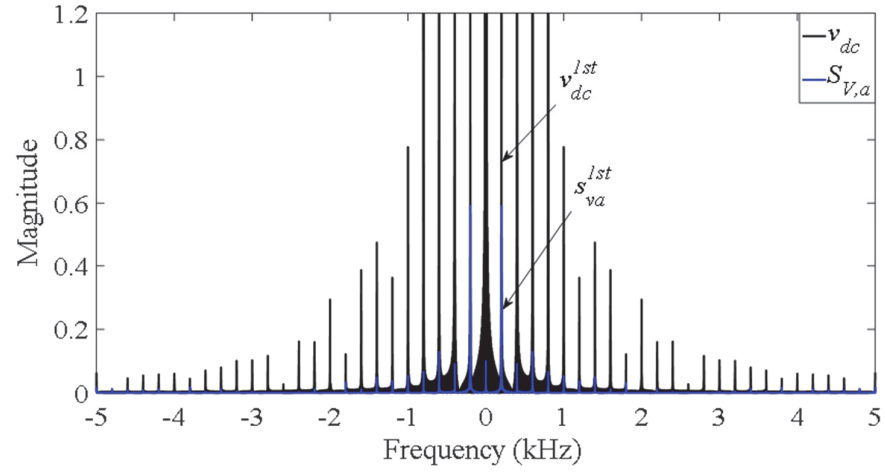

Figure. 3. 94. Frequency spectrum of the rectifier output voltage (v_{dc}) and voltage switching function of phase *a*

3.19 Comparison between computation time of the models

In the previous section, accuracy of the developed models has been validated. In this section, computational performance in terms of computation time of the developed models of the uncontrolled diode bridge rectifier is studied. The models under study are time-domain and DP-domain models using *Method. 2*. In the DP-model. 30 harmonics were considered, so the smallest sample time was set as 16e-5 s. The same sample time was set for the time-domain model. CPU time taken by the time-domain model for each step was 118.64 μs and for the DP-domain model was 153.76 μs. As was expected, time-domain model is more efficient in terms of computation time. However, by reducing number of harmonics in the DP-domain it is possible to significantly increase its computation speed.

3.20. Experimental Validation of the Proposed Models of uncontrolled Rectifier.

To validate the effectiveness of the proposed method, two experimental tests have been performed. Fig 3.95 and 3.96 show the experimental setup. The test rig consists of three-phase commutation inductor, three-phase diode bridge rectifier, and R-L load. The inductance of each commutation inductor is 135 μH. R-L load consists of an inductor with 3 mH inductance and a resistor with 53 Ω.

3.20.1 Case 1. Unbalanced Input Voltages

In this test, AC-side voltages are supplied by a programmable power source as:

$$v_a = 152 \cdot \cos(\omega \cdot t)$$

$$v_b = 132 \cdot \cos\left(\omega \cdot t - \frac{2 \cdot \pi}{3}\right)$$

$$v_c = 97 \cdot \cos\left(\omega \cdot t + \frac{\pi}{2}\right)$$

where

$$\omega = 400 * 2 * \pi$$

In this test, three-phase unbalanced voltages have been supplied to the rectifier. Phase voltages, one phase current, the output voltage of rectifier, and output current of rectifier have been captured by means of voltage and current probes. Then, using the proposed models in Section 3.17 (*Method 2*), measured input voltages are transferred to the DC-side. From output current of the rectifier, AC-side phase currents are estimated.

Figure. 3. 95. Rectifier and AC-side components of the experimental setup

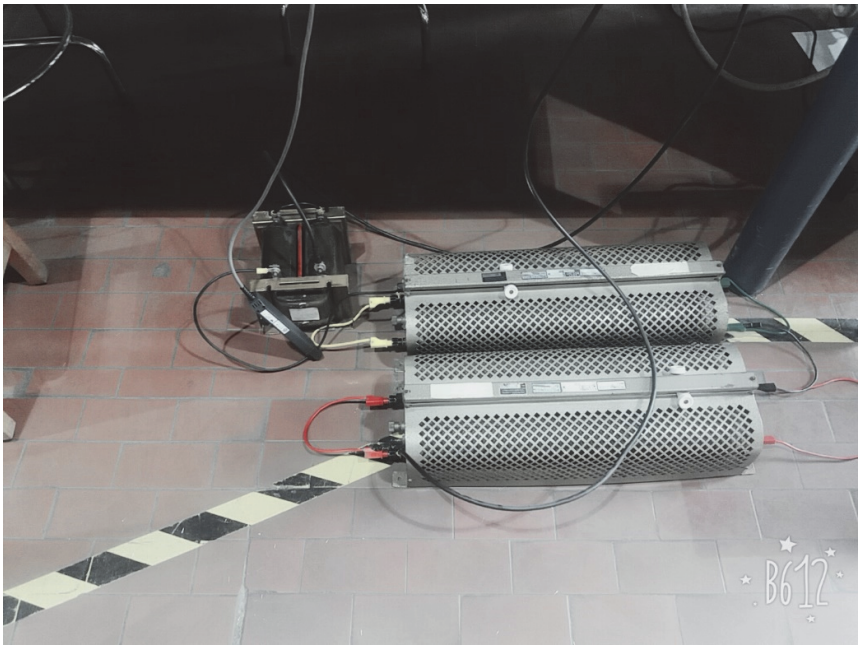

Figure. 3. 96. DC-side components of the experimental setup

Measured waveforms are shown in Fig 3.97. Calculated voltage switching functions and current switching function of phase *a* are shown in Fig 3.98. The estimated output voltage of the rectifier by means of estimating absolute switching functions (Section 3.17) is compared with the measured waveform in Fig 3.99.

Output voltage of the rectifier estimated by DP-domain switching functions (Section 3.17) is compared with the measured waveform in Fig 3.100. Measure waveform of rectifier output current and estimated output current of the rectifier using absolute switching functions and DP-domain switching functions are shown in Fig 3.101. Fig. 3.102, shows measured current of phase a and estimated current calculated by DP-domain switching functions.

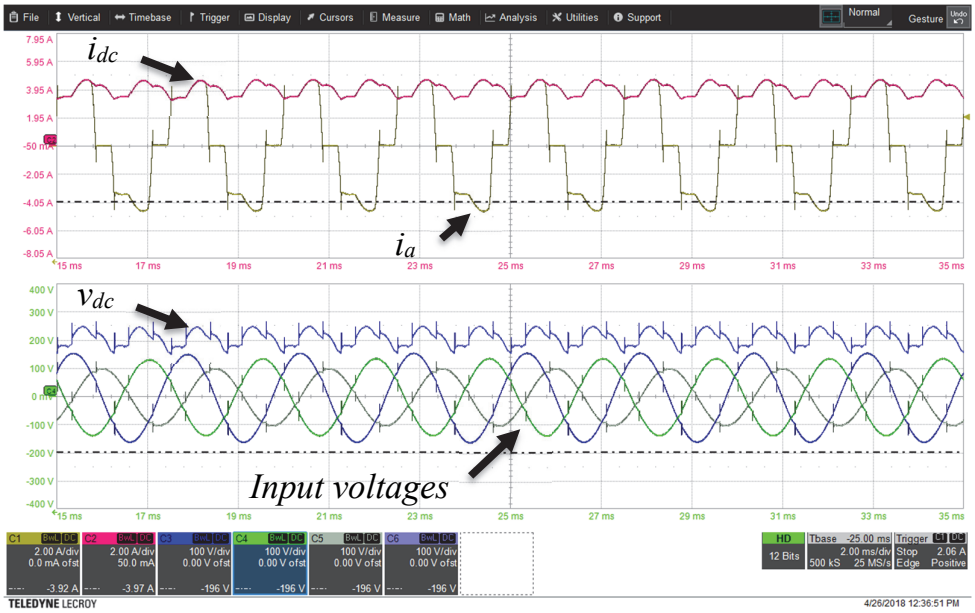

Figure. 3. 97. Measured waveforms

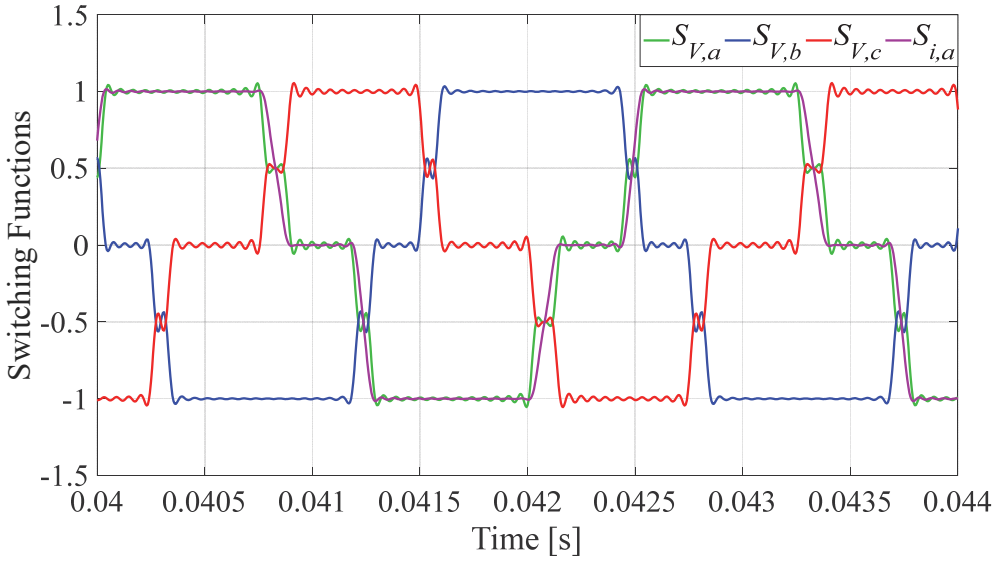

Figure. 3. 98. voltage switching functions and current switching function of phase *a*

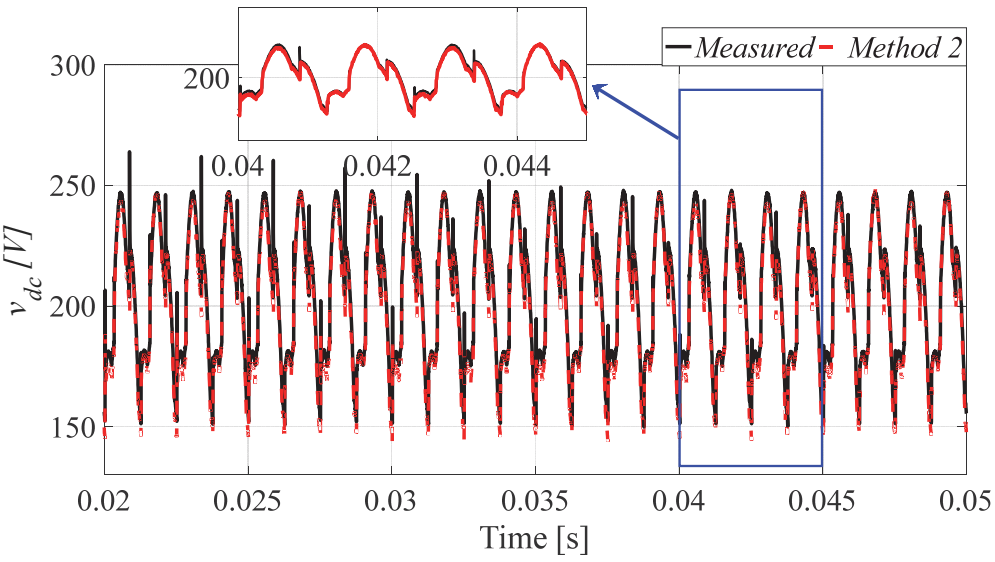

Figure. 3. 99. Measured and estimated output voltage of rectifier, using absolute switching functions

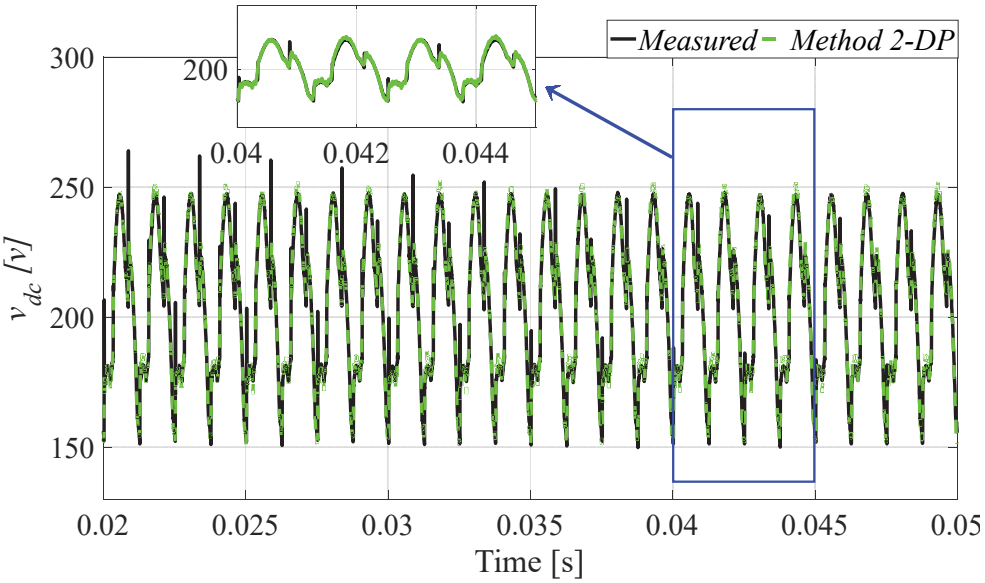

Figure. 3. 100. Measured and estimated output voltage of rectifier, using switching functions in DP-domain

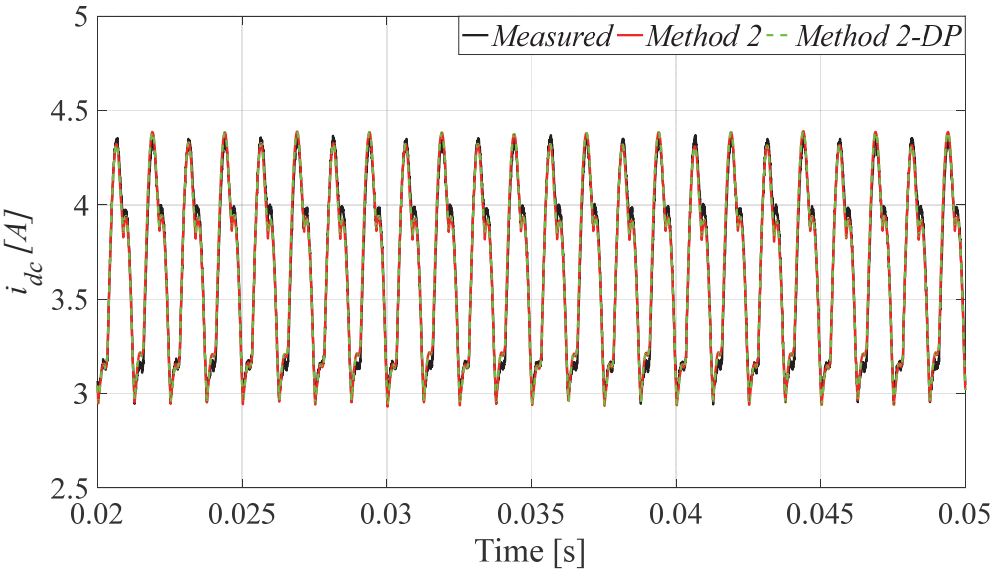

Figure. 3. 101. Measured and estimated output voltage of rectifier, using switching functions in DP-domain and absolute form of switching functions

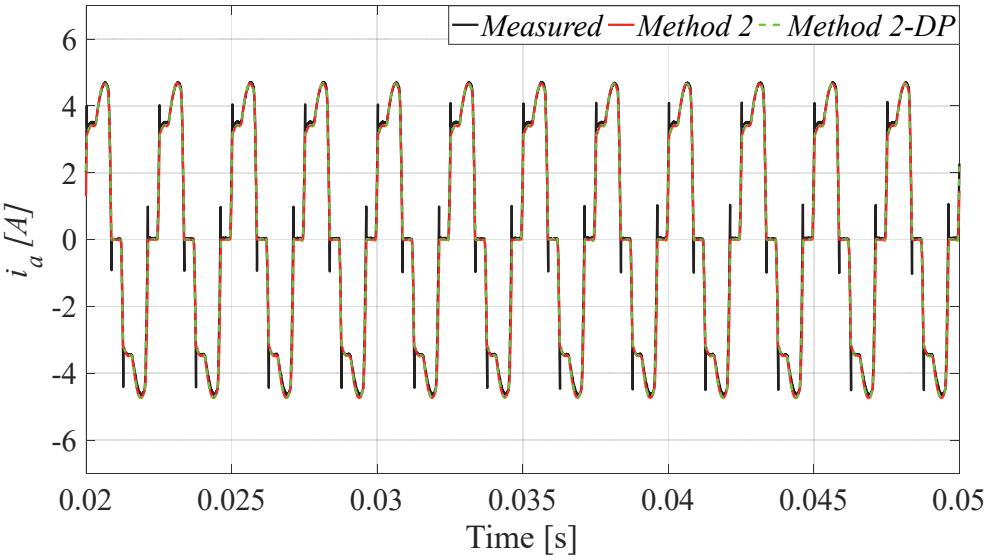

Figure. 3. 102. Measured and estimated current of phase *a*, using switching functions in DP-domain

3.20.2 Case. 2: Unbalanced Input Voltages Containing Second Harmonic.

In this test, input voltages contain a second harmonic component with magnitude equal to 70% of the fundamental component's magnitude. Input voltages of the rectifier are as follows:

$$v_a = 115 \cdot \sqrt{2} \cdot \cos(\omega \cdot t) + 0.7 \cdot 115 \cdot \sqrt{2} \cdot \cos\big(2(\omega \cdot t + 90°)\big)$$

$$v_b = 70 \cdot \sqrt{2} \cdot \cos(\omega \cdot t - 120°) + 0.7 \cdot 70 \cdot \sqrt{2} \cdot \cos\big(2 \cdot (\omega \cdot t - 120° + 90°)\big)$$

$$v_c = 100 \cdot \sqrt{2} \cdot \cos(\omega \cdot t + 70°) + 0.7 \cdot 100 \cdot \sqrt{2} \cdot \cos\big(2 \cdot (\omega \cdot t + 70° + 90°)\big)$$

where

$$\omega = 400 * 2 * \pi$$

In this test, output voltage and current of the rectifier, input voltages, and current of phase *b*are measured by means of voltage and current probs. Then, the same input voltages are inserted to the proposed model of the rectifier using *Method 2* (Section 3.17). The measured waveforms are depicted in Fig 3.103. Fig 3.104 shows voltage switching functions and current switching function of phase *a* using switching functions in DP-domain representation. Absolute switching functions are depicted in Fig 3.105. Uneven commutation intervals can be seen in Fig 3.104 and 3.105. For instance, in accordance with (3.97) to (3.99), the commutation interval between phase *a* and phase *c* is shorter than the commutation interval between phase *b* and phase *c*. The output voltage of the rectifier estimated by *Method 2* using absolute switching functions and DP-domain representation of switching functions are compared to the measured waveform in Fig. 3.106, and Fig. 3.107, respectively. Fig. 3.108 shows the output current of the rectifier estimated by the proposed method using absolute switching functions of *Method. 2* in comparison with the measured waveform. Comparison between the measured current of phase *b* and its estimated waveform using DP-domain form of switching functions of *Method 2* is depicted in Fig. 3.109.

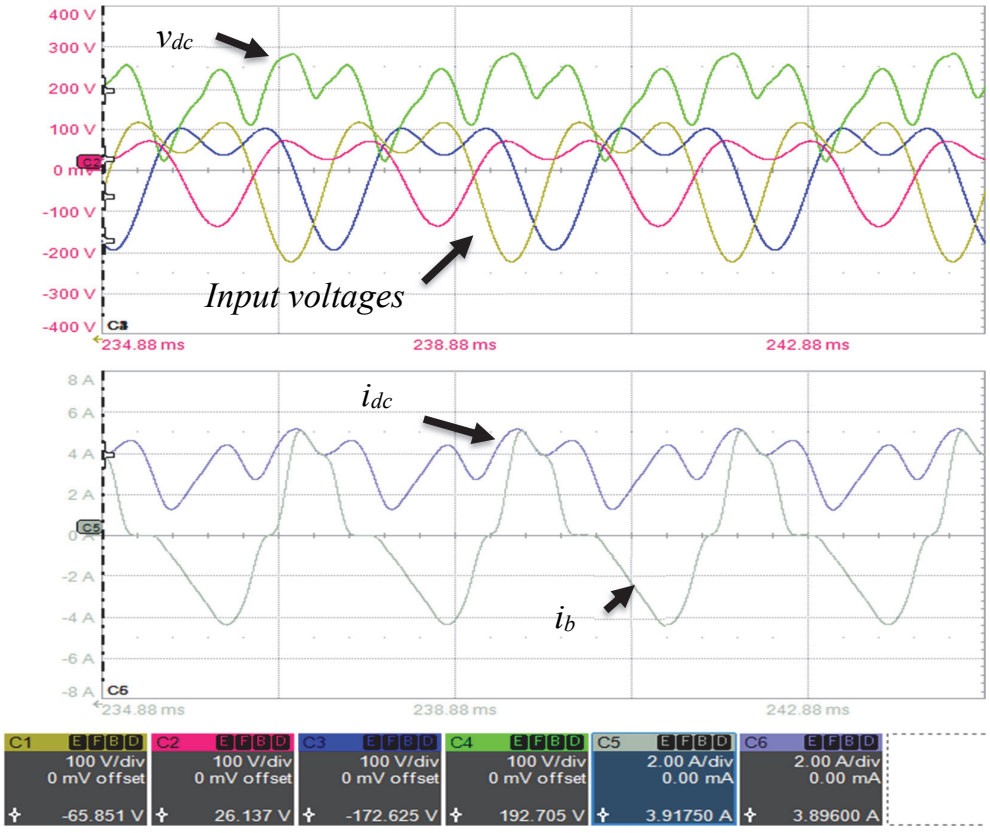

Figure. 3. 103. Measured waveforms

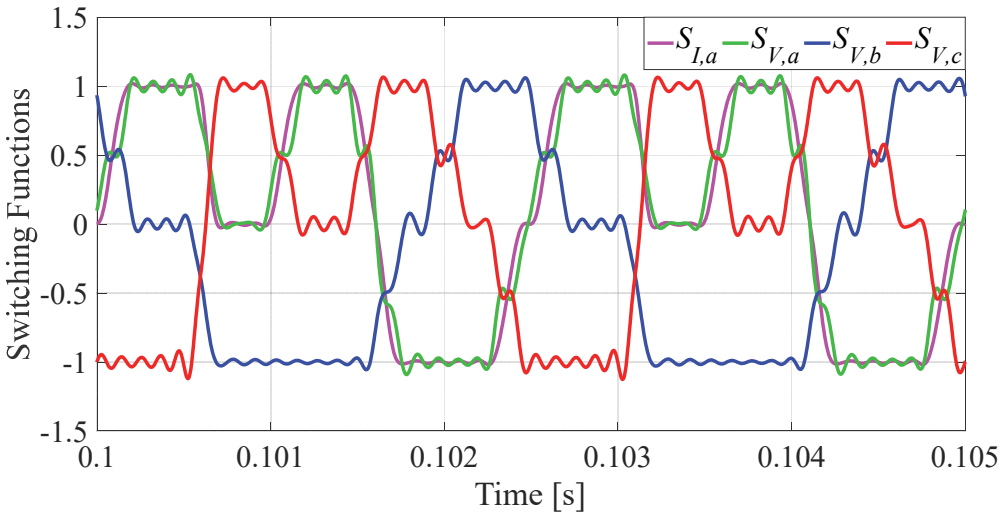

Figure. 3. 104. voltage switching functions and current switching function of phase *a* using DP-domain representation of *Method 2*

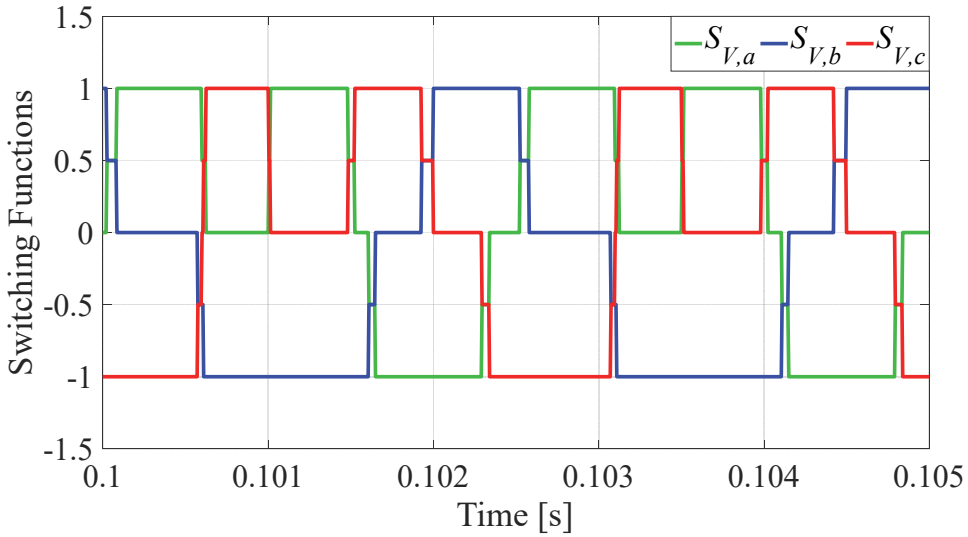

Figure. 3. 105. Absolute voltage switching functions using *Method 2*

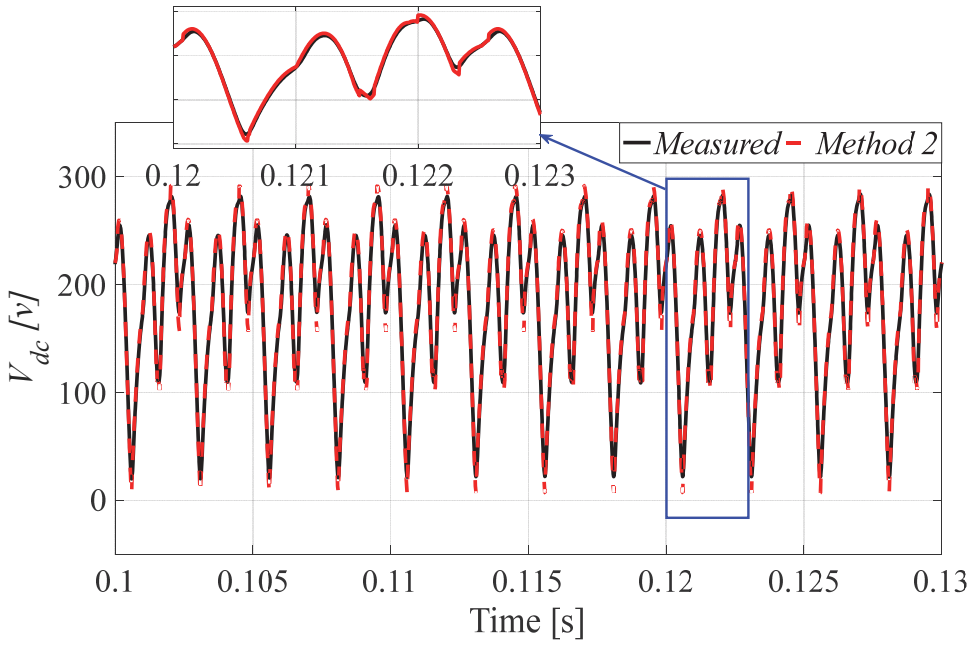

Figure. 3. 106. Measured and estimated output voltage of the rectifier using absolute switching functions

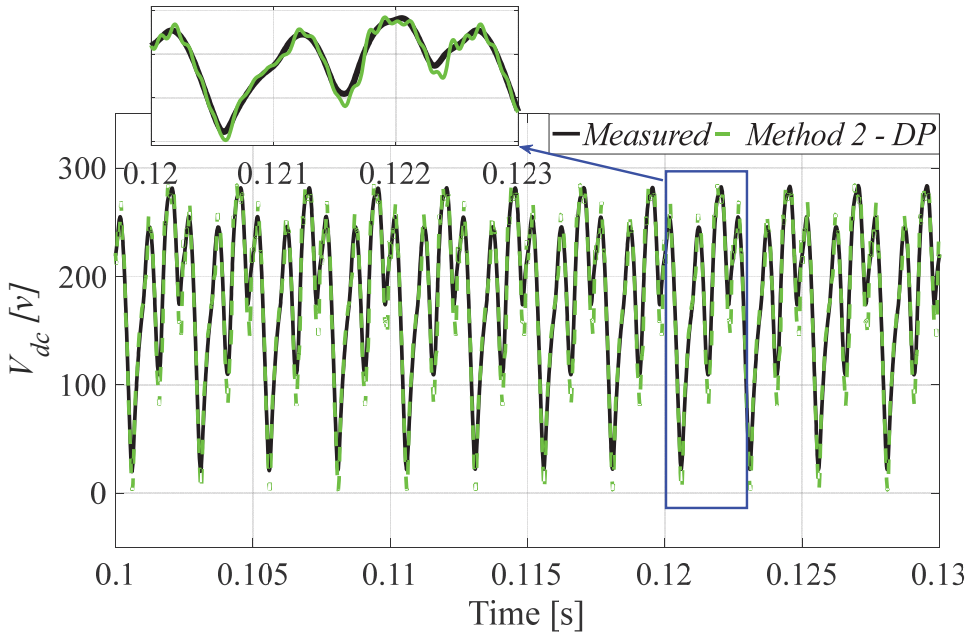

Figure. 3. 107. Measured and estimated output voltage of the rectifier using switching functions in DP-domain

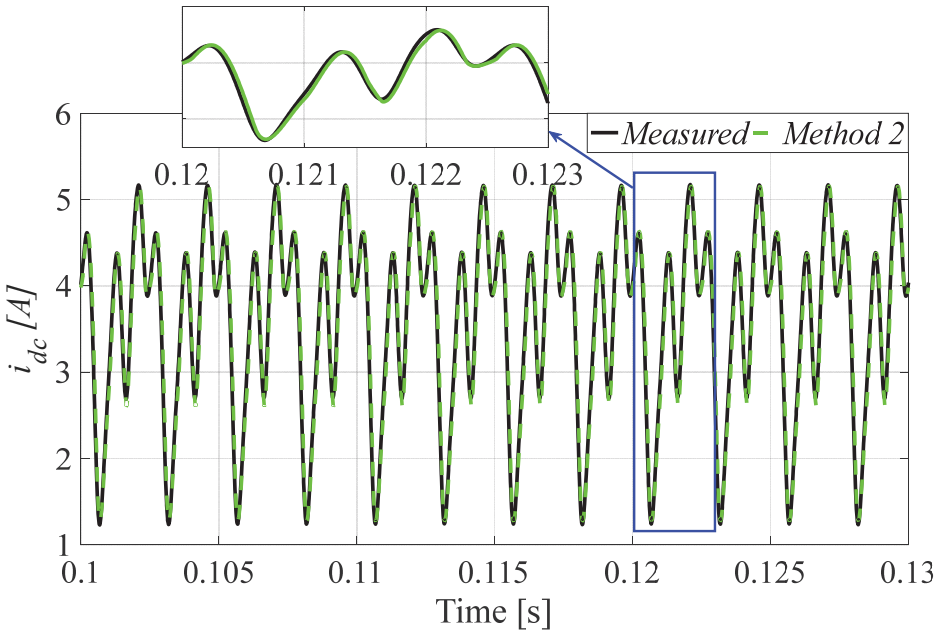

Figure. 3. 108. Measured and estimated output current of the rectifier, using absolute switching functions

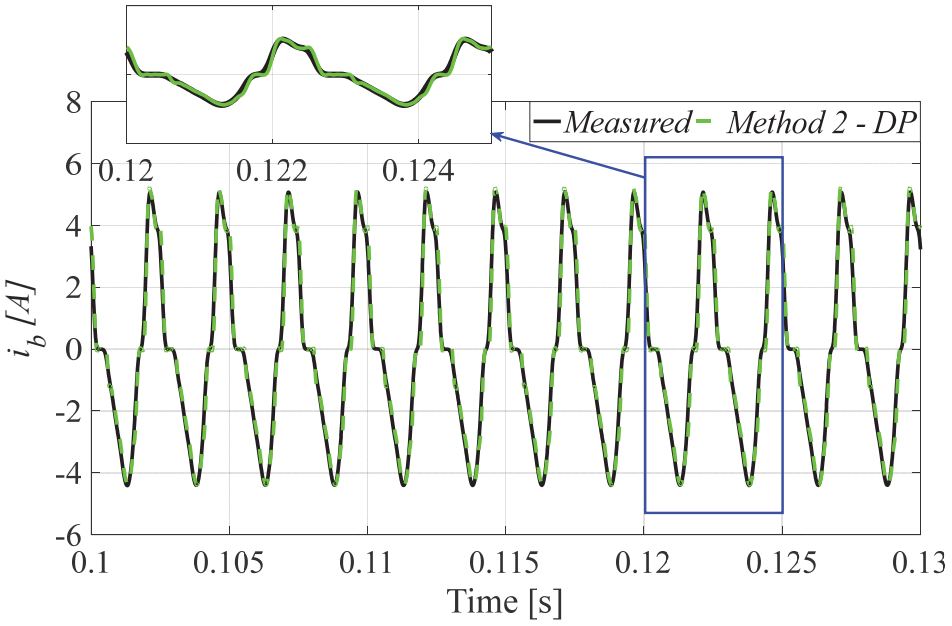

Figure. 3. 109. Measured and estimated current of phase *b*, using switching functions in DP-domain.

Chapter 4

Phase Variable Model of Aircraft Brushless Exciter

4.1 Introduction

This chapter deals with modeling of the three-stage brushless synchronous machine. The goal is to provide a model of the machine for simulation purpose. The model must be able to perform in both starting and generating operations. Since in part of starting process excitation of ME is AC, induced voltages in armature windings are not balanced three phase voltages. Therefore, a *D*-*Q* transformation of quantities does not yield to time-invariant quantities, so it is not reasonable to apply an extra transformation to variables when does not result in an advantage.

Adequate modeling of the main exciter is extremely important for studying the dynamic behavior of the system. The uncontrolled diode rectifier connected to the armature winding of the exciter makes the system more complicated. As a result, adequately considering the coupling effects of the power electronics part and armature windings of the brushless exciter is necessary. Based on the voltage and inductance of the armature windings, the uncontrolled diode rotating rectifier operates in different commutation modes [55]-[58]. So, the model of the rotating rectifier must be able to deal with all operation modes of the rectifier. Such a model is proposed in Chapter .3 of this thesis.

Since the ME armature voltages are supply voltages of the rotating rectifier, the precise knowledge of the ME inductance which contributes in commutation process of the rotating rectifier (hereafter called the commutation inductance) is required to get a good ME model. In this chapter, a method based on Finite Element (FE) analysis is proposed to identify the commutation inductance.

A model of the brushless exciter based on self and mutual inductances obtained from FE analysis is presented in [59]. This model uses an algorithm which determines the states of the rectifier operation by checking the exciter armature voltages and currents in each step time. In [60], a model of the brushless exciter based on a state machine has been proposed. Neither of the presented models in [59] and [60] considered the exact value of the commutation inductance. Numerical and parametric average value models of brushless exciter have been proposed in [61]-[65]. These models use a numerical average model of the rectifier obtained from data sets given by a detailed model. The reported detail models are based on nonlinear Simulink SimPowerSystem toolbox or state machine. Since the commutation inductance is not considered in the detailed models, the developed model of the exciter-rectifier system is not accurate.

In this chapter, a phase variable Simulink model of the exciter-rectifier system is developed. The proposed Simulink model uses the current-flux linkage nonlinear relationships obtained from FE analysis to determine back-emf of the machine windings. Identification methods are described in Section 4.3. In addition, a simple FE analysis method for commutation inductance identification is proposed. The structure of the implemented model is presented in Section 4.4. Section 4.55 contains the model verification using the comparison with the FE analysis.

4.2 Phase variable Model

In this chapter, two phase-variable Simulink/Matlab models of the brushless exciter based on current-flux linkage nonlinear functions of the exciter machine is developed. In order to identify these functions, a Finite Element (FE) analysis is performed. The first model is based on sets of data obtained from FE analysis and saved in look-up tables. While the second model uses Fourier series approximation to map magnetic characteristics of the machine. Voltage and flux formulations of the developed phase variable model of the exciter are expressed as follows.

$$v_j = R_j \cdot i_j + \frac{d\lambda_j}{dt}\,, \quad j,k = a,b,c,e \tag{4.1}$$

$$[i] = [i_a \;\; i_b \;\; i_c \;\; i_e] \tag{4.2}$$

$$\lambda_j = f(\vartheta, [i]) = \lambda_{j,a} + \lambda_{j,b} + \lambda_{j,c} + \lambda_{j,e} \tag{4.3}$$

where V, i, and λ, are the instantaneous voltage, current, and flux linkage of the machine windings, respectively. R is the resistance of the machine windings.

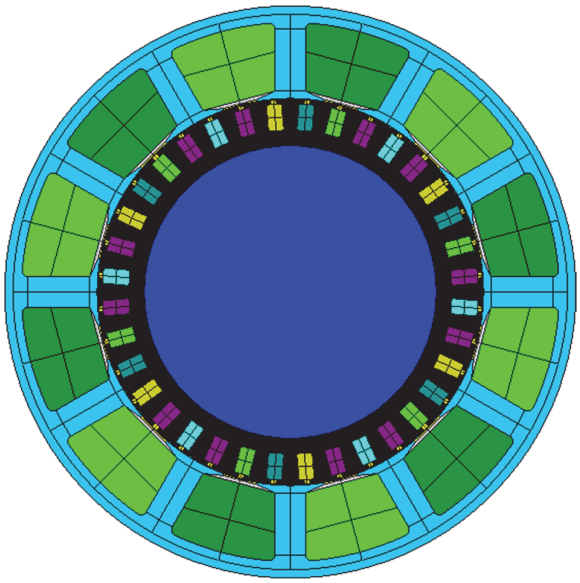

Figure. 4. 1. Brushless exciter FE model

In (4.3), the "*a*", "*b*" and "*c*" indexes indicate three phases of armature windings and "*e*" index indicates field winding (excitation winding); ϑ is rotor position of the machine and *f* indicates the nonlinear current-flux linkage function. Actually, the flux linkages are nonlinear functions of the rotor position and machine currents. In this paper, to describe the nonlinear current-flux linkage functions, Look-Up Tables (LUT) with linear interpolation method are used. Dataset of the LUTs are directly determined from a FE model, using the Flux-2D software.

4.3. Finite Element Analysis and Parameters Identification

In this section, the required parameters and current-flux linkage relationships are determined through a circuit-coupled FE analysis of the brushless exciter machine. Then the obtained data sets of the current-flux linkage relationships are saved into 2-D tables. In addition, a method to determine the commutation inductance is proposed.

4.3.1. Current-Flux Linkage Relationships Identification

In order to identify current-flux linkage nonlinear relationships, a FE model of a 12 pole brushless exciter has been built (Fig. 4.1). The modeled brushless exciter contains a single-phase field winding (stator) and three-phase armature windings (rotor).

Each winding is fed by a range of current whereas other windings are open. For each value of the injected current, the flux linkages are calculated for a complete electric period (rotor angular position changes from 0° to 360° electrical degrees). Then, the obtained data sets are saved in LUTs.

Using phase variable model, geometry space harmonics and saturation effects are taken into account. The only assumption in the modeling is that inductance saturation of each winding depends on its own current. With this assumption, some of the saturation effects are not considered even though, since exciter machines are usually operating in their linear operating region, this assumption does not have a significant effect [59].

Fig. 4.2.a shows the flux linkage of the armature phase a winding caused by magnetizing the field winding ($\lambda_{a,e}$). Fig 4.2.b shows flux linkage of the field winding induced by its current ($\lambda_{e,e}$).

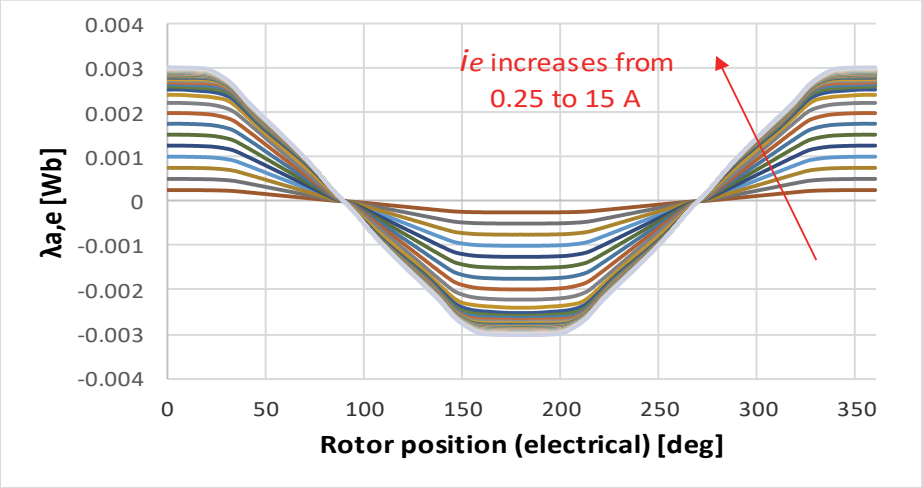

(a)

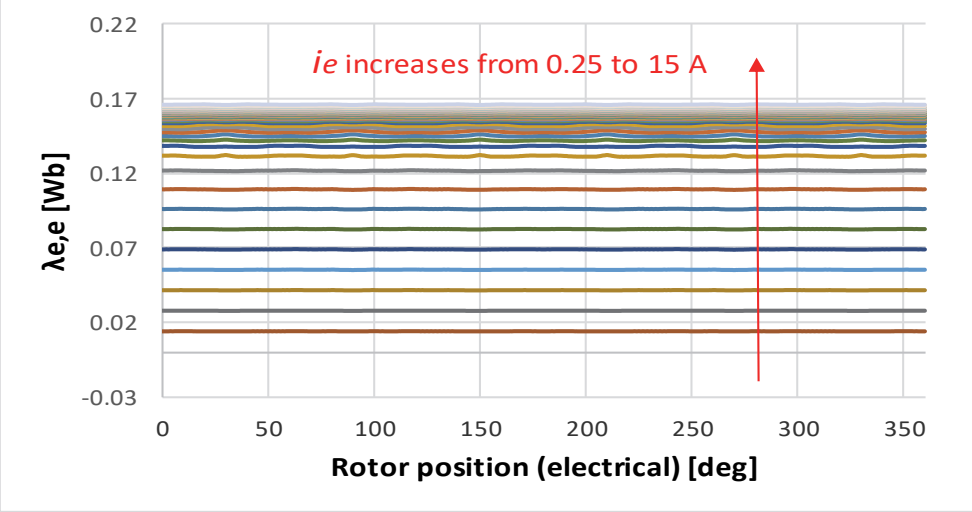

(b)

Figure. 4. 2. Current-flux linkage profiles obtained from FE analysis. (a) variation of $\lambda_{a,e}$ with increasing of i_e, (b) variation of $\lambda_{e,e}$ with increasing of i_e

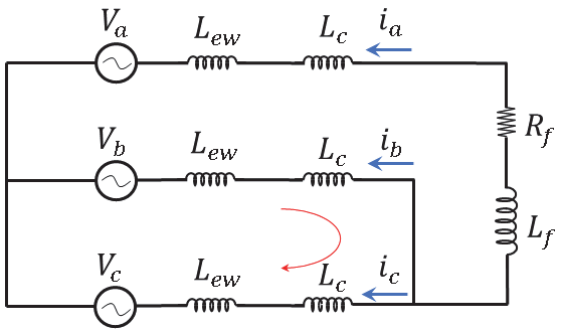

Figure. 4. 3. Equivalent circuit of exciter-rectifier during commutation interval

4.3.2. Identification of the Commutating Inductance

In this section, commutation inductance (L_c) to be used in the Simulink model is calculated. During the commutation interval, the finite commutation time interval of the rectifier diodes makes line-to-line short-circuit between armature phases of the exciter. Therefore, the inductance which contributes in the equivalent circuit of the exciter and the rotating rectifier (Fig. 4.3) is not one of the exciter steady-state inductances.

Since the commutation interval is very short, L_c may be assumed as one of the sub-transient inductances of the machine. Because the rotating rectifier is connected to the rotor windings of the exciter, once a commutation short-circuit occurs between the armature phases, the air-gap flux cannot change instantaneously and remains constant, according to the constant flux linkage theory [66]. In this case, the flux changes during the commutation intervals remain inside the rotor (since short-circuits occur between rotor windings). Hence, the inductance which contributes in equivalent circuits during commutation can be considered as sub-transient inductance.

To estimate the commutation inductance using FE analysis, two methods can be used: the magneto-static method and the transient analysis method. In this paper, the magneto-static FE technique is performed. The proposed magneto-static technique exploits the simplification method presented in [67], therefore is more optimal in terms of the required computation time.

Since the commutation inductance is realized as an inductance defined at specific instants of the machine transient response to an applied short-circuit occurs during diodes current commutation, instead of solving the transient equations in a large time span, only an instant of time which is of interest for commutation inductance estimation is concerned. Thus, using boundary conditions, regions of the problem domain which contribute in the commutation inductance estimation were isolated from other regions to simplify the problem. Based on the constant flux linkage theory, these regions for the commutation inductance estimation are the rotor of the brushless exciter and its windings.

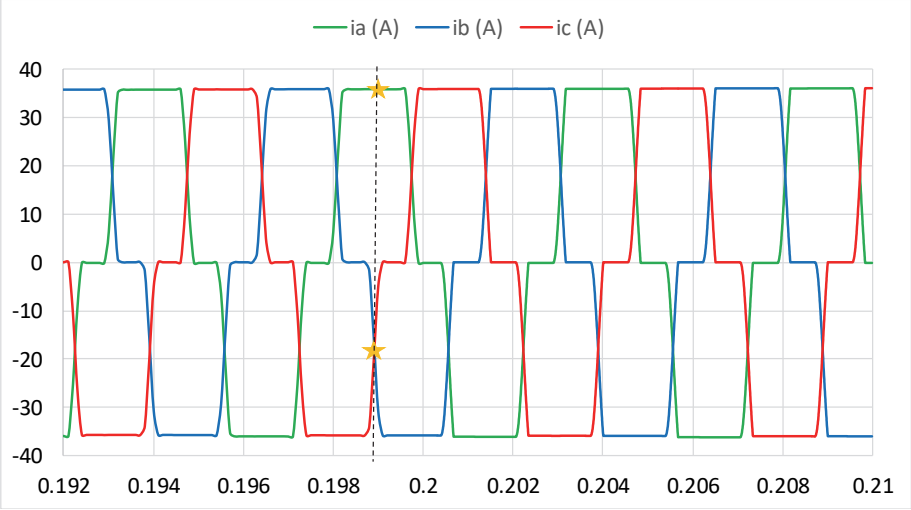

Figure. 4. 4. Brushless exciter's armature windings currents

Fig. 4.4 shows the brushless exciter's armature winding currents. As can be derived from Fig. 4.4, the indicated instant at the middle of a commutation interval can be referred to the condition which the direct axis (d-axis) of the armature currents (and mmf) coincides with phase *a* axis (a-axis). To simulate this condition in FE simulation model, the armature windings currents should be set as:

$$i_a = I_d, \quad i_b = -\frac{I_d}{2}, \quad i_c = -\frac{I_d}{2} \tag{4.4}$$

where I_d is the d-axis current and is set for a value range from 5 to 15 A.

The rotor position is set so that the d-axis takes up the same place as the a-axis. The stator winding is not fed. Therefore, the commutation inductance can be considered as the d-axis inductance during commutation interval and is calculated as:

$$L_c = L_d = \frac{\lambda_a}{I_d} \tag{4.5}$$

Fig. 4.5 shows flux distributions during the commutation interval. Since the implemented FE model was a 2D model, at the end the value of end-winding was added to the implemented model. The end-winding inductance has been calculated based on equations in [68]. The calculated end-winding inductance and commutation inductance are reported in Table. 4.1.

Table. 4. 1**.** Calculated end-winding and commutation inductances

Parameter	**Abbreviation**	**Value**	**Unit**
Commutation Inductance	L_c	2.32	µH
End-Winding Inductance	L_{ew}	5.1	µH

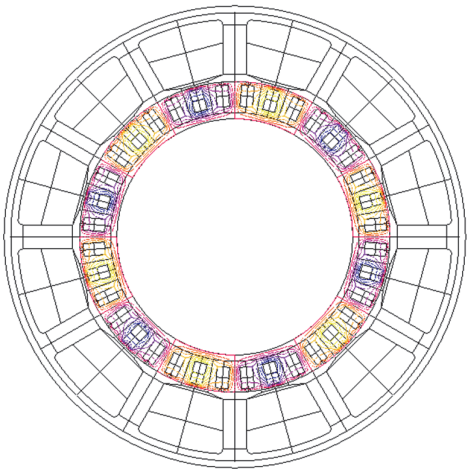

Figure. 4. 5. Flux distribution based on implemented commutation inductance identification technique

4.4 Implementation

To implement exciter's rotor and stator blocks, current or flux linkage can be chosen as the state variable. The developed model uses flux linkage as the state variable for stator model and the winding currents for rotor model. The advantages of these choices are described in the following subsections.

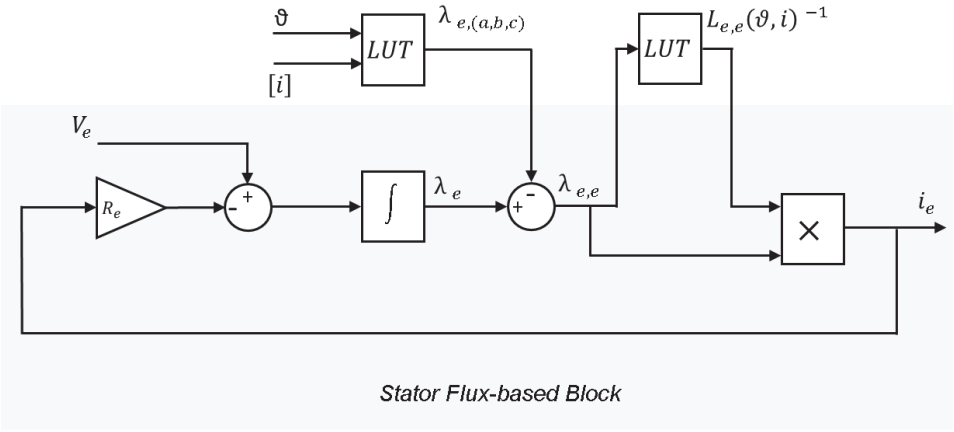

Figure. 4. 6. Stator flux-based Simulink block

4.4.1. Implementation of the brushless exciter's Stator Block

The schematic of the implemented flux-based block of the stator is shown in Fig. 4.6, where the linkage flux of the field winding is the state variable. Choosing the linkage flux as the state variable provides a direct interface between the input of the stator block and the power electronics part which feeds the field winding. Therefore, input of the stator flux-based block is excitation voltage (V_e), while output of the block is excitation current (I_e). The developed stator model uses the following formulae:

$$\lambda_e = \int (V_e - R_e \cdot i_e) \tag{4.6}$$

$$\lambda_{e,e} = \lambda_e - \left(\lambda_{e,a} - \lambda_{e,b} \cdot \lambda_{e,c}\right) \tag{4.7}$$

$$i_e = \lambda_{e,e} \cdot L_{e,e}(\vartheta, i_e)^{-1} \tag{4.8}$$

where $L_{e,e}(\vartheta,i_e)^{-1}$ is the inverse of the apparent self-inductance of the stator winding.

Since the flux is chosen as a state variable, the inverse of the apparent inductance is required to obtain the current. Apparent inductances can be calculated from the current-flux linkage data sets as follows.

$$L_{j,k}(\vartheta, i_k) = \frac{\lambda_{j,k}}{i_k} \quad , \quad j,k - a,b,c,e \tag{4.9}$$

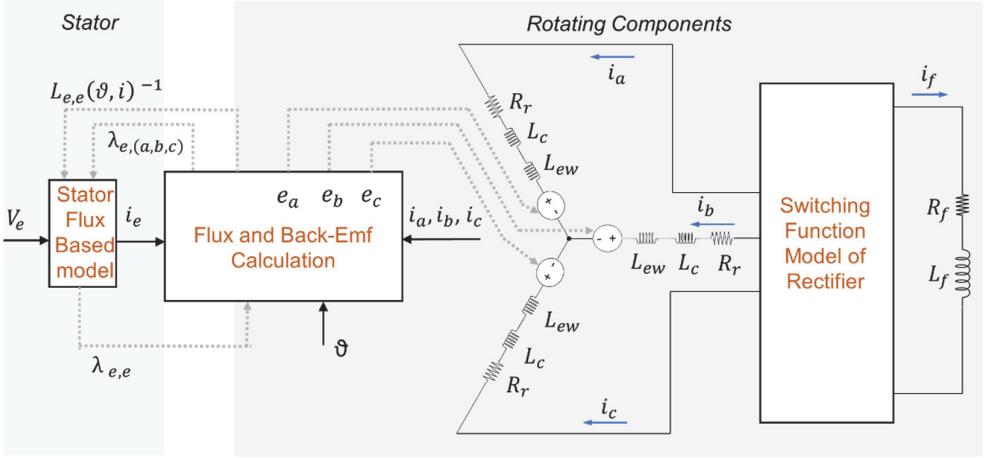

Figure. 4. 7. Simulink implementation of the developed brushless exciter model

4.4.2. Implementation of the Rotating Components Block

In order to provide a direct interface with the rotating rectifier which is modeled base on switching function method proposed in Chapter .3 (Section 3.17), rotor currents are chosen as the state variables. This makes the direct connection between the output of the rotor block and the rotating rectifier possible. A complete schematic of the implemented brushless exciter PD block is shown in Fig. 4.7.

Outputs of the rotor block are the induced voltages in armature windings which are modeled as controlled voltage sources. The commutation inductance (L_c) and end-winding inductance (L_{ew}) are modeled as constant parts of the machine inductances. The armature windings' back-emf is calculated as follows.

$$e_j = \frac{d\lambda_j}{dt} = \frac{d}{dt}\left(\lambda_{j,e} + \lambda_{j,a} + \lambda_{j,b} + \lambda_{j,c}\right), \qquad j = a, b, c.e \tag{4.10}$$

4.5. Results and Performance Comparison between Simulink and FE Models

In this section, the performance of the developed exciter Simulink model is proven by comparing its results with a transient magnetic simulation carried out by Flux-2D FE software. The characteristics of the FE simulation are reported in Table. 4.2. The comprised parameters are: armature windings fluxes, armature windings induced voltages, and output voltage and current of the rotating rectifier.

In addition, the computational efficiency of the developed phase variable Simulink model and the implemented FE have been compared using a computer with Intel core i7-3.6 GHz processor and 8 GB RAM. The developed Simulink model takes 5.1 s to complete 1.2 second simulation with a time step of 1e-6 s. The FE model, however, needs 800 min to perform the simulation for the same time period with the time step of 1e-4 s (12001 computation steps).

Table. 4. 2. FE transient magnetic simulation parameters

FE simulation Parameters	**Value**	**Unit**
Field winding current of the brushless exciter	3·sin(400·π·t*)	A
Rotation speed	250·t	RPM
Simulation time interval	1.2	s
Simulation time step value	1e-4	s
Number of computation steps	12001	

* *t* is the simulation time

4.5.1. Armature Flux-Linkages

The flux linkages of the armature winding obtained from the FE analysis and Simulink model are shown in Fig. 4.8.a, 4.8.b, and 4.8.c. Fig. 4.8.d shows magnification of a part of the Fig. 4.8a. From these figures, it can be derived that the flux linkage waveforms obtained by the Simulink model are very close to those obtained by the FE simulation. This justifies that the developed Simulink model is capable of precisely representing the nonlinear current-flux linkage relationships.

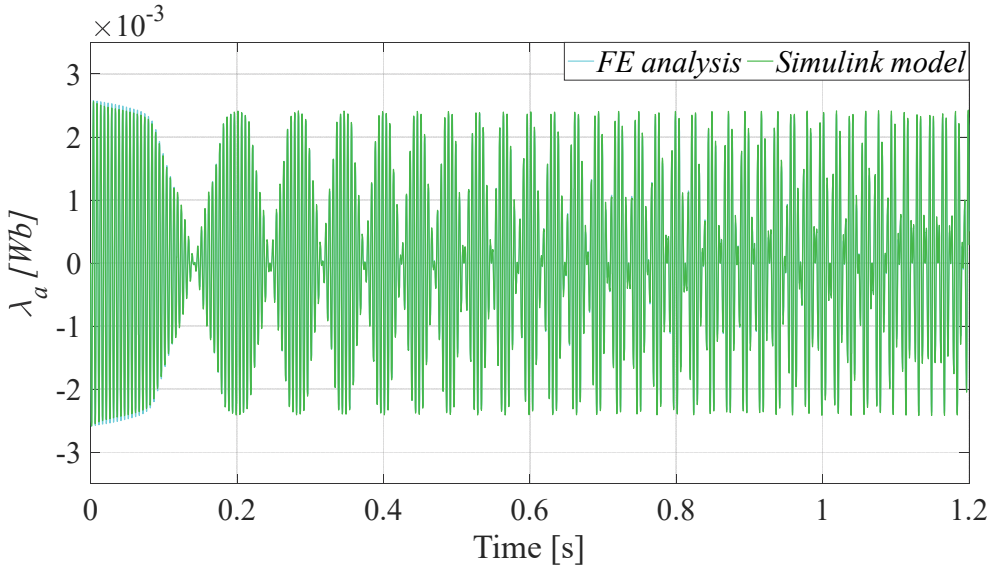

(a)

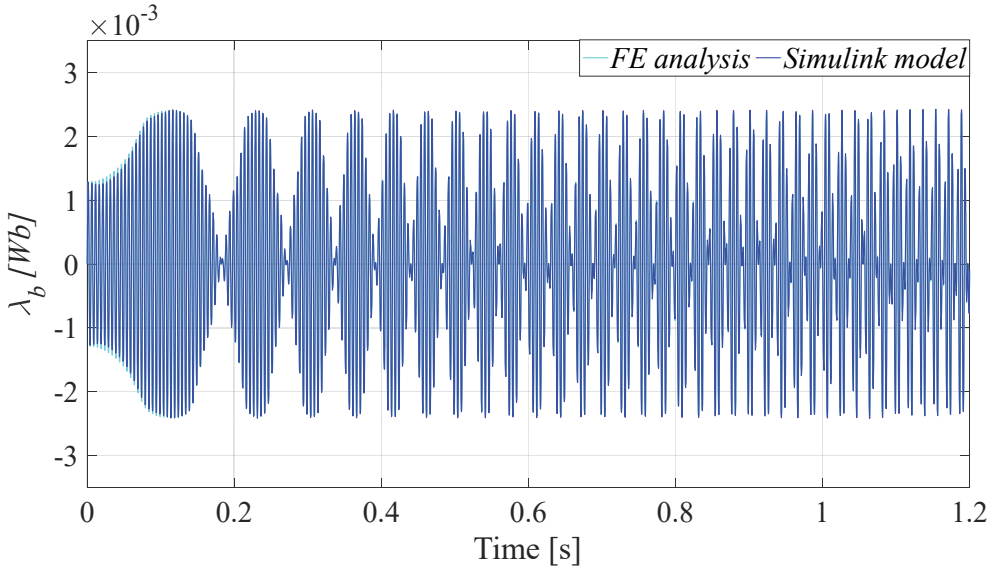

(b)

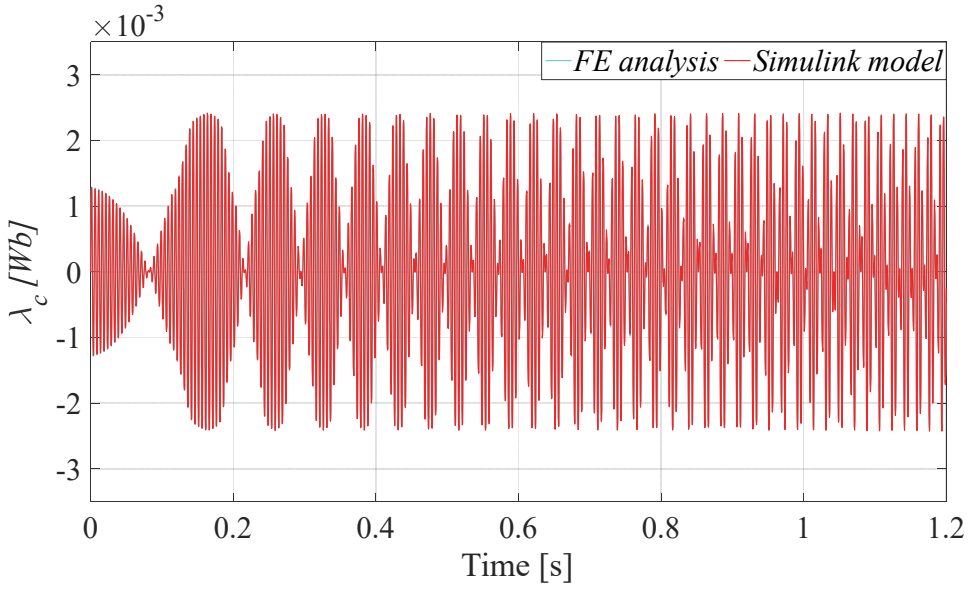

(c)

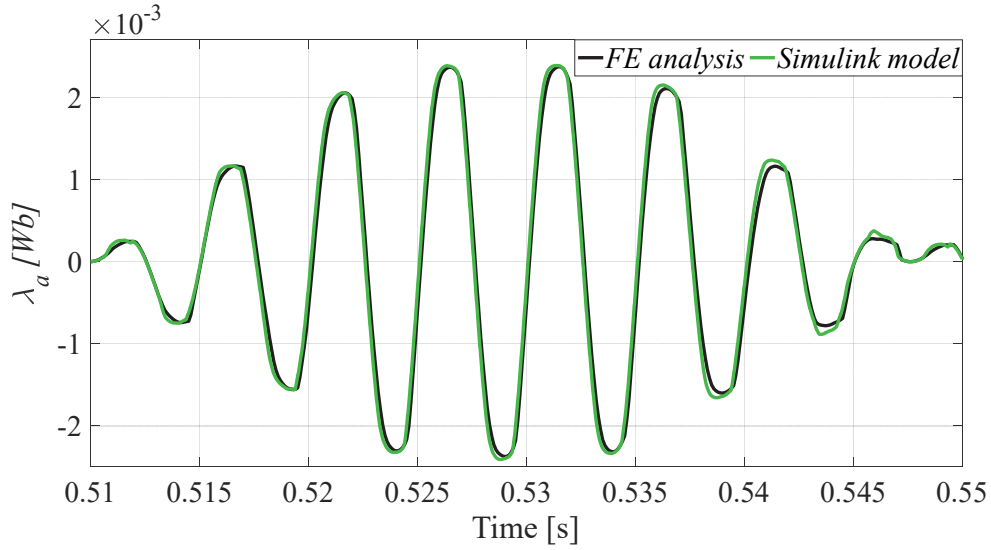

(d)

Figure. 4. 8. Armature fluxes obtained by the Simulink model and FE analysis. (a) Armature phase a linkage flux, λ_a (Wb), (b) Armature phase b linkage flux, λ_b (Wb), (c) Armature phase c linkage flux, λ_c (Wb), (d) Zoom of λ_a in time interval between 0.51 s to 0.55 s

4.5.2. Armature Induced Voltages

The induced voltages in armature windings from the FE simulation and the developed Simulink model are plotted in Fig. 4.9.a, 4.9.b, and 4.9.c. The magnified waveform of Fig. 4.9.a in the time interval between 0.51 to 0.55 s is shown in Fig. 4.9.d.

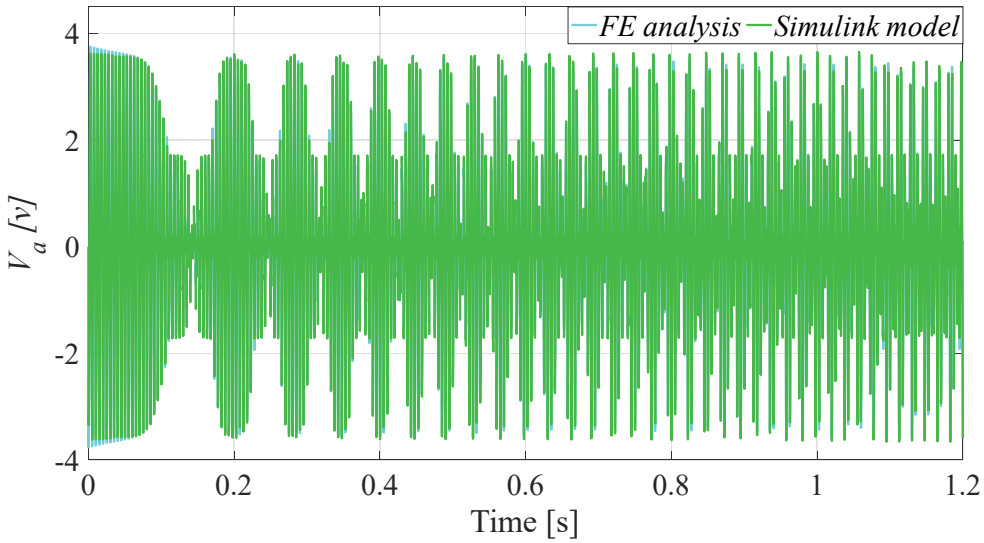
FE analysis
Simulink model
4
2
0
-2
-4
V_a [v]
0
0.2
0.4
0.6
0.8
1
1.2
Time [s]

(a)

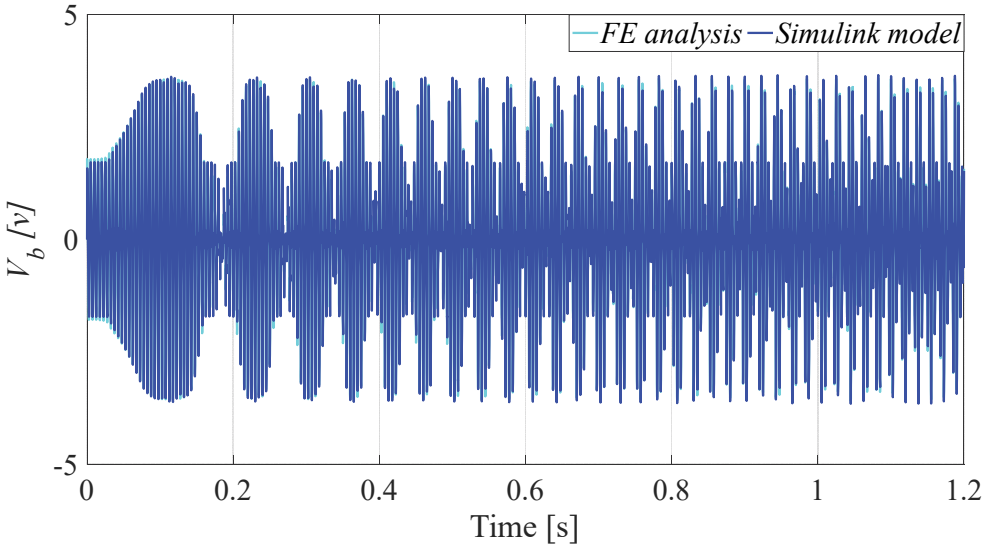
FE analysis
Simulink model
5
0
-5
V_b [v]
0
0.2
0.4
0.6
0.8
1
1.2
Time [s]

(b)

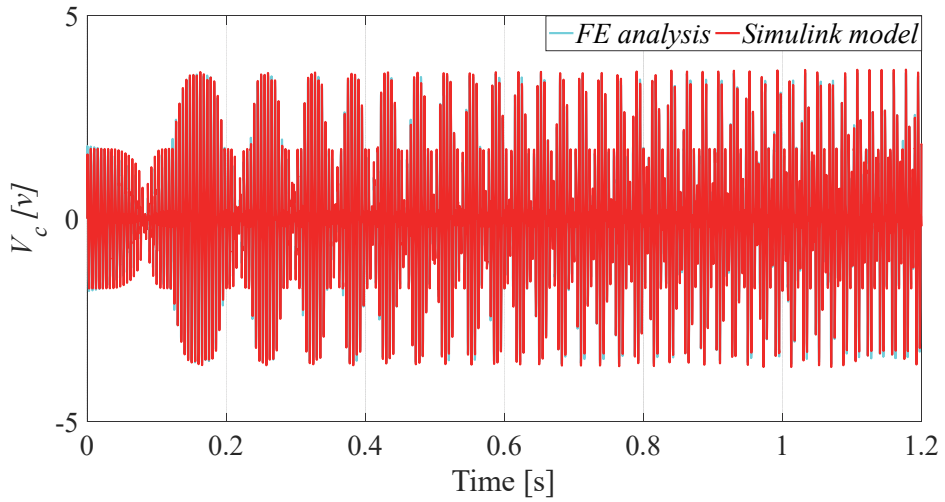

(c)

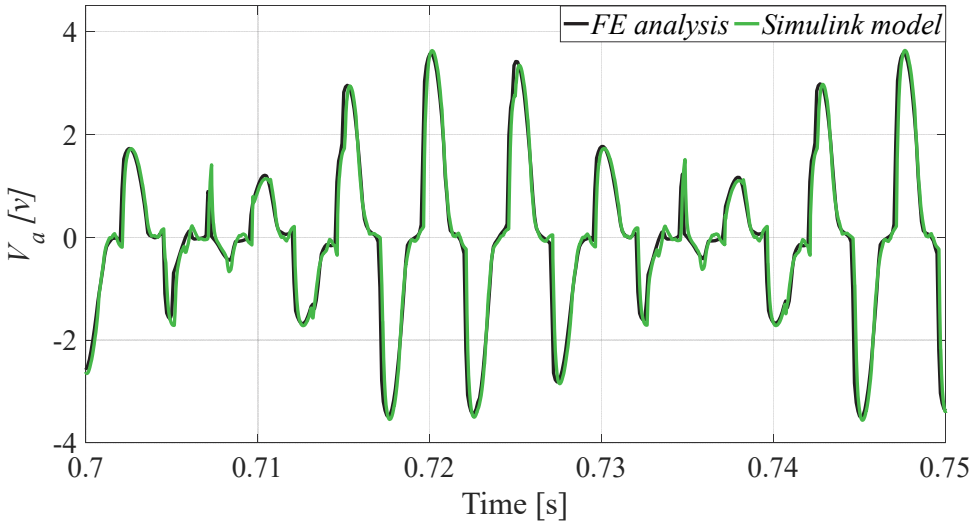

(d)

Figure. 4. 9. Armature voltages obtained by FE analysis and the developed Simulink model. (a) Armature phase a voltage V_a (V), (b) Armature phase b voltage V_b (V), (c) Armature phase c voltage, V_c (V), (d) Zoom of V_a in time interval between 0.51 s to 0.55 s

4.5.3. Rotating rectifier outputs

Fig. 4.10 shows the rotating rectifier output voltage and current. The magnifications of the waveforms in Fig. 4.10.b and Fig. 4.10.d show the accuracy of the developed phase variable Simulink model.

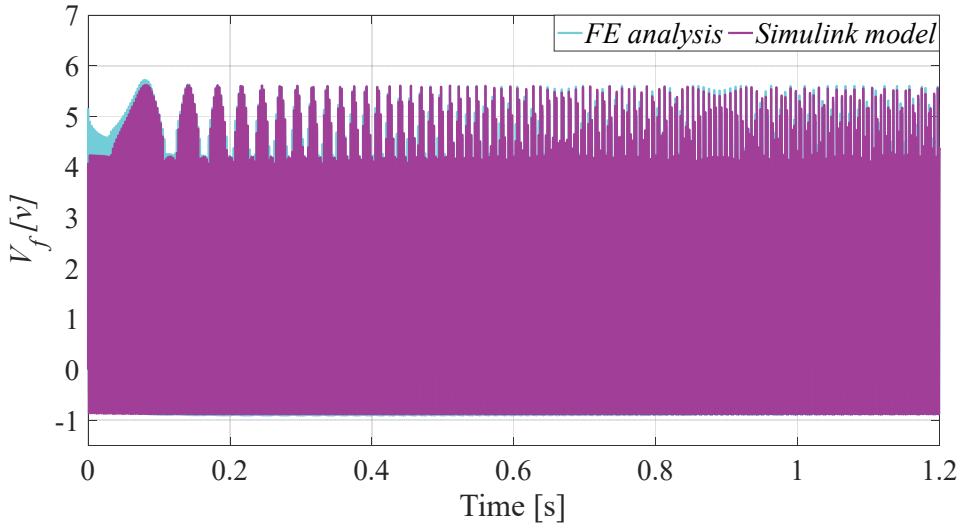
FE analysis
Simulink model
V_f [v]
Time [s]
7
6
5
4
3
2
1
0
-1
0
0.2
0.4
0.6
0.8
1
1.2

(a)

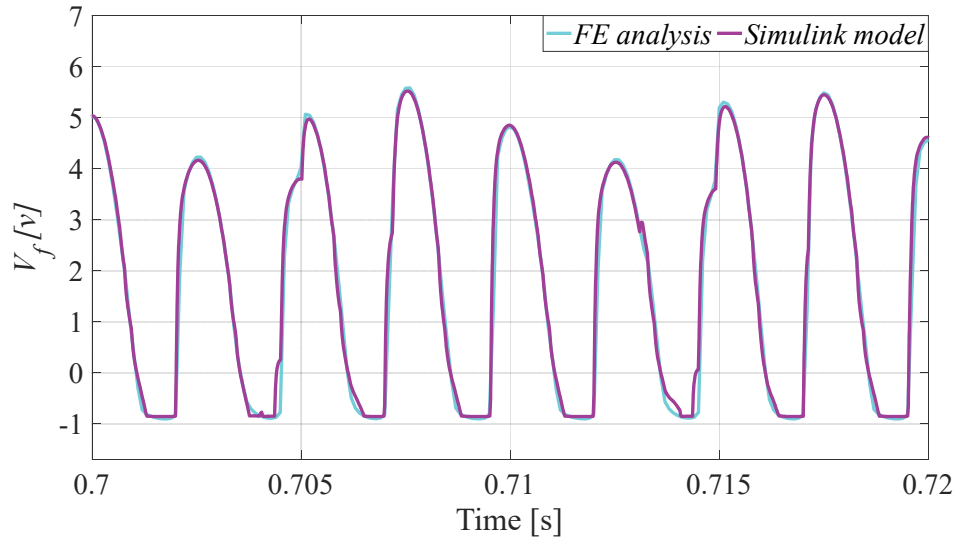
FE analysis
Simulink model
V_f [v]
Time [s]
7
6
5
4
3
2
1
0
-1
0.7
0.705
0.71
0.715
0.72

(b)

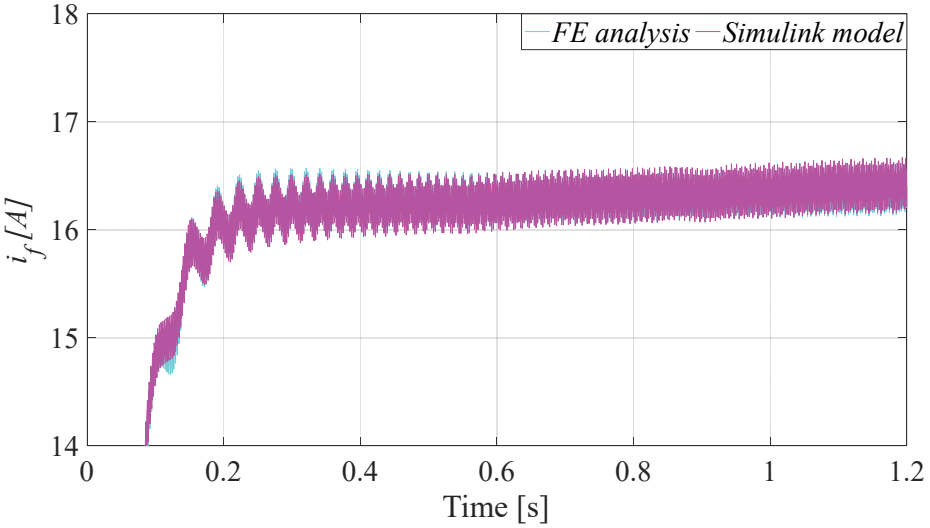

(c)

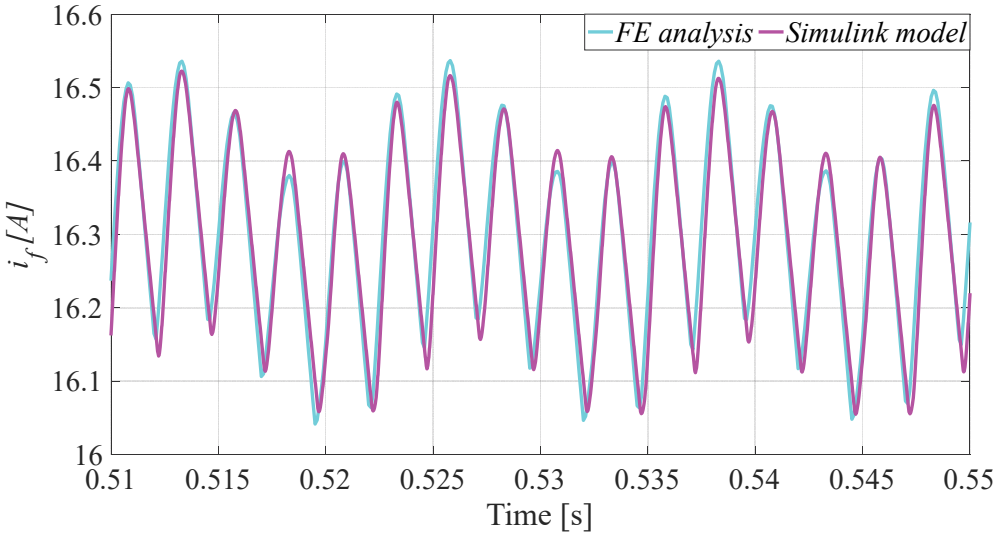

(d)

Figure. 4. 10. The rotating rectifier outputs. (a) Rotating rectifier output voltage obtained by FE analysis and the Simulink model (V_d). (b) Zoom of V_d in time interval between 0.51 s to 0.55 s. (c) Rotating rectifier output current (Field current of the main generator i_f). Zoom of i_f in time interval between 0.51 s to 0.55 s

4.6 Model of Three-stage Brushless Synchronous Machine Based on Fourier Series Inductance Mapping

In this section, magnetic characteristics of the machine are represented using Fourier Series method. In this modeling method, nonlinear relationships among flux linkages with windings' currents and rotor position are mapped by Fourier series approximation method [69]-[72].

Similar to the previous method based on lookup tables, the implemented model in this section takes care of magnetic non-linearities. The first step of Fourier series modeling is to decide which harmonic component of quantities are desired. Taking into account harmonics of inductances results in a more accurate model. Harmonics of inductances in excitation frequency (f_{exc}) frame are considered as follows:

4.6.1 Self-inductance of the field winding, L_{ff}:

In this case, 0^{th}, 1^{st}, and 2^{nd} harmonics are of more importance. In AC excitation modes where field current is AC, 1^{st} and 2^{nd} harmonics of L_{ff} represents saturation effect when field current changes from positive to negative values and when the amplitude of field current changes from zero to maximum and vice versa. Profile of L_{ff} is shown in Fig 4.11. Fig 4.12 shows L_{ff} and its 0^{th} harmonic versus the sum of its 0^{th}, and 1^{st}harmonics.

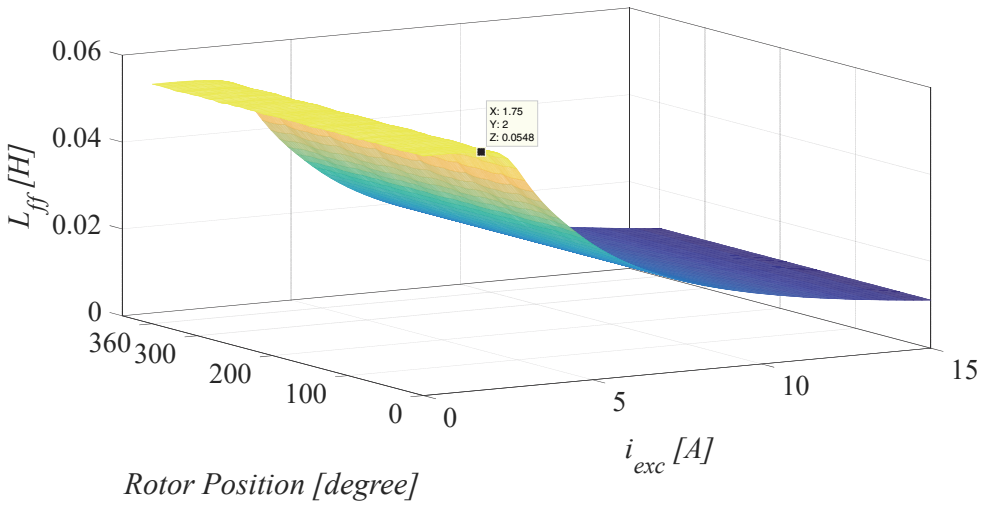

Figure. 4. 11. L_{ff} versus excitation current and rotor position

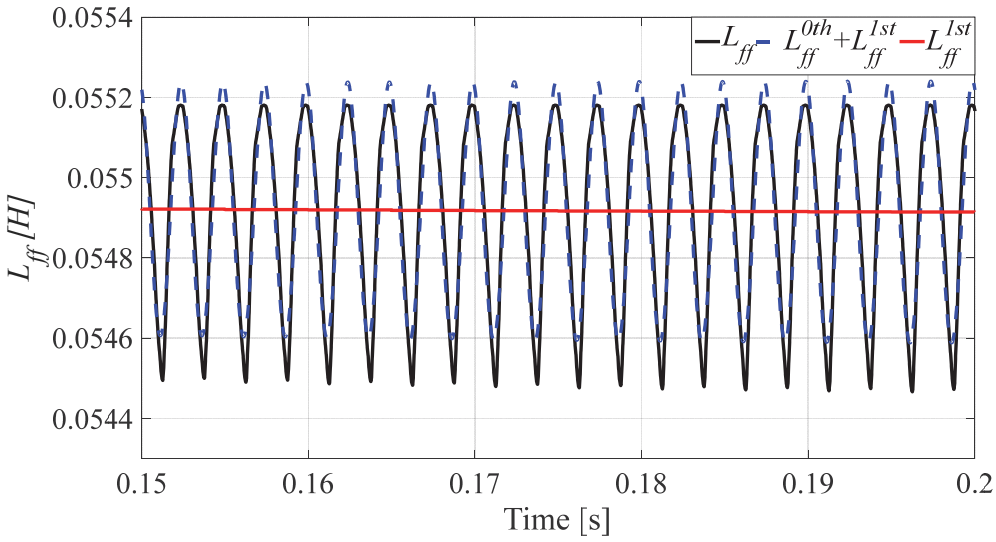

Figure. 4. 12. L_{ff} and its approximation bysum of its 0^{th} and 1^{st} harmonics

As can be seen in Fig 4.11. saturation effect for excitation currents higher than 2 A is significant. From harmonics analysis of FE analysis data, L_{ff} is maped using following functions:

$$L_{ff}(\theta) = 0.0919 - 1.4977 \times 10^{-4} \cdot \cos(0.6283 \cdot \theta) - 2.2573 \times 10^{-6} \cdot \sin(0.6283 \cdot \theta) - 9.1967 \times 10^{-5} \cdot \cos(2 \cdot 0.6283 \cdot \theta) + 1.4657 \times 10^{-5} \sin(2 \cdot 0.6283 \cdot \theta) + 1.2687 \times 10^{-4} \cdot \cos(3 \cdot 0.6283 \cdot \theta) + 2.8837 \times 10^{-7} \cdot \sin(3 \cdot 0.6283 \cdot \theta) \quad (4.11)$$

And nonlinear relationships of saturation effect is:

$$L_{ff}^{sat}(i_{exc}) = 0.9914 - 0.1381 \cdot \cos(3.491 \cdot i_{exc}) + 0.05104 \cdot \sin(3.491 \cdot |i_{exc}|) - 0.01942 \cdot \cos(2 \cdot 3.491 \cdot i_{exc}) - 0.03783 \cdot \sin(2 \cdot 3.491 \cdot |i_{exc}|) + 0.007984 \cdot \cos(3 \cdot 3.491 \cdot i_{exc}) - 0.0063 \cdot \sin(3 \cdot 3.491 \cdot |i_{exc}|) \quad (4.12)$$

Taking into account position dependencies (slot harmonics) and saturation effect, L_{ff} is represented as:

$$L_{ff}(\theta, i_{exc}) = L_{ff}(\theta) \cdot L_{ff}^{sat}(i_{exc}) \quad (4.13)$$

4.6.2 Mutual inductance between field and armature windings, M_{rs}:

As the most effective inductance in the model, for M_{rs} more harmonic components are considered. M_{rs} versus current and position is shown in Fig 4.13. For M_{rs}, 0^{th}, 1^{st}, 2^{nd}, 3^{rd}, 4^{th}, and 5^{th} harmonics are considered.

0^{th} harmonic represents the fixed value of the inductance. 1^{st} and 2^{nd} harmonics represent saturation effects. 3^{rd}, 4^{th}, and 5^{th} provide more details of slot harmonics effects. Fig 4.14 shows M_{rs} versus sum of its 0^{th}, 1^{st}, and 2^{nd} harmonics.

As can be seen in Fig 4.13, slot harmonics have a significant effect on the value of Mrs. The reason is that number of teeth in rotor and stator are not equal (number of rotor's teeth are more than stator's teeth) and interactions among them impose ripples on the value of M_{rs}.

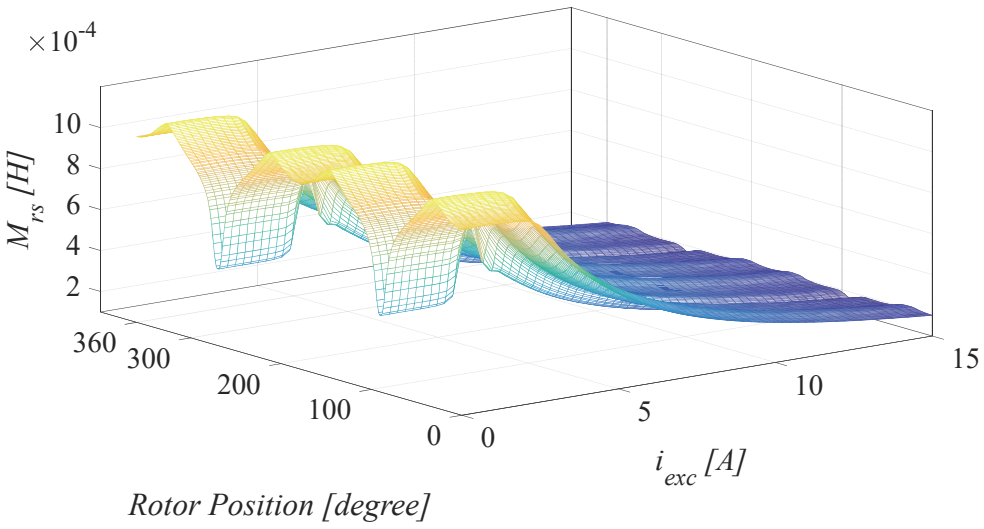

Figure. 4. 13. M_{rs} versus excitation current and rotor position

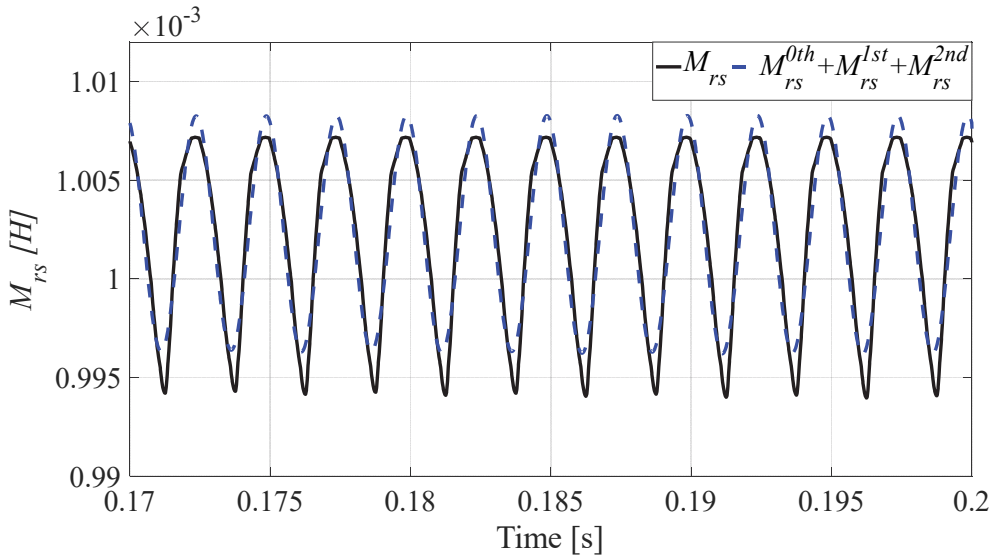

Figure. 4. 14. M_{rs} and its approximation bysum of its 0^{th}, 1^{st}, and 2^{nd} harmonics

M_{rs} can be approximated by following nonlinear functions:

$$M_{rs}(\theta) = 0.0033 \cdot \sin(0.1047 \cdot \theta + 2.618) + 1.7334 \times 10^{-4} \cdot \sin(0.5236 \cdot \theta - 2.617) - 4.4743 \times 10^{-5} \cdot \sin(0.3141 \cdot \theta - 1.57) + 3.8086 \times 10^{-5} \cdot \sin(1.151 \cdot \theta + 0.5657) + 1.5869 \times 10^{-5} \cdot \sin(0.7337 \cdot \theta - 0.54444) \quad (4.14)$$

$$M_{rs}^{sat}(i_{exc}) = 0.7505 + 0.2086 \cdot \cos(1.315 \cdot i_{exc}) + 0.2162 \cdot \sin(1.315 \cdot |i_{exc}|) + 0.06063 \cdot \cos(2 \cdot 1.315 \cdot i_{exc}) - 0.01894 \cdot \sin(2 \cdot 1.315 \cdot |i_{exc}|) + 0.0108 \cdot \cos(3 \cdot 1.315 \cdot i_{exc}) - 0.05655 \cdot \sin(3 \cdot 1.315 \cdot |i_{exc}|) - 0.01363 \cdot \cos(4 \cdot 1.315 \cdot i_{exc}) - 0.01949 \cdot \sin(4 \cdot 1.315 \cdot |i_{exc}|) - 0.01624 \cdot \cos(5 \cdot 1.315 \cdot i_{exc}) + 0.005754 \cdot \sin(5 \cdot 1.315 \cdot |i_{exc}|) \quad (4.15)$$

$$M_{rs}(\theta, i_{exc}) = M_{rs}(\theta) \cdot M_{rs}^{sat}(i_{exc}) \quad (4.16)$$

4.6.3 Self-inductance of armature windings, L_{rr}

Fig 4.15 shows profile of L_{rr}. As can be derived from Fig. 4.15, for L_{rr} saturation effect is not significant and position dependency is more considerable. Equations (4.17), (4.18), and (4.19) represent approximation of L_{rr}.

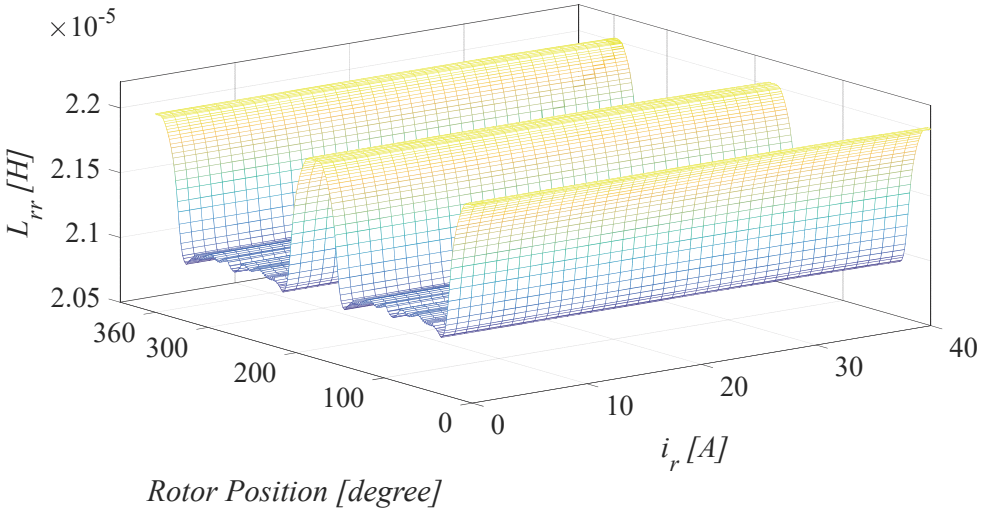

Figure. 4. 15. L_{rr} versus rotor current (i_r) and rotor position

$$L_{rr}(\theta) = 5.6219 \times 10^{-5} - 0.2356 \times 10^{-6} \cdot \cos(0.2094 \cdot \theta) - 0.4081 \times 10^{-6} \cdot \sin(0.2094 \cdot \theta) - 0.2452 \times 10^{-6} \cdot \cos(2 \cdot 0.2094 \cdot \theta) + 0.4247 \times 10^{-6} \sin(2 \cdot 0.2094 \cdot \theta) + 0.3986 \times 10^{-6} \cdot \cos(3 \cdot 0.2094 \cdot \theta) + 0.099 \times 10^{-9} \cdot \sin(3 \cdot 0.2094 \cdot \theta) \quad (4.17)$$

$$L_{rr}^{sat}(i_r) = 0.9997 + 0.0001055 \cdot \cos(0.9821 \cdot i_r) - 1.244 \times 10^{-5} \cdot \sin(0.9821 \cdot |i_r|) + 7.161 \times 10^{-5} \cdot \cos(2 \cdot 0.9821 \cdot i_r) - 5.178 \times 10^{-5} \cdot \sin(2 \cdot 0.9821 \cdot |i_r|) - 0.0002825 \cdot \cos(3 \cdot 0.9821 \cdot i_r) - 0.0002829 \cdot \sin(3 \cdot 0.9821 \cdot |i_r|) \quad (4.18)$$

$$L_{rr}(\theta, i_r) = L_{rr}(\theta) \cdot L_{rr}^{sat}(i_r) \quad (4.19)$$

4.6.4 Mutual inductance of armature windings, M_{rr}:

Mutual inductance of armature windings versus rotor current and rotor position is shown in Fig 4.16. Because of the small effect of saturation, in the approximation of M_{rr}, saturation effect is neglected. The nonlinear function which represents rotor position dependency of M_{rr} is:

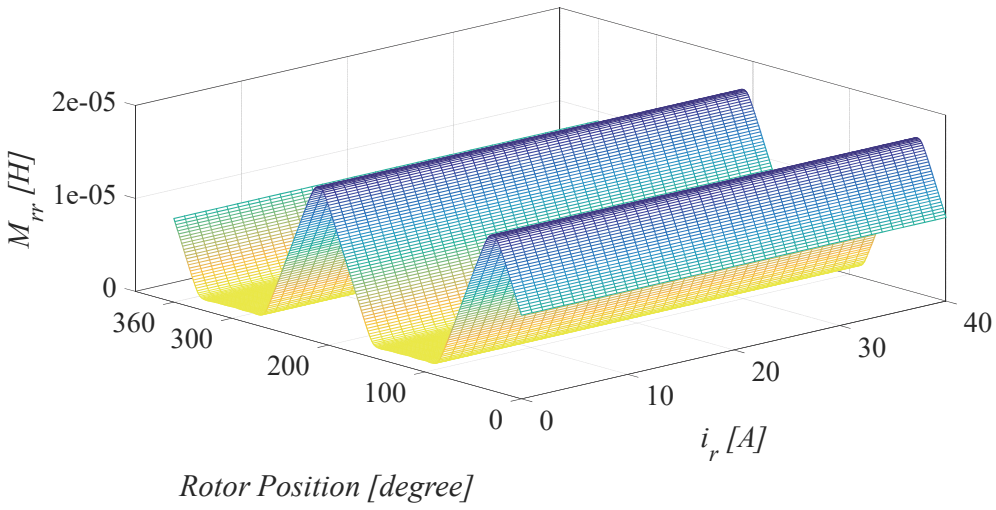

Figure. 4. 16. M_{rr} versus rotor current (i_r) and rotor position

$$M_{rr}(\theta) = 1.7684 \times 10^{-5} - 2.2048 \times 10^{-5} \cdot \cos(0.2094 \cdot \theta) + 0.1417 \times 10^{-7} \cdot \sin(0.2094 \cdot \theta) + 7.0935 \times 10^{-6} \cdot \cos(2 \cdot 0.2094 \cdot \theta) - 0.1642 \times 10^{-7} \sin(2 \cdot 0.2094 \cdot \theta) + 0.084 \times 10^{-6} \cdot \cos(3 \cdot 0.2094 \cdot \theta) + 0.2225 \times 10^{-8} \cdot \sin(3 \cdot 0.2094 \cdot \theta) \quad (4.20)$$

4.7 Simulation results of the model based on Fourier series approximation of inductances

Simulation results of the model based on Fourier series are shown in Fig 4.17 to 4.21. In this simulation, the excitation current is 1 A, 200 Hz and rotation speed is 1500 RPM. Armature phase voltages are shown in Fig 4.17. fig 4.18 shows armature currents. Output current and voltage of the rotating rectifier are shown in Fig 4.19, and 4.20, respectively.

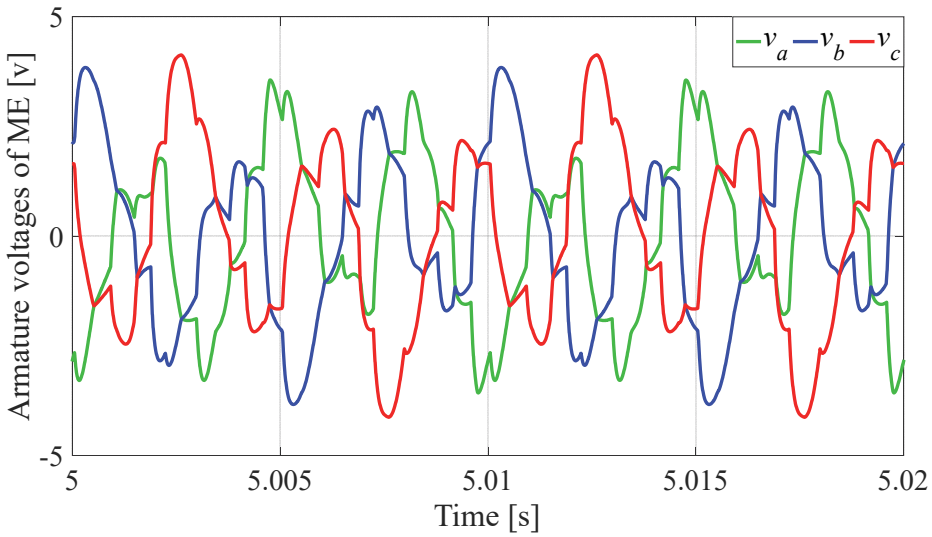

Figure. 4. 17. Armature phase voltages

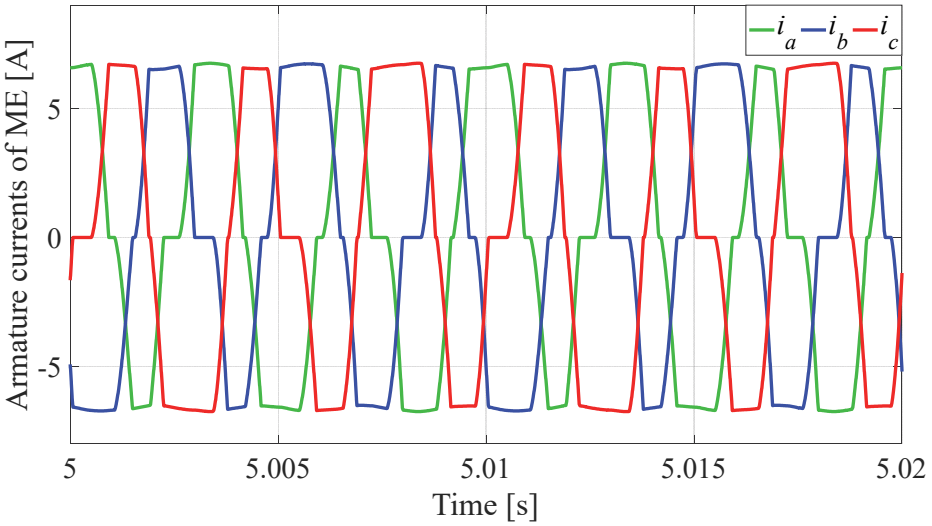

Figure. 4. 18. Armature currents

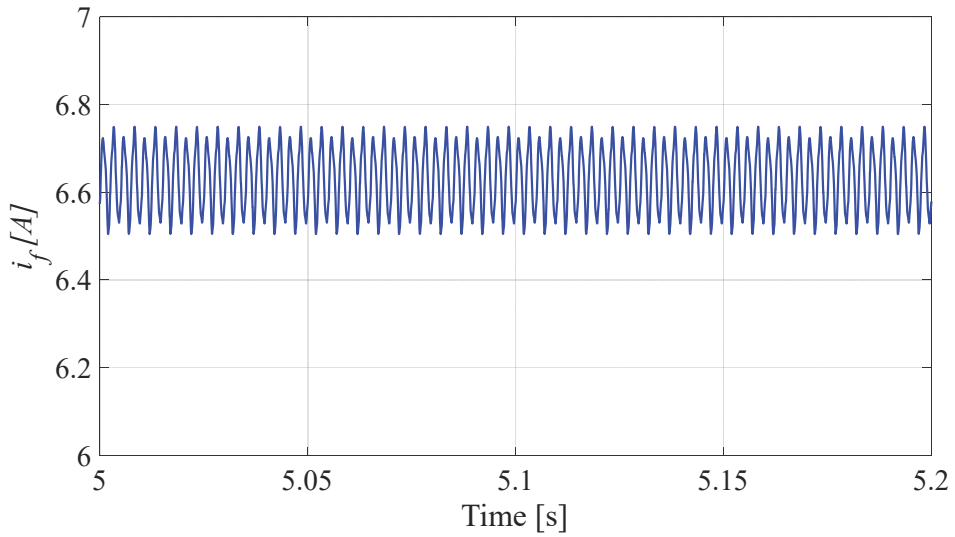

Figure. 4. 19. MG field current

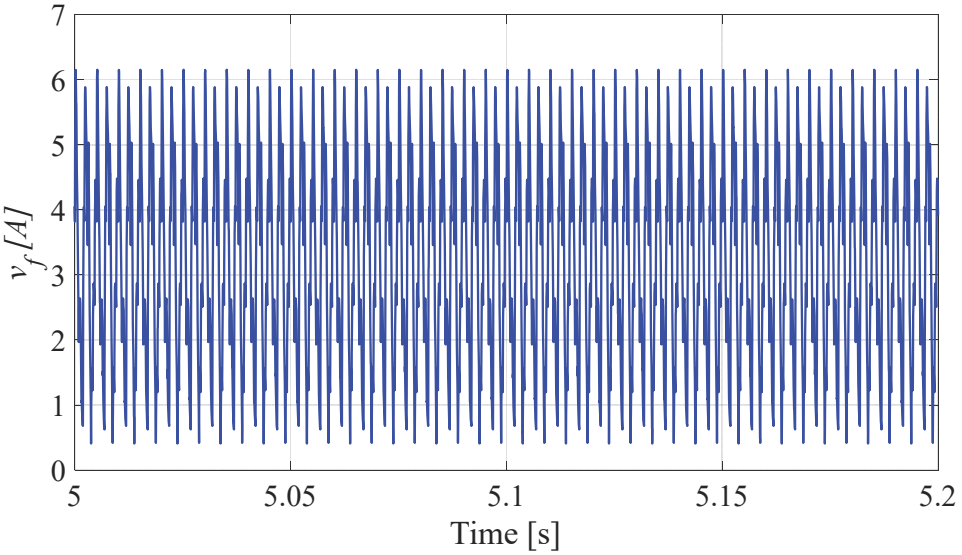

Figure. 4. 20. Output voltage of the rotating rectifier

Chapter 5

Experimental Magnetics Characteristics Identification of Three-Stage Brushless Synchronous Starter-Generator

5.1 Introduction

The main advantage of flux-adjustable machines over PM machines is their inherent ability of controllability of their field excitation flux. This potential capability provides more degree of freedom for drive control system and results in extension of constant power speed range employing field flux control rather than implementing flux weakening which is based on imposing negative *d*-axis current. Skipping need of flux weakening in high-speed operations brings about less copper and iron losses which improves the efficiency of the derive in high-speed operations [73]-[75].

In [76], excitation control of the wound rotor synchronous machine for traction application using slip rings is presented. The presented excitation current control is based on maximum torque per ampere technique. In [77], a field flux control method is presented which leads unity power factor operation at steady states. In addition, in the proposed discrete time field excitation control, field flux is changed with respect to torque command in order to improve dynamic response of the drive.

Considering efficiency of the drive as the main goal, maximum torque-speed curves of wound rotor synchronous machine and hybrid excitation synchronous machine are calculated and presented in [78], and [79], respectively. In these studies, iron and copper losses were not considered. Also, magnetic saturation effect was neglected.

However magnetic saturation effect in wound rotor synchronous machines is significant, and for accurate magnetic mapping of the machine must be taken into account.

Extracting magnetic characteristics of electric machines is of importance for design and control purposes [80]-[82]. Magnetic map of an electric machine describes relationships between windings' flux linkages and currents. The magnetic map provides important information for control purposes such as finding the optimal combination of field current and armature currents. Describing the importance of field excitation control in torque control of three-stage brushless synchronous starter-generator the main objective of this chapter.

Magnetic map of an electrical machine can be obtained using FE analysis [83]. Usually, this is done in the design stage of the machine and all details of the machine design, such as lamination, materials, and configuration of windings must be known. For a given built machine with unknown magnetic characteristics, experimental magnetic map identification must be performed [84]. However, post-design experimental extraction of the magnetic map can give valuable feedback to designers [85]. Experimental magnetic characteristics identification is divided into offline and online categories. In this chapter, an offline magnetic map extraction of the three-stage brushless synchronous machine is presented.

In [86]-[92], various experimental magnetic identification methods are presented. Advantages of obtaining an accurate magnetic map are as follows.

- From an accurate magnetic map, torque production capability of the machine can be estimated.
- Accurate Maximum Torque per Ampere (MTPA) curve can be calculated.
- Online torque estimation can be achieved.
- Accurate value of machine's inductances can be obtained which are of importance in the tuning of the current control system.

In this chapter, the goal of the experimental magnetic map identification procedure is to extract steady-state flux linkages of the machine. The extracted magnetic map represents flux linkages as a function of *d*- and *q*-axis currents while field excitation current is constant. Including magnetic maps in torque and speed control systems, the experimentally obtained magnetics maps are validated by several experimental tests.

5.2 Procedure of the Experimental Magnetic Map Identification

In *dq* coordinate, flux linkages as the function of *d*- and *q*-axis currents are:

$$\lambda_d = f(i_d, i_q) \tag{5.1}$$

$$\lambda_q = g(i_d, i_q) \tag{5.2}$$

With constant and maximum field current fed by the ME, and considering corresponding currents of all operating points of the machine, different combinations of *d*- and *q*-axis (i_d and i_q) current are applied to the stator windings of the MG. Applied i_d and i_q are changed from $i_{d,min}$ to $i_{d,max}$ and $i_{q,min}$ to $i_{q,max}$, respectively. Fig 5.1 shows mapped area of applied currents. Exact values of currents are interpolated from predefined equally spaced arrays of current values as:

$$i_{d,i} = i_{d,min} + i \cdot \Delta i_d\,, \qquad i = 1, 2, 3 \tag{5.3}$$

$$i_{q,j} = i_{q,min} + j \cdot \Delta i_q\,, \qquad j = 1, 2, 3 \tag{5.4}$$

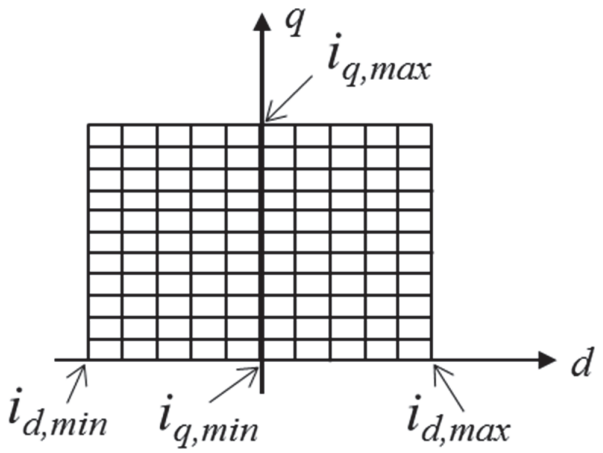

Figure. 5. 1. *d*- and *q*-axis current mesh

For a given combination of applied i_d and i_q and at constant rotation speed, steady-state voltage equations of the MG are:

$$v_{d,ij} = R_s \cdot i_{d,i} - \omega_e \cdot \lambda_{q,ij} \tag{5.5}$$

$$v_{q,ij} = R_s \cdot i_{q,j} + \omega_e \cdot \lambda_{d,ij} \tag{5.6}$$

where, R_s is stator resistance of MG. ω_e is electrical speed. $\lambda_{d,ij}$ and $\lambda_{q,ij}$ are flux linkages corresponding to the applied *d*- and *q*-axis currents, respectively.

In order to compensate resistance voltage drop in (5.5) and (5.6), the voltage vectors ($v_{d,ij}$ and $v_{q,ij}$) are first measured in motoring operation. In this case, current vector is $i_{d,i} + j \cdot i_{q,j}$. Then, generating operation is emulated by imposing a conjugate form of the vector current in motoring operation ($i_{d,i} - j \cdot i_{q,j}$). In generating operation, again voltage vector is measured. Then the average of voltage vectors in motoring and generating operations is calculated. As can be derived from (5.5) and (5.6), this average voltage is independent of stator resistance. The first and the second current vectors generate two flux linkage vectors which are conjugate of each other. So, resistive terms of the measured voltage vectors (equations (5.5) and (5.6)) in motoring and generating operation modes have positive and negative signs, respectively. Therefore, in the averaging process, these resistive terms are eliminated.

The experimental test is performed after heating up the machine to reach its thermal steady-state condition. However, during imposing current pulses, stator resistance may vary. This variation of the stator resistance prevents eliminating of the resistive terms in voltage averaging process. In order to compensate the variation of stator resistance due to temperature increase, another current pulse in motoring operation is applied to the stator windings. Since the duration of imposing current pulses even for all three operation modes, the average value of the resistances in the first and third intervals is equal to the stator resistance in the second interval. This is shown in Fig 5.2. The relationship among stator resistances in three intervals is as follows.

$$R_{s,ij,2} = \frac{R_{s,ij,1} + R_{s,ij,3}}{2} \tag{5.7}$$

where 1, 2, and 3 represent sequence number of test intervals.

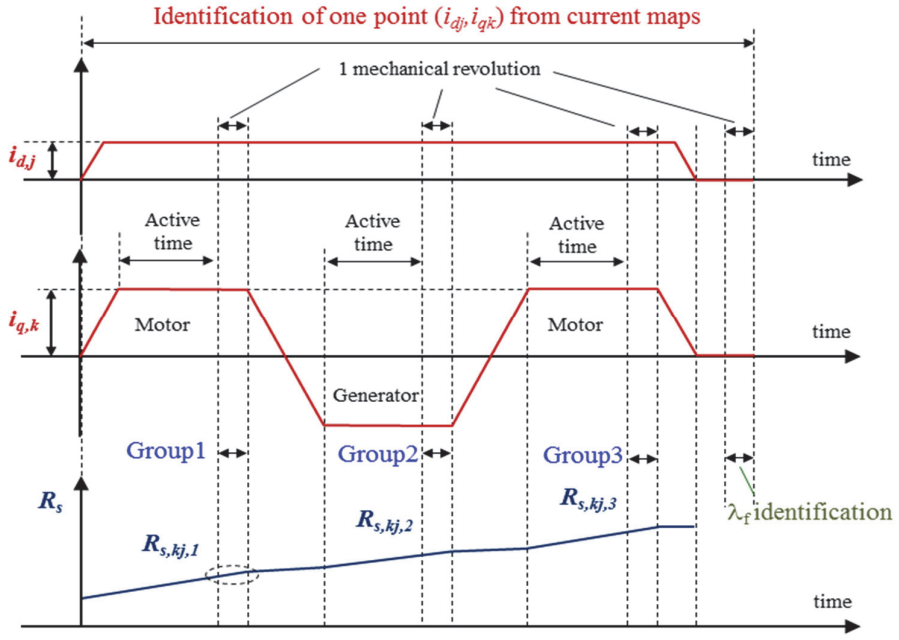

Figure. 5. 2. Sequence of imposed current pulses and variation of stator resistance due to temperature increase

At the end of each set of current pulse imposing, mean values of measured voltages, currents and rotation speed are calculated for one mechanical period as three groups. Corresponding equations of the three groups of quantities are as follows.

Group 1, first motoring operation:

$$v_{d,ij,1} = R_{s,ij,1} \cdot i_{d,i} - \omega_{e,1} \cdot \lambda_{q,ij,1} \tag{5.8}$$

$$v_{q,ij,1} = R_{s,ij,1} \cdot i_{q,j} + \omega_{e,1} \cdot \lambda_{d,ij,1} \tag{5.9}$$

Group 2, generating operation:

$$v_{d,ij,2} = R_{s,ij,2} \cdot i_{d,i} - \omega_{e,2} \cdot \lambda_{q,ij,2} \tag{5.10}$$

$$v_{q,ij,2} = -R_{s,ij,2} \cdot i_{q,j} + \omega_{e,2} \cdot \lambda_{d,ij,2} \tag{5.11}$$

Group 3, second motoring operation:

$$v_{d,ij,3} = R_{s,ij,3} \cdot i_{d,i} - \omega_{e,3} \cdot \lambda_{q,ij,3} \tag{5.12}$$

$$v_{q,ij,3} = R_{s,ij,3} \cdot i_{q,j} + \omega_{e,3} \cdot \lambda_{d,ij,3} \tag{5.13}$$

As mentioned before, to eliminate stator resistance variation due to the temperature rising, first, the averaging process applied for the first and the third test interval. Then, the average value of the resulted value and the quantities corresponding to the third test interval is calculated. Averaging equations of flux linkages are as follows.

$$\lambda_{d,ij} = \frac{1}{2} \cdot \frac{v_{q,ij,2} + \frac{v_{q,ij,1} + v_{q,ij,3}}{2}}{\omega_{mean,ij}} \tag{5.14}$$

$$\lambda_{q,ij} = -\frac{1}{2} \cdot \frac{\frac{v_{d,ij,1} + v_{d,ij,3}}{2} - v_{d,ij,2}}{\omega_{mean,ij}} \tag{5.15}$$

where, $\omega_{mean,ij}$ is mean value of rotation speed in three test intervals.

$$\omega_{mean,ij} = \frac{1}{3} \cdot \left(\omega_{e,1} + \omega_{e,2} + \omega_{e,3}\right) \tag{5.16}$$

5.3 Hardware implementation of magnetics map identification for three-stage brushless synchronous starter-generator

The described identification procedure has been implemented experimentally to identify magnetic characteristics of three-stage brushless synchronous starter-generator. The implemented experimental setup consists of a 25kvA three-stage brushless synchronous starter-generator, a permanent magnet servomotor employed as a prime mover, modular power converter to excite field winding of ME and stator windings of MG, and a battery emulator which supplies the modular converter. The experimental setup is shown in Fig 5.3. Schematic of the test rig is shown in Fig 5.4 which presents more details of the experimental test rig. Characteristics of the starter-generator are presented in Table 5.1.

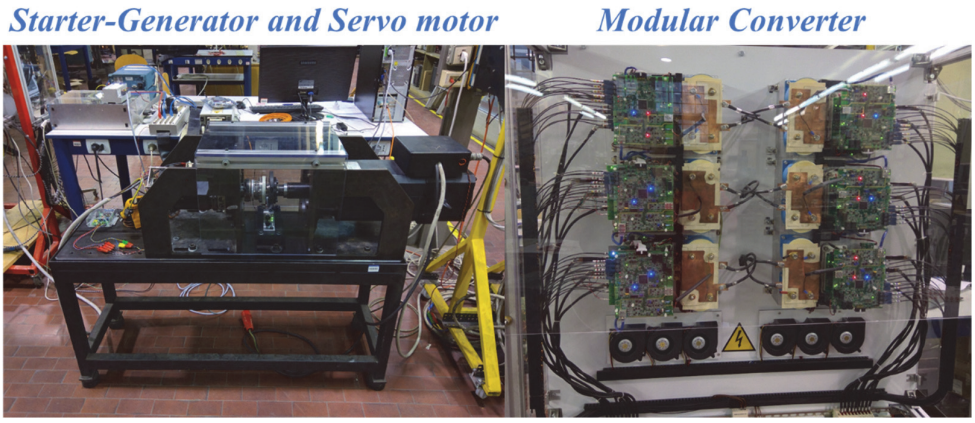

Figure. 5. 3. Experimental setup

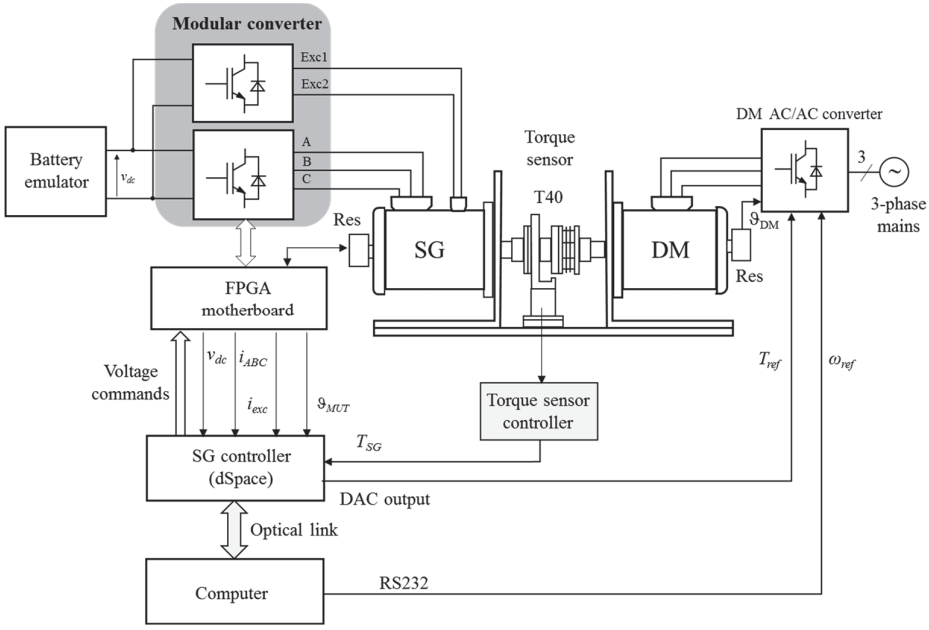

Figure. 5. 4. Schematic diagram of the experimental setup

Table. 5. 1. Parameters of the tested starter-generator

	value	Unit
Rated phase (rms) voltage at 12000 RPM	115	V
Rated excitation current (dc)	0.5	A
Rated current (rms)	72	A
Pole-pairs	2	—

The used torque sensor is a T40 sensor from HBM Gmbh which is shown in Fig 5.5. Rated torque of the torque sensor is 100 Nm.

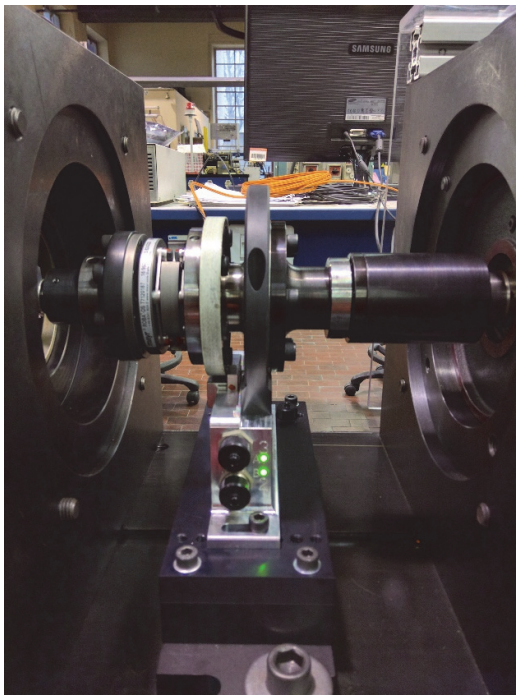

Figure. 5. 5. Torque sensor

Switching frequency of the modular converter is 8 kHz and peak value of phase currents is limited at 50 A. The battery emulator is a 50-kw dc source which supplies the modular converter via 270 Vdc DC-link (Fig 5.6).

Figure. 5. 6. Battery emulator

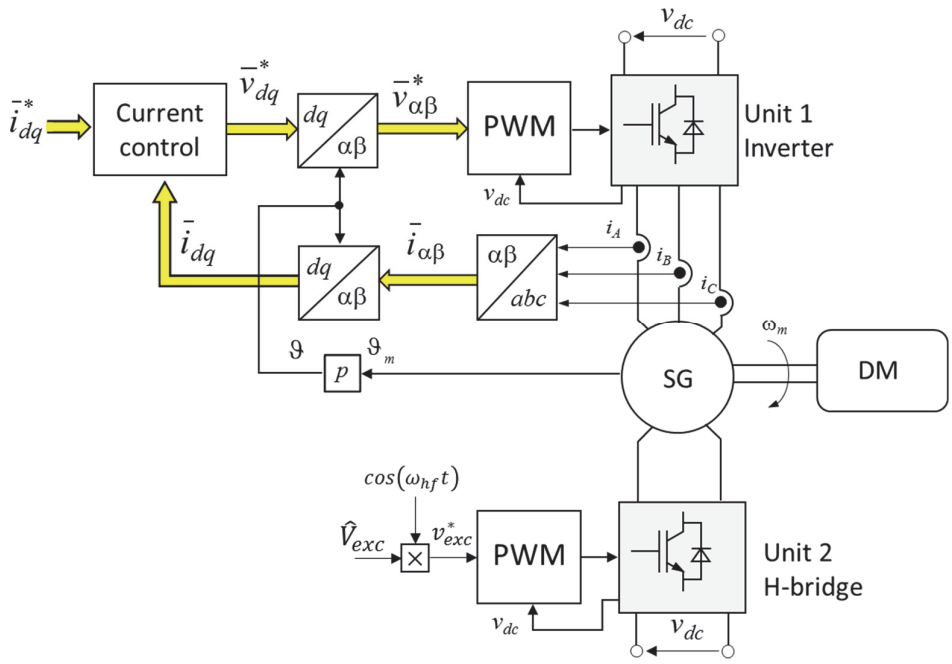

Figure. 5. 7. Implemented current control system

Implemented current control scheme is shown in Fig 5.7. Excitation field winding of ME is fed at 400 Hz with a peak reference voltage of 350V.

In the experimental test, the active time duration for getting the steady-state operation at the constant speed after a current variation is set at 1s. The identification procedure uses a motoring-generating-motoring operation sequence by inverting the sign of the q-axis current, while the d-axis current is constant. As mentioned before, this sequence eliminates the influence of the stator resistance in the back-emf voltage calculation.

Experimental magnetic mapping has been performed at constant speed (200 RPM) with 350 vdc excitation voltage of ME. Limits of imposed m×n current mesh are as follows:

$i_{q,min}$=0 and $i_{q,max}$=50A, n = 11

$i_{d,min}$=-20A and $i_{d,max}$=20A, m = 11

Fig 5.8 shows an interval of the magnetic mapping procedure where i_d is 20A and i_q is 50 A.

As mentioned before, the implemented experimental procedure uses 11×11 current mesh as reference currents for the current control system. Therefore, two 11×11 flux maps are obtained for λ_d and λ_q. Also, for each operation point, measured torque has been stored as another (11 × 11) map. At the end of the experimental test, the d-axis current vector, the q-axis current vector, the flux maps (d- and q-axis fluxes) and the torque map have been processed off-line in Matlab.

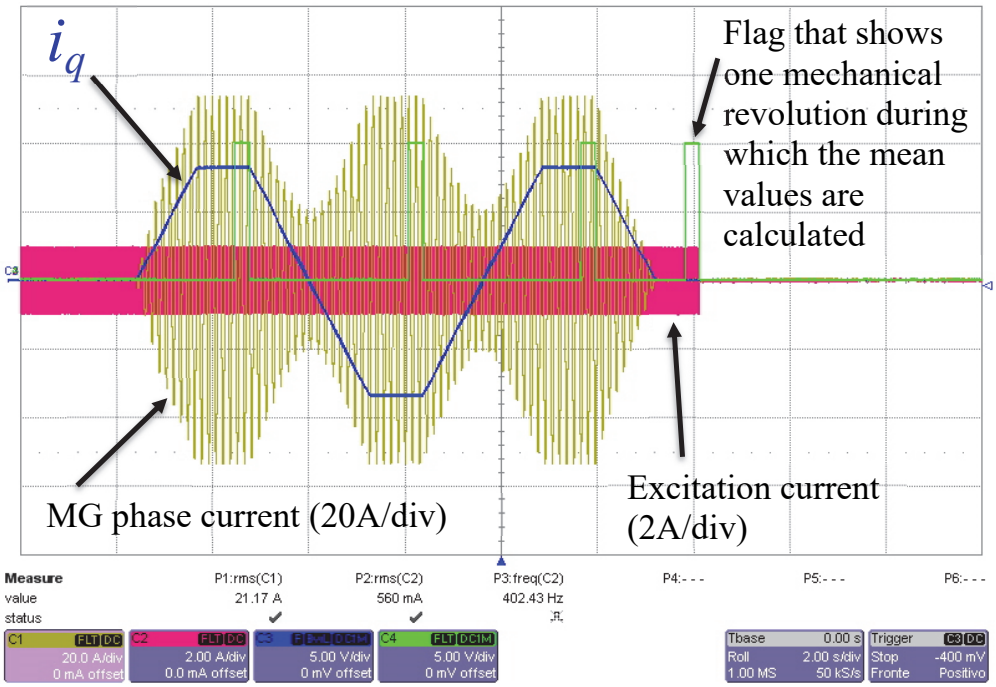

Figure. 5. 8. One interval of the magnetics mapping procedure, i_d = 20 A and i_q = 50 A

5.3.1 Experimental magnetics identification results

In this section, results of the experimental magnetic characteristics identification procedure are presented. The main aim of the identification procedure is to map *d*- and *q*-axis fluxes with respect to various combinations of *d*- and *q*-axis currents. However, using obtained data during the experimental identification procedure, MTPA profile and *dq* inductance profiles have been identified.

5.3.1.1. d- and q-axis fluxes mapping

Fig 5.9 shows *d*-axis flux versus *d*-axis current with different values of *q*-axis current. As can be seen, the influence of the *q*-axis current due to the armature reaction (cross-saturation) is significant. At no-load *d*-axis flux is 80.74 mVs and when i_q is 50A, *d*-axis flux is 63.49 mVs.

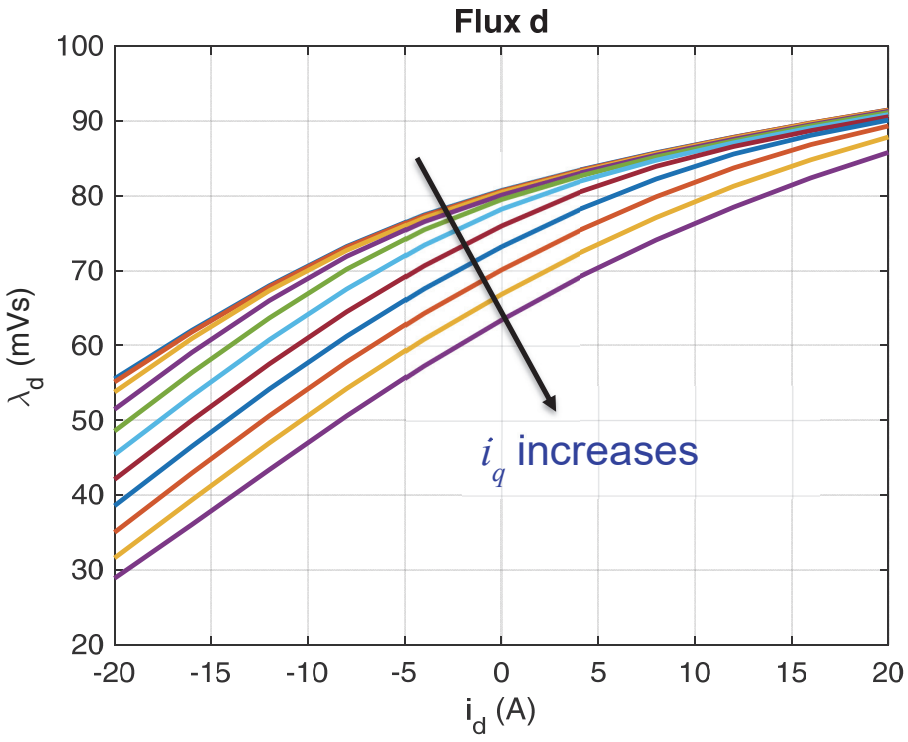

Figure. 5. 9. *d*-axis flux versus *d*-axis current at different values of *q*-axis current

q-axis flux as the function of *d*- and *q*-axis currents is shown in Fig 5.10. Like *q*-axis flux, *d*-axis flux significantly influenced by cross-saturation effect.

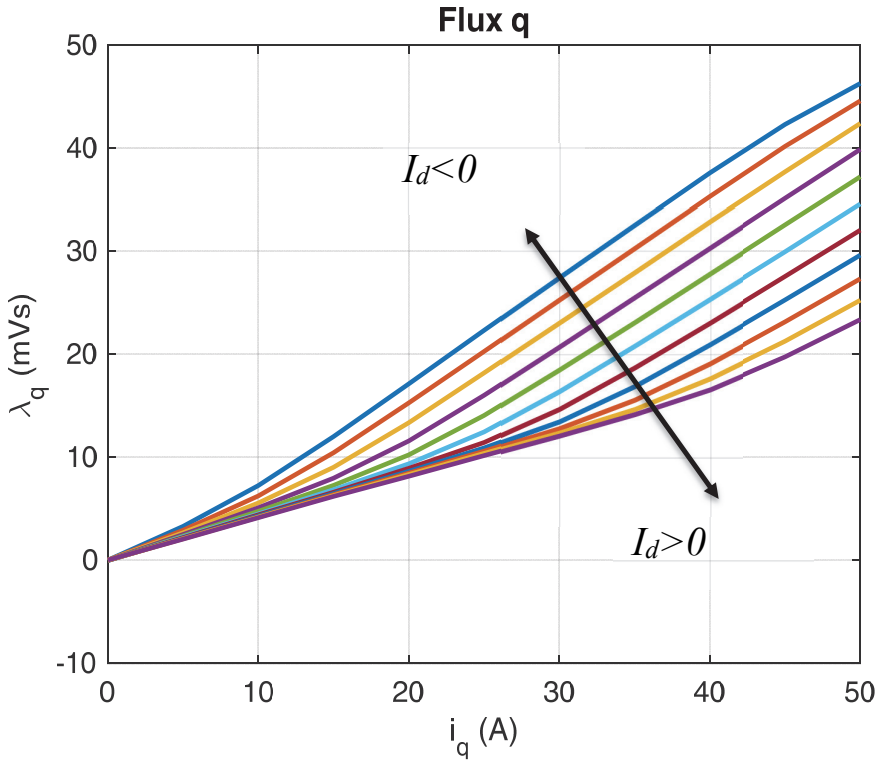

Figure. 5. 10. *q*-axis flux versus *q*-axis current at different values of *d*-axis current

5.3.1.2 Extracting Maximum Torque per Ampere (MTPA) profile using measured torque data

Using obtained *d*- and *q*-axis flux maps, steady-state performance of the machine can be evaluated. Torque equation in *dq* reference frame is:

$$T = \frac{3}{2} \cdot p \cdot \left(\lambda_d \cdot i_q - \lambda_q \cdot i_d\right) \tag{5.17}$$

Since d- and q-axis fluxes are known, for a given current vector, voltage vector and generated torque can be calculated from (5.5)-(5.6), and (5.17), respectively. From these data, MTPA profile of the machine is calculated an shown in Fig 5.11.

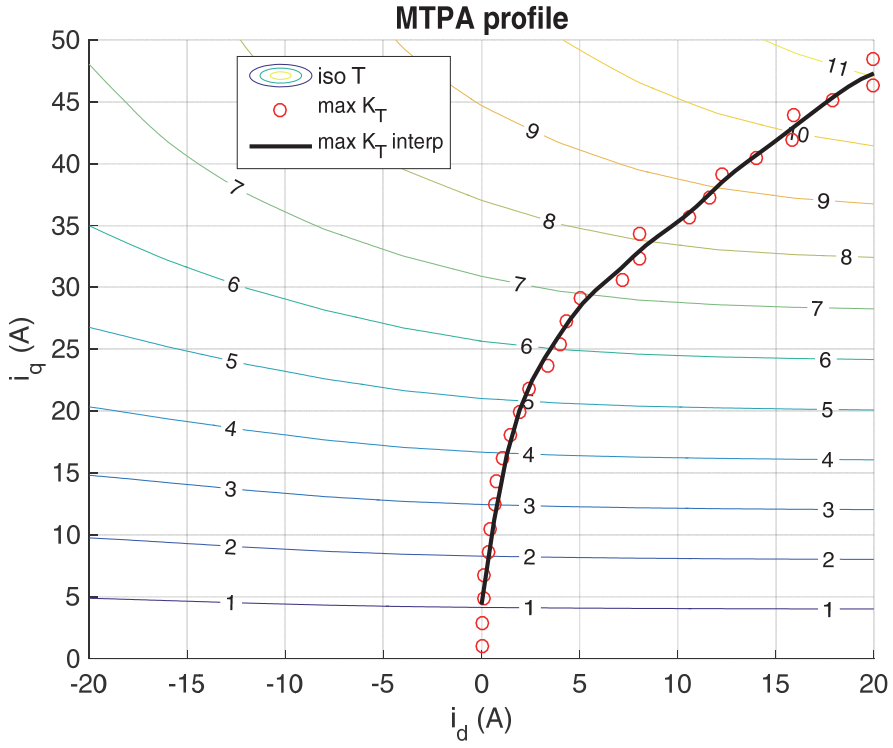

Figure. 5. 11. MTPA profile using experimental data

Another representation of MTPA profile which is the optimum combination of i_d and i_q versus torque is shown in Fig 5.12. As can be seen in Fig 5.11 and Fig 5.12, for the given field current, maximum torque can be achieved when i_d is positive. Optimum combinations of i_d and i_q are stored as a 32 points look-up tables. The input of the look-up tables is the reference torque and their outputs are i_d and i_q.

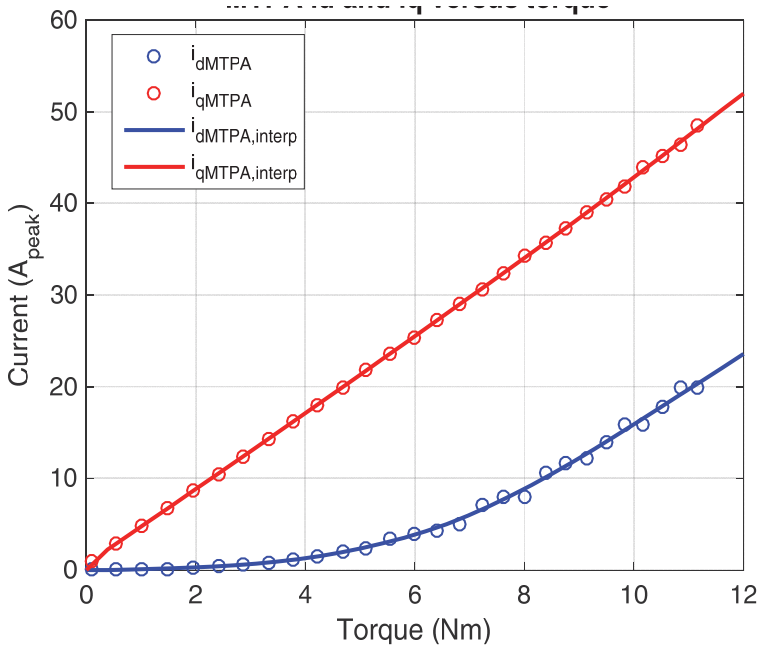

Figure. 5. 12. Optimum combination of id and iq versus required torque

Since during the identification procedure, torque was measured and captured, MTPA can be estimated from the measured data. Fig 5.13 shows MTPA profiles obtained by calculating the torque using (5.17) and measured values of torque. In Fig 5.13, the curve indicated by the dashed line is MTPA profile obtained from the measured torque data and the curve indicated by solid line is MTPA profile obtained from calculated torque.

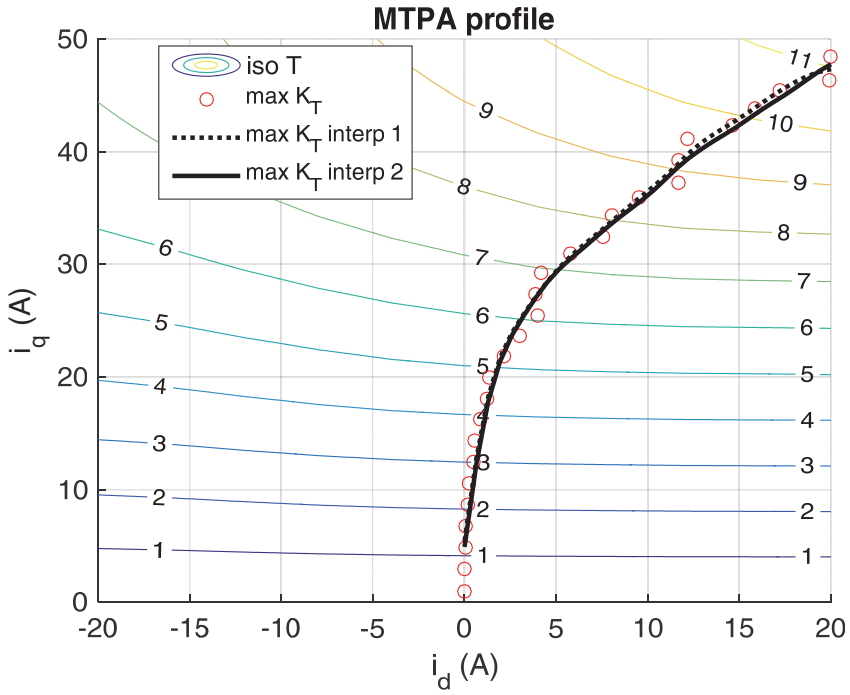

Figure. 5. 13. Comparison of the MTPA profile obtained from measured torque data and the MTPA profile obtained from calculated torque

5.3.1.3 d- and q-axis Inductances mapping

Using flux data, *d*- and *q*-axis inductances have been mapped. These inductance trajectories can be used for tuning current control system. Knowledge of inductances leads to avoiding current control issues due to inductance variations according to the operation point in the (*d*,*q*) currents plane. *d*- and *q*-axis inductances versus *d*- and *q*-axis currents are shown in Fig 5.14 and Fig 5.15, respectively.

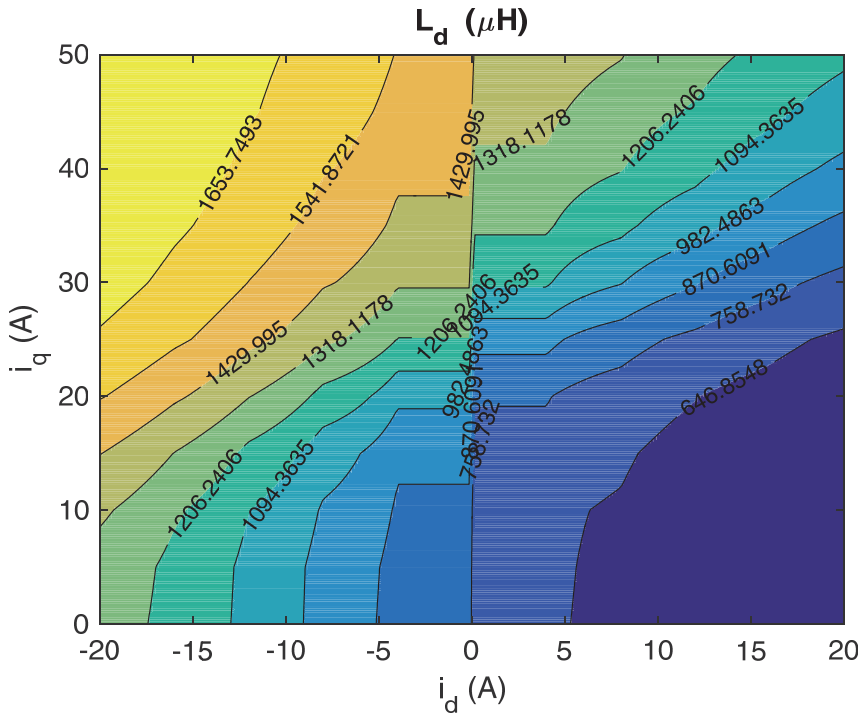

Figure. 5. 14. *d*-axis inductance versus i_d and i_q

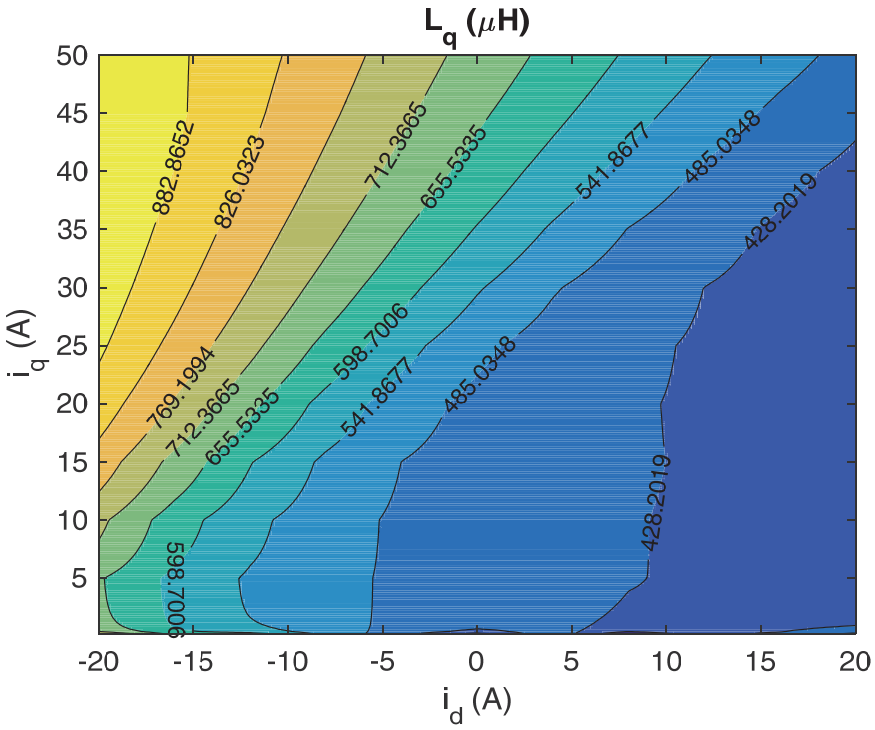

Figure. 5. 15. *q*-axis inductance versus i_d and i_q

5.4 Experimental verification of magnetics maps

In this section, torque control and speed control are implemented on the under-test machine. Both control schemes use experimentally obtained magnetics maps. MTPA profile is used in order to determine the optimum combination of *d*- and *q*-axis currents based on required torque. Inductance profiles are used for tuning current controllers.

5.4.1 Torque control

Schematics of the implemented torque control scheme is shown in Fig 5.16. Reference torque is the input of the MTPA profile. MTPA profile determines the optimum combinations of *d*- and *q*-axis currents which are references of the current control loop. Rotor position estimation is performed using position information obtained from a resolver which has been installed into the starter-generator machine. These data are converted from analog to digital using a resolver to digital converter. Three torque control tests have been implemented. The first test was performed at constant reference torque while reference speed of the prime mover has fast acceleration (test. 1). In the second test, imposed speed by the prime mover is constant and the reference torque has fast transitions (test. 2). The third test investigates the performance of the machine in steady-state (test. 3).

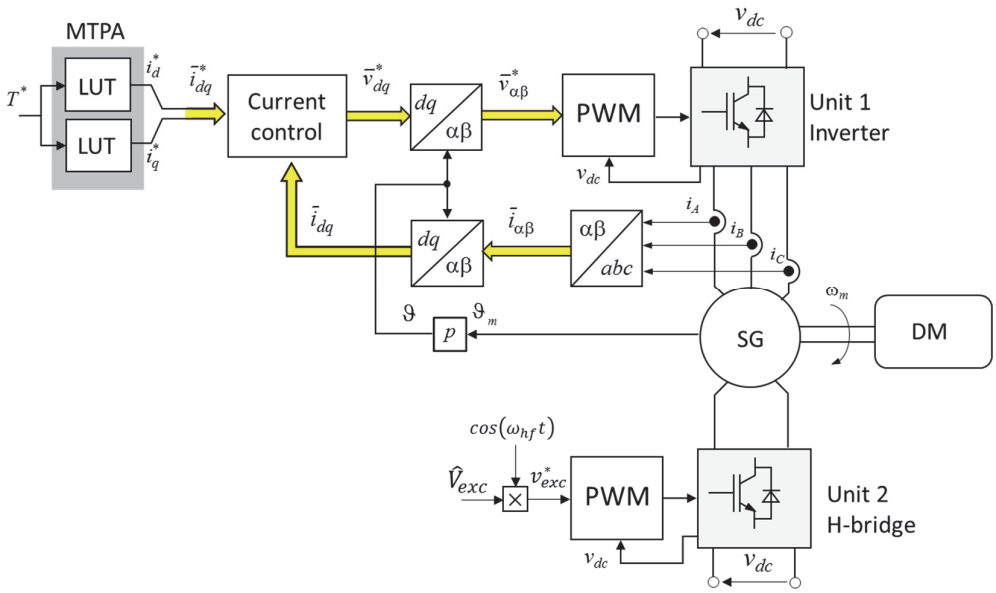

Figure. 5. 16. Diagram of the implemented torque control scheme

5.4.1.1 Torque control test. 1: Fast acceleration from standstill with a reference torque value of 11Nm

Fig 5.17.a shows reference waveform of the imposed speed by the prime mover (PM servomotor). Reference torque has been set at 11 Nm. Fig 5.17.b shows the reference torque, measured torque and filtered measured torque waveforms.

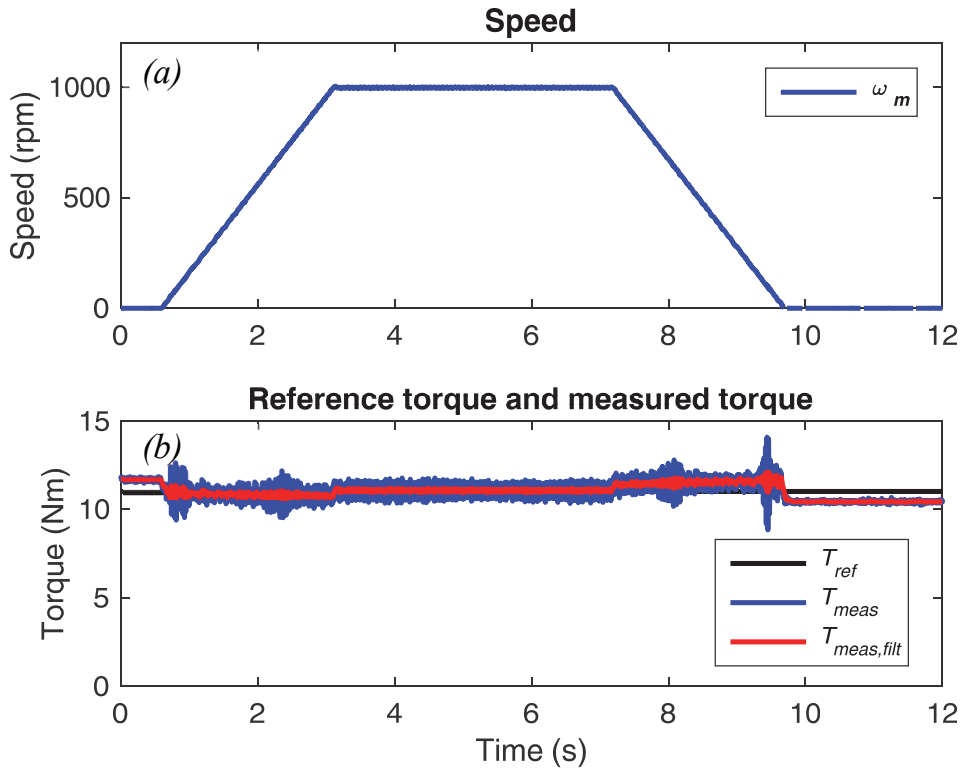

Figure. 5. 17. Reference and measured waveforms of torque control test.1. (a) Reference speed. (b) Reference torque, measured torque and filtered measured torque waveforms

D- and *q*-axis currents are shown in Fig 5.18.a. Current of MG stator phase *a* is shown in Fig 5.18.b. As can be derived from the results, using MTPA, correct combination of *d*- and *q*-axis currents have been determined and the machine was capable to generate the required torque.

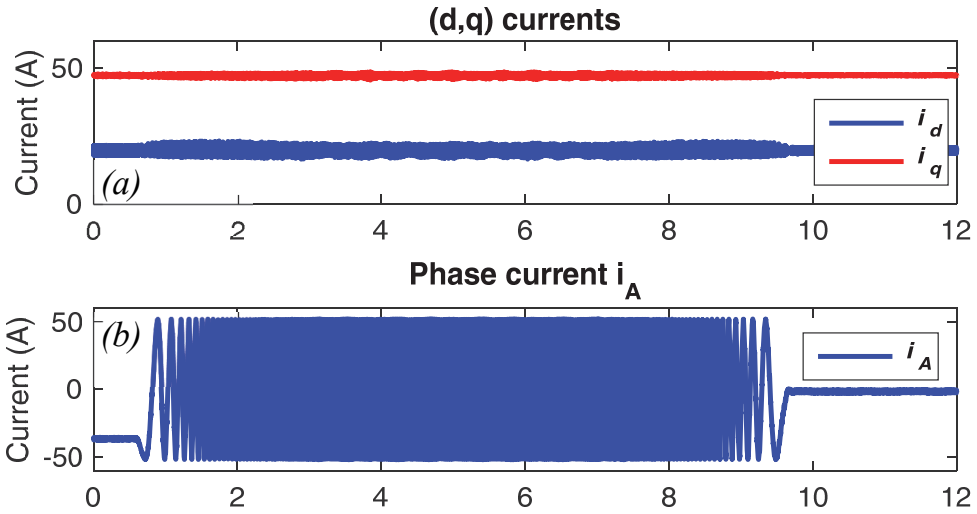

Figure. 5. 18. Measured current waveforms in the torque control test. 1. (a) *d*- and *q*-axis currents. (b) Current of MG stator phase *a*

5.4.1.2 Torque control test. 2: Fast torque transients at constant speed of 1000 rpm

In this test, the imposed speed by the prime mover has been set at 1000 RPM. The waveform of the speed is shown in Fig 5.19.a. Reference torque and generated torque waveforms are shown in Fig 5.19.b. This test also proves good performance of the torque control tuned based on the magnetic maps. Reference and measured current waveforms are shown in Fig 5.20.

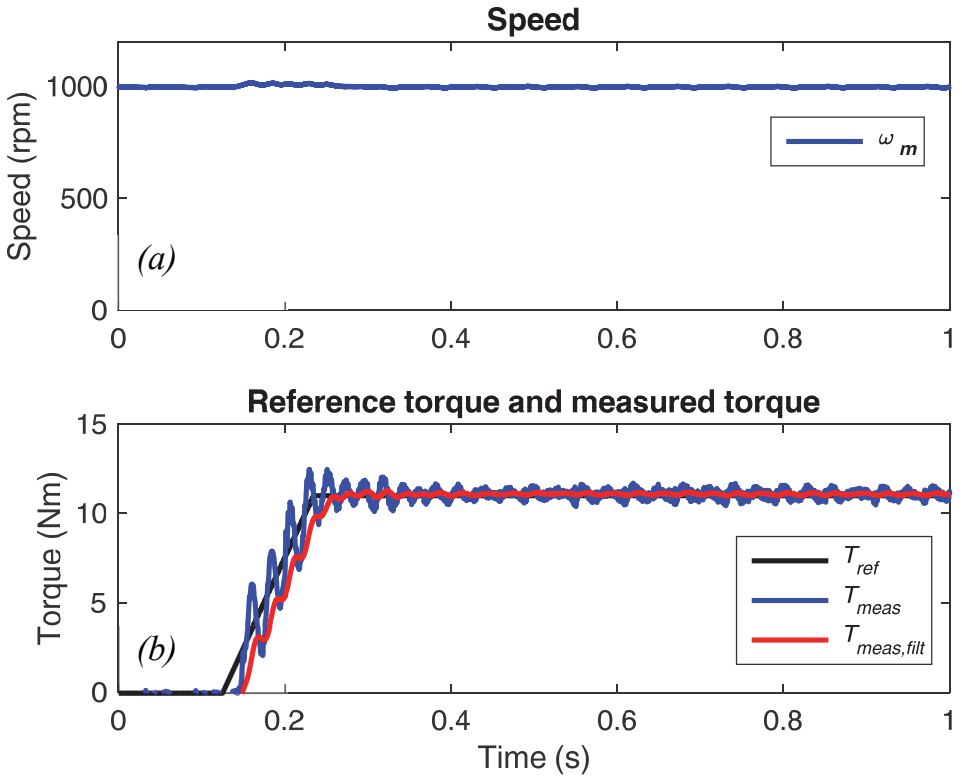

Figure. 5. 19. Results of torque control test. 2. (a) Reference speed imposed by the prime mover. (b) Reference torque and generated torque waveforms

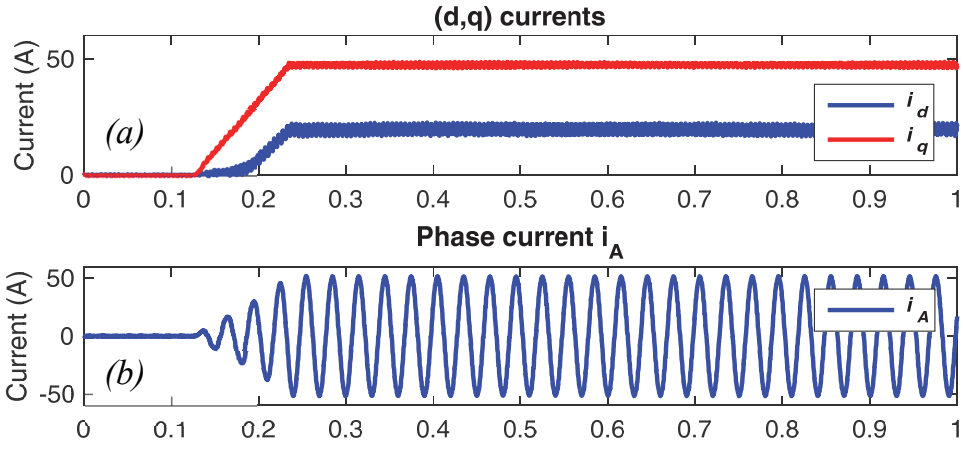

Figure. 5. 20. Measured current waveforms of torque control test.2. (a) *d*- and *q*-axis currents. (b) MG stator phase *a* current

5.4.1.3 Torque control test .3: Steady-state operation at 1000 rpm with 11 Nm

In this test, the performance of the implemented drive at constant speed and constant torque under torque control has been investigated. Waveforms of measured currents are shown in Fig 5.22.

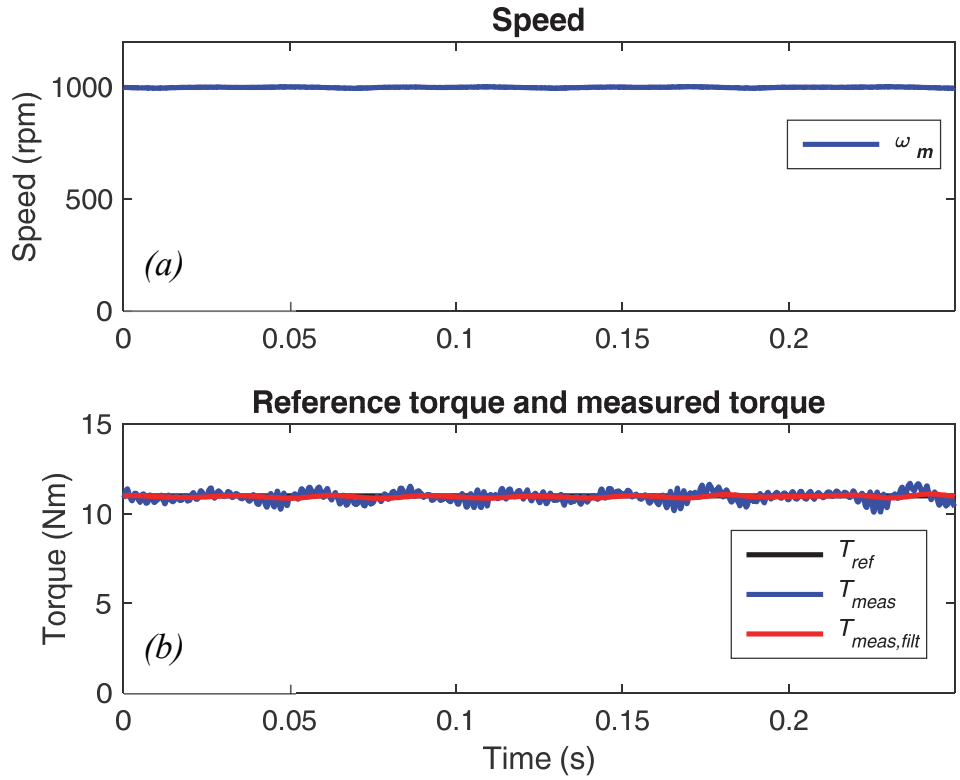

Figure. 5. 21. Speed and torque waveforms of torque control test .3. (a) Imposed speed by the prime mover. (b) Reference torque and measured generated torque waveforms

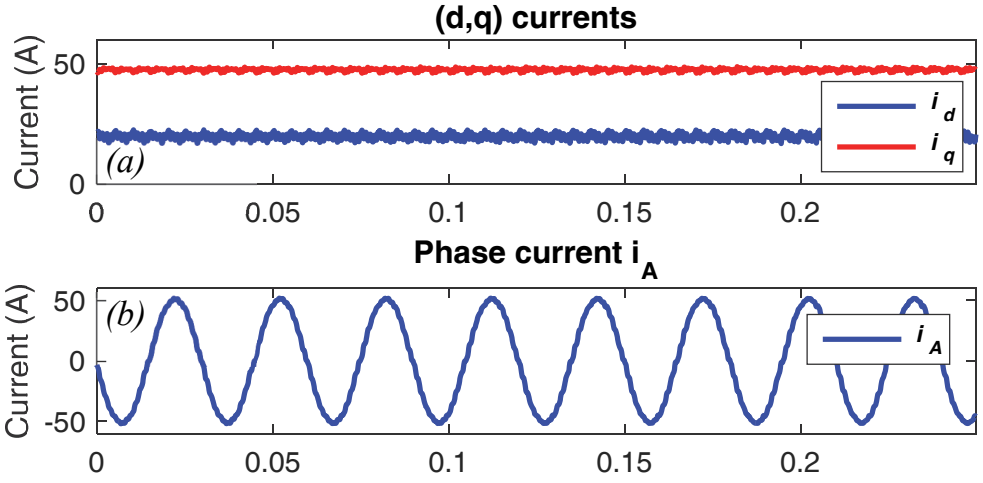

Figure. 5. 22. Measured current waveforms of torque control test. 3. (a) *d*- and *q*-axis currents. (b) MG stator phase *a* current

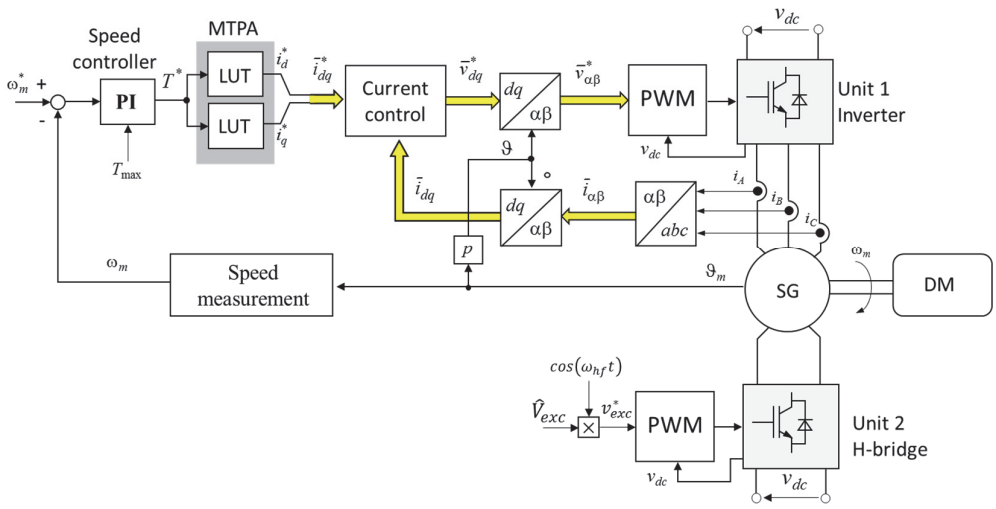

Figure. 5. 23. Schematic diagram of the implemented speed control

5.4.2 Speed Control

In this test, speed control has been implemented on the starter generator and the torque has been imposed by the prime mover. Schematic diagram of the implemented speed control is shown in Fig 5.23. The output of the PI speed controller has been limited at 11 Nm which corresponds to maximum torque that can be generated by the maximum MG stator current (50 A). This test was performed at two different conditions as follows:

Speed control test. 1: Starting from controlled zero speed and constant load torque followed by acceleration up to 1000 rpm.

Speed control test. 2: Speed loop performance for load rejection at 1000 rpm.

5.4.2.1 Speed control test. 1: Speed control with an active load of 8 Nm.

During entire the test, the imposed torque by the prime mover was set at 8 Nm. Reference and actual speed waveforms are shown in Fig 5.24.a. Fig 5.24.b shows reference torque and measured torque waveforms of the starter-generator. MG stator current waveforms are shown in Fig 5.25.

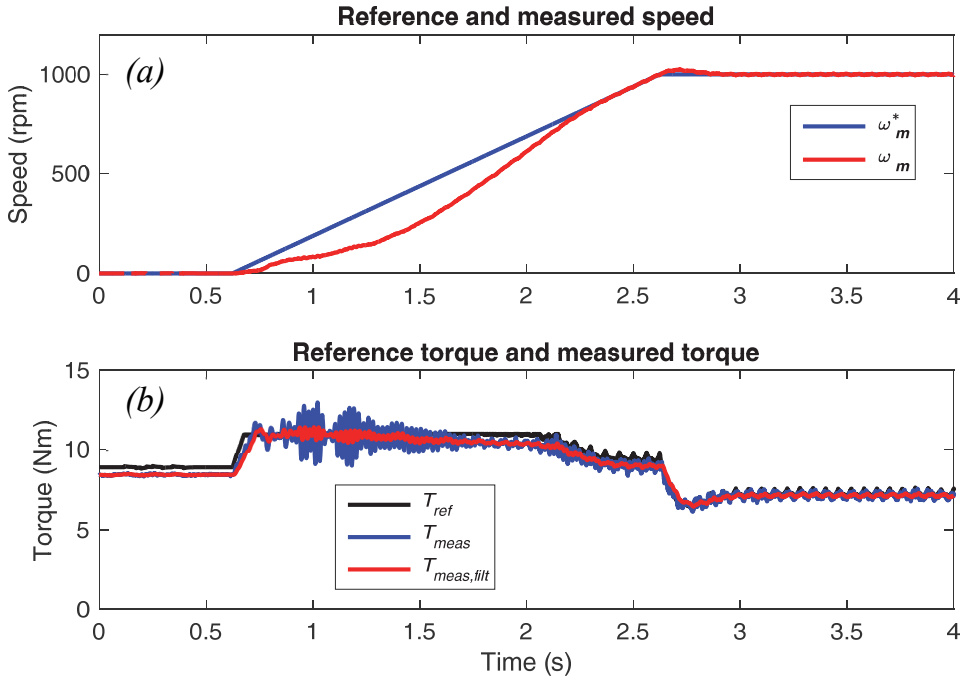

Figure. 5. 24. Speed and torque waveforms of speed control test. 1. (a) Reference and actual speed waveforms. (b) Reference and measured torque waveforms

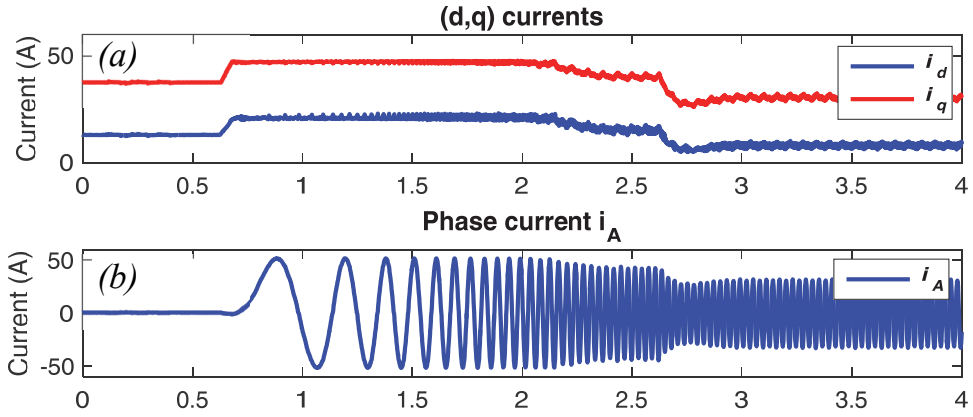

Figure. 5. 25. Measured current waveforms of speed control test. 1. (a) *d*- and *q*-axis currents. (b) MG stator phase *a* current

5.4.2.2 Speed control test. 2: Speed loop performance for load rejection at 1000 rpm.

In this test, using the prime mover, a load torque of about 10.5 Nm is applied to the machine and then removed. Reference speed and actual speed waveforms are shown in Fig 5.26.a. generated reference torque of the speed controller and actual measured torque waveforms are shown in Fig 5.26.b. Also, Mg stator current waveforms are shown in Fig 5.27.

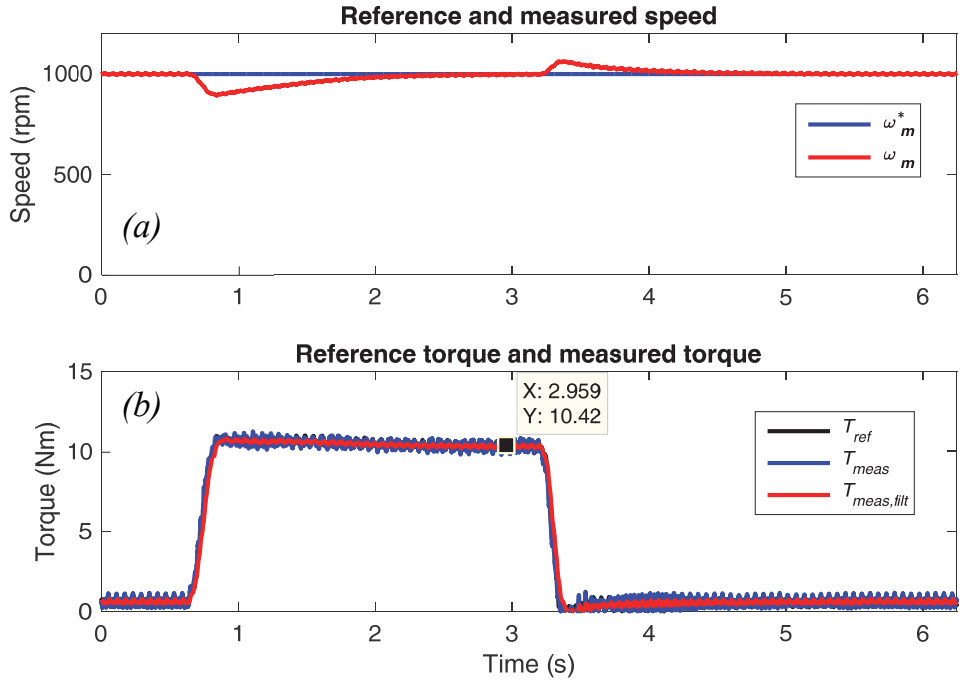

Figure. 5. 26. Speed and torque waveforms of speed control test. 2. (a) Reference and actual speed waveforms. (b) Reference and measured torque waveforms

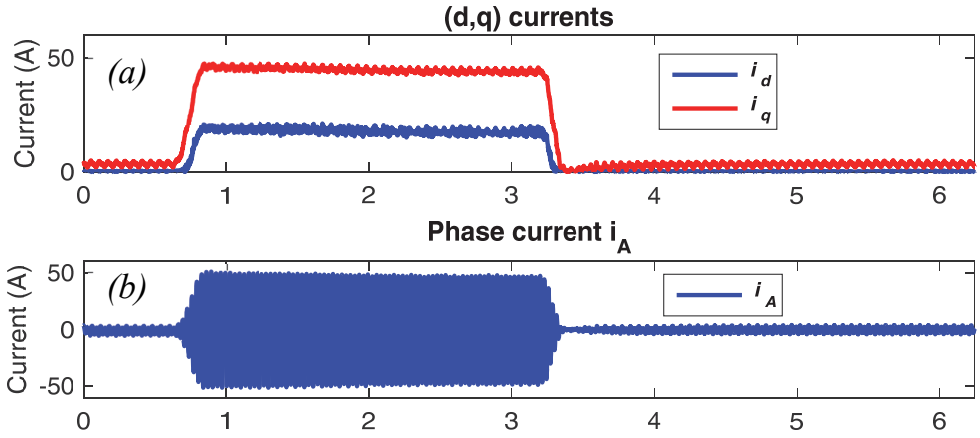

Figure. 5. 27. Measured current waveforms of speed control test. 2. (a) *d*- and *q*-axis currents. (b) MG stator phase *a* current

Chapter 6

An Excitation Procedure for Single-phase Brushless Exciter with Seamless Transitions in Starting mode of the Three-stage Brushless Synchronous Starter-generator

6.1 Introduction

Since safety is a crucial requirement for aircraft power systems, brushless electric machines are the preferred solution for Integrated Starter-Generator system (ISG) due to their advantages of high safety level and low maintenance requirement [93]-[94].Among the brushless machines, the Wound Rotor Synchronous Machine (WRSM) with brushless excitation system is a popular solution due to its simplicity and better reliability with respect to Permanent Magnet (PM) machines since the field excitation can be controlled [95]. Typically, a brushless WRS machine is a three-stage machine consisted of a PM three-phase Pre-Exciter (PE), the Main Exciter (ME) and the Main Generator (MG) that are mounted on the same shaft, as shown in Fig. 6.1 [96].

At starting, the PE cannot be used to supply the ME field winding through the DC-DC converter (Fig. 6.1). In this case, the DC-DC converter is fed by a DC bus [97]. The voltages induced in the three-phase ME rotor windings are rectified by a rotating diode bridge rectifier and applied to the field winding of the MG, providing the MG field current I_f. On the MG side, the stator windings are supplied by a three-phase inverter. At standstill, the DC excitation cannot be used for the ME since there is no relative speed between the ME excitation field and the ME rotor.

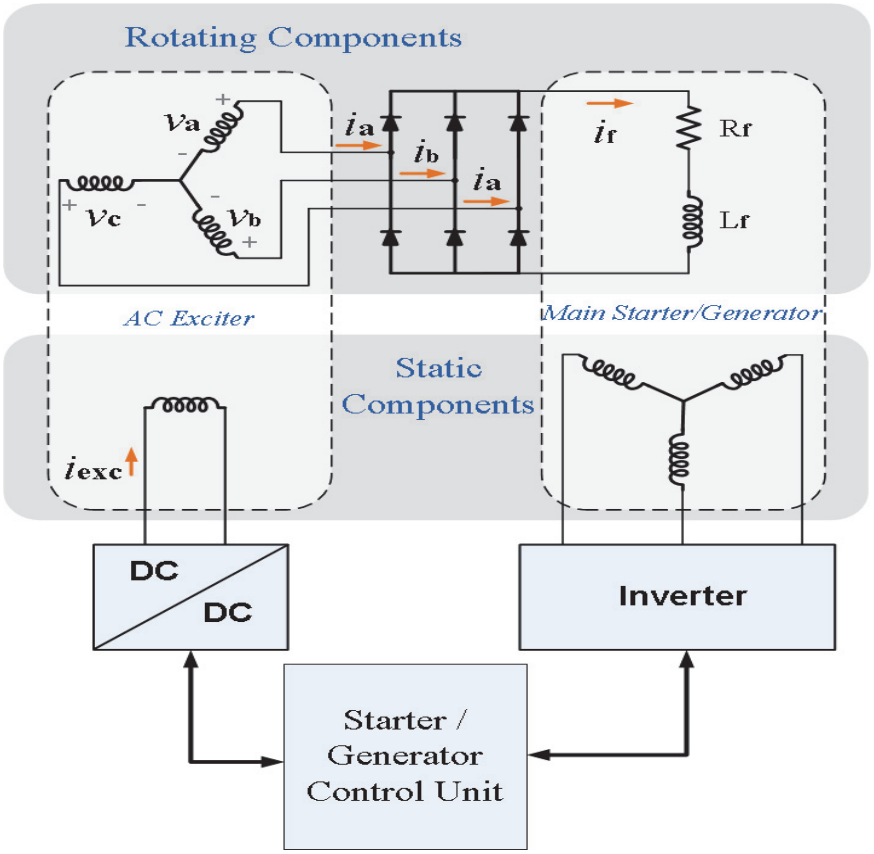

Figure. 6. 1. Three-stage brushless synchronous starter generator for aircraft in start-up operation mode (without pre-exciter)

Therefore, AC excitation is needed for the ME. As the speed increases, the excitation must be changed from AC to DC. The power converter for ME supply can be a simple bridge DC-DC converter that can easily provide both AC and DC excitations for the ME during starting and generation. Therefore, the single-phase exciter is fully compatible with the existing aircraft Generator Control Units (GCU) since the power converter used for the excitation can be easily performed by the same GCU that controls the entire system. However, the single-phase ME needs a particular attention in case of AC excitation since it produces a pulsating magnetic field. To produce a rotating magnetic field, polyphase ME stator windings can be used, as in [98]-[104]. These solutions have better performance with AC excitation, but they need more complicated power converters.

Moreover, the transition from AC excitation to DC excitation is performed with relays and additional wiring, so the system reliability is reduced. For these reasons, the single-phase ME solution is preferable for the industry with respect to the polyphase solutions in terms of compatibility, size, simplicity, and safety. In addition, it must be emphasized that the starting time with AC excitation is very small when compared with the generation and starting time with normal DC excitation, so the use of polyphase ME windings is not justified only for a very small part of the starting. For this reason, it is more convenient to find the proper AC excitation solution of the ISG with single-phase ME.

The few papers dealing with the starting of an ISG with single-phase ME provided solutions based on intensive experimental tests to find the relationship between the ME excitation current and the MG field current.

In [105], a linear relation between excitation current I_{exc} and MG field current I_f was obtained for a three-stage WRS machine by experimental tests. An exponential function was proposed in [106] representing the relationship between the excitation frequency and speed. Although the proposed function can be used to find the instant of the AC to DC excitation transition, since the relationship between the required excitation frequency and speed obtained from experimental data using curve fitting, it works only for the machine used for the test and therefore it is not a generic solution.

In [102], a two-phase ME is designed which produces a rotating field when AC excitation is required. In addition, an excitation frequency control is proposed which keeps the MG field current constant by keeping constant the frequency of the induced armature voltages. However, the proposed solution needs additional relays and wiring for excitation switching from AC to DC. Moreover, the influence of the commutation voltage drop that is different in AC and DC excitation conditions, was not considered.

To the best of the authors' knowledge, an analytical study to get the relationship between the ME excitation current and the MG field current with AC and DC supply (including the seamless transition and the optimal speed at which the transition should be performed) has not been addressed in the literature.

Therefore, a universal excitation control strategy based on analytical study of ME during engine starting mode is proposed in this chapter to keep constant the MG field during the entire starting operation. Moreover, the proposed strategy presents a seamless transition between AC and DC excitation and provides the optimal speed at which the transition should be performed.

This chapter is organized as follows. Three starting excitation modes are defined and modeled analytically in sections 2 to 4. The influence of the exciter rotor inductance and resistance on the MG field current is described in Section 5. Then, all possible transition conditions of the MG field current are analysed in Section 6 using the revolving field theory. An excitation current control is proposed to obtain quasi-constant MG field current during the starting, with seamless transitions between different excitation modes. Moreover, the proposed procedure specifies an optimum speed when the AC excitation should be switched to DC excitation. Simulation and experimental verifications are reported in sections 8 and 9, respectively.

6.2 ME Operation at Starting

There are two ambiguous issues with starting of a three-stage brushless synchronous starter generator during its start operation as follows.

What is the value of MG field current under a given excitation?

In practice, the obtainable MG field current at standstill is measured by experimental tests using open rotor measurement.

Knowing the MG field current is essential for optimal control of the machine in starting mode. In this chapter, as a solution an excitation control strategy is proposed which keeps constant the known MG field current at standstill during the entire starting process. This is performed by keeping constant the rotating rectifier output voltage.

At which speed, AC excitation should be switched to DC excitation?

When the machine is at standstill, AC excitation is required since there is no relative speed between the field and rotor windings. The AC excitation at standstill will be called hereinafter the first excitation mode.

When the machine starts rotating, the ME excitation remains AC up to a certain rotor speed ω_{r_acdc}, at which the excitation should become DC. The operation with rotor rotation below ω_{r_acdc} and AC excitation is called the second excitation mode. The third excitation mode starts when the rotor speed exceeds ω_{r_acdc} and the ME excitation changes from AC to DC.

In this chapter, switching functions of the rotating rectifier in all excitation modes are calculated in Section 4. By knowing the switching function of the rotating rectifier, now it is possible to calculate the rotating rectifier output voltage during entire start process.

The proposed excitation control uses the MG field current at standstill I_{f1} as the reference value for the MG field current at the next two excitation modes (I_{f2} in the second excitation mode, and I_{f3} in the third excitation mode). Thus, the AC excitation current amplitude in the second excitation mode I_{exc2} is controlled to keep the I_{f2} equal to I_{f1}. Meanwhile, the required DC excitation I_{exc3} to provide I_{f3} equal to I_{f1} is calculated. Once the required DC excitation I_{exc3} becomes equal to the amplitude of the I_{exc2}, the excitation switches from AC to DC. In this case, transitions of the MG field current between different excitation modes are smooth and its value is kept constant.

6.3 Analytical Model of the Single-phase Brushless Exciter

Equations of ME armature voltages are as following.

$$v_a = R_r \cdot i_a + \frac{d}{dt}[-L_{rr} \cdot i_a - M_{rr} \cdot i_b - M_{rr} \cdot i_c + M_{rs} \cdot i_{exc} \cdot \cos(\omega_r t + \vartheta_0)] \tag{6.1}$$

$$v_b = R_r \cdot i_b + \frac{d}{dt}\left[-M_{rr} \cdot i_a - L_{rr} \cdot i_b - M_{rr} \cdot i_c + M_{rs} \cdot i_{exc} \cdot \cos\left(\omega_r t + \vartheta_0 + \frac{2\pi}{3}\right)\right] \tag{6.2}$$

$$v_c = R_r \cdot i_c + \frac{d}{dt}\left[-M_{rr} \cdot i_a - M_{rr} \cdot i_b - L_{rr} \cdot i_c + M_{rs} \cdot i_{exc} \cdot \cos\left(\omega_r t + \vartheta_0 - \frac{2\pi}{3}\right)\right] \tag{6.3}$$

where, R_r is armature winding resistance. L_{rr}, and M_{rr} are self-inductance and mutual inductance of armature windings, respectively.

M_{rs} is mutual inductance between field and armature windings. I_{exc} is excitation current (field current of ME). ω_r is rotation speed, and ϑ_0 is initial electrical rotor position.

Voltage equation of ME field winding is:

$$v_{exc} = R_f \cdot i_{exc} + \frac{d}{dt}\left[-M_{rs} \cdot i_a \cdot \cos(\omega_r t + \vartheta_0) - M_{rs} \cdot i_b \cdot \cos\left(\omega_r t + \vartheta_0 + \frac{2\pi}{3}\right) - M_{rs} \cdot i_c \cdot \cos\left(\omega_r t + \vartheta_0 - \frac{2\pi}{3}\right) + L_f \cdot i_{exc}\right] \tag{6.4}$$

where, R_f and L_f are resistance and self-inductance of the field winding, respectively.

6.3.1 Armature reaction

From (6.4), armature reaction flux is:

$$\lambda_B = M_{rs} \cdot i_a \cdot \cos(\omega_r t + \vartheta_0) + M_{rs} \cdot i_b \cdot \cos\left(\omega_r t + \vartheta_0 + \frac{2\pi}{3}\right) + M_{rs} \cdot i_c \cdot \cos\left(\omega_r t + \vartheta_0 - \frac{2\pi}{3}\right) \tag{6.5}$$

Based on switching function method (Chapter 3), (6.5) can be expanded as follows.

$$\lambda_B = \overbrace{M_{rs} \cdot i_f \cdot \left[S_a \cdot \cos(\omega_r t + \vartheta_0) + S_b \cdot \cos\left(\omega_r t + \vartheta_0 + \frac{2\pi}{3}\right) + S_c \cdot \cos\left(\omega_r t + \vartheta_0 - \frac{2\pi}{3}\right)\right]}^{K} \quad (6.6)$$

where S_a, S_b, and S_c are switching functions of phase a, phase b, and phase c, respectively.

To show the increment of λ_B with respect to speed, v_{exc} with constant amplitude and frequency (150 v, 200Hz) is applied to field winding of ME and speed increases from 0 (at $t=0.5s$) to 2500 RPM (at $t=3s$). i_f is increasing with respect to speed. Then waveform of λ_B divided by i_f is shown in Fig 6.2. As can be seen in Fig. 6.2, λ_B is constant. The reason is that, in (6.6), the maximum value of the term indicated by K is always $\sqrt{3}$. Also, the frequency of armature reaction flux (λ_B) and back-emf (the derivative of λ_B) is equal to the excitation frequency (f_{exc}).

6.3.2 Induced voltages in armature windings

In this thesis, presented analytical model uses revolving field theory to analytically describe the pulsating field which is produced by the ME single-phase field winding. This pulsating field can be decomposed into two imaginary rotating fields which are rotating in opposite directions with an amplitude equal to half of the real stationary field magnitude. The field that rotates in the same direction of the rotor is called forward rotating field (λ_{FW}), while the field that rotates in opposite direction is called rhe backward rotating field (λ_{BW}).

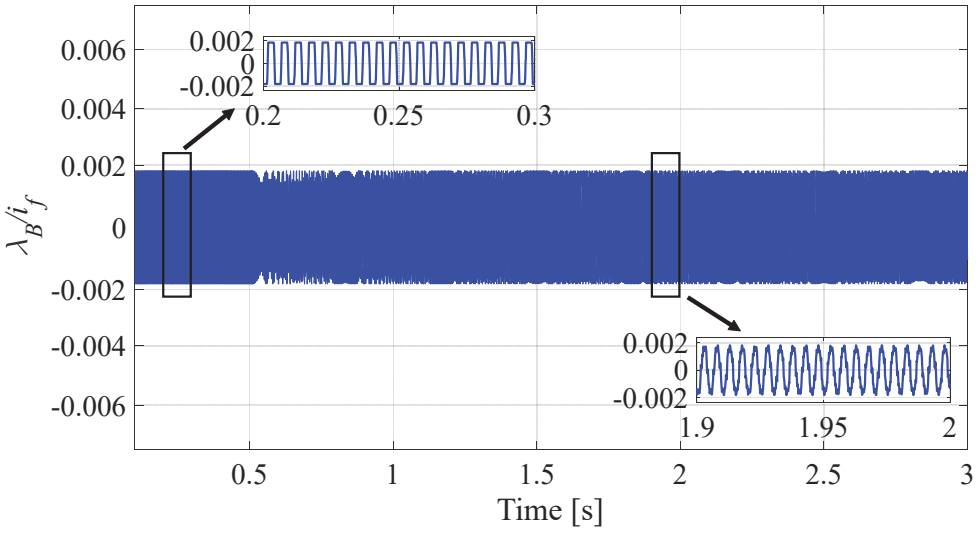

Figure. 6. 2. Increment of armature reaction flux with respect to speed

Induced three-phase voltages on armature windings are:

$$v_a = \frac{1}{2} \cdot M_{rs\_exc} \cdot I_{exc} \cdot \{(2-s) \cdot \omega_{exc} \cdot \cos((2-s) \cdot \omega_{exc} t + \vartheta_0) + s \cdot \omega_{exc} \cdot \cos(s \cdot \omega_{exc} \cdot t - \vartheta_0)\} \quad (6.7)$$

$$v_b = \frac{1}{2} \cdot M_{rs\_exc} . I_{exc} \cdot \left\{(2-s) \cdot \omega_{exc} \cdot \cos\left((2-s) \cdot \omega_{exc} \cdot t + \frac{2 \cdot \pi}{3} + \vartheta_0\right) + s \cdot \omega_{exc} \cdot \cos(s \cdot \omega_{exc} \cdot t - \frac{2 \cdot \pi}{3} - \vartheta_0)\right\} \quad (6.8)$$

$$v_c = \frac{1}{2} \cdot M_{rs\_exc} \cdot I_{exc} \cdot \left\{(2-s) \cdot \omega_{exc} \cdot \cos\left((2-s)\omega_{exc} \cdot t + \frac{4 \cdot \pi}{3} + \vartheta_0\right) + s \cdot \omega_{exc} \cdot \cos(s \cdot \omega_{exc} \cdot t - \frac{4 \cdot \pi}{3} - \vartheta_0)\right\} \quad (6.9)$$

The above equations explicitly demonstrate the revolving field theory; the first term on the right side of equal sign denotes an armature voltage component induced by the backward rotating flux, while the second term represents a voltage component induced by the forward rotating flux.

6.4 Starting Excitation Modes

In this section, with respect to speed and excitation type (AC or DC), different excitation modes are defined.

6.4.1 AC excitation at standstill

When the machine is at standstill, rotor position is ϑ_0, ω_r is equal to zero, and slip is unity. As a result, the induced phase voltages in armature windings can be rewritten as follows.

$$v_a = M_{rs\_exc} \cdot I_{exc} \cdot \omega_{exc} \cdot \cos(\omega_{exc} t) \cdot \cos(\vartheta_0) \quad (6.10)$$

$$v_b = M_{rs\_exc} \cdot I_{exc} \cdot \omega_{exc} \cdot \cos(\omega_{exc} t) \cdot \cos(\vartheta_0 + \frac{2 \cdot \pi}{3}) \quad (6.11)$$

$$v_c = M_{rs\_exc} \cdot I_{exc} \cdot \omega_{exc} \cdot \cos(\omega_{exc} t) \cdot \cos(\vartheta_0 + \frac{4 \cdot \pi}{3}) \quad (6.12)$$

From the equations (6.10) to (6.12), it results that two of the phase voltages have the same phase, while the third phase has a 180° phase shift. Since armature windings feed a rotating diode rectifier bridge, only two phases which have phase shift to each other and have largest amplitudes contribute in voltage rectification.

The third phase just carries current during phase commutations which leads to three-phase short-circuit. This phenomenon will be investigated in detail in Section 6.5.

In this chapter, to figure out the relationship between input voltages of the rotating rectifier and its output voltage which governs field current of MG, switching functions of the rotating rectifier in all excitation modes are calculated. Switching function method is described in detail in [107] and Chapter .3 of this thesis. Using the switching functions, the output of the rectifier is:

$$v_{dc} = v_a \cdot S_a + v_b \cdot S_b + v_c \cdot S_c - 2 \cdot V_{on} \tag{6.13}$$

Switching function vector of the rotating rectifier in the first excitation mode, with the armature resistance neglected, is calculated as follows.

$$S_{a,b,c} = \frac{4}{\pi} \cdot \begin{bmatrix} \Delta_a \cdot \cos(\omega_{exc} t) \\ \Delta_b \cdot \cos(\omega_{exc} t) \\ \Delta_c \cdot \cos(\omega_{exc} t) \end{bmatrix} \tag{6.14}$$

where the coefficient ($4/\pi$) is calculated from the Fourier series calculation of the switching functions [107]. Δ_a, Δ_b, and Δ_c depend on the initial rotor position (ϑ_0) and are expressed in Table.6.1. Substituting (6.14) in (6.13), rotating rectifier output voltage in the first excitation mode can be calculated. Its mean value over one electrical period ($\frac{1}{2\cdot\pi} \cdot \int_0^{2.\pi} V_{dc}$) is:

$$v_{dc1} = \frac{2}{\pi} \cdot M_{rs-exc} \cdot I_{exc} \cdot \omega_{exc} \cdot \left(\cos(\vartheta_0) \cdot \Delta_a + \cos\left(\vartheta_0 + \frac{2\cdot\pi}{3}\right) \cdot \Delta_b + \cos\left(\vartheta_0 + \frac{4\cdot\pi}{3}\right) \cdot \Delta_c\right) - 2 \cdot V_{on} \tag{6.15}$$

where, V_{on} is forward voltage of rectifier diodes.

Table. 6. 1. Δ_a, Δ_b, and Δ_c functions in the first excitation mode

Initial Rotor Position ϑ_0	Δ_a	Δ_b	Δ_c
$0^\circ \le \vartheta_0 < 30^\circ$	1	-1	0
$30^\circ \le \vartheta_0 < 60^\circ$	1	-1	0
$60^\circ \le \vartheta_0 < 90^\circ$	0	-1	1
$90^\circ \le \vartheta_0 < 120^\circ$	0	-1	1
$120^\circ \le \vartheta_0 < 150^\circ$	-1	0	1
$150^\circ \le \vartheta_0 < 180^\circ$	-1	0	1
$180^\circ \le \vartheta_0 < 210^\circ$	-1	1	0
$210^\circ \le \vartheta_0 < 240^\circ$	-1	1	0
$240^\circ \le \vartheta_0 < 270^\circ$	0	1	-1
$270 \le \vartheta_0 < 300^\circ$	0	1	-1
$300^\circ \le \vartheta_0 < 330^\circ$	1	0	-1
$330^\circ \le \vartheta_0 < 360^\circ$	1	0	-1

Equation. (6.15) indicates that the rotating rectifier output voltage at standstill depends on the initial rotor position, excitation current amplitude I_{exc} and frequency ω_{exc}.

6.4.2 AC excitation at low speed

When the machine starts rotating up to the rotor speed ω_{r_acdc}, the excitation remains AC. During this interval, the induced phase voltages on armature windings are the same as (6.7) to (6.9).

As rotation speed increases, the frequency of voltage component induced by the backward imaginary field increases while the frequency of voltage component induced by the forward field decreases. Hence, the sum of two voltage components is like a beat signal which voltage component induced by backward field is its carrying signal and another voltage component induced by the forward field is a modulating signal. Calculating switching functions of such voltages is presented in Chapter .3. Detailed demonstrations are as follows.

For simplicity, in (6.7), (6.8), and (6.9), following assumptions can be made:

$$\frac{1}{2} \cdot M_{rs_{exc}} \cdot I_{exc} = 1$$

$$\vartheta_0 = 0$$

$$(2 - s) \cdot \omega_{exc} = \omega_{exc} + \omega_r = a$$

$$s \cdot \omega_{exc} = \omega_{exc} - \omega_r = b$$

Therefore, the equation (6.7) can be rewritten as:

$$v_a = a \cdot \cos(a \cdot t) + b \cdot \cos(b \cdot t) \tag{6.16}$$

Thus, during the second excitation mode, induced voltages in the armature windings are sum of the two cosine terms with different amplitudes and frequencies. The complex form of the two cosine voltages is:

$$Re\{a \cdot e^{jat} + b \cdot e^{jbt}\} = R_e\{e^{jat} \cdot [a + b \cdot e^{j(b-a)t}]\} \quad (6.17)$$

where *Re* indicates the real part of a complex expression.

During the second excitation mode, the condition $a>b$ is always valid, so "a" is the dominant frequency (average frequency of the resulting voltage).

In other words, the low frequency-low amplitude voltage component "$b \cdot cos(b \cdot t)$" (the red vector in Fig. 6.3) modulates the amplitude of the high frequency-high amplitude voltage component "$a \cdot cos(a \cdot t)$" (the black vector in Fig. 6.3). In addition, the low frequency-low amplitude voltage component leads to a variation of the high frequency-high amplitude voltage component phase.

In Fig. 6.3, the blue vector represents the sum of the two voltage components. The amplitude of the resulting voltage is:

$$A = |a + b \cdot e^{j(a-b)t}| = \sqrt{a^2 + b^2 + 2 \cdot a \cdot b \cdot \cos((b-a) \cdot t)} \quad (6.18)$$

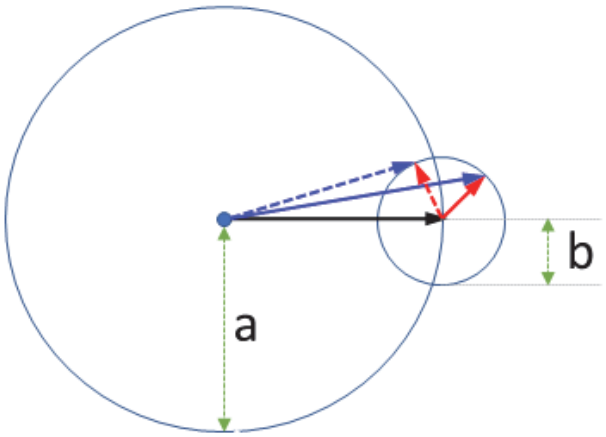

Figure. 6. 3. Armature voltages in the second excitation mode (complex representation of equation (6.6))

For phases b and c, amplitudes are:

$$B = Amplitude\ of\ phase\ b = \sqrt{a^2 + b^2 + 2 \cdot a \cdot b \cdot \cos((b-a) \cdot t - \frac{4 \cdot \pi}{3})} \quad (6.19)$$

$$C = Amplitude\ of\ phase\ c = \sqrt{a^2 + b^2 + 2 \cdot a \cdot b \cdot \cos((b-a) \cdot t - \frac{8 \cdot \pi}{3})} \quad (6.20)$$

Phase deviation of the high frequency-high amplitude voltage component due to the low frequency-low amplitude voltage component is:

$$\theta_A = \tan^{-1}\left(\frac{b\cdot\sin((b-a)\cdot t)}{a+b\cdot\cos((b-a)\cdot t)}\right) \tag{6.21}$$

For phases *b* and *c*, phase deviations are:

For phase *b*:

$$\theta_B = \tan^{-1}\left(\frac{b\cdot\sin((b-a)\cdot t-\frac{4\cdot\pi}{3})}{a+b\cdot\cos((b-a)\cdot t-\frac{4\cdot\pi}{3})}\right) \tag{6.22}$$

For phase *c*:

$$\theta_C = \tan^{-1}\left(\frac{b\cdot\sin((b-a)\cdot t-\frac{8\cdot\pi}{3})}{a+b\cdot\cos((b-a)\cdot t-\frac{8\cdot\pi}{3})}\right) \tag{6.23}$$

Thus, induced voltages in the armature of the ME in the second excitation mode ((6.7), (6.8), (6.9)) are:

$$v_a = \frac{1}{2}\cdot M_{rs_{exc}}\cdot I_{exc}\cdot A\cdot\cos(\boldsymbol{a}\cdot\boldsymbol{t}+\theta_A) \tag{6.24}$$

$$v_b = \frac{1}{2}\cdot M_{rs_{exc}}\cdot I_{exc}\cdot B\cdot\cos(\boldsymbol{a}\cdot\boldsymbol{t}+\frac{2\cdot\pi}{3}+\theta_B) \tag{6.25}$$

$$v_c = \frac{1}{2}\cdot M_{rs_{exc}}\cdot I_{exc}\cdot C\cdot\cos(\boldsymbol{a}\cdot\boldsymbol{t}+\frac{4\cdot\pi}{3}+\theta_C) \tag{6.26}$$

Switching functions of the rotating rectifier in this mode are

$$S_{a,b,c} = \frac{2\cdot\sqrt{3}}{\pi}\left[\begin{array}{c} \frac{v_a}{\omega_{exc}\cdot\sqrt{(2-s)^2+s^2+2\cdot s\cdot(2-s)\cdot\cos(2\cdot\omega_r\cdot t)}} \\ \frac{v_b}{\omega_{exc}\cdot\sqrt{(2-s)^2+s^2+2\cdot s\cdot(2-s)\cdot\cos\left(2\cdot\omega_r\cdot t+\frac{4\cdot\pi}{3}\right)}} \\ \frac{v_c}{\omega_{exc}\cdot\sqrt{(2-s)^2+s^2+2\cdot s\cdot(2-s)\cdot\cos\left(2\cdot\omega_r\cdot t+\frac{8\cdot\pi}{3}\right)}} \end{array}\right] \tag{6.27}$$

where the coefficient ($\frac{2\cdot\sqrt{3}}{\pi}$) is calculated from the Fourier series calculation of the switching functions [107]. Substituting (6.27) in (6.13) and calculating mean value, the simplified average value of the rectifier DC output voltage, in the second excitation mode, can be written as

$$v_{dc2} = \frac{3\cdot\sqrt{3}\cdot M_{rs\_exc}\cdot I_{exc}\cdot\omega_{exc}}{\pi^2}\cdot E[\pi, s\cdot(2-s)] - 2\cdot V_{on} \tag{6.28}$$

where E is an incomplete elliptic integral of the second kind [108].

Usually, AC excitation is needed when slip is between 1 (at standstill to 1) and zero. For slips less than zero, the rotation speed is enough to establish sufficient coupling between single-phase field winding and armature windings of ME. Therefore, AC excitation is no longer required. Hence, in (6.28), $s\cdot(2\text{-}s)$ changes from 1 to 0 and it is possible to replace the elliptic integral with an approximated function. By curve fitting, an approximated function for $E[\pi, s\cdot(2\text{-}s)]$ can be written as :

$$E = -4.004x^6 + 10.27x^5 - 10.14x^4 + 4.571x^3 - 1.13x^2 - 0.7044x + 3.14 \tag{6.29}$$

where $x = s\cdot(2\text{-}s)$.

The equation. (6.28) demonstrates that below ω_{r_acdc}, the DC output voltage variation depends on I_{exc} , ω_{exc}, and the $E[\pi, s\cdot(2\text{-}s)]$.

6.4.3 DC excitation at high speed

The third excitation mode starts when excitation changes from AC to DC. In this case, induced voltages in armature windings are

$$v_a = -(I_{exc}\cdot M_{rs-exc}\cdot\omega_r\cdot\sin(\omega_r t)) \tag{6.30}$$

$$v_b = -(I_{exc}\cdot M_{rs-exc}\cdot\omega_r\cdot\sin(\omega_r t + \tfrac{2\cdot\pi}{3})) \tag{6.31}$$

$$v_c = -(I_{exc}\cdot M_{rs-exc}\cdot\omega_r\cdot\sin(\omega_r t + \tfrac{4\cdot\pi}{3})) \tag{6.32}$$

Switching function vector of the rotating rectifier in this mode is

$$S_{abc} = \frac{2\cdot\sqrt{3}}{\pi} \cdot \begin{bmatrix} \sin(\omega_r t) \\ \sin(\omega_r t + \frac{2\cdot\pi}{3}) \\ \sin(\omega_r t + \frac{4\cdot\pi}{3}) \end{bmatrix} \tag{6.33}$$

Using (6.33) in (6.13) and calculating its mean value, mean value of rectifier output voltage, in the third excitation mode, becomes

$$v_{dc3} = \frac{3\cdot\sqrt{3}}{\pi} \cdot I_{exc} \cdot M_{rs_{exc}} \cdot \omega_r - 2 \cdot V_{on} \tag{6.34}$$

As results from (6.34), DC output voltage of the rotating rectifier during the third excitation mode is proportional with DC excitation current and rotor speed.

6.5 Effects of front-end Inductance on rectifier output voltage

As described in Chapter .3, AC-side front-end inductances lead to a finite commutation interval when the output current of rectifier switches between rectifier legs. During the commutation interval, two or more diodes are carrying current which makes a line-to-line short-circuit between armature phases [109]. Based on commutation duration, there are three operation modes for a rectifier which are described in detail in [110]. Commutation influence on the output voltage is a voltage drop that is usually modeled by a virtual resistance R_{com}. This resistance will be obtained in the next subsection for the different excitation modes.

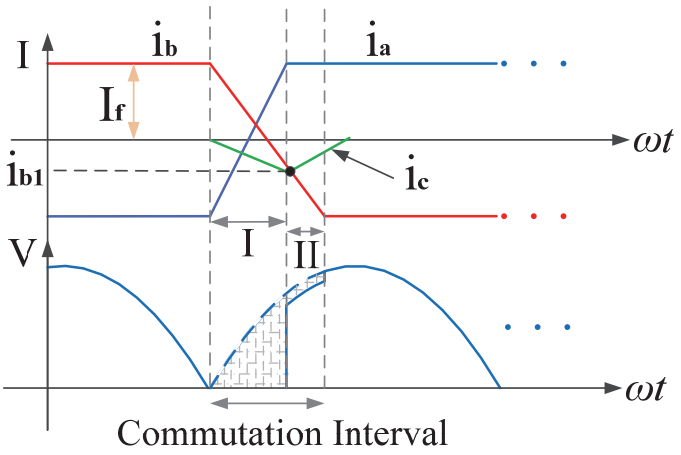

Figure. 6. 4. Commutation interval waveform in the first excitation mode

6.5.1 Commutation voltage drop in the first excitation mode

In the first excitation mode, supply voltages of the rotating rectifier are two-phase with 180˚phase shift. Fig. 6.4 shows the interval in which positive current is transferring from phase *b* to phase *a* and voltage of phase *a* is higher than phase *b*. So, current commutation of phase *a* is faster than of phase *b*, and the phase *c* carries difference of the phase *a* current and the phase *b* current.

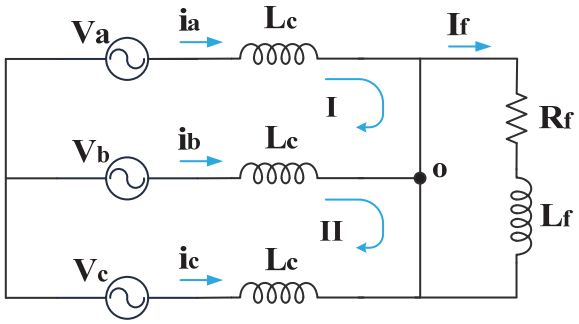

a

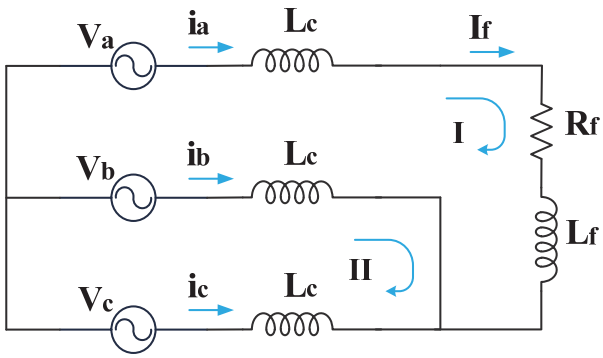

b

Figure. 6. 5. Equivalent circuit of the rotating rectifier during commutation in the first excitation mode. a) First mode. b) Second mode

During commutation, there are two distinct modes (Fig. 6.5.a). In the first mode, always more than three diodes are on. Fig. 6.5.a shows the equivalent circuit of this mode Applying KVL in the indicated loops yields:

$$-v_{ab} + L_c \cdot \frac{di_a}{dt} - L_c \cdot \frac{di_b}{dt} = 0 \tag{6.35}$$

$$-v_{bc} + L_c \cdot \frac{di_b}{dt} - L_c \cdot \frac{di_c}{dt} = 0 \tag{6.36}$$

Applying KCL at point O yields

$$i_c = -(i_a + i_b) \tag{6.37}$$

Substituting (6.37) in (6.36)

$$L_c \cdot \frac{di_b}{dt} = \frac{1}{2} \cdot \left(v_{bc} - L_c \cdot \frac{di_a}{dt}\right) \tag{6.38}$$

Substituting (6.38) in (6.35), the time interval needed by the phase *a* current to reach I_f is

$$\Delta t = \frac{3 \cdot L_c \cdot I_f}{\left(v_{ab} + \frac{1}{2} \cdot v_{bc}\right)} \tag{6.39}$$

In (6.39), v_{ab} and v_{bc} can be calculated from (6.10), (6.11), and (6.12). For the first commutation mode, $di_a = 2 \cdot I_f$ and $di_b = i_{b1} - I_f$, where i_{b1} is current of the phase *b* at the end of the first commutation mode. Substituting (6.39) in (6.38), at the end of the first mode, phase *b* current is

$$i_{b1} = -\sqrt{3} \cdot I_f \cdot \tan(\vartheta_0) \tag{6.40}$$

Rewriting (6.35)

$$v_{ab} = L_c \cdot \frac{di_a}{dt} - L_c \cdot \frac{di_b}{dt} \tag{6.41}$$

Multiplying both sides of (6.41) by $dt \cdot \omega_{exc}$ and integrating for 180° interval yields

$$\frac{1}{\pi} \int_0^{t1} v_{ab} \cdot d(\omega_{exc} t) = \frac{1}{\pi} \cdot \left(\int_{-I_f}^{I_f} L_c \cdot \omega_{exc} \cdot d(i_a) - \int_{I_f}^{i_{b1}} L_c \cdot \omega_{exc} \cdot d(i_b)\right) \tag{6.42}$$

The left side of (6.42) is voltage drop during this mode that is lost every 180°. This voltage drop can be modelled by a resistor at the rectifier output.

$$R_{com} = (6 + 2 \cdot \sqrt{3} \cdot \tan(\vartheta_0)) \cdot f_{exc} \cdot L_c \tag{6.43}$$

When phase *a* current gets its final value (I_f), the second mode starts. Fig. 6.5.b shows equivalent circuit of the second mode. During this mode, only three diodes are conducting. Applying KVL in the indicated loop

$$v_{ab} - v_d = -L_c \cdot \frac{di_b}{dt} \tag{6.44}$$

Left side of (6.44) is voltage drop due to commutation in the second mode. Multiplying both side of (6.44) and integrating for 180° interval yield:

$$\frac{1}{\pi} \cdot \int_{t_1}^{t_2} (v_{ab} - v_d) \cdot d(\omega_{exc} t) = -\frac{1}{\pi} \cdot \int_{i_{b1}}^{-I_f} L_c \cdot \omega_{exc} \cdot di_b \tag{6.45}$$

$$R_{com} = (2 - 2 \cdot \sqrt{3} \cdot \tan(\vartheta_0)) \cdot f_{exc} \cdot L_c \tag{6.46}$$

Finally, total voltage drop due to commutation for the first excitation phase can be represented by sum of resistances from (6.43) and (6.46) as

$$R_{com1} = 8 \cdot f_{exc} \cdot L_c \tag{6.47}$$

At initial positions of 0° and 180°, where V_b and V_c are equal, only first commutation mode happens. Applying KCL at point O yields

$$i_c = i_b = -\frac{1}{2} \cdot i_a \tag{6.48}$$

Substituting (6.48) in (6.35)

$$v_{ab} = \frac{3}{2} \cdot L_c \cdot \frac{di_a}{dt} \tag{6.49}$$

Calculating average value of (6.49) for 180° as in (6.42), R_{com} is obtained.

$$6 \cdot f_{exc} \cdot L_c \tag{6.50}$$

6.5.2 Commutation voltage drop in the second and third excitation modes

In the case of a three-phase system with 120̊ phase shift between phases (like in the third excitation mode), in each electrical period of the input voltages, six commutations happen. For each commutation, $f \cdot L_c$ represents the resistance to model the commutation voltage drop.

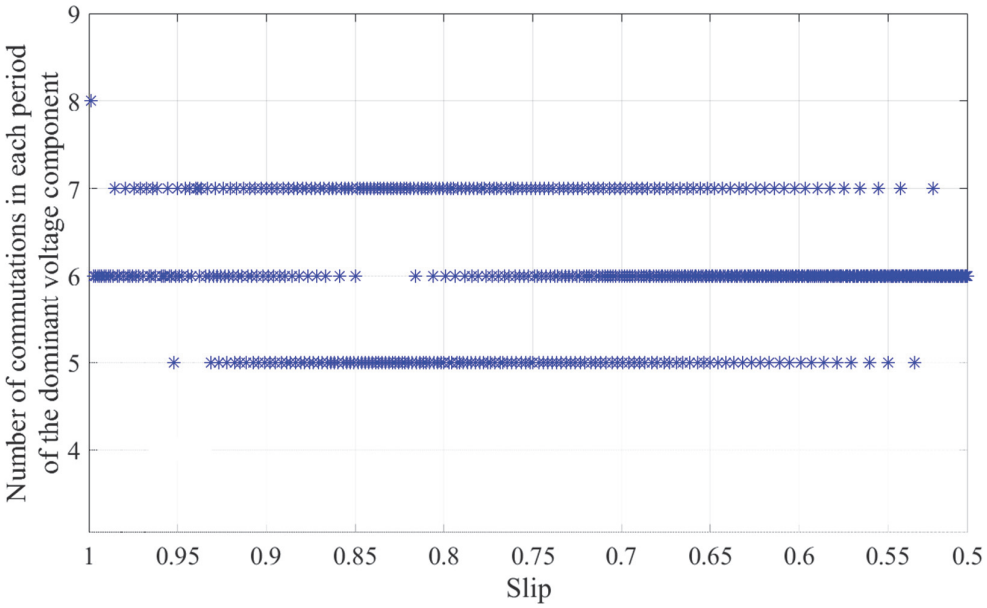

Figure. 6. 6. Number of commutations in each period of the dominant voltage component

Fig. 6.6 shows the number of commutations during each period of the dominant voltage component in the second excitation mode ($a \cdot t = (\omega_{exc} + \omega_r) \cdot t$). As can be seen, in the second excitation mode, during each period of the dominant voltage component, almost six commutations happen. Therefore, with a good approximation, the frequency of the dominant voltage component (carrying component) can be considered in the calculation of R_{com}. Thus, R_{com} for the second and third excitation modes is:

$$R_{com2,3} = 6 \cdot f \cdot L_C \tag{6.51}$$

where f for the second excitation mode is $f_{exc} + \omega_r/(2 \cdot \pi)$, and for the third excitation mode is $\omega_r/(2 \cdot \pi)$.

6.5.3 Commutation inductance

In this section, commutation inductance (L_c) is calculated for the analytical model. As mentioned before, during the commutation interval, line-to-line short-circuit occurs. Hence, the commutation inductance is not a steady-state machine inductance. According to constant flux linkage theory, once short-circuit occurs between armature phases, airgap flux remains constant.

Therefore, armature flux variations at the beginning of short-circuit interval retain inside the rotor. Hence, the inductance used by the equivalent circuits during commutation can be calculated based on induced fluxes in the rotor during commutation process.

To estimate L_c with FE analysis, two methods are used which are: magnetostatic and transient analysis.

FE analysis based on both methods are as follows:

Magnetostatic method based on [109]: Since commutation inductance is realized as an inductance defined at specific instants of the machine transient response to an applied short-circuit occurring during diodes current commutation, instead of solving transient equations in a large time span, only an interval of time which is of interest for commutation inductance estimation can be considered. Thus, using boundary conditions, regions of the problem domain which contribute to the commutation inductance estimation are isolated from other regions which leads to simplifying the problem. Based on the constant flux linkage theory, these regions for commutation inductance estimation are the rotor of the ME and its windings. In this method, based on the proposed technique in [109], to simplify the calculation of the commutation inductance, a boundary condition for FE analysis is defined to keep rotor flux linkages, during commutation interval, inside the rotor. Then, the magnetostatic analysis is performed to calculate *d*- and *q*-axis inductances. In this thesis, the average value of *d*- and *q*-axis inductances is chosen as L_c.

Transient analysis: A transient FE analysis is performed for the ME. In this method, field winding of ME is excited by a range of excitation current and the ME armature windings are connected to a rectifier fed MG field winding. The simulation is continued until the MG field current reached its steady state value. Then a commutation interval is selected and for one-time step, based on (6.36), L_c is calculated.

Since the implemented FE model was a 2D model, at the end value of end-winding was added to the estimated inductance. As a result, L_c is the sum of the estimated inductance during commutation interval and the end-winding inductance. The end-winding inductance has been calculated based on equations in [110].

It was concluded that, in our case (commutation inductance estimation), the method based on the magnetostatic analysis presented in [109] is more optimal in terms of the required computation time. However, to prove the implemented method, also a transient FE analysis was implemented.

6.5.4 Effect of armature resistance

When armature phases are in conduction interval (when there is no commutation between armature phases), two phases carry the rectifier output current I_f. In this case, the voltage drop due to the armature resistance is $2 \cdot R_r \cdot I_f$. This is the voltage drop of each line voltage.

From (6.10) to (6.12), it should be noted that in the first excitation mode, when ϑ_0 is 0° and 180°, the amplitude of v_a is twice the amplitude of v_b and v_c. Thus, i_b and i_c are equal. The amplitude of i_b and i_c is half of the amplitude of i_a. In this case, the voltage drop of each line voltage is $\frac{3}{2} \cdot R_r \cdot I_f$.

During commutation intervals, one phase carries I_f and the commutating phases carry less than I_f. Therefore, the voltage drop of the line voltage is less than $2 \cdot R_r \cdot I_f$. In this chapter, this phenomenon is neglected, and the voltage drop due to the armature resistance is considered constant.

6.6 MG Field Current Transition Modes

Usually, excitation current amplitude and frequency are kept constant during the starting with AC excitation. This method will be called hereafter as the uncontrolled method. In this method, the MG field current will not be constant during the starting process. Moreover, the switching between AC excitation and DC excitation is often done at a speed that is chosen experimentally, as in [96] and [105].

In this chapter, the proposed excitation control method aims at obtaining a constant MG field current during starting, by controlling the ME excitation current amplitude, while the excitation frequency is constant. Transition modes of the MG field current are:

First transition mode – is the transition between AC excitation at standstill and AC excitation at low speed.

Second transition mode – is the transition between the AC excitation at low speed and DC excitation.

6.6.1 First transition mode

The first transition mode happens when the machine begins to rotate. Since induced rotor voltages and therefore rotating rectifier output voltage are different in the standstill and rotating conditions, there is a transition condition for the MG field current.

Fig. 6.7 shows the $E[\pi, (s\cdot(2\text{-}s)]$ versus slip that changes from 1 to -1. From (6.28) and Fig. 6.7, it results that the output voltage of the rotating rectifier increases by increasing the rotation speed when the amplitude and frequency of excitation current are constant. However, as soon as the rotor starts rotating, the output voltage of rotating rectifier may become lower or higher than its standstill value.

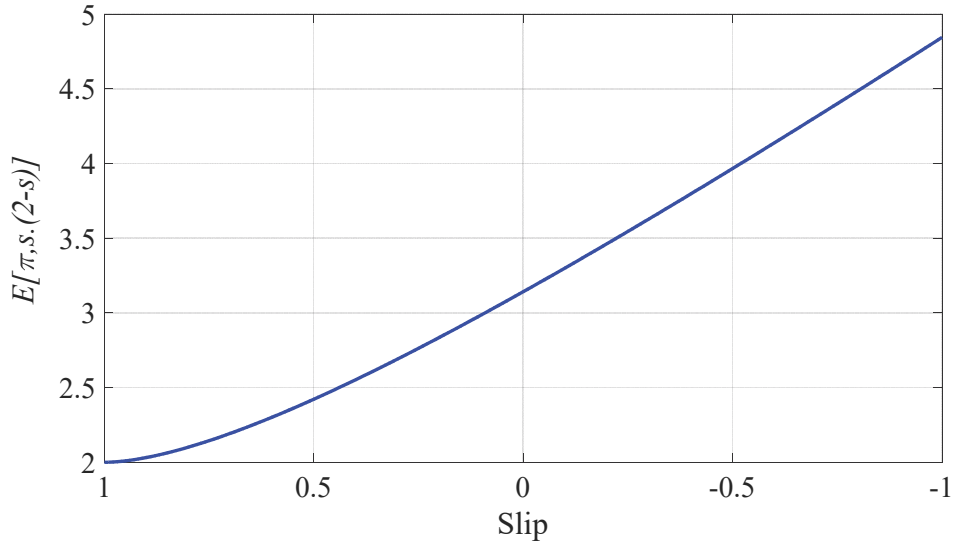

Figure. 6. 7. Elliptical integral versus slip

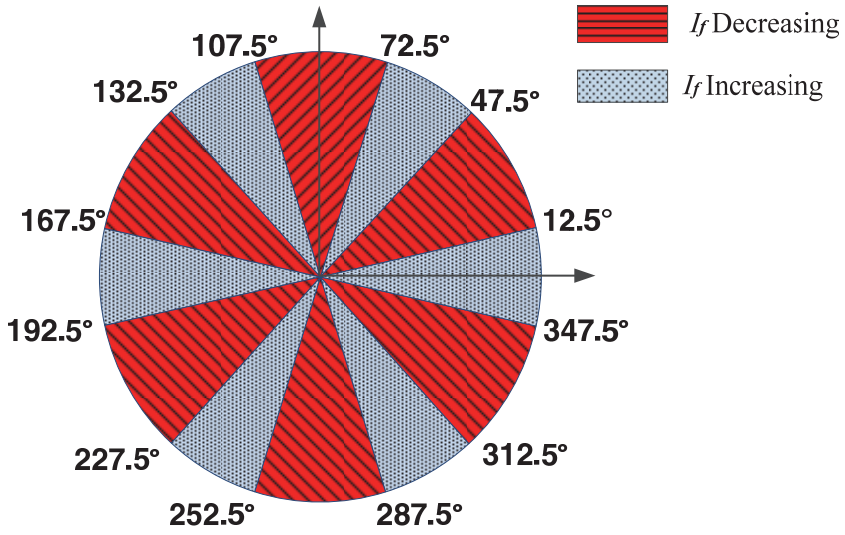

Figure. 6. 8. First transient mode condition based on rotor initial position

Comparing (6.15) and (6.28) for the initial position changing from 0 to 2.π, all possible transient conditions for the first transition mode based on initial rotor position are shown in Fig. 6.8. Areas with red color show conditions wherein the output voltage of the rotating rectifier decreases after rotation and other areas indicate the conditions with output voltage increases.

As can be seen in Fig. 6.8, in the most of conditions, the rotating rectifier output voltage and respectively the MG field current decrease when the machine starts rotating.

I_{f1} and I_{f2} are the MG field current in the first and the second excitation modes, and can be written as:

$$I_{f1} = \frac{v_{dc1}}{R_f + R_{com1} + 2 \cdot R_r} \tag{6.52}$$

$$I_{f2} = \frac{v_{dc2}}{R_f + R_{com2} + 2 \cdot R_r} \tag{6.53}$$

To keep the MG field current constant ($I_{f1} = I_{f2}$), the amplitude of exciter field current (I_{exc}) should be changed. Using the proposed method, the rotating rectifier output voltage is controlled in an open-loop fashion by controlling the ME excitation current amplitude.

Using (6.15), (6.28) and (6.52), (6.53), excitation current for the second excitation mode is calculated by (6.54) as

$$I_{exc2} = v_{dc1} \cdot \frac{\pi^2 \cdot (R_f + R_{com2} + 2 \cdot R_r)}{3 \cdot \sqrt{3} \cdot M_{rs-exc} \cdot \omega_{exc} \cdot E(\pi, s \cdot (2 - s)) \cdot (R_f + R_{com1} + 2 \cdot R_r)} \tag{6.54}$$

For the ME, the impact of the armature current reaction is assumed negligible since current control is employed. In addition, the saturation effects on the $M_{rs\text{-}exc}$ are taken into account by using the 2-D look-up table obtained from Finite Element (FE) analysis instead of a constant value.

6.6.2 Second transition mode

When the machine is in rotating condition, at an optimum speed (slip) which is found by the excitation controller, the AC excitation should switch to DC excitation.

The output current of the rectifier in the third excitation mode is:

$$I_{f3} = \frac{v_{dc3}}{R_f + R_{com3} + 2 \cdot R_r} \tag{6.55}$$

From (6.28), (6.34) and (6.54), (6.55), to achieve constant MG field current (I_{f3} = I_{f2}), amplitude of DC excitation current during the third excitation phase should be:

$$I_{exc3} = v_{dc2} \cdot \frac{\pi \cdot (R_f + R_{com3} + 2 \cdot R_r)}{3 \cdot \sqrt{3} \cdot M_{rs-exc} \cdot \omega_r \cdot (R_f + R_{com2} + 2 \cdot R_r)} \tag{6.56}$$

6.7 Proposed Excitation current control

Fig. 6.9 shows the flowchart of the proposed excitation control algorithm. The method generates the proper excitation current amplitude I^*_{exc} that is provided to a closed-loop excitation current scheme using the DC-DC converter that supplies the ME excitation winding (Fig. 6.1). The closed-loop excitation current control is simple and therefore will not be analysed in this chapter.

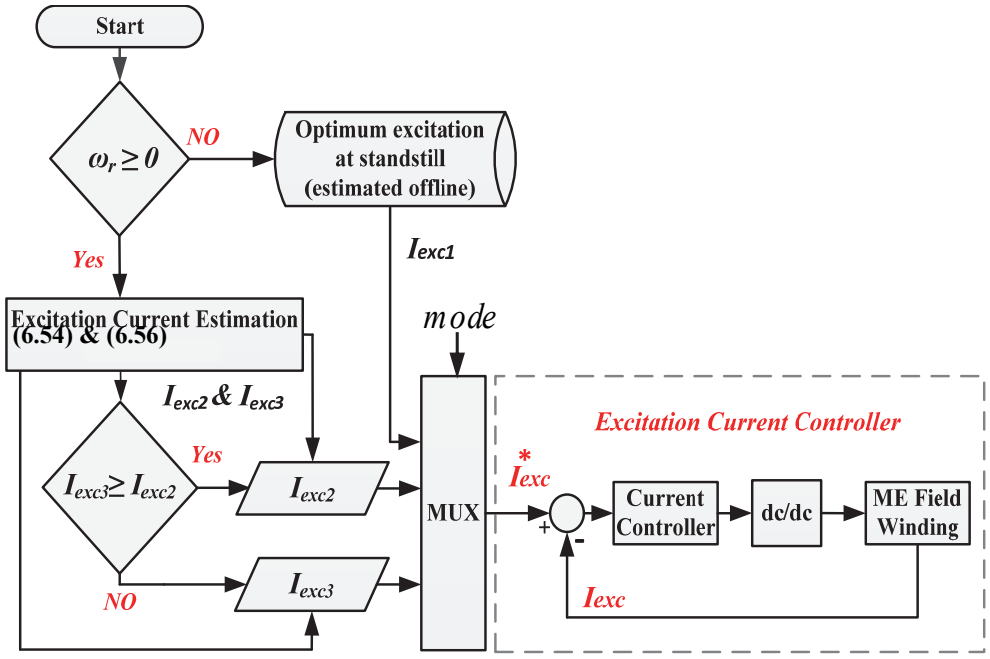

Figure. 6. 9. Structure of the proposed excitation control algorithm

The proposed excitation control uses equations (6.54) and (6.56) to calculate the required excitation current in the second and third excitation modes, I_{exc2}, and I_{exc3}, respectively. Once I_{exc3} becomes equal to I_{exc2}, the excitation switches from AC to DC.

The amplitude of the excitation reference current is obtained from three different values (MUX block in Fig. 6.9) corresponding to three operation modes described below:

At standstill (Mode 1), the DC-DC converter operates as single-phase inverter and the excitation current reference is sinusoidal having the amplitude I_{exc1}. This current reference is obtained from a preliminary experimental evaluation.

As soon as the rotor starts moving (Mode 2), the amplitude of the excitation current becomes I_{exc2}., while its frequency does not change. The amplitude I_{exc2} is calculated from (6.54). At the same time, (6.56) is evaluated.

The DC excitation is engaged when I_{exc2}= I_{exc3} (Mode 3). The I^*_{exc} becomes a DC value that is equal to I_{exc3}.

Fig. 6.10 shows the ratio of the DC excitation current amplitude (I_{exc3}) to the AC excitation current in the second excitation mode (I_{exc2}). From Fig. 6.10, it results that the ME excitation can switch from AC to DC at a value that is equal to the amplitude of the AC excitation in the second excitation mode $\left(\frac{I_{exc3}}{I_{exc2}} = 1\right)$ leading to a smooth transition.

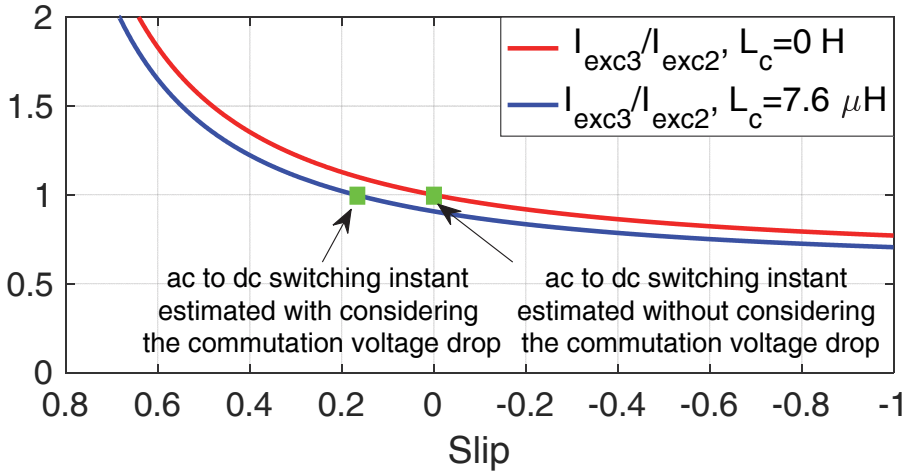

Figure. 6. 10. Ratio of controlled DC excitation current amplitude to amplitude of AC excitation current in the second excitation mode

As can be seen in Fig. 6.10, commutation voltage drop has a significant effect on the estimation of the optimum instant for excitation switching from AC to DC (the slip at which I_{exc3} = I_{exc2}). Furthermore, since in the controlled method output voltage of the rectifier is controlled to be constant, the second transient is smooth.

6.8 Simulation Results

A numerical phase variable model of the brushless exciter is built based on FE analysis using Flux-2D software (Chapter 4). Using FE technique, for all rotor positions and various current ranges, all current-flux linkage nonlinear functions have been estimated and modeled in Simulink/Matlab environment using 2-D lookup tables. These nonlinear functions have been estimated for different rotor positions and full current ranges. Hence, geometry space harmonics and saturation effects are taken into account.

Fig. 6.11, Fig 6.12, and Fig 6.13 show simulation results using the controlled and uncontrolled excitation methods for the first and second excitation modes. Excitation current at standstill is 3A, 200Hz sinusoidal current. The test is performed for initial positions of 0° and 30° which represent maximum decrease and increase of MG field current at the first transition mode. Fig. 6.11 shows the MG field current using controlled and uncontrolled excitation methods.

As can be seen in Fig. 6.11, when the initial position is 30°, at the first transition mode the MG field current suddenly decreases and when the initial position is 0°, the MG field current has an overshoot. However, using the controlled excitation method, the MG field current is kept constant.

Fig. 6.12 and 6.13 show the rotating rectifier output voltage for the same excitation as Fig. 6.11, for the uncontrolled and controlled excitation methods, respectively.

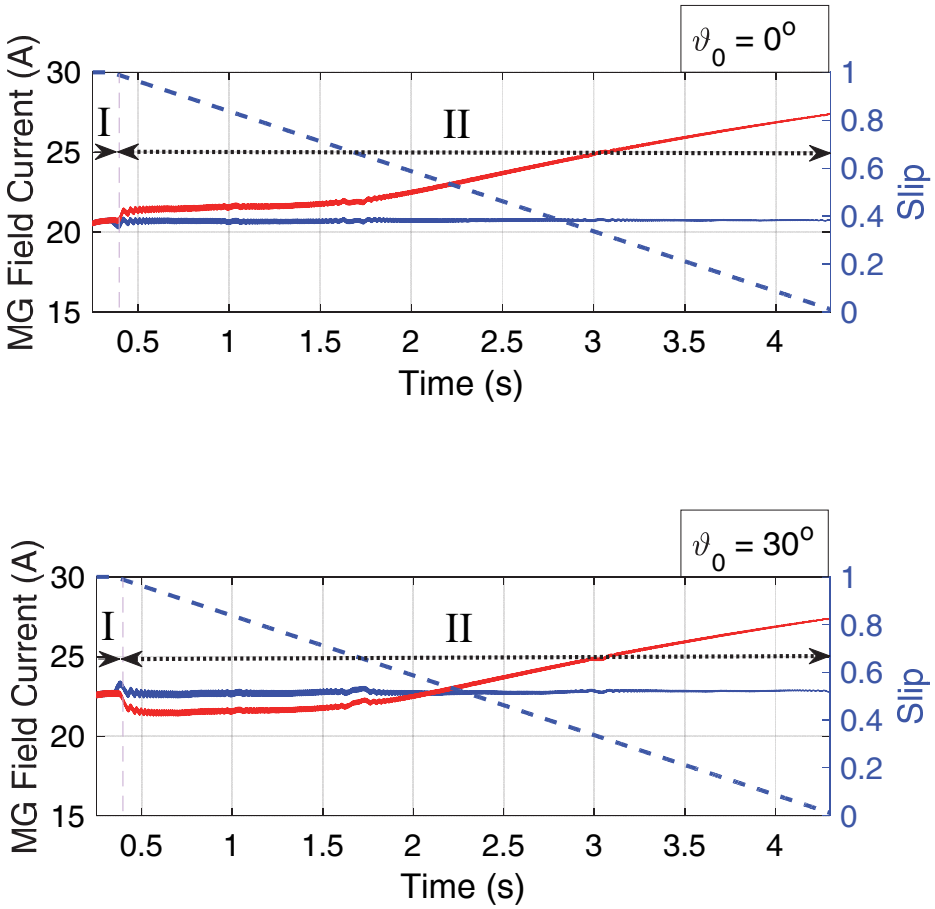

Figure. 6. 11. MG field current using the controlled and uncontrolled excitation methods

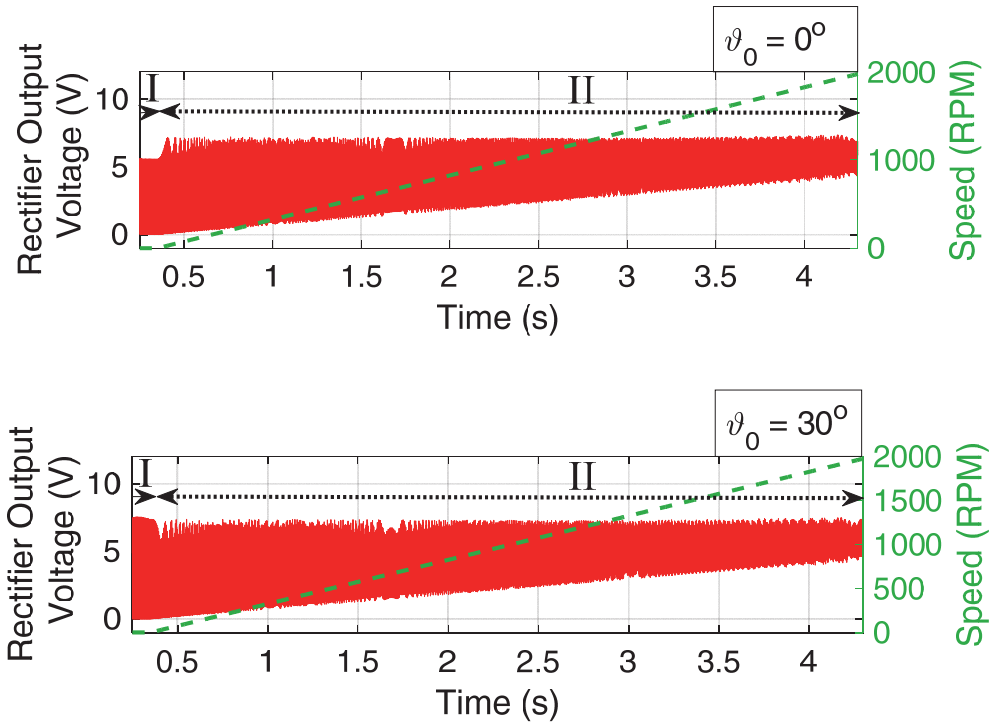

Figure. 6. 12. Rotating rectifier output voltage using the uncontrolled excitation method, ϑ_0 is 0° and 30°

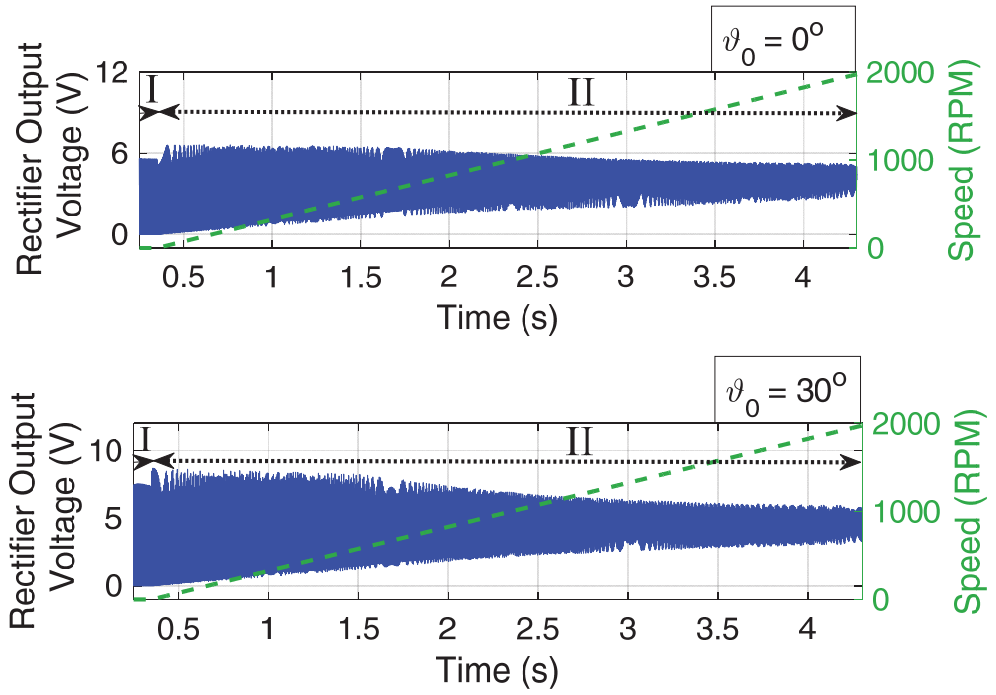

Figure. 6. 13. Rotating rectifier output voltage using the controlled excitation method, ϑ_0 is 0° and 30°

As can be seen, based on (6.54), changing the excitation current at the second excitation mode I_{exc2} led to a constant average value of the rectifier output voltage.

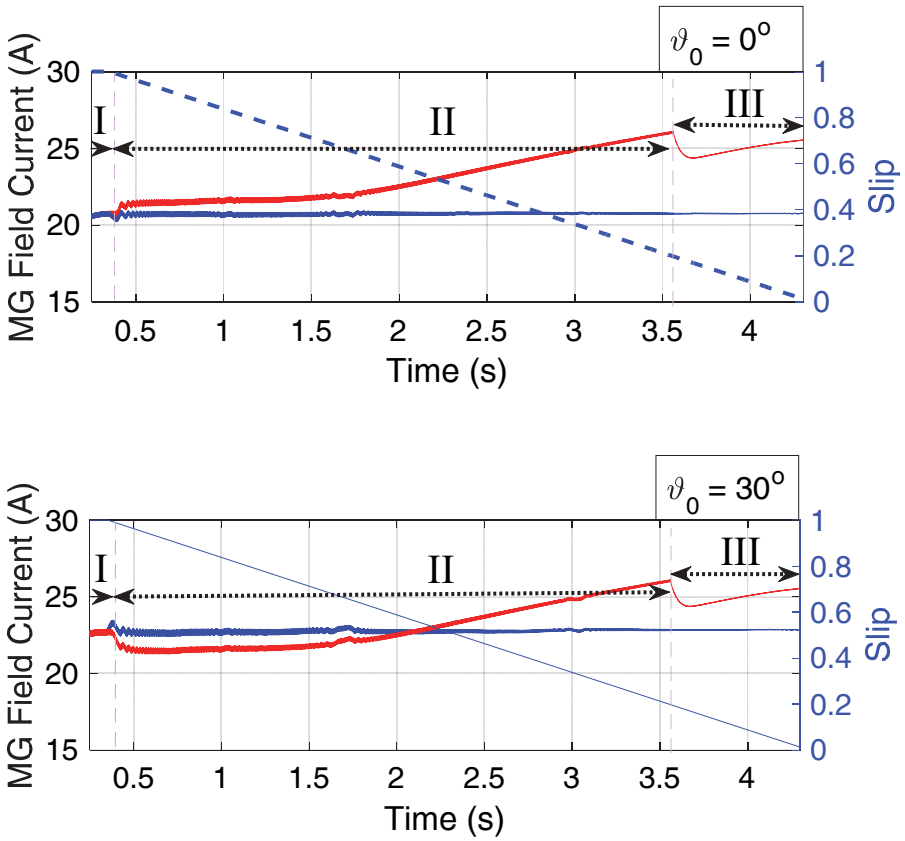

Figure. 6. 14. MG field current using the controlled and uncontrolled excitation methods

For all excitation modes, the MG field current with and without ME excitation control is shown in Fig.6.14. Fig.6.15 shows the controlled exciter field current with 0˚and 30˚initial positions.

It can be noted from Fig. 6.14 that behaviour of the MG field current without ME excitation control depends on the initial rotor position.

In order to compare the results of ME excitation with and without excitation control, at the same point as controlled excitation method, uncontrolled AC excitation (I_{exc2}) has been switched to a DC excitation current (I_{exc3}) that is equal with the amplitude of AC excitation rms current.

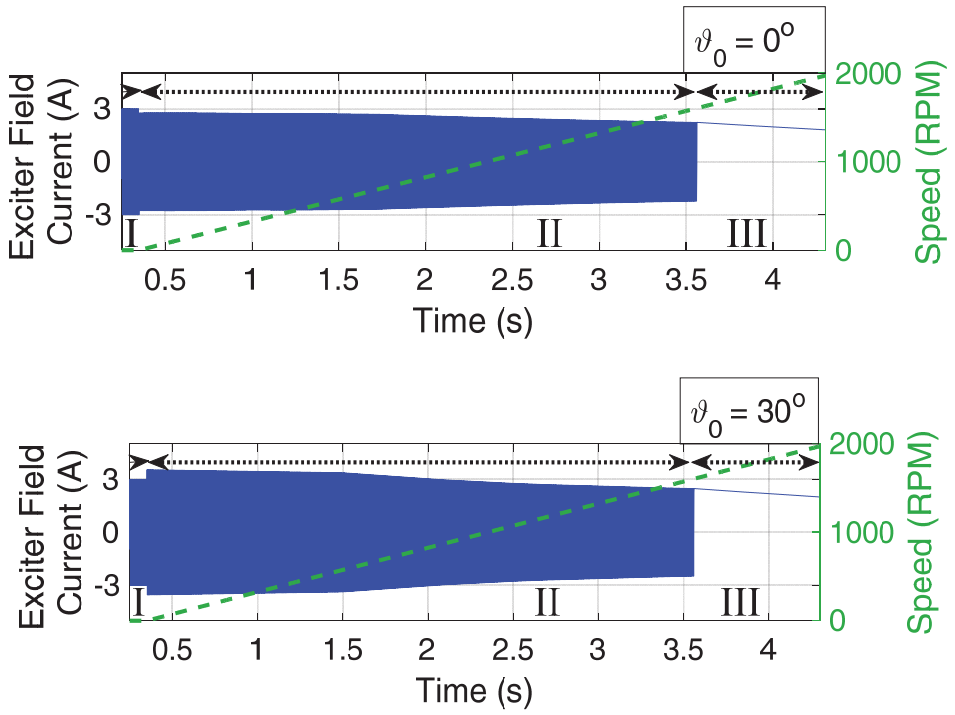

Figure. 6. 15. Controlled excitation current

The Fig. 6.16 shows the rectifier output voltage for uncontrolled excitation method for all excitation modes, when initial rotor position is 0˚and 30˚. Results of the same condition but using the proposed excitation control method are shown in Fig. 6.17.

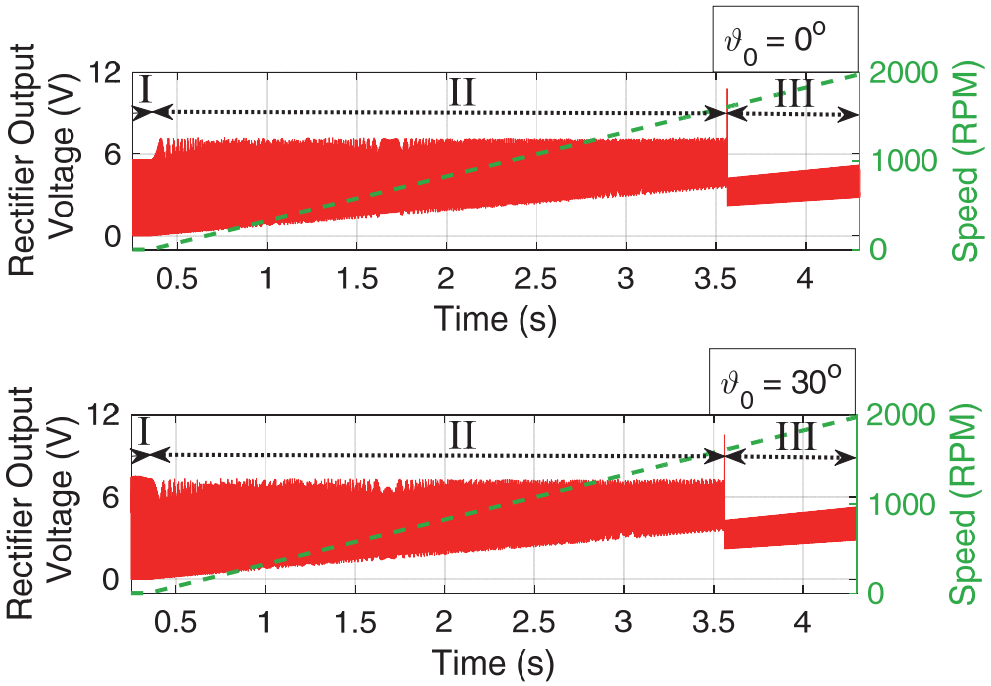

Figure. 6. 16. Rotating rectifier output voltage using the uncontrolled excitation method, ϑ_0 is 0˚and 30˚

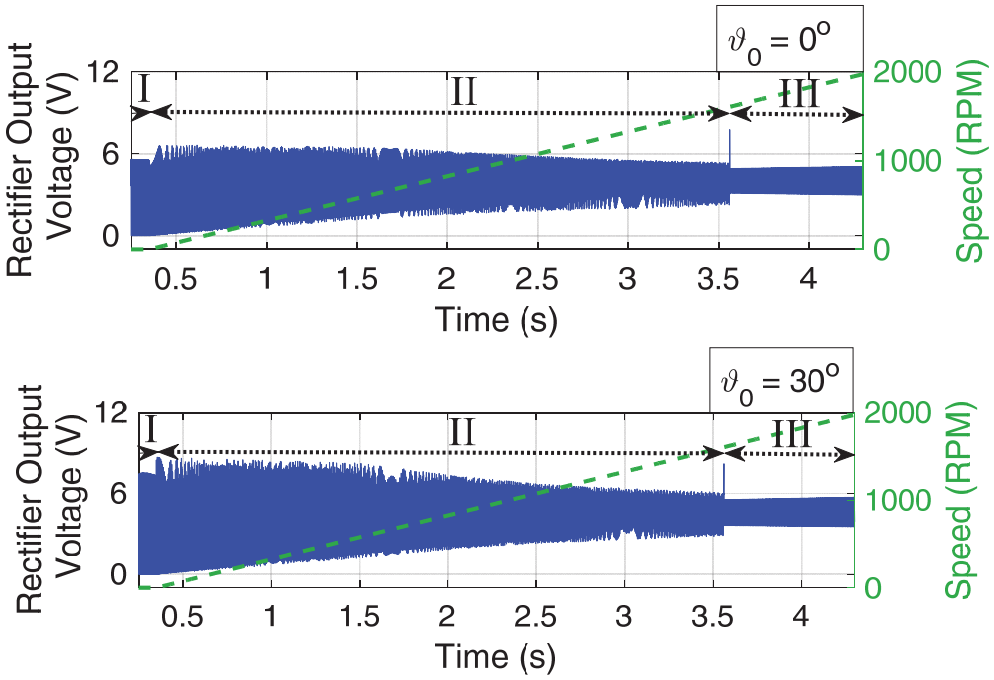

Figure. 6. 17. Rotating rectifier output voltage using the controlled excitation method, ϑ_0 is 0° and 30°

6.9 Experimental Results

To demonstrate the feasibility of the proposed excitation control, a scaled-down experimental test rig was built. The experimental setup is shown in Fig. 6.18 and consists of a two-stage brushless synchronous generator (10kVA-1500rpm) and a prime mover driven by an industrial inverter.

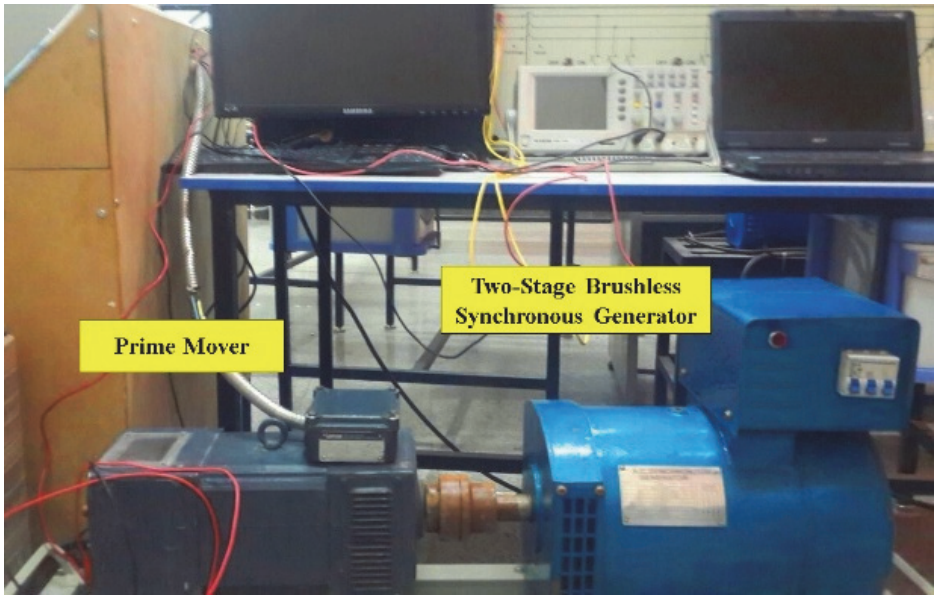

Figure. 6. 18. Experimental test rig

Since the output voltage of the rotating rectifier was not available, an indirect method was implemented to demonstrate that the MG field current has been kept constant during the entire starting process. For both controlled and uncontrolled excitation tests, whilst prime mover rotates the generator from standstill to 2000 rpm, the generator output voltages were saved at the no-load condition. For the controlled method, the excitation controller receives the reference excitation current according to the flowchart shown in Fig. 6.9.

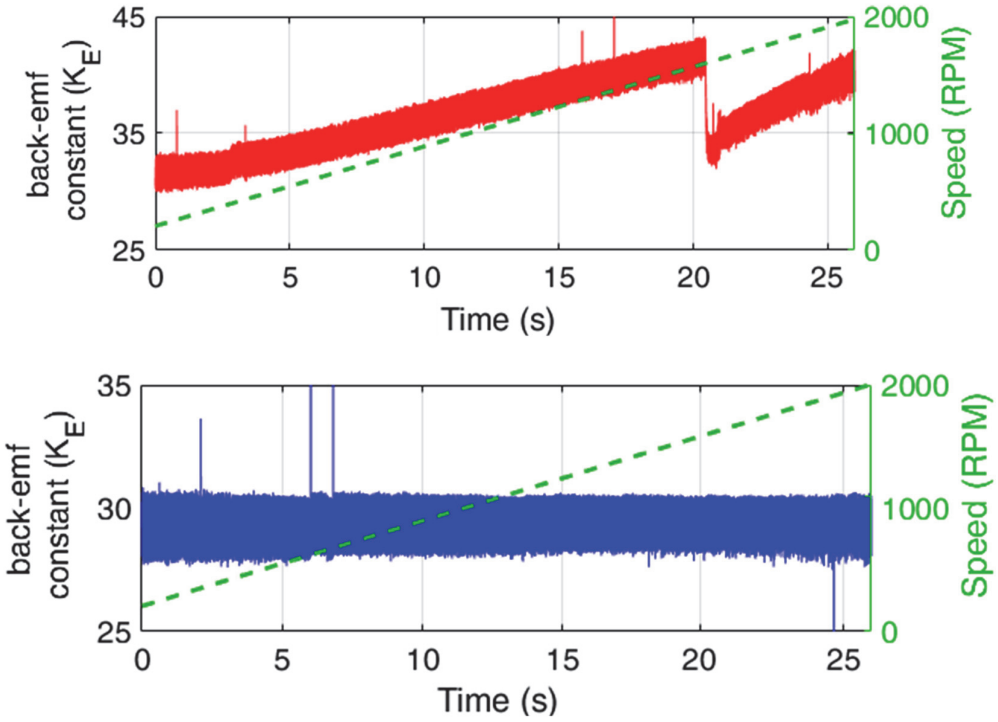

Figure. 6. 19. Back-emf constant of MG output voltage (KE) using the uncontrolled and controlled excitation methods

Then a post-processing was performed as follows. The three-phase voltages were transformed to (d,q) voltages and then d-axis voltage quantity was divided by speed and multiplied by 100. The resulting quantity is the back-emf constant defined as

$$K_E = \frac{V_d}{N_r} \cdot 100 \tag{6.57}$$

where N_r is rotor speed in RPM.

In this test, for uncontrolled excitation method, the amplitude of reference field current is 0.7A and its frequency is 200Hz. The prime mover rotates the MG from 0 to 2000 rpm in 30 seconds. After the implementation of the proposed excitation control strategy, the speed at which excitation current switched from AC to DC was captured. This speed was used for uncontrolled excitation case for the switching between AC and DC excitation. In the uncontrolled excitation test, the amplitude of DC excitation current is the rms value of AC excitation current.

For controlled excitation test, excitation current reference at standstill was set at 0.7 A. At 2000 RPM, excitation current reference determined by excitation controller was 0.5 A.

Fig. 6.19 shows the back-emf constant, after post-processing the saved data, for uncontrolled and controlled excitation methods. Since at standstill and very low speeds, the captured data were very noisy, Fig 6.19 shows the waveform of the back-emf constant from almost 200 RPM.

As can be seen in Fig. 6.19, under controlled excitation method, the back-emf constant does not change by increasing the rotation speed, so it can be concluded that the MG field current is constant. Moreover, the results demonstrate that using the ME excitation current control, the second transition (ME excitation current switching from AC to DC) is smooth.

Chapter 7

Field Current Estimation of Main Generator

7.1 Introduction

Accurate and optimum torque control of the three-stage brushless synchronous starter-generator in start process requires a current map of MG. The current map determines optimum combination among MG field current, and MG stator currents according to the load conditions. Among the currents in the current map, MG field current is of most importance and has a critical impact in choosing the optimum currents combination. The saturation level of the MG rotor varies according to the MG field current. In addition, MG field current significantly affects direct-axis (L_d) and quadrature-axis (L_q) inductances. By virtue of the MG field current importance in torque control of the three-stage brushless synchronous starter-generator, accurate information of the MG field current is a prerequisite of a successful control system.

In brushless electric machines, the field current is not accessible. One possible solution for rotor current data acquisition is to mount a sensor on the rotor. Measured data can be transferred from the rotor by using wireless data transfer technologies such as Bluetooth [111] and Wi-Fi [112]-[114]. Due to electromagnetic interference (EMI) generated by the magnetic field of the machine and also power electronic parts, the performance of wireless data transfer systems for rotor data measurement encounters serious disturbances and malfunction. Since reliability is a critical requirement for starter-generator in the aircraft application, wireless rotor data measurement technique is not feasible for brushless synchronous starter-generator.

Consequently, MG field current must be estimated. To the best knowledge of the author, in the literature, no method has been proposed for estimating MG field current of the three-stage brushless synchronous machine using single phase main exciter.

Since MG mostly operates in saturation state of its magnetic field, MG field current from MG side of the three-stage brushless synchronous machine is not feasible. especially, during the starting process where high torque is required, and MG stator currents are high, saturation effects are more significant. Therefore, it is more reasonable and convenient to estimate the MG field current from the exciter side of the machine. In [115], two methods are proposed for the machine using the main exciter with three-phase field winding. The first method relies on estimating the rotor currents of the main exciter. From the estimated rotor currents, using a simple and inaccurate model of diode bridge rectifier, the MG field current was estimated. In the second method, first, rotor voltages of the main exciter are estimated. Then using the former-mentioned model of the diode bridge rectifier, the output voltage of the rotating rectifier is estimated. Then by knowing MG field winding resistance, MG field current is calculated.

In [116], an estimation method for MG field current is proposed. The proposed method again is applicable for three-phase main exciter. In the proposed method, both currents and voltages of the main exciter are estimated. Then they are considered as input voltages and currents of the rotating rectifier model. The proposed method relies on a Parametric Average Value Model (PAVM) of the rotating diode bridge rectifier. In the PAVM modeling technique, the diode bridge rectifier is modeled as a variable impedance. This impedance is estimated from a dataset saved in a 2-D look-up table. Look-up table data is provided from a detailed simulation in different operating conditions. It is like training data collection step of Artificial Neural Network (ANN) learning process. Inputs of the look-up table used for modeling the rotating rectifier are rotor currents and voltages. Since the frequency of the rotor's quantities are changing and as it has been mentioned and analyzed in Chapter. 3, the frequency of input voltages plays a critical rule in the performance of a diode bridge rectifier. Therefore, representing the rotating rectifier as a variable impedance is not feasible. Especially in the starting process where high MG field current is required, inaccuracy of the proposed model is more significant. As a potential solution, a 3-D look-up table having exciter's rotor currents, voltages and frequency as its inputs can provide more accuracy in estimating of the MG field current.

In this chapter, an estimation method for MG field current estimation is proposed. In the proposed estimation method, estimation of exciter rotor currents and voltages are not required. This leads to the increasing of the accuracy of the proposed MG field current estimation method.

7.2 Proposed MG field current estimation

From Chapter. 4, the voltage equation of the field winding of the main exciter is:

$$v_{exc} = r_f \cdot i_{exc} + \frac{d}{dt}\Big[L_{ff} \cdot i_{exc} - M_{rs} \cdot i_a \cdot \cos(\omega t) - M_{rs} \cdot i_b \cdot \cos\Big(\omega t - \frac{2\pi}{3}\Big) - M_{rs} \cdot i_c \cdot \cos\Big(\omega t + \frac{2\pi}{3}\Big)\Big] \quad (7\text{-}1)$$

Based on relationships between input currents of the rotating rectifier (i_a, i_b, and i_c) and its output current (i_f), from Chapter. 3, (7.1) can be rewritten as:

$$v_{exc} = r_f \cdot i_{exc} + \frac{d}{dt}\Big[L_{ff} \cdot i_{exc} - M_{rs} \cdot i_f \cdot S_a \cdot \cos(\omega t) - M_{rs} \cdot i_f \cdot S_b \cdot \cos\Big(\omega t - \frac{2\pi}{3}\Big) - M_{rs} \cdot i_f \cdot S_c \cdot \cos\Big(\omega t + \frac{2\pi}{3}\Big)\Big] \quad (7\text{-}2)$$

Factoring of i_f in (7.2), and integrating of both sides yields:

$$\int\big(v_{exc} - r_f \cdot i_{exc}\big) = L_{ff} \cdot i_{exc} - i_f \cdot M_{rs} \cdot \Big[S_a \cdot \cos(\omega t) - S_b \cdot \cos\Big(\omega t - \frac{2\pi}{3}\Big) - S_c \cdot \cos\Big(\omega t + \frac{2\pi}{3}\Big)\Big] \quad (7\text{-}3)$$

The maximum value of the term in the bracket in the right side of (7-3), except at standstill, always is the square root of three. At standstill, knowing the rotor position, its value can be calculated by using predefined functions presented in Table 6.1(chapter 6). The formula for calculation of the MG field current is:

$$i_f = \frac{envelope[L_{ff} \cdot i_{exc} - \int(v_{exc} - r_f \cdot i_{exc})]}{\sqrt{3} \cdot M_{rs}} \quad (7\text{-}4)$$

where v_{exc} and i_{exc} are measured.

To achieve an accurate estimation of the MG field current, self-inductance of field winding and mutual inductance between field and armature of the main exciter must be calculated. As mentioned in Section. 1, in the case of exciter which has low magnetic loading, these inductances accurately can be calculated.

The numerator of (7-4) can be calculated by various methods. One can be Hilbert transform [117]-[119]. In this thesis, the numerator of (7-4) is calculated as follows.

The frequency of the numerator of (7-4) is equal to excitation voltage frequency (f_{exc}) which is known. Delaying the numerator of (7-4) by the quarter of its period, the second signal can be obtained which is in quadrature with the original signal. Then, these signals must be transformed into the DQ rotating frame. *d*-axis quantity of the transformation is the envelope of the numerator of (7-4). Fig.7.1 shows the block diagram of the proposed MG field current estimation.

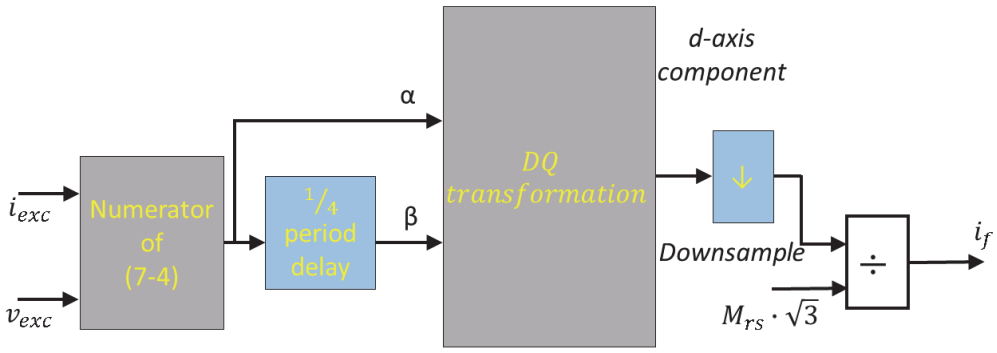

Figure. 7. 1. Block diagram of the proposed MG field current estimation method

7.3 Validation of the proposed MG field current estimation.

To validate the effectiveness of the proposed MG field current estimation method, simulation and experimental tests in steady state and transient conditions are performed.

7.3.1 Simulation Results

In the simulation study, first, at standstill, field winding of the exciter is fed by 60v, 200 Hz excitation voltage while the MG stator d-axis current is 20A and its q-axis current is 40A. Then, at *t=0.55 s*, rotation speed starts to increase. At *t=1s*, speed is 135 *RPM*. This test is performed for the machine in different standstill initial positions. Fig. 7.2 shows the simulation results when the initial position is 0̊, and 30̊. In this section, estimated MG field current is indicated by $i_{f\text{-}est}$.

Performance of the proposed method in a transient condition where excitation voltage suddenly changes is shown in Fig. 7.3. In this test, at $t = 0.8s$, excitation voltage (v_{exc}) is changed suddenly from 60 v to 40 v. Then, at $t = 1.5\ s$, the excitation voltage is changed from 40 v to 65 v. As can be seen in Fig. 7.3, the estimated MG field current follows real waveform of the MG field current. Fig. 7.4 shows the simulation results for another transient condition. In this test, the excitation voltage is kept constant at 60 v, 200 Hz. At $t = 0.8\ s$, MG stator current is increased suddenly and at $t = 1.5\ s$, back to its previous value. Again, it can be derived from the results that the proposed method is successful in following the reals MG field current.

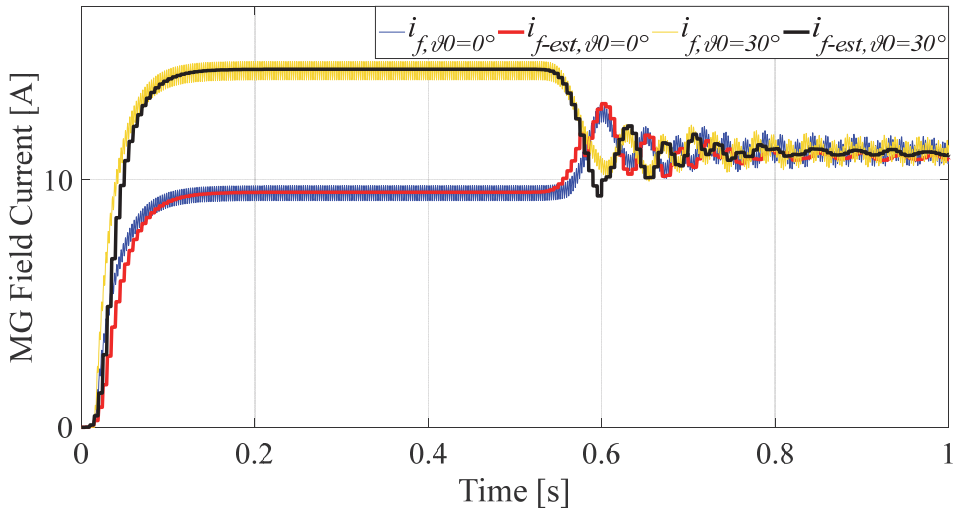

Figure. 7. 2. Real and estimated MG field current for different standstill initial positions

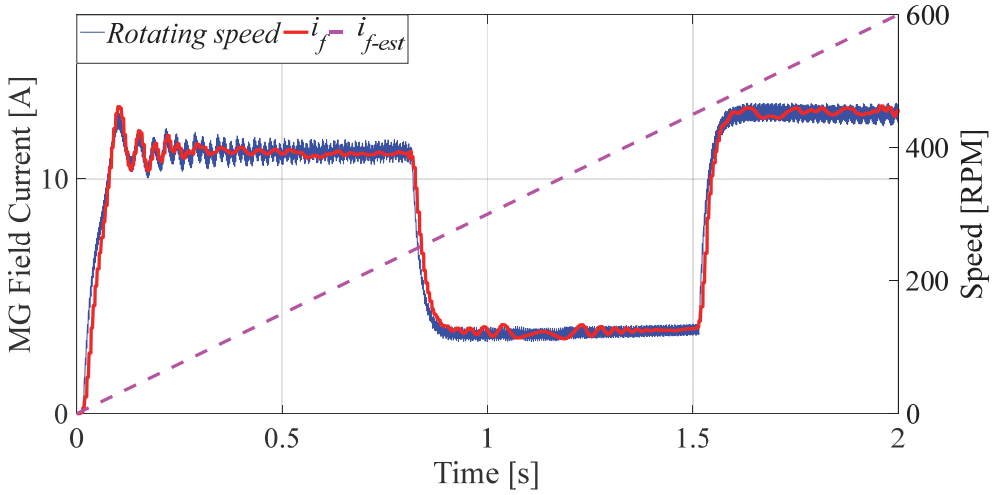

Figure. 7. 3. Real and estimated MG field current when excitation voltage is change suddenly

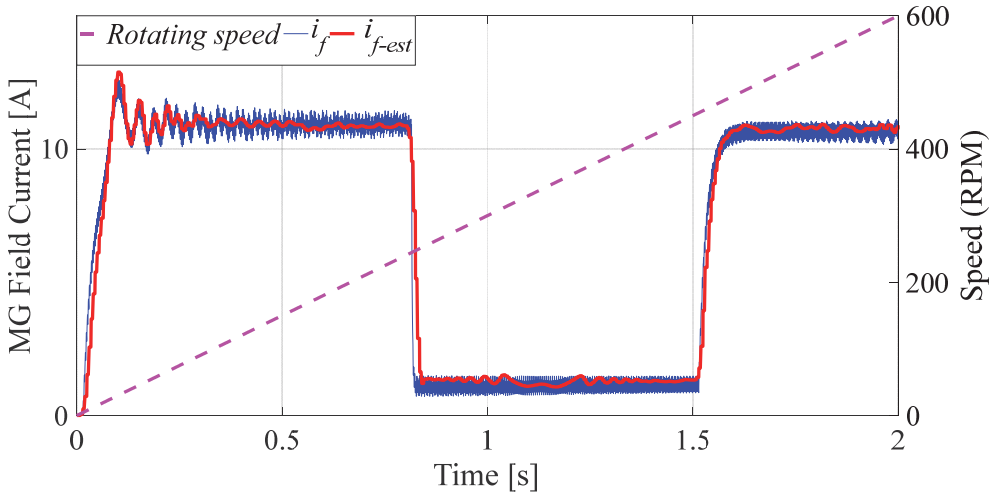

Figure. 7. 4. Real and estimated MG field current when MG stator currents or MG field resistance is changed suddenly

7.3.2 Experimental Results

In this section, in order to demonstrate the accuracy of the proposed MG field current estimation method, experiments in steady-state and transient are performed. The test rig consists of a DC machine as the prime mover and a wound-rotor asynchronous machine. Field windings (rotor windings) of the asynchronous machine are supplied through slip-rings and its armature windings (stator windings) are connected to a series R-L load through an uncontrolled diode bridge rectifier. *R-L* load emulates Field winding of the MG. In this manner, measuring MG field current and excitation current of the exciter are possible. Fig 7.5 shows the experimental setup.

In order to cover all excitation modes, four different steady-state and transient tests are carried out as follows:

1) Case. 1: Step-changes of the excitation voltage at standstill with AC excitation (*excitation mode. 1*)

2) Case. 2: Step-changes of the excitation voltage at low speed with AC excitation (*excitation mode. 2*)

3) Case. 3: Steady-state DC excitation at high speed (*excitation mode. 3*).

4) Case. 4: Step-change of the rotating rectifier loading condition (*emulating step change of d-axis current of the MG's stator currents*).

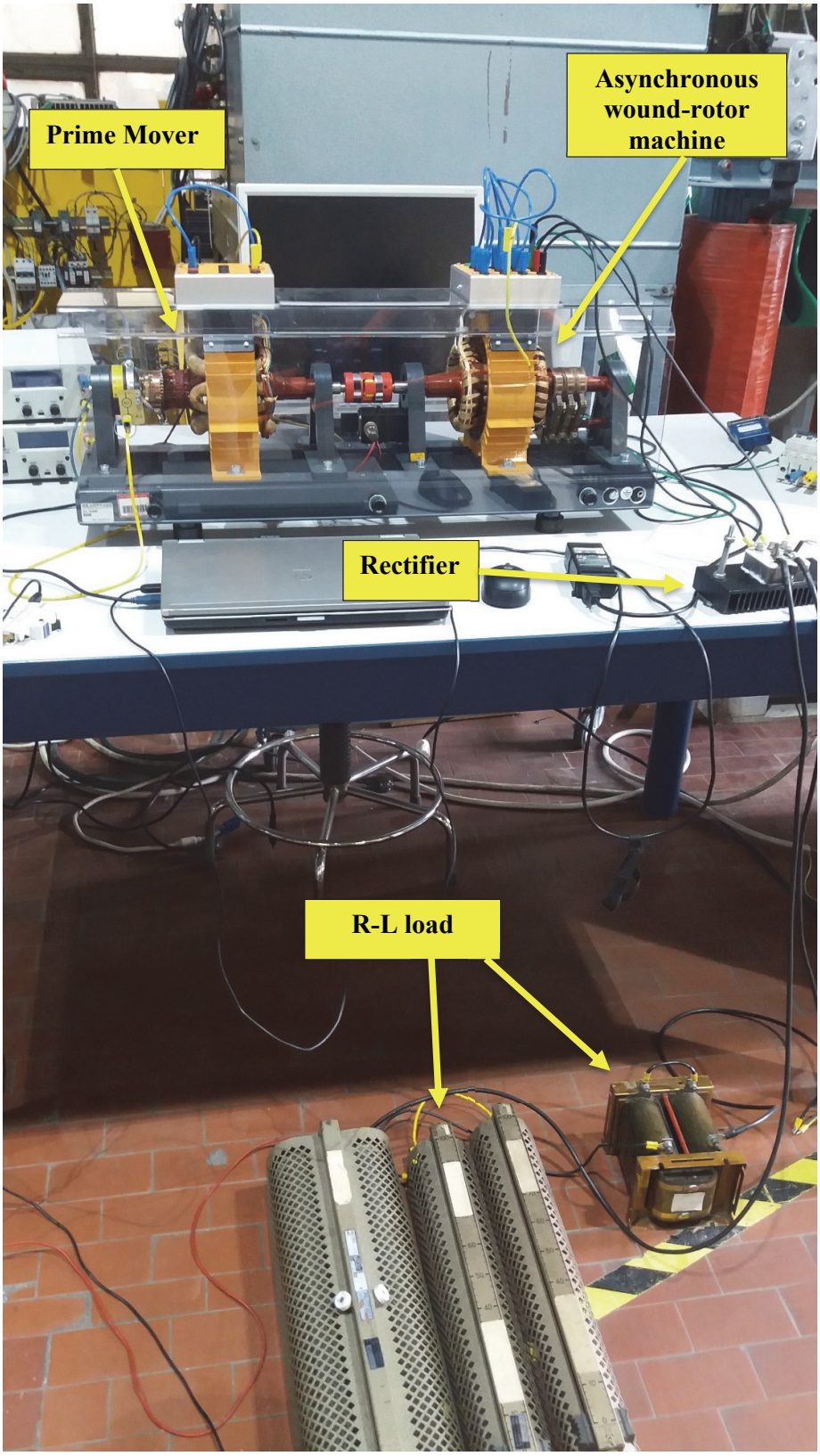

Figure. 7. 5. Experimental test platform

7.3.2.1. Case. 1: step-changes of the Excitation voltage at standstill with AC excitation (excitation mode. 1):

In this test, the machine was at standstill. First, the field winding of the exciter was supplied by 12.5 v @ 400 Hz. Then, at *t=0.713 s*, magnitude of the excitation voltage was instantly changed to 27.6 v. The third step-change of the excitation voltage occurred at *t= 1.694 s* where magnitude of the excitation voltage was changed from 27.6 v to 18.8 v. The measured waveforms of the excitation voltage, excitation current, and MG field current are shown in Fig. 7.6. Comparison between the measured MG field current and the estimated MG field current is depicted in Fig 7.6.

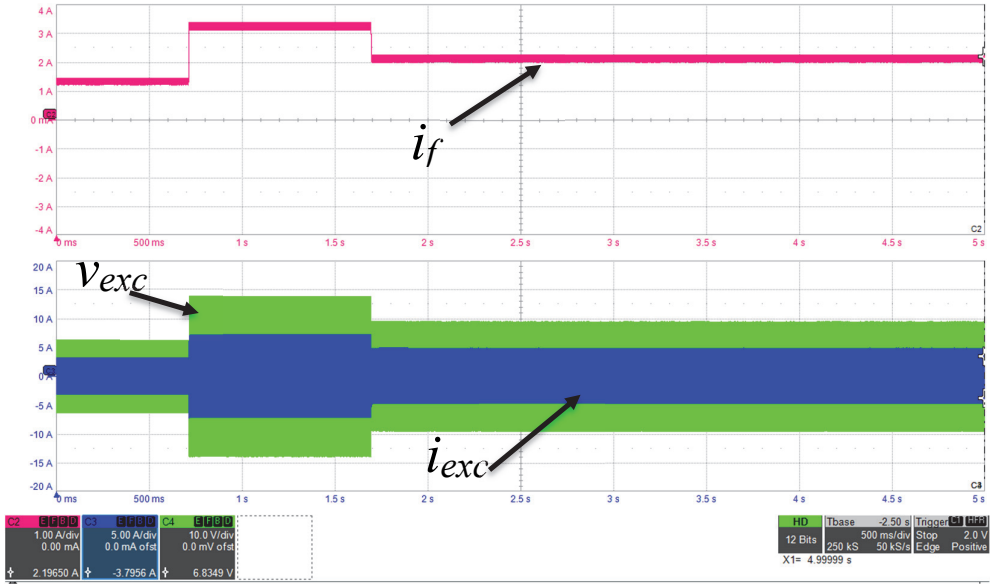

Figure. 7. 6. Measured field voltage and current of the exciter and field current of the MG at the first excitation mode under step-change of the excitation voltage

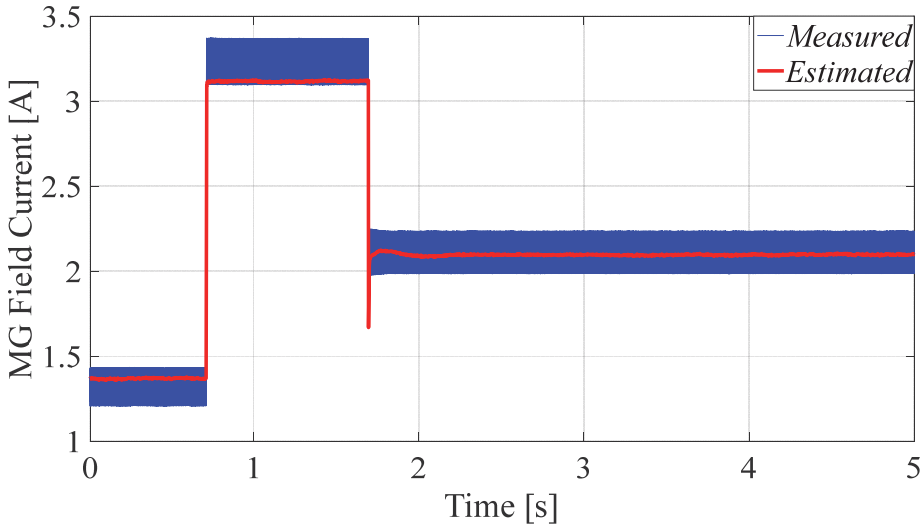

Figure. 7. 7. Comparison between measured and estimated field current of MG at the first excitation mode under step-change of the excitation voltage

As can be seen in Fig. 7.7, since the mutual inductance between field and armature windings of the exciter (M_{rs_exc}) was considered as a constant value (without considering the saturation effect), for the higher value of the MG field current (when the excitation voltage is 27.6 v), the estimated MG field current seems not equal to the mean value of the MG field current. So, in order to improve the accuracy of the estimation technique, inductance profile in accordance with the excitation current is required.

7.3.2.2. Case. 2: Step-changes of the excitation voltage at low speed with AC excitation (excitation mode. 2)

In this test, speed of the machine was set at 2180 RPM. First, field winding of the exciter was supplied by 18.8 v @ 400 Hz. Then, at $t = 1.973\ s$, the excitation voltage was instantly changed to 12.5 v. At $t= 2.975\ s$, the excitation voltage was changed to 27.6 v and at $t= 3.956\ s$ it was backed to 18.8 v. The measured MG field current and field voltage and current of the exciter are shown in Fig. 7.8. comparison between measured and estimated MG field current is depicted in Fig. 7.9.

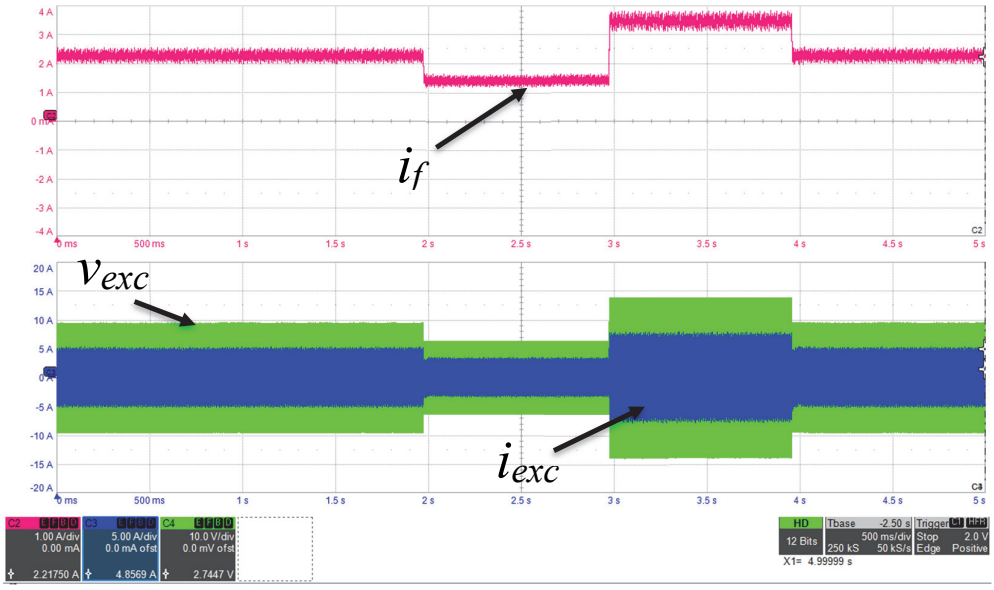

Figure. 7. 8. Measured field voltage and current of the exciter and field current of the MG at the second excitation mode under step-change of the excitation voltage

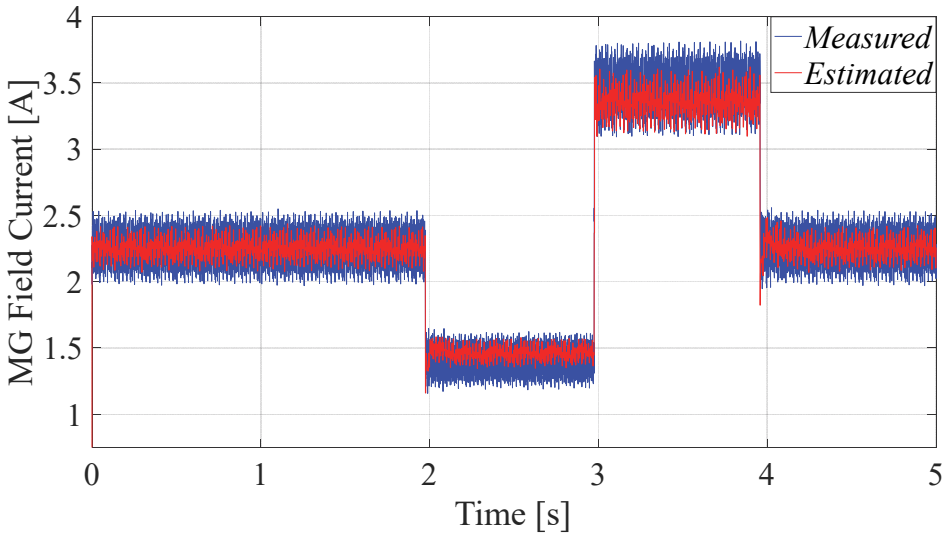

Figure. 7. 9. Comparison between measured and estimated field current of MG at the second excitation mode under step-change of the excitation voltage

7.3.2.3. Case. 3: Steady-state DC excitation at high speed (excitation mode. 3).

Experimental test in steady-state was carried out with exciting the field winding of the exciter by 5.4 A at *2870 RPM*. Measured MG field current and the exciter field voltage and current are shown in Fig. 7.10. Comparison between measured and estimated MG field current is shown in Fig. 7.11.

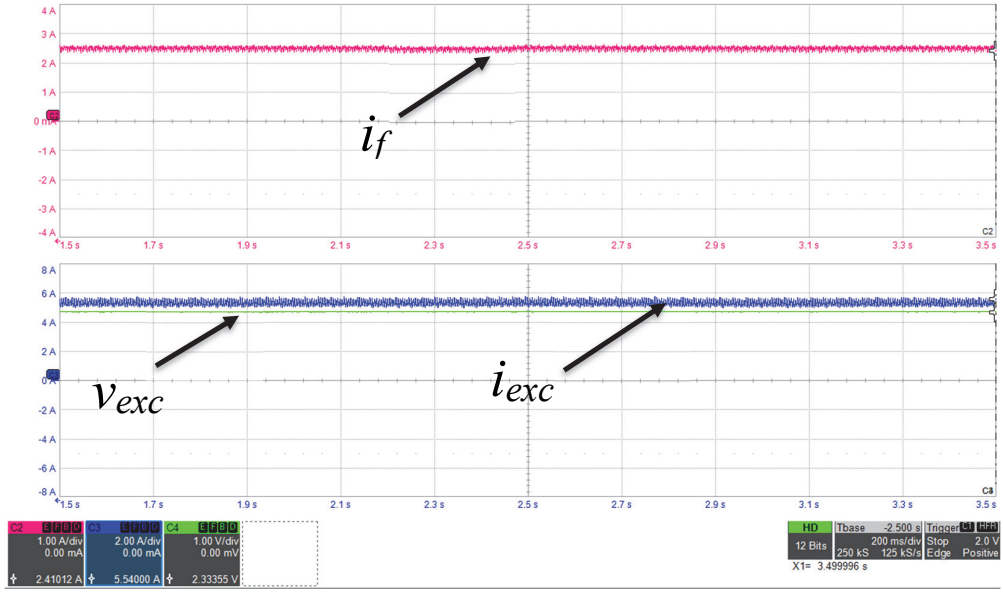

Figure. 7. 10. Measured field voltage and current of the exciter and field current of the MG at the third excitation mode

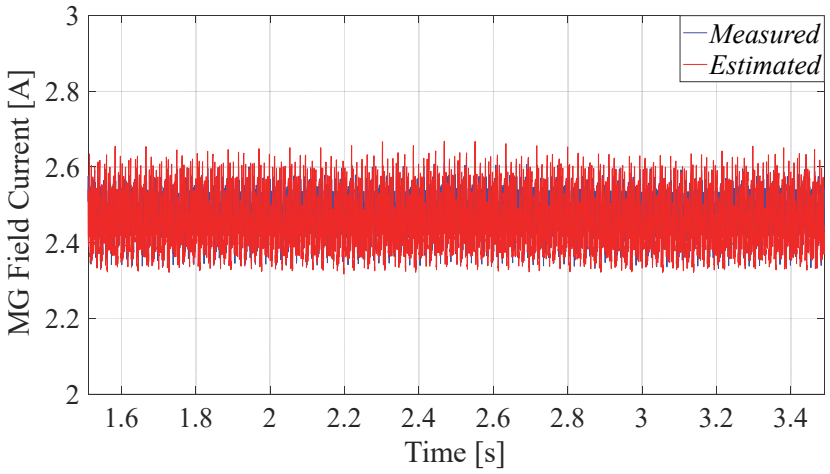

Figure. 7. 11. Comparison between measured and estimated field current of MG at the third excitation mode

7.3.2.4. Case. 4: Step-change of the rotating rectifier loading condition (emulating step change of d-axis current of the MG's stator currents).

In this test, at the second excitation mode where rotor speed was 2400 *RPM*, load resistor of the rectifier was changed from one value to another value while the excitation voltage was kept constant. This load change emulates back-emf change in the MG field winding due to suddenly change of stator currents of MG. In this test, the load resistor was set at 0.5 Ω, then at $t= 1.711\ s$, the load resistor was suddenly changed to 19.27 Ω. In accordance with (7.4), by decreasing the MG field current, the excitation current was forced to decrease. Measured MG field current and the exciter field voltage and current are shown in Fig. 7.12. Comparison between the measured MG field current and the estimated MG field current is depicted in Fig 7.13.

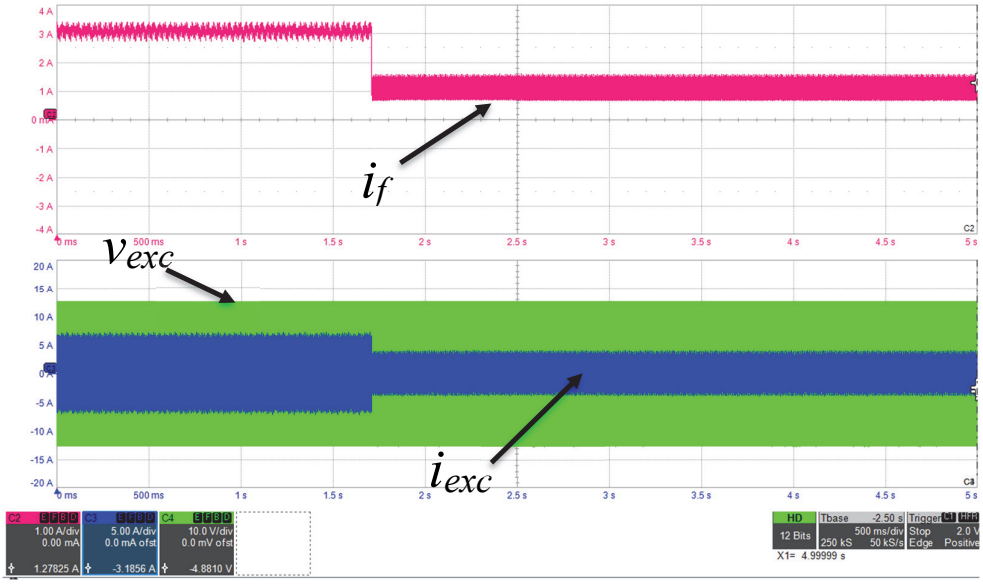

Figure. 7. 12. Measured field voltage and current of the exciter and field current of the MG under step-change of the rectifier load

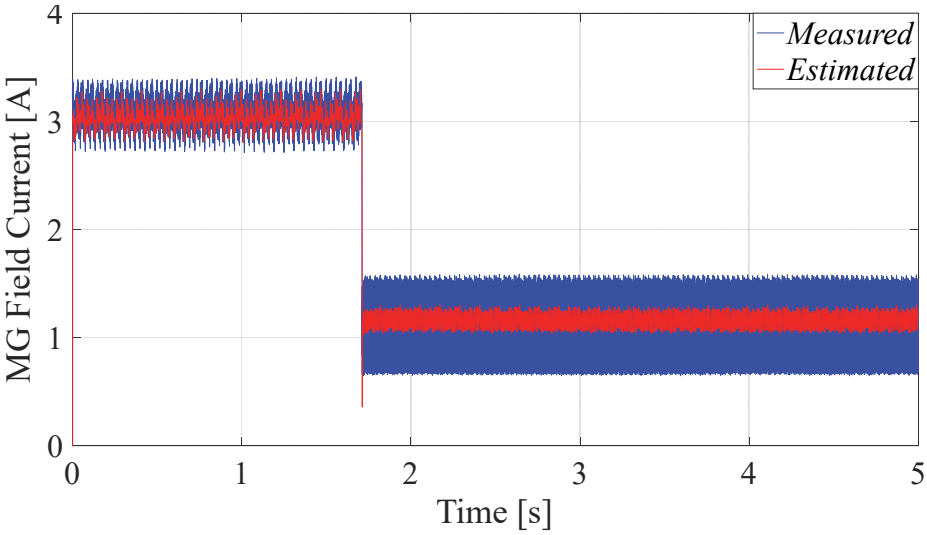

Figure. 7. 13. Comparison between measured and estimated field current of MG under step-change of the rectifier load

Chapter 8

Conclusions

8.1 Summary and Contributions

In this thesis, performance of the three-stage brushless synchronous machine as starter-generator has been investigated and two excitation control methods were proposed. As the first step, two models of the three-stage brushless synchronous machine based on switching function technique have been presented. To provide an analytical framework to determine and conceptualize relationships between field excitation of the ME and field current of the MG, the analytical equations governing ME, the rotating rectifier, and MG have been developed. These equations were developed for different operation modes of the three-stage brushless synchronous machine which have been defined in accordance with rotation speed and ME's field excitation type (AC and DC). Exploiting the analytical formulas, for the first time, various phenomena which are occurred during start-up process of the three-stage brushless synchronous machine have been defined, namely unbalanced armature voltages of ME, harmonics of armature voltages of ME, and transients of MG field current. The analytical framework also provides a possibility to find an optimum instant for ME's field excitation switching from AC to DC. In addition, using the developed switching function method for the rotating rectifier, a novel technique for estimating and control the field current of MG has been proposed. Contributions of the thesis are as follows.

In **Chapter. 1**, the motivations behind the research were presented by describing aircraft's power system, start-up process requirements of the starter-generator, and influence of the rotating rectifier in the performance of the three-stage brushless synchronous starter-generator. The limitations of the available solutions were explained, and goals of the thesis were outlined.

Chapter. 2 presented applications of the power electronics in the aircraft distributed power system. In accordance with the severely unbalanced voltages which are induced in the armature windings of the ME and were described in Chapter. 1, in **Chapter 3** two novel models of the rotating rectifier have been proposed. The proposed models are capable to consider any kind of input voltage unbalanced conditions and harmonics. Contributions presented in Chapter. 3 are as follows:

- Correct voltage and current switching functions of the uncontrolled diode bridge rectifier in the time- and DP-domain have been presented. In Section 3.10, it was analytically described that the presented switching functions of the uncontrolled diode bridge rectifier under balance voltage condition in the literature were resulted from a miscalculation in Fourier series calculation of switching functions.
- The proposed models in this chapter are presented in both time- and DP-domains. While the time-domain model has fast dynamic, the DP-domain model offers flexible accuracy and efficient performance in respect of required computation time.
- The phenomenon of uneven commutation intervals under unbalanced voltage conditions has been presented and proper equations to calculate commutation interval time between phases has been proposed. This phenomenon has not been addressed in the literature.
- A new model of the uncontrolled diode bridge rectifier in unbalanced condition based on the switching function method in time-domain and DP-domain has been presented. The presented models in the literature use fixed switching functions with constant switching intervals. In Chapter 3, it was described that based on magnitude and phase of the input voltages the corresponding switching functions are varied under different input voltages. So, in this chapter, a novel technique has been presented to recalculate and update the switching functions in accordance with the input voltages.
- Unbalance factor (amount of unbalance) does not affect performance of the proposed model. Therefore, the proposed model can deal with wide range of unbalance and fault conditions.
- Considering all harmonics of the AC-side, two new methods for modelling of the uncontrolled diode bridge rectifier were proposed.
- Unlike other method in time-domain and DP-domain presented in the literature, performance of the proposed model is not limited by amplitude of harmonics even when due to harmonics presence, phase sequence of AC-side voltages changes. Therefore, for the case of modelling and investigation of three-stage brushless synchronous machine, the proposed models are able to fully and accurately describe the relationships between AC-side (armature windings of ME) and DC-side (field winding of MG) of the rotating rectifier.

In **Chapter 4** two phase-variable models of the brushless exciter machine were proposed. The first model employs look-up tables and interpolation technique to

extract magnetic characteristics of the machine from the datasets obtained from the FE analysis. The second model, uses Fourier series for harmonics mapping of machine's inductances with considering geometry dependencies and saturation effects. Both models of the ME are connected to the model of the rotating rectifier proposed in Chapter 3. The switching function model of the rotating rectifier provides interfacing between ME armature windings and MG field winding. Using the proposed model of the rotating rectifier, it is possible to describe interactions between the ME and MG.

For further investigations and validations**,** in **Chapter 5** some experimental tests were implemented on a 25kw three-stage brushless starter-generator as following**:**

- An experimental procedure for magnetic mapping of a given three-stage brushless synchronous starter-generator was presented.
- Magnetic maps of the starter-generator were extracted experimentally.
- From obtained magnetic maps, MTPA profile of the starter generator was estimated. Also, profiles of inductances were estimated.
- To validate the experimental magnetic mapping procedure, several tests based on torque and speed controls were performed.

In addition to the presented numerical models of ME and MG in Chapter 4, in **Chapter 6** an analytical framework for ME and MG was developed. Considering the single-phase field winding of the ME, the governing equations of the ME and MG were obtained using the revolving fields theory. These equations were presented in *abc* frame to provide better conceptual presentation of the ME's armature voltages which are input voltages of the rotating rectifier. The presented equations of the armature voltages of ME were derived as function of excitation current, excitation frequency and slip of the machine. Other contributions of this chapter are as follows:

- According to the field excitation of ME, three excitation modes for the starter-generator were defined. For each excitation mode, based on the methods presented in Chapter 3, average value of the rotating rectifier output voltage was calculated.
- At standstill, dependency of the generated MG field current to initial rotor position is explained and defined analytically.
- Two transitions modes of MG field current were defined and explained analytically.
- A new universal excitation control procedure for brushless synchronous starter-generator was proposed. The proposed method is valid for generators employing single-phase stator exciter. During entire starting

process, the proposed excitation control can keep MG field current constant by means of controlling the excitation current. Therefore, the proposed excitation control leads to a constant and known MG field current. This feature improves controllability of the ISG during starting.

Knowing the MG field current, MTPA profile is able to estimate optimum combinations of MG stator currents with respect to reference torque.

- Also, in the proposed excitation control, suppressing of MG field current transitions was considered.
- Based on the presented methods in the literature, the instant at which field excitation of ME can be changed from AC to DC usually is determined from experimental offline tests. One major drawback of the method based on experimental tests is that it is not generic and only is applicable to the tested machine. To the best knowledge of the author, for the first time, optimum instant for the excitation switching from AC to DC has been determined analytically in this thesis. In addition, two transient modes of the MG field current were defined and described analytically. Using the proposed method for determining the optimum switching instant of the ME's field excitation, a seamless transition of the MG field current was obtained.
- The effectiveness and feasibility of the proposed excitation control were validated by the experimental tests.

In **Chapter 7,** a novel and accurate MG field current estimation has been proposed. The presented estimation method can be used to control the MG field current by means of controlling the field excitation of the ME. Using the proposed method, MG field current is controllable; so, one degree of freedom is added for the control purpose. Simulation and experimental test were implemented to validate the proposed MG field current estimation technique.

8.2 Future Work

The research presented in this thesis may be developed and continued in some directions. The following concepts are currently under consideration by the author.

- **Improving the parametric average-value model of the uncontrolled rectifier.**

  In the general parametric average-value of the uncontrolled rectifier presented in [29] and the model used for estimating MG field current presented in [116], frequency of the rectifier input voltages and consequently the commutation voltage drops are not considered. In these models, a single parametric coefficient establishes the relationships

between AC- and DC-sides of the rectifier. Using the presented equations of the rectifier output voltage average-value in Chapter .6, it is possible to include commutation effects in the model of the parametric model of the rectifier based on the frequency of input voltages.

- **Developing DP-domain model of the three-stage brushless synchronous starter-generator.**

As described in Chapter. 4, in modeling of the inductances, some harmonics are of more importance. This is valid also for the voltages and currents. Using DP-domain representation of the machine variables (inductances, voltages, and currents), it is possible to develop a model of the three-stage brushless synchronous starter-generator in DP-domain with capability of selecting harmonics of interest. For example, MG field current can be represented by its DC component (zero order DP). In addition, in DP-domain derivatives are represented as multiplication terms leading to a simple average modelling by avoiding time-domain derivatives.

- **Using MG field current estimation technique in torque control system.**

As mentioned in Chapter. 7, for optimum torque control of the three-stage starter-generator, optimum combination of *d*-axis, *q*-axis and field currents of MG is required. In this case, MTPA profile should be a 3-D look-up table which its outputs are *d*-axis, *q*-axis and field currents of the MG. Using the proposed method in Chapter. 7, it is possible to estimate the MG field current and then control it in accordance with the reference value of the MG field current obtained from the MTPA profile.

References

[1] N. Nagel, "Actuation Challenges in the More Electric Aircraft: Overcoming Hurdles in the Electrification of Actuation Systems," in IEEE Electrification Magazine, vol. 5, no. 4, pp. 38-45, Dec. 2017.

[2] Briere, D., and Traverse, P. AIRBUS A320/A330/A340 electrical flight controls - A family of fault-tolerant systems. In Fault-Tolerant Computing, 1993 (FTCS-23). The Twenty-Third International Symposium on Digest of Papers, June 22-24, 1993, 616–623.

[3] Ian Moir, Allan Seabridge. Aircraft Systems. England, John Wiley, 2008.

[4] M. Sinnett. (2007). 787 no-bleed systems: Saving fuel and enhancing operational efficiencies. Aero Quarterly. [Online]. pp. 1–11. Available: http://www.boeing.com/commercial/aeromagazine/articles/qtr_4_07/AERO_Q407_article2.pdf.

[5] P. Wheeler and S. Bozhko, "The More Electric Aircraft: Technology and challenges.," in *IEEE Electrification Magazine*, vol. 2, no. 4, pp. 6-12, Dec. 2014.

[6] Jie Chang and Anhua Wang, "New VF-power system architecture and evaluation for future aircraft," in *IEEE Transactions on Aerospace and Electronic Systems*, vol. 42, no. 2, pp. 527-539, April 2006.

[7] Y. Jia and K. Rajashekara, "Induction Machine for More Electric Aircraft: Enabling New Electrical Power System Architectures," in *IEEE Electrification Magazine*, vol. 5, no. 4, pp. 25-37, Dec. 2017.

[8] J. A. Rosero, J. A. Ortega, E. Aldabas and L. Romeral, "Moving towards a more electric aircraft," in *IEEE Aerospace and Electronic Systems Magazine*, vol. 22, no. 3, pp. 3-9, March 2007.

[9] J. Chen, C. Wang and J. Chen, "Investigation on the Selection of Electric Power System Architecture for Future More Electric Aircraft," in *IEEE Transactions on Transportation Electrification*.

[10] P. R. Wilson, "Advanced aircraft power electronics systems — The impact of simulation, standards and wide band-gap devices," in *CES Transactions on Electrical Machines and Systems*, vol. 1, no. 1, pp. 72-82, March 2017.

[11] M. Guacci, D. Bortis, I. F. Kovačević-Badstübner, U. Grossner and J. W. Kolar, "Analysis and design of a 1200 V All-SiC planar interconnection power module for next generation more electrical aircraft power electronic building

blocks," in *CPSS Transactions on Power Electronics and Applications*, vol. 2, no. 4, pp. 320-330, December 2017.

[12] Reyad Abdel-Fadil, Ahmad Eid, Mazen Abdel-Salam, "Electrical distribution power systems of modern civil sircrafts," in *2ndInternational Conference on Energy systems and Technologies,* pp. 201-210, Egypt, February 2013.

[13] Z. Zhang, J. Li, Y. Liu, Y. Xu and Y. Yan, "Overview and development of variable frequency AC generators for more electric aircraft generation system," in *Chinese Journal of Electrical Engineering*, vol. 3, no. 2, pp. 32-40, September 2017.

[14] Y. Jia and K. Rajashekara, "An Induction Generator-Based AC/DC Hybrid Electric Power Generation System for More Electric Aircraft," in *IEEE Transactions on Industry Applications*, vol. 53, no. 3, pp. 2485-2494, May-June 2017.

[15] T. Yang, S. Bozhko, J. M. Le-Peuvedic, G. Asher and C. I. Hill, "Dynamic Phasor Modeling of Multi-Generator Variable Frequency Electrical Power Systems," in *IEEE Transactions on Power Systems*, vol. 31, no. 1, pp. 563-571, Jan. 2016.

[16] E. Ganev, "Selecting the Best Electric Machines for Electrical Power-Generation Systems: High-performance solutions for aerospace More electric architectures.," in *IEEE Electrification Magazine*, vol. 2, no. 4, pp. 13-22, Dec. 2014.

[17] F. Bu, S. Zhuang, W. Huang, N. Su and Y. Hu, "Asymmetrical Operation Analysis for Dual Stator-Winding Induction Generator Variable Frequency AC Generating System With Unbalanced Loads," in *IEEE Transactions on Industrial Electronics*, vol. 64, no. 1, pp. 52-59, Jan. 2017.

[18] Haitham Abu-Rub, Mariusz Malinowski and Kamal Al-Haddad, " Power Electronics for Renewable Energy Systems, Transportation and Industrial Applications, John Wiley, 2014.

[19] A. Baghramian, A. Cross and A. Forsyth, "Interactions within heterogeneous systems of uncontrolled rectifiers for aircraft electrical power systems," in *IET Electrical Systems in Transportation*, vol. 1, no. 1, pp. 49-60, March 2011.

[20] H. Zhu *et al*., "Average modeling of three-phase and nine-phase diode rectifiers with improved AC current and DC voltage dynamics," *31st Annual Conference of IEEE Industrial Electronics Society, 2005. IECON 2005.*, Raleigh, NC, 2005, pp. 6 pp

[21] F. J. Chivite-Zabalza and A. J. Forsyth, "A Passive 36-Pulse AC–DC Converter With Inherent Load Balancing Using Combined Harmonic Voltage And

Current Injection," in *IEEE Transactions on Power Electronics*, vol. 22, no. 3, pp. 1027-1035, May 2007.

[22] A. Cross, A. Baghramian and A. Forsyth, "Approximate, average, dynamic models of uncontrolled rectifiers for aircraft applications," in *IET Power Electronics*, vol. 2, no. 4, pp. 398-409, July 2009.

[23] M. F. Iacchetti, G. M. Foglia, A. Di Gerlando and A. J. Forsyth, "Analytical Evaluation of Surface-Mounted PMSG Performances Connected to a Diode Rectifier," in *IEEE Transactions on Energy Conversion*, vol. 30, no. 4, pp. 1367-1375, Dec. 2015.

[24] J. Jatskevich and T. Aboul-Seoud, "Impedance characterization of a six-phase synchronous generator-rectifier system using average-value model," *Canadian Conference on Electrical and Computer Engineering 2004 (IEEE Cat. No.04CH37513)*, 2004, pp. 2231-2234 Vol.4.

[25] I. Jadric, D. Borojevic and M. Jadric, "Modeling and control of a synchronous generator with an active DC load," in *IEEE Transactions on Power Electronics*, vol. 15, no. 2, pp. 303-311, Mar 2000.

[26] I. Jadric, D. Borojevic and M. Jadric, "A simplified model of a variable speed synchronous generator loaded with diode rectifier," *PESC97. Record 28th Annual IEEE Power Electronics Specialists Conference. Formerly Power Conditioning Specialists Conference 1970-71. Power Processing and Electronic Specialists Conference 1972*, St. Louis, MO, 1997, pp. 497-502 vol.1.

[27] S. Chiniforoosh *et al*., "Steady-state and dynamic performance of front-end diode rectifier loads as predicted by dynamic average-value models," *2014 IEEE PES General Meeting | Conference & Exposition*, National Harbor, MD, 2014, pp. 1-1.

[28] Y. Zhang and A. M. Cramer, "Numerical Average-Value Modeling of Rotating Rectifiers in Brushless Excitation Systems," in *IEEE Transactions on Energy Conversion*, vol. 32, no. 4, pp. 1592-1601, Dec. 2017

[29] J. Jatskevich, S. D. Pekarek and A. Davoudi, "Parametric average-value model of synchronous machine-rectifier systems," in *IEEE Transactions on Energy Conversion*, vol. 21, no. 1, pp. 9-18, March 2006.

[30] H. Atighechi, S. Chiniforoosh, S. Ebrahimi and J. Jatskevich, "Using Multiple Reference Frame Theory for Considering Harmonics in Average-Value Modeling of Diode Rectifiers," in *IEEE Transactions on Energy Conversion*, vol. 31, no. 3, pp. 872-881, Sept. 2016.

[31] J. Jatskevich, S. D. Pekarek and A. Davoudi, "Fast procedure for constructing an accurate dynamic average-value model of synchronous machine-rectifier

systems," in *IEEE Transactions on Energy Conversion*, vol. 21, no. 2, pp. 435-441, June 2006.

[32] S. Ebrahimi, N. Amiri, H. Atighechi, Y. Huang, L. Wang and J. Jatskevich, "Generalized Parametric Average-Value Model of Line-Commutated Rectifiers Considering AC Harmonics With Variable Frequency Operation," in *IEEE Transactions on Energy Conversion*, vol. 33, no. 1, pp. 341-353, March 2018.

[33] Predrag Pejovic,"Three-phase diode rectifiers with low harmonics,"Spring ,2007

[34] M. A. Elizondo, F. K. Tuffner and K. P. Schneider, "Simulation of Inrush Dynamics for Unbalanced Distribution Systems Using Dynamic-Phasor Models," in *IEEE Transactions on Power Systems*, vol. 32, no. 1, pp. 633-642, Jan. 2017.

[35] H. Ye and K. Strunz, "Multi-Scale and Frequency-Dependent Modeling of Electric Power Transmission Lines," in *IEEE Transactions on Power Delivery*, vol. 33, no. 1, pp. 32-41, Feb. 2018.

[36] K. Mudunkotuwa, S. Filizadeh and U. Annakkage, "Development of a hybrid simulator by interfacing dynamic phasors with electromagnetic transient simulation," in *IET Generation, Transmission & Distribution*, vol. 11, no. 12, pp. 2991-3001, 8 24 2017.

[37] C. Narduzzi, M. Bertocco, G. Frigo and G. Giorgi, "Fast-TFM--Multifrequency Phasor Measurement for Distribution Networks," in *IEEE Transactions on Instrumentation and Measurement*.

[38] T. Yang, S. Bozhko and G. Asher, "Fast functional modelling of diode-bridge rectifier using dynamic phasors," in *IET Power Electronics*, vol. 8, no. 6, pp. 947-956, 6 2015.

[39] T. Wu, S. V. Bozhko, G. M. Asher and D. W. P. Thomas, "A fast dynamic phasor model of autotransformer rectifier unit for more electric aircraft," *2009 35th Annual Conference of IEEE Industrial Electronics*, Porto, 2009, pp. 2531-2536.

[40] L. Wei, N. N. Guskov, R. A. Lukaszewski and G. L. Skibinski, "Mitigation of Current Harmonics for Multipulse Diode Front-End Rectifier Systems," in *IEEE Transactions on Industry Applications*, vol. 43, no. 3, pp. 787-797, May-june 2007.

[41] Seung-Gi Jeong and Ju-Yeop Choi, "Line current characteristics of three-phase uncontrolled rectifiers under line voltage unbalance condition," in *IEEE Transactions on Power Electronics*, vol. 17, no. 6, pp. 935-945, Nov 2002.

[42] D. Basic, "Input Current Interharmonics of Variable-Speed Drives due to Motor Current Imbalance," in *IEEE Transactions on Power Delivery*, vol. 25, no. 4, pp. 2797-2806, Oct. 2010.

[43] S. Chiniforoosh *et al*., "Dynamic Average Modeling of Front-End Diode Rectifier Loads Considering Discontinuous Conduction Mode and Unbalanced Operation," in *IEEE Transactions on Power Delivery*, vol. 27, no. 1, pp. 421-429, Jan. 2012.

[44] Y. Huang, L. Dong, S. Ebrahimi, N. Amiri and J. Jatskevich, "Dynamic Phasor Modeling of Line-Commutated Rectifiers With Harmonics Using Analytical and Parametric Approaches," in *IEEE Transactions on Energy Conversion*, vol. 32, no. 2, pp. 534-547, June 2017.

[45] R. Stoicescu, K. Miu, C. O. Nwankpa, D. Niebur and Xiaoguang Yang, "Three-phase converter models for unbalanced radial power-flow studies," in *IEEE Transactions on Power Systems*, vol. 17, no. 4, pp. 1016-1021, Nov. 2002.

[46] M. Bauta and M. Grotzbach, "Noncharacteristic line harmonics of AC/DC converters with high DC current ripple," in *IEEE Transactions on Power Delivery*, vol. 15, no. 3, pp. 1060-1066, Jul 2000.

[47] R. L. Witzke, J. V. Kresser and J. K. Dillard, "Influence of A-C reactance on voltage regulation of 6-phase rectifiers," in *Transactions of the American Institute of Electrical Engineers, Part I: Communication and Electronics*, vol. 72, no. 3, pp. 244-253, July 1953.

[48] C. Liu, A. Bose and P. Tian, "Modeling and Analysis of HVDC Converter by Three-Phase Dynamic Phasor," in *IEEE Transactions on Power Delivery*, vol. 29, no. 1, pp. 3-12, Feb. 2014.

[49] J. G. Mayordomo, L. F. Beites, Á. Carbonero, X. Yang and W. Xu, "An Analytical Procedure for Calculating Harmonics of Three-Phase Uncontrolled Rectifiers Under Nonideal Conditions," in *IEEE Transactions on Power Delivery*, vol. 30, no. 1, pp. 144-152, Feb. 2015.

[50] H. Shin, Y. Son and J. I. Ha, "Grid Current Shaping Method with DC-Link Shunt Compensator for Three-Phase Diode Rectifier-Fed Motor Drive System," in *IEEE Transactions on Power Electronics*, vol. 32, no. 2, pp. 1279-1288, Feb. 2017.

[51] A. Testa *et al*., "Interharmonics: Theory and Modeling," in *IEEE Transactions on Power Delivery*, vol. 22, no. 4, pp. 2335-2348, Oct. 2007.

[52] L. Hu and R. Yacamini, "Harmonic transfer through converters and HVDC links," in *IEEE Transactions on Power Electronics*, vol. 7, no. 3, pp. 514-525, Jul 1992.

[53] Y. Sun, C. Dai, J. Li and J. Yong, "Frequency-domain harmonic matrix model for three-phase diode-bridge rectifier," in *IET Generation, Transmission & Distribution*, vol. 10, no. 7, pp. 1605-1614, 5 5 2016.

[54] Z. Bing and J. Sun, "Frequency-Domain Modeling of Multipulse Converters by Double-Fourier Series Method," in *IEEE Transactions on Power Electronics*, vol. 26, no. 12, pp. 3804-3809, Dec. 2011.

[55] A, Deriszadeh and R. Bojoi, "A Phase Variable Model of Aircraft Brushless Exciter Based on Finite Element Analysis and Its Coupling with the Rotating Rectifier Circuit," International Journal of Applied Engineering Research., vol. 13, no. 2, pp. 1238-1246, February, 2018.

[56] S. Nadarajan, S. K. Panda, B. Bhangu, and A. K. Gupta, "Hybrid Model for Wound-Rotor Synchronous Generator to Detect and Diagnose Turn-to-Turn Short-Circuit Fault in Stator Windings," IEEE Trans. Ind. Elec., vol. 62, no. 3, pp. 1888-1900, March 2015

[57] C. Anghel, "A novel start system for an aircraft auxiliary power unit", Conf. Rec. 35th Intersociety Energy Conversion Engineering Conf. and Exhibit, Las Vegas, NV, USA, 24-28 July 2000, Volume: 1, pp. 7 – 11.

[**58]** N. Mohan, T.M. Undeland, W.P. Robbins, "Power electronics: converters, applications and design", New Jersey, John Wiley & Sons, INC, 2003.

[59] A. Darabi and C. Tindall, "Brushless exciter modeling for small salient pole alternators using finite elements," in IEEE Transactions on Energy Conversion, vol. 17, no. 3, pp. 306-312, Sep 2002.

[60] V. Ruuskanen, M. Niemela, J. Pyrhonen, S. Kanerva and J. Kaukonen, "Modelling the brushless excitation system for a synchronous machine," in IET Electric Power Applications, vol. 3, no. 3, pp. 231-239, May 2009.

[61] Y. Zhang and A. M. Cramer, "Numerical Average-Value Modeling of Rotating Rectifiers in Brushless Excitation Systems," in IEEE Transactions on Energy Conversion, vol. 32, no. 4, pp. 1592-1601, Dec. 2017.

[62] J. Jatskevich, S. D. Pekarek and A. Davoudi, "Fast procedure for constructing an accurate dynamic average-value model of synchronous machine-rectifier systems," in IEEE Transactions on Energy Conversion, vol. 21, no. 2, pp. 435-441, June 2006.

[63] J. Jatskevich, S. D. Pekarek and A. Davoudi, "Parametric average-value model of synchronous machine-rectifier systems," in IEEE Transactions on Energy Conversion, vol. 21, no. 1, pp. 9-18, March 2006.

[64] J. Jatskevich and S. D. Pekarek, "Numerical Validation of Parametric Average-Value Modeling of Synchronous Machine–Rectifier Systems for Variable Frequency Operation," in IEEE Transactions on Energy Conversion, vol. 23, no. 1, pp. 342-344, March 2008.

[65] N. Jiao, W. Liu, Z. Zhang, T. Meng, J. Peng and Y. Jiang, "Field Current Estimation for Wound-Rotor Synchronous Starter–Generator With Asynchronous Brushless Exciters," in IEEE Transactions on Energy Conversion, vol. 32, no. 4, pp. 1554-1561, Dec. 2017.

[66] A. Bernard, G. Ronald, Pr. Harley, "The General Theory of Alternating Current Machines: Application to Practical Problems", Springer Netherlands, 1978.

[67] C. N. Ashtiani and D. A. Lowther, "Simulation of the Transient and Subtransient Reactances of a Large Hydrogenerator by Finite Elements," IEEE Transactions on Power Apparatus and Systems, vol. PAS-103, no. 7, pp. 1788-1794, July 1984.

[68] A. Boglietti, A. Cavagnino and M. Lazzari, "Computational Algorithms for Induction-Motor Equivalent Circuit Parameter Determination—Part I: Resistances and Leakage Reactances," in IEEE Transactions on Industrial Electronics, vol. 58, no. 9, pp. 3723-3733, Sept. 2011.

[69] B. Fahimi, G. Suresh, J. Mahdavi and M. Ehsami, "A new approach to model switched reluctance motor drive application to dynamic performance prediction, control and design," *PESC 98 Record. 29th Annual IEEE Power Electronics Specialists Conference (Cat. No.98CH36196)*, Fukuoka, 1998, pp. 2097-2102 vol.2.

[70] A. Khalil and I. Husain, "A Fourier Series Generalized Geometry-Based Analytical Model of Switched Reluctance Machines," in *IEEE Transactions on Industry Applications*, vol. 43, no. 3, pp. 673-684, May-june 2007.

[71] R. Dutta, M. F. Rahman and L. Chong, "Winding Inductances of an Interior Permanent Magnet (IPM) Machine With Fractional Slot Concentrated Winding," in *IEEE Transactions on Magnetics*, vol. 48, no. 12, pp. 4842-4849, Dec. 2012.

[72] Z. Q. Zhu, B. Lee, L. Huang and W. Chu, "Contribution of Current Harmonics to Average Torque and Torque Ripple in Switched Reluctance Machines," in *IEEE Transactions on Magnetics*, vol. 53, no. 3, pp. 1-9, March 2017.

[73] W. Q. Chu, Z. Q. Zhu, J. Zhang, X. Liu, D. A. Stone and M. P. Foster, "Investigation on Operational Envelops and Efficiency Maps of Electrically Excited Machines for Electrical Vehicle Applications," in *IEEE Transactions on Magnetics*, vol. 51, no. 4, pp. 1-10, April 2015.

[74] J. de Santiago *et al*., "Electrical Motor Drivelines in Commercial All-Electric Vehicles: A Review," in *IEEE Transactions on Vehicular Technology*, vol. 61, no. 2, pp. 475-484, Feb. 2012.

[75] A. M. El-Refaie, "Motors/generators for traction/propulsion applications: A review," in *IEEE Vehicular Technology Magazine*, vol. 8, no. 1, pp. 90-99, March 2013.

[76] C. Rossi, D. Casadei, A. Pilati and M. Marano, "Wound Rotor Salient Pole Synchronous Machine Drive for Electric Traction," *Conference Record of the 2006 IEEE Industry Applications Conference Forty-First IAS Annual Meeting*, Tampa, FL, 2006, pp. 1235-1241.

[77] Y. Nie, I. P. Brown and D. C. Ludois, "Deadbeat-Direct Torque and Flux Control for Wound Field Synchronous Machines," in *IEEE Transactions on Industrial Electronics*, vol. 65, no. 3, pp. 2069-2079, March 2018

[78] W. Q. Chu *et al*., "Computationally efficient method and investigation of operational envelopes of hybrid and electrically excited machines," *2014 Ninth International Conference on Ecological Vehicles and Renewable Energies (EVER)*, Monte-Carlo, 2014, pp. 1-5.

[79] Y. Amara, L. Vido, M. Gabsi, E. Hoang, A. H. Ben Ahmed and M. Lecrivain, "Hybrid Excitation Synchronous Machines: Energy-Efficient Solution for Vehicles Propulsion," in *IEEE Transactions on Vehicular Technology*, vol. 58, no. 5, pp. 2137-2149, Jun 2009.

[80] E. Armando, R. Bojoi, P. Guglielmi, G. Pellegrino and M. Pastorelli, "Experimental methods for synchronous machines evaluation by an accurate magnetic model identification," *2011 IEEE Energy Conversion Congress and Exposition*, Phoenix, AZ, 2011, pp. 1744-1749.

[81] S. Hall, F. J. Márquez-Fernández and M. Alaküla, "Dynamic Magnetic Model Identification of Permanent Magnet Synchronous Machines," in *IEEE Transactions on Energy Conversion*, vol. 32, no. 4, pp. 1367-1375, Dec. 2017.

[82] S. Wiedemann, S. Hall, R. M. Kennel and M. Alaküla, "Dynamic Testing Characterization of a Synchronous Reluctance Machine," in *IEEE Transactions on Industry Applications*, vol. 54, no. 2, pp. 1370-1378, March-April 2018.

[83] G. Pellegrino, B. Boazzo and T. M. Jahns, "Magnetic Model Self-Identification for PM Synchronous Machine Drives," in *IEEE Transactions on Industry Applications*, vol. 51, no. 3, pp. 2246-2254, May-June 2015.

[84] S. A. Odhano, R. Bojoi, Ş. G. Roşu and A. Tenconi, "Identification of the Magnetic Model of Permanent-Magnet Synchronous Machines Using DC-Biased Low-Frequency AC Signal Injection," in *IEEE Transactions on Industry Applications*, vol. 51, no. 4, pp. 3208-3215, July-Aug. 2015.

[85] S. A. Odhano *et al*., "Identification of Three-Phase IPM Machine Parameters Using Torque Tests," in *IEEE Transactions on Industry Applications*, vol. 53, no. 3, pp. 1883-1891, May-June 2017.

[86] S. A. Odhano, R. Bojoi, M. Popescu and A. Tenconi, "Parameter identification and self-commissioning of AC permanent magnet machines - A review," *2015 IEEE Workshop on Electrical Machines Design, Control and Diagnosis (WEMDCD)*, Torino, 2015, pp. 195-203.

[87] S. A. Odhano, P. Giangrande, R. I. Bojoi and C. Gerada, "Self-Commissioning of Interior Permanent- Magnet Synchronous Motor Drives With High-Frequency Current Injection," in *IEEE Transactions on Industry Applications*, vol. 50, no. 5, pp. 3295-3303, Sept.-Oct. 2014.

[88] E. Armando, P. Guglielmi, G. Pellegrino and R. Bojoi, "Flux linkage maps identification of synchronous AC motors under controlled thermal conditions," *2017 IEEE International Electric Machines and Drives Conference (IEMDC)*, Miami, FL, 2017, pp. 1-8.

[89] S. A. Odhano *et al*., "Parameter extraction for three phase IPM machines through simple torque tests," *2015 IEEE Energy Conversion Congress and Exposition (ECCE)*, Montreal, QC, 2015, pp. 1892-1898.

[90] A. Cavagnino, R. Bojoi, Z. Gmyrek and M. Lefik, "Stator Lamination Geometry Influence on the Building Factor of Synchronous Reluctance Motor Cores," in *IEEE Transactions on Industry Applications*, vol. 53, no. 4, pp. 3394-3403, July-Aug. 2017.

[91] R. Bojoi, A. Cavagnino, M. Cossale and S. Vaschetto, "Methodology for the IPM motor magnetic model computation based on finite element analysis," *IECON 2014 - 40th Annual Conference of the IEEE Industrial Electronics Society*, Dallas, TX, 2014, pp. 722-728.

[92] S. A. Odhano, R. Bojoi, Ş. G. Roşu and A. Tenconi, "Identification of the Magnetic Model of Permanent-Magnet Synchronous Machines Using DC-Biased Low-Frequency AC Signal Injection," in *IEEE Transactions on Industry Applications*, vol. 51, no. 4, pp. 3208-3215, July-Aug. 2015.

[93] S. Nadarajan, S. K. Panda, B. Bhangu, and A. K. Gupta, "Online Model-Based Condition Monitoring for Brushless Wound-Field Synchronous Generator to Detect and Diagnose Stator Windings Turn-to-Turn Shorts Using Extended Kalman Filter," *IEEE Trans. Ind. Elec.*, vol. 63, no. 5, pp. 3228-3241, May 2016.

[94] S. Nadarajan, S. K. Panda, B. Bhangu, and A. K. Gupta, "Hybrid Model for Wound-Rotor Synchronous Generator to Detect and Diagnose Turn-to-Turn Short-Circuit Fault in Stator Windings," *IEEE Trans. Ind. Elec.*, vol. 62, no. 3, pp. 1888-1900, March 2015.

[95] A. Griffo, D. Drury, T. Sawata, and P. H. Mellor, "Sensorless starting of a wound-field synchronous starter/generator for aerospace applications," *IEEE Trans. Ind. Elec.*, vol. 59, no. 9, pp. 3579-3587, Sept. 2012.

[96] C. Anghel, "A novel start system for an aircraft auxiliary power unit", *Conf. Rec. 35th Intersociety Energy Conversion Engineering Conf. and Exhibit*, Las Vegas, NV, USA, 24-28 July 2000, Volume: 1, pp. 7 – 11.

[97] A. Maalouf, M. Wissem Naouar, E. Monmasson, A. A. Naassani, S. Leballois and J. Y. midy, "Digital control of a brushless excitation synchronous starter/generator in the generation mode," *34th Annual Conf. of IEEE Ind. Elec.*, Orlando, FL, 2008, pp. 1155-1160.

[98] A. Griffo, R. Wrobel, P.H. Mellor, and J.M. Yon, "Design and Characterization of a Three-Phase Brushless Exciter for Aircraft Starter/Generator", *IEEE Trans. Ind. Appl.*, Vol.49, No.5, pp.2100-2115, 2013.

[99] H. Huang, D. Karipides, M. Abbas, and D. Tsui, "Aircraft Engine Starter/Generator and Controller", US Patent US 2009/0174188 A1, 2009.

[100] D. N. Teneja, H. Huang, G. A. Padgett, J. Zywot, P. J. Wirsch, and M. A. Abbas, "Dual-structured Aircraft Engine Starter/Generator", US Patent 7687928 B2, 2010.

[101] N. Jiao, W. Liu, Z. Zhang, T. Meng, J. Peng, and Y. Jiang, "Field Current Estimation for Wound-Rotor Synchronous Starter-Generator with Asynchronous Brushless Exciters," *IEEE Trans. on Energy Conversion*, vol.PP, no.99, pp.1-1

[102] Z. Zhang, W. Liu, D. Zhao, S. Mao, T. Meng and N. Jiao, "Steady-state performance evaluations of three-phase brushless asynchronous excitation system for aircraft starter/generator," *IET Electric Power Applications*, vol. 10, no. 8, pp. 788-798, 9 2016.

[103] V. Ruuskanen, M. Niemela, J. Pyrhonen, S. Kanerva and J. Kaukonen, "Modelling the brushless excitation system for a synchronous machine," *IET Elec Power Appl*, vol. 3, no. 3, pp. 231-239, May 2009.

[104] A. Maalouf, L. Idkhajine, S. L. Ballois and E. Monmasson, "Field programmable gate array-based sensorless control of a brushless synchronous starter generator for aircraft application", *IET Electric Power Applications*, vol. 5, no. 1, pp. 181-192, January 2011.

[105] R. H. Williams, M. P. Foster, D. A. Stone and S. R. Minshull, "Utilizing existing aircraft wound field generators for starter-generators," Conf. Rec ECCE Asia, Jeju, 2011, pp. 691-696.

[106] N. Jiao, W. Liu, T. Meng, J. Peng and S. Mao, "Design and Control of a Two-Phase Brushless Exciter for Aircraft Wound-Rotor Synchronous Starter/Generator in the Starting Mode," *IEEE Trans. Power Electron*., vol. 31, no. 6, pp. 4452-4461, June 2016.

[107] Marouchos, C. C.: 'The Switching Function: analysis of power electronic circuits' (Circuits, Devices and Systems, 2006).

[108] 'Elliptic Integral – Wikipedia', https://en.wikipedia.org/wiki/Elliptic_integral#Incomplete_elliptic_integral_of_the_second_kind

[109] O. N. Acosta, "Interphase Transformer for Multiple Connected Power Rectifiers," *IEEE Transactions on Industry and General Applications*, vol. IGA-1, no. 6, pp. 423-428, Nov. 1965.

[110] Mohan, N., Undeland, T.M., Robbins, W.P.: 'Power electronics: converters, applications and design' (New Jersey, John Wiley & Sons, INC, 2003).

[111] D. X. Llano, S. Abdi, M. Tatlow, E. Abdi and R. A. McMahon, "Energy harvesting and wireless data transmission system for rotor instrumentation in electrical machines," in *IET Power Electronics*, vol. 10, no. 11, pp. 1259-1267, 9 9 2017.

[112] E. Abdi-Jalebi and R. McMahon, "Application of Real-Time Rotor Current Measurements Using Bluetooth Wireless Technology in Study of the Brushless Doubly-Fed (Induction) Machine (BDFM)," *Conference Record of the 2006 IEEE Industry Applications Conference Forty-First IAS Annual Meeting*, Tampa, FL, 2006, pp. 1557-1561.

[113] P. S. Kumar, L. Xie, K. Thiha, B. H. Soong, V. Vaiyapuri and S. Nadarajan, "Rotor mounted wireless sensors for condition monitoring of brushless synchronous generator," *IECON 2017 - 43rd Annual Conference of the IEEE Industrial Electronics Society*, Beijing, 2017, pp. 3221-3226.

[114] M. Bergeron, J. Cros, J. Niehenke, J. R. Figueroa and C. Messier, "Hydro Generator Damper Bar Current Measurement at Wanapum Dam," in *IEEE Transactions on Energy Conversion*, vol. 31, no. 4, pp. 1510-1520, Dec. 2016.

[115] P. C. Kjaer, T. Kjellqvist and C. Delaloye, "Estimation of field current in vector-controlled synchronous machine variable-speed drives employing brushless asynchronous exciters," in *IEEE Transactions on Industry Applications*, vol. 41, no. 3, pp. 834-840, May-June 2005.

[116] N. Jiao, W. Liu, Z. Zhang, T. Meng, J. Peng and Y. Jiang, "Field Current Estimation for Wound-Rotor Synchronous Starter–Generator With Asynchronous Brushless Exciters," in *IEEE Transactions on Energy Conversion*, vol. 32, no. 4, pp. 1554-1561, Dec. 2017.

[117] S. Lu and X. Wang, "A New Methodology to Estimate the Rotating Phase of a BLDC Motor With Its Application in Variable-Speed Bearing Fault Diagnosis," in *IEEE Transactions on Power Electronics*, vol. 33, no. 4, pp. 3399-3410, April 2018.

[118] C. Wang, X. Liu and Z. Chen, "Incipient Stator Insulation Fault Detection of Permanent Magnet Synchronous Wind Generators Based on Hilbert–Huang Transformation," in *IEEE Transactions on Magnetics*, vol. 50, no. 11, pp. 1-4, Nov. 2014.

[119] A. G. Espinosa, J. A. Rosero, J. Cusidó, L. Romeral and J. A. Ortega, "Fault Detection by Means of Hilbert–Huang Transform of the Stator Current in a PMSM With Demagnetization," in *IEEE Transactions on Energy Conversion*, vol. 25, no. 2, pp. 312-318, June 2010.

Doctoral Dissertation
Doctoral Program in Electrical, Electronics and Communication Engineering
(30th Cycle)

Analysis, Modeling and Excitation Control of Three-Stage Brushless Starter-Generators for Aircraft Applications

Adel Deriszadeh

Supervisors
Prof. Radu Bojoi, Supervisor
Prof. Alberto Tenconi, Co-Supervisor

Doctoral Examination Committee:
Prof. Angelo Tani, Referee, Università di Bologna
Prof. Davide Barater, Referee, Università di Modena e Reggio Emilia

Politecnico di Torino
April 30, 2018